Gene discovery and mechanism of disease in the myopathies

Heather Best

Primary supervisor: A/Prof Sandra Cooper

Associate supervisors: The Late A/Prof Nigel Clarke, Dr Michaela Yuen and Dr Frances Lemckert

A thesis submitted in fulfilment of the requirements for the degree of Doctor of Philosophy

The Institute for Neuroscience and Muscle Research

The Children's Hospital at Westmead, Sydney, NSW, Australia

Discipline of Child and Adolescent Health, Faculty of Medicine

The University of Sydney, NSW, Australia

February 2018

STATEMENT OF ORIGINALITY

The contents of this thesis have not been presented for the award of a degree or diploma at this or any other university. The data presented are the original work of the author except where specifically indicated in the text.

AUTHOR CONTRIBUTION

Chapter 2 Part A of this thesis is published as:

O'Grady, G. L., **Best, H.A.,** Oates, E.C., Kaur, S., Charlton, A., Brammah, S., Punetha, J., Kesari, A., North, K.N., Ilkovsli, B., Hoffman, E.P., Clarke, N.F. (2015). "Recessive ACTA1 variant causes congenital muscular dystrophy with rigid spine." Eur J Hum Genet **23**, 883-886

Heather Best carried out the functional characterisation of the *ACTA1* variant which became Figure 2 E-L of our publication. Heather contributed to drafting/revising the manuscript.
NB: Dr Gina O'Grady's PhD thesis included this publication. Dr O'Grady collated the clinical data for Patient 1 and 2, interpreted NGS results, drafted the manuscript, constructed the figures, and managed all aspects of paper submission.

Chapter 4 Part A of this thesis is published as:

O'Grady, G. L., [α] **H. A. Best, [α]** T. E. Sztal, [α] V. Schartner, [#] M. Sanjuan-Vazquez, [#] S. Donkervoort, [#] O. Abath Neto, R. B. Sutton, B. Ilkovski, N. B. Romero, T. Stojkovic, J. Dastgir, L. B. Waddell, A. Boland, Y. Hu, C. Williams, A. A. Ruparelia, T. Maisonobe, A. J. Peduto, S. W. Reddel, M. Lek, T. Tukiainen, B. B. Cummings, H. Joshi, J. Nectoux, S. Brammah, J. F. Deleuze, V. O. Ing, G. Ramm, D. Ardicli, K. J. Nowak, B. Talim, H. Topaloglu, N. G. Laing, K. N. North, D. G. MacArthur, S. Friant, N. F. Clarke, R. J. Bryson-Richardson, C. G. Bonnemann, J. Laporte[§] and S. T. Cooper[§] (2016). "Variants in the Oxidoreductase PYROXD1 Cause Early-Onset Myopathy with Internalized Nuclei and Myofibrillar Disorganization." Am J Hum Genet **99**(5): 1086-1105.
[α] These authors jointly share first authorship
[#] These authors jointly share second authorship
[§] These authors jointly share senior authorship

This publication was the result of collaboration between multiple international translational genomics programs establishing variants within *PYROXD1* as a new genetic cause of early onset myopathy. Heather Best was involved in the functional characterisation of *PYROXD1*. Heather developed and optimised lab tools to study PYROXD1 and subsequently performed characterisation of patient variants at the molecular genetic and protein level. As PYROXD1 was previously uncharacterised Heather carried out localisation studies of PYROXD1 in an overexpression system as well as primary cell lines and skeletal muscle. These experiments became four and a half out of nine figures in our paper. Heather played a major role in manuscript preparation, submission and production of Figures 1, 3-6.
NB: Dr Gina O'Grady's PhD thesis included this publication. Dr O'Grady was involved in analysis of WES data for family A, reviewed the affected siblings, helped coordinate international collaboration, collated clinical data on all families (Table1) and made a significant contribution to drafting of the manuscript and preparation of Figures 1 and 2

ACKNOWLEDGEMENTS

I began my PhD journey under the primary supervision of the Late A/Prof Nigel Clarke. Late A/Prof Clarke's outstanding clinical skill and passion for pushing medical science forward has left a huge hole within the INMR and the field of gene discovery.

A/Prof Sandra Cooper was instrumental in carrying on The Late A/Prof Clarke's legacy, and whom I was fortunate to come under primary supervision of. A/Prof Cooper's drive and scientific skill are inspirational. A/Prof Cooper was a brilliant mentor to me and her support and guidance has shaped me into the scientist I am today. I appreciate the time A/Prof Cooper invested in me and am grateful for the opportunities granted.

Dr Michaela Yuen is an outstanding scientist, immensely loyal friend and whom I feel privileged to have worked alongside. Dr Yuen has been a huge support to me during my time at the INMR, guiding me through my junior scientific training with kindness and dedication. I would like to thank Dr Yuen for believing in me and supporting me through the good and bad times of my PhD.

I would like to thank Dr Biljana Ilkovski for her valuable guidance through the first year of my PhD and past and present members of the gene discovery team for their support and enabling enjoyable collaborative projects. I would also like to thank Adam Bournazos for assisting with experiments within the LMOD project.

I am grateful to Dr Frances Lemckert who helped me navigate the world of mouse work with patience and enthusiasm. Prof Patrick Tam, Dr Nicolas Fossat and Vanessa Jones at the Children's Medical Research Institute (CMRI) have been fantastic collaborators and I am very grateful for their help and expertise in mouse embryology. The transgenic facility at the Kids Research Institute (KRI) have been instrumental in the establishment of the Pyroxd1 mouse

project. In particular I would like to express my gratitude to Kim Hewitt and Karen Knight for their hard work in a rapidly expanding project.

I would like to thank our wonderful collaborators scattered all over the globe and the willing participation of patients and their families to the projects within this thesis. Without their support gene discovery would not be possible.

I have been very fortunate to work in a lab of talented and friendly scientists. I would like to thank past and present INMR members for creating a friendly work environment and for their support during my PhD. In particular I would like to mention Greg Redpath, Fiona Lee, Natalie Woolger and Matthew Summers.

I am grateful for the Australian Post-graduate award (APA) and Muscular Dystrophy NSW PhD Scholarship (MDNSW) for supporting me during my PhD project. I would also like to thank the Research Operations team at the KRI who have enabled an efficient working environment.

My biggest thank-you is to my family. Who have supported me through my university years and made the undertaking of this PhD possible. In particular my Mum, Christine Best, who has always encouraged me to shoot for the stars and supported me in whatever I chose to undertake. And also, my step-sister, Katherine Barnsley, who has been a huge support to me during my time in Sydney.

ABSTRACT

Congenital myopathy and muscular dystrophy are two groups of inherited muscle diseases characterised by muscle weakness, and sub-classified by hallmark pathological features within a skeletal muscle biopsy. In order to understand the pathogenesis of inherited muscle disorders, and develop or apply therapies based on mechanistic insight, one must elucidate deep knowledge of the associated gene, genetic variant and the function of the encoded protein.

This thesis focuses on three aspects of gene discovery in the inherited myopathies: (1) Identification of a novel variant and phenotype for a known disease gene; (2) understanding the functional role of a recently identified disease gene in skeletal muscle biology and disease; and (3) discovering a novel disease gene for congenital myopathy.

We identified the first recessive variant within *ACTA1* (encoding α-skeletal actin) as the genetic cause of congenital muscular dystrophy with rigid spine. This case uniquely describes recessive *ACTA1* variants where α-skeletal actin protein is expressed. The unique clinical and histological presentation expands the spectrum of *ACTA1* disease, and will help guide clinical care and future genetic diagnoses.

Our team identified *LMOD3* (leiomodin-3) as a novel disease gene for severe nemaline myopathy (NM). *KLHL40* (encoding kelch-like family member 40) is another disease gene for severe NM. A recent study suggests mouse Klhl40 protects mouse Lmod3 protein from proteasome-mediated degradation, with the mechanistic basis of *KLHL40*-NM resulting from secondary loss of LMOD3. We investigated the regulation of human LMODs by human KLHL40, and unexpectedly found evidence that disputes the central paradigm that KLHL40 protects LMOD3 from proteasome-mediated degradation.

We identified *PYROXD1* as a new genetic cause of early-onset congenital myopathy. We provide the first characterisation of *PYROXD1* as a nuclear-cytoplasmic oxidoreductase and our discovery highlights oxidative distress as a core mechanistic pathway in the myopathies. We derived a mouse model of *Pyroxd1* deficiency, determining that global loss of mouse *Pyroxd1* is embryonic lethal. We subsequently developed a mouse model with skeletal muscle knock-out of *Pyroxd1* – as a means to elucidate the role of *PYROXD1* in biology and disease.

CONFERENCE PROCEEDINGS SUPPORTING THIS THESIS

Invited oral presentations

2016, Gage Muscle Conference, Canberra, ACT, Australia
Mutations in an oxidoreductase cause early-onset myopathy
Best HA, O'Grady GL and Cooper ST

2018, MDNSW meeting, Sydney, NSW, Australia
Identifying a new genetic mechanism of muscle disease
Best HA[α], O'Grady GL[α], Sztal TE[α], Schartner V[#], Sanjuan-Vazquez M[#], Donkervoort S[#], Neto OA, Sutton RB, Ilkovski B, Romero NB, Stojkovic T, Dastgir J, Waddell LB, Boland A, Hu Y, Williams C, Maisonobe T, Peduto AJ, Reddel SW, Lek M, Tukiainen T, Cummings B, Joshi H, Nectoux J, Brammah S, Deleuze J-F, Ruparelia A, Ing VO, Ramm G, Ardicli D, Nowak KJ, Talim B, Topaloglu H, Laing NG, North KN, MacArthur DG, Friant S, Clarke NF, Bryson-Richardson RJ, Bonnemann CG, Laporte J[§], Cooper ST[§]
[α] These authors jointly share first authorship
[#] These authors jointly share second authorship
[§] These authors jointly share senior authorship

Oral conference presentations

2017, Model Organisms in Human Health Australia (MOHHA) Melbourne, Australia
PYROXD1: a novel early-onset myopathy gene, essential for life, and a key to unlock how altered redox impacts muscle pathology. This was a joint presentation with Dr Tamar Sztal
Best HA[α], O'Grady GL[α], Sztal TE[α], Schartner V[#], Sanjuan-Vazquez M[#], Donkervoort S[#], Neto OA, Sutton RB, Ilkovski B, Romero NB, Stojkovic T, Dastgir J, Waddell LB, Boland A, Hu Y, Williams C, Maisonobe T, Peduto AJ, Reddel SW, Lek M, Tukiainen T, Cummings B, Joshi H, Nectoux J, Brammah S, Deleuze J-F, Ruparelia A, Ing VO, Ramm G, Ardicli D, Nowak KJ, Talim B, Topaloglu H, Laing NG, North KN, MacArthur DG, Friant S, Clarke NF, Bryson-Richardson RJ, Bonnemann CG, Laporte J[§], Cooper ST[§]
[α] These authors jointly share first authorship
[#] These authors jointly share second authorship
[§] These authors jointly share senior authorship

2017, NSW and ACT Cell & Developmental Biology Meeting (ANZSCB), Sydney,Australia,
PYROXD1: a novel early-onset myopathy gene. Previously undescribed, essential for life and a key to unlock how altered redox impacts muscle pathology.
Best HA[α], O'Grady GL[α], Sztal TE[α], Schartner V[#], Sanjuan-Vazquez M[#], Donkervoort S[#], Neto OA, Sutton RB, Ilkovski B, Romero NB, Stojkovic T, Dastgir J, Waddell LB, Boland A, Hu Y, Williams C, Maisonobe T, Peduto AJ, Reddel SW, Lek M, Tukiainen T, Cummings B, Joshi H, Nectoux J, Brammah S, Deleuze J-F, Ruparelia A, Ing VO, Ramm G, Ardicli D, Nowak KJ, Talim B, Topaloglu H, Laing NG, North KN, MacArthur DG, Friant S, Clarke NF, Bryson-Richardson RJ, Bonnemann CG, Laporte J[§], Cooper ST[§]
[α] These authors jointly share first authorship
[#] These authors jointly share second authorship
[§] These authors jointly share senior authorship

2016, European muscle conference, Montpellier, France
PYROXD1: a novel early-onset myopathy gene, essential for life, and a key to unlock how altered redox impacts muscle pathology
YOUNG INVESTIGATOR AWARD
Best HA[α], O'Grady GL[α], Sztal TE[α], Schartner V[#], Sanjuan-Vazquez M[#], Donkervoort S[#], Neto OA, Sutton RB, Ilkovski B, Romero NB, Stojkovic T, Dastgir J, Waddell LB, Boland A, Hu Y, Williams C, Maisonobe T, Peduto AJ, Reddel SW, Lek M, Tukiainen T, Cummings B, Joshi H, Nectoux J, Brammah S, Deleuze J-F, Ruparelia A, Ing VO, Ramm G, Ardicli D, Nowak KJ, Talim B, Topaloglu H, Laing NG, North KN, MacArthur DG, Friant S, Clarke NF, Bryson-Richardson RJ, Bonnemann CG, Laporte J[§], Cooper ST[§]
[α] These authors jointly share first authorship
[#] These authors jointly share second authorship
[§] These authors jointly share senior authorship

2014, Gage Muscle Conference, Canberra, ACT, Australia
Autosomal recessive mild muscular dystrophy caused by a novel missense mutation in α-skeletal actin
Best HA, Ilkovski B and Clarke NF

Poster conference presentations

2017, The Australian Society for Medical Research (ASMR) Annual Scientific Meeting, Sydney, NSW, Australia
PYROXD1: a novel early-onset myopathy gene, essential for life, and a key to unlock how altered redox impacts muscle pathology
Best HA[α], O'Grady GL[α], Sztal TE[α], Schartner V[#], Sanjuan-Vazquez M[#], Donkervoort S[#], Neto OA, Sutton RB, Ilkovski B, Romero NB, Stojkovic T, Dastgir J, Waddell LB, Boland A, Hu Y, Williams C, Maisonobe T, Peduto AJ, Reddel SW, Lek M, Tukiainen T, Cummings B, Joshi H, Nectoux J, Brammah S, Deleuze J-F, Ruparelia A, Ing VO, Ramm G, Ardicli D, Nowak KJ, Talim B, Topaloglu H, Laing NG, North KN, MacArthur DG, Friant S, Clarke NF, Bryson-Richardson RJ, Bonnemann CG, Laporte J[§], Cooper ST[§]
[α] These authors jointly share first authorship
[#] These authors jointly share second authorship
[§] These authors jointly share senior authorship

2016, European muscle conference 2016, Montpellier, France
PYROXD1: a novel early-onset myopathy gene, essential for life, and a key to unlock how altered redox impacts muscle pathology
YOUNG INVESTIGATOR PRIZE
Best HA[α], O'Grady GL[α], Sztal TE[α], Schartner V[#], Sanjuan-Vazquez M[#], Donkervoort S[#], Neto OA, Sutton RB, Ilkovski B, Romero NB, Stojkovic T, Dastgir J, Waddell LB, Boland A, Hu Y, Williams C, Maisonobe T, Peduto AJ, Reddel SW, Lek M, Tukiainen T, Cummings B, Joshi H, Nectoux J, Brammah S, Deleuze J-F, Ruparelia A, Ing VO, Ramm G, Ardicli D, Nowak KJ, Talim B, Topaloglu H, Laing NG, North KN, MacArthur DG, Friant S, Clarke NF, Bryson-Richardson RJ, Bonnemann CG, Laporte J[§], Cooper ST[§]
[α] These authors jointly share first authorship
[#] These authors jointly share second authorship
[§] These authors jointly share senior authorship

2015, The Australian Society for Medical Research (ASMR) Annual Scientific Meeting, Sydney, NSW, Australia
Molecular characterisation of leiomodin-3, a new disease gene for nemaline myopathy
Best HA, Yuen M, Ilkovski B, Cooper ST,Clarke NF

2014, Combio, Canberra, ACT Australia
Characterisation of differential splice isoforms of the leiomodins, a protein family recently implicated in actin filament regulation
Best HA, Yuen M, Ilkovski B, Clarke NF

ABBREVIATIONS

A-H	Actin-binding domain
ATP	adenosine triphosphatase
BACK	BTB and C-terminal kelch repeats
BCA	Bicinchoninic acid assay
bp	base pair
BSA	Bovine serum albumin
BTB/POZ	Broad complex, tramtrack and bric à brac/poxviruses and zinc finger
cDNA	Complimentary deoxyribonucleic acid
CDS	Coding sequence
CMRI	Children's medical research institute
Cul3	Cullin 3
D	Day
DAI	Double-stranded RNA-activated inhibitor
DEPC	Diethyl pyrocarbonate
DNA	Deoxyribonucleic acid
dNTP	Deoxyribonucleotide triphosphate
dsRNA	Double-stranded RNA
DTT	DL-Dithiothreitol
E	Embryonic day
E1	Ubiquitin-activating enzyme 1
E2	Ubiquitin-carrier proteins
E3	Ubiquitin-ligases
EDTA	Ethylenediaminetetraacetic acid
En2	En2 splice acceptor
F1	Generation one
F2	Generation two
F-actin	Filamentous actin
FBS	Foetal bivine serum
FRT	Flippase recognition taregt
G-actin	Globular actin
GFP	Green fluorescent protein
hBactP	Human beta actin promoter
HBSS	Hanks Balanced Salt Solution
Het	Heterozygous
HI FCS	Heat inactivated calf serum
hKLHL40	human KLHL40 expression construct
hLMOD1	human LMOD1 expression construct
hLMOD2	human LMOD2 expression construct
hLMOD3	human LMOD3 expression construct
Hom	Homozygous

IKMC	International knockout mouse consortium
INMR	The Institute for Neuroscience and muscle research
IRES	Internal ribosome entry site
kDa	Kilodalton
KLHL40/*KLHL40*	Human kelch-like family member 40 protein/gene
Klhl40/Klhl40	Mouse kelch-like family member 40 protein/gene
KLHL41/*KLHL41*	Human kelch-like family member 41 protein/gene
Klhl41/*Klhl41*	Mouse kelch-like family member 41 protein/gene
KO	Knock-out
KOMP	Knock-out mouse project
LMOD1/*LMOD1*	Human leiomodin-1 protein/gene
Lmod1/*Lmod1*	Mouse leiomodin-1 protein/gene
LMOD2/*LMOD2*	Human leiomodin-2 protein/gene
Lmod2/*Lmod2*	Mouse leiomodin-2 protein/gene
LMOD3/*LMOD3*	Human leiomodin-3 protein/gene
Lmod3/*Lmod3*	Mouse leiomodin-3 protein/gene
LoxP	Lox sequence
LRR	Leucine rich repeat
Lys	Lysine
M	Month
MEF	Myocyte enhancer factor-2
Min	Minute
mKlhl40	Mouse Klhl40 expression construct
mLmod3	Mouse Lmod3 expression construct
MQ	MilliQ
mRNA	Messenger ribonucleic acid
MRTF	Myocardin-related transcription factor
NEM	N-ethylmaleimide
Neo	Neomycin resistance gene
NES	Nuclear export signal
NLS	Nuclear localisation signal
NM	Nemaline myopathy
NMD	Nonsense mediated decay
O/N	Over night
pA	SV40 polyadenylation sequence
PAGE	polyacrylamide gel electrophoresis
PBS	Phospahte buffer saline
PBST	Phospahte buffer saline Tween 20
PCR	Polymerase chain reaction
p-eIF2-α	phosphorylated eIF2-α
PFA	Paraformaldyhyde
PHF	Primary human fibroblasts
PI	Protease inhibitors
PKR	Phosphokinase R
PNDR	Pyridine nucleotide disulfide reductase

PPI	Phosphatse inhibitors
PTC	Premature termination codon
PYROXD1/*PYROXD1*	Human Pyridine nucleotide disulfide oxidoreductase protein/gene
Pyroxd1/*Pyroxd1*	Mouse Pyridine nucleotide disulfide oxidoreductase protein/gene
RIPA	RadioImmunoPrecipitation Assay
RPKM	Reads per kilobase per million
SAP	Shrimp alkaline phosphatase
SDS	Sodium dodecyl sulfate
Sec	Seconds
SRF	Serum response factor
T	Transfected
TAE	Tris-acetate-ethylenediaminetetraacetic acid
TM-h	Tropomysoin binding domain
TMOD	Tropomodulin
Ub	Ubiquitin
UT	Untransfected
UTR	Untranslated region
VA	Virus associated
W	Week
WH2	Wiskott-Aldrich Syndrome
WT	Wild type
Y	Year

TABLE OF CONTENTS

TABLE OF FIGURES

INDEX OF TABLES

Chapter 1 - General Introduction

1.1 Skeletal muscle

Skeletal muscle consists of bundles of multinucleated muscle cells (myofibres) (Engel & Franzini-Armstrong, 2004; Frontera & Ochala, 2015). Within the myofibre are tightly packed myofibrils which are made up of repeating sarcomeres, the contractile unit of skeletal muscle. Sarcomeres are bordered by the Z-band, appearing as electron dense lines on electron microscopy. The thin filaments are anchored in the Z-band and extend into the centre of the sarcomere, the M-band. The thin filaments are predominately made up of filamentous actin, tropomyosin and the troponin complex. The M-band anchors the thick filament, which interdigitate the thin filaments. The thick filaments are predominantly made up of myosin and are electron dense, appearing as dark areas on electron microscopy (A-band). The thin filaments are less electron dense and areas only of thin filaments appear as lighter areas on electron microscopy (I-band). This contrast gives a straited appearance to skeletal muscle (Figure 1.1).

Muscle contraction occurs when myosin heads within the thick filament bind to actin within the thin filament and pull the thin filament towards the centre of the sarcomere. This shortens the sarcomere and the synchronised shortening of sarcomeres contracts the muscle and generates force (Engel & Franzini-Armstrong, 2004). This is termed the sliding filament theory and was proposed simultaneously by Huxley & Niedergerke (1954) and Huxley & Hanson (1954). In a relaxed sarcomere, tropomyosin masks the myosin-binding sites on actin, preventing muscle contraction. The positioning of tropomyosin is regulated by the troponin complex (Engel & Franzini-Armstrong, 2004).

A muscle contracts in response to an action potential carried by the motor neuron to the myofibre (Engel & Franzini-Armstrong, 2004; Frontera & Ochala, 2015). The action potential depolarises the myofibre through the T-tubule network, triggering calcium release from the sarcoplasmic reticulum into the cytosol of the myofibril. The released calcium binds troponin C within the troponin complex. Binding of calcium to troponin C shifts tropomyosin, unmasking the myosin binding site on actin and allowing the sarcomere to contract (Engel & Franzini-Armstrong, 2004).

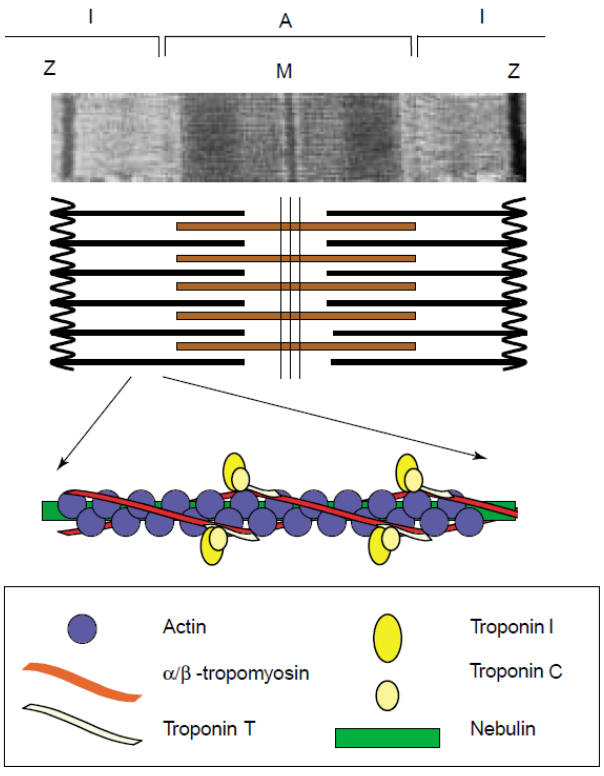

Figure 1.1: Sarcomere structure. Electron microscopy and aligned schematic of a single sarcomere and a section of the thin filament: Z-band (Z), M-band (M), I-band (I) and A-band (A). Reproduced from Sanoudou and Beggs (2001)

1.2 Inherited myopathies and project aims

Variants within genes encoding proteins responsible for skeletal muscle structure and function are associated with muscle disease (www.musclegenetable.fr). Identifying the genetic basis of muscle disease is the first step to elucidating the disease mechanism and to develop, or apply, mechanistic-based treatments. This thesis is divided into three projects which stem from the gene discovery programme of the Institute for Neuroscience and Muscle Research (INMR). Our goal is to provide a genetic diagnosis for our patients, and use this knowledge to guide clinical care and research into disease mechanism. Detailed descriptions of the sarcomeric components and the muscle disease of research focus are included in the introductions within the following chapters.

Chapter two will focus on the first missense recessive variant within *ACTA1*, encoding α-skeletal actin, as the genetic cause of congenital muscular dystrophy with rigid spine. The aim of this part of my PhD was to perform histological and molecular characterisation of patient skeletal muscle to determine if the identified variant within *ACTA1* was pathogenic.

Chapter three will focus on two disease genes for nemaline myopathy: *LMOD3*, encoding leiomodin-3, and *KLHL40*, encoding kelch-like family member 40. The aim of this part of my PhD was to deepen our understanding of nemaline myopathy pathogenesis, by further understanding the LMOD family as regulators of thin filament length, and the link between KLHL40 and LMOD3 in humans.

Chapter four will focus on variants within the oxidoreductase *PYROXD1* as a new genetic cause of congenital myopathy. The aim of this part of my PhD was: (1) To provide the first characterisation of PYROXD1 and *PYROXD1*-myopathy; and (2) generate two mouse models to further our understanding of PYROXD1 in fundamental biology and disease.

Chapter 2 - *ACTA1*: A novel missense variant expands the clinical and histological spectrum of *ACTA1* variants and congenital muscular dystrophy

Prologue

As part of the gene discovery program of the INMR, targeted next-generation sequencing identified a novel variant in alpha-skeletal actin (*ACTA1*) that expands the phenotypic and histological spectrum associated with *ACTA1* variants and congenital muscular dystrophy. This finding has been published as a short report. I am second author on this publication which is presented as Part A of this chapter.

My role in this research study also involved the molecular characterisation of the *ACTA1* Val154Leu variant. These experiments and lines of investigation were necessary for, but not included in, our short report and are presented in Part B of this chapter.

2.1 Introduction

2.1.1 α-skeletal actin

Mammalian actins

Alpha skeletal actin is encoded by *ACTA1*, one of six mammalian actin genes, and is the major actin isoform in skeletal muscle. Actin is highly conserved between species and amino acid conservation is greater than 90% between actin isoforms (Sheterline, Clayton, & Sparrow, 1998). Despite this large amount of sequence homology, each actin isoform is expressed in specific cell types and carries out distinct functional roles. The two non-muscle actins are cytoplasmic β-actin (*ACTB*) and cytoplasmic γ-actin (*ACTG1*). Cytoplasmic β- and γ-actin are important components of the cytoskeleton and are involved in many processes including cell movement, vesicle transport and cell division (Sheterline et al., 1998). There are four muscle specific actin isoforms that are major constituents of the sarcomere, and are essential for muscle contraction: Smooth muscle expresses two actins - smooth muscle α-actin (*ACTA2)* and smooth muscle γ-actin (*ACTAG2*); and striated muscle expresses two actins - cardiac actin (*ACTC)* and α-skeletal actin (*ACTA1*).

Cardiac actin is the major actin expressed in cardiac muscle and extraocular muscle. In skeletal muscle, cardiac actin is the predominant foetal actin isoform. It is highly expressed *in utero* and down regulated shortly after birth to be replaced by α-skeletal actin, the dominant actin in adult skeletal muscle (Ilkovski, Clement, Sewry, North, & Cooper, 2005). Due to the high conservation between isoforms and species, each residue within α-skeletal actin is considered functionally important. The Exome Variant Server (http://evs.gs.washington.edu/EVS/) documents only four missense changes within *ACTA1* in healthy individuals – c.334C>T p.Leu112Phe; c.662C>A p.Arg208Ser; c.745G>A p.Val249Iso; c.1095C>G p.Asn365Glu.

Monomeric α-skeletal actin

The nascent polypeptide chain of α-skeletal actin consists of 377 residues. Cleavage of the first two residues – methionine and cysteine, and methylation of the third – aspartic acid, are required to produce the mature, correctly folded polypeptide (Sheterline et al., 1998). G-actin is the monomeric form of actin consisting of two domains, named the 'large' and 'small' domains. These domains are further divided into 4 subdomains (Figure 2.1). Two clefts are situated between the domains – the hydrophobic pocket and the ATP-binding pocket (Kabsch, Mannherz, Suck, Pai, & Holmes, 1990). ATP and a metal ion (Ca^{2+} or Mg^{2+}) bind within the ATP-binding pocket (Sheterline et al., 1998). The two domains of actin are linked by two polypeptide chains called the hinge region (Kabsch et al., 1990). The hinge region allows substantial movement of the two domains relative to each other, allowing molecules to bind within the two clefts (Sheterline et al., 1998).

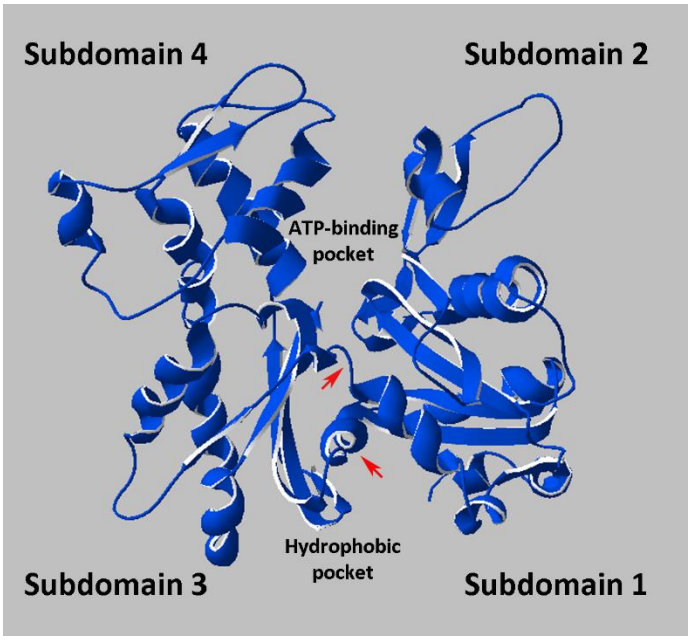

Figure 2.1: Monomeric α-skeletal actin. G-actin showing the four subdomains, ATP-binding pocket, hydrophobic pocket and the two polypeptide chains making up the hinge region (red arrows). Molecular modelling of α-skeletal actin was carried out in DeepView/Swiss-Pdb Viewer (v 4.1.0) http://www.expasy.org/spdbv/(4) from the crystal structure solved by Kabsch et al. (1990).

Filamentous α-skeletal actin

Functional α-skeletal actin is a filamentous structure (F-actin) formed by polymerisation of monomeric actin (G-actin). The formation of F-actin is a two-step process – nucleation followed by polymerisation. Nucleation is the formation of an unstable trimer of ATP-bound G-actin monomers termed the 'nucleus' (Kasai, Asakura, & Oosawa, 1962). Polymerisation is the subsequent addition of ATP-bound G-actin monomers to the nucleus. ATP bound to the G-actin is hydrolysed to ADP + P_i which stabilises the monomeric subunits (Sheterline et al., 1998). Addition of G-actin monomers in non-muscle cells occurs more rapidly at the plus end (barbed end) of the actin filament and there is very little, if any, monomeric addition at the minus end (pointed end) (Pollard, 1986).

Subdomains 1 and 3 are orientated towards the plus end (barbed end, towards the Z-band) and subdomains 2 and 4 are orientated towards the minus ends (pointed end, towards the M-band). Subdomains 1 and 2 are orientated towards the outer edge of F-actin. Residues on the surface of subdomains 1 and 2 are able to interact with a variety of proteins. Subdomains 3 and 4 are orientated towards the inner-edge of F-actin. Residues on the surface of subdomains 3 and 4 are able to interact with neighbouring actin monomers (Engel & Franzini-Armstrong, 2004).

Sarcomere thin filament

α-Skeletal actin is the major component of the sarcomere thin filament. Sarcomere contraction occurs when myosin heads on the thick filament bind to actin and pull the thin filament towards the centre of the sarcomere, the M-band (A. F. Huxley & Niedergerke, 1954; H. Huxley & Hanson, 1954). Aligned thin filaments are required for efficient muscle contraction and regulation of a consistent thin filament length is paramount for efficient muscle contraction and force generation. Therefore, actin filament turnover dynamics are slow and tightly regulated (R. S. Littlefield & Fowler, 2008a). In contrast to skeletal muscle, non-muscle actin is highly

dynamic to allow adaptation to the cells changing environmental demands. Actin turnover requires a constant exchange between actin bound in thin filaments and soluble monomeric G-actin molecules.

Within the sarcomere thin filament, the plus end (barbed end) of the actin filament is bound to the Z-band by α-actinin and capped by CapZ. The minus end (pointed end) is orientated towards the M-band and is capped by tropomodulin. In contrast to non-muscle actin filaments, in sarcomeric thin filaments, monomers are added to both the barbed and pointed-ends (Kouchi, Takahashi, & Shimada, 1993; R. Littlefield, Almenar-Queralt, & Fowler, 2001). In striated muscle, regulation of the thin filament occurs predominantly at the pointed ends and involves a number of factors (reviewed in R. S. Littlefield & Fowler, 2008b).

2.1.2 Skeletal α-actin disease

Establishing ACTA1 as a disease gene

The existence of variants within *ACTA1* as a genetic cause of muscle disease was first suggested in 1995 (Laing, 1995; Laing et al., 1995). In 1997 Goebel *et al* reported three congenital myopathy patients with actin aggregates within their skeletal muscle biopsy (Goebel et al., 1997). *ACTA1* variants were identified within these patients in 1999 (Nowak et al.), establishing *ACTA1* as a disease gene for congenital myopathy. Over 200 disease-causing variants within *ACTA1* have now been identified (https://databases.lovd.nl/shared/variants/ACTA1/unique).

Clinical presentation

Variants within *ACTA1* are a common genetic cause of congenital myopathy (Laing et al., 2009; Nowak et al., 1999). Patients typically present with a severe congenital myopathy phenotype. Severe congenital myopathy patients often die within the first year of life and others require assisted ventilation (Laing et al., 2009; Sparrow et al., 2003). However *ACTA1* disease phenotypes lie on a spectrum ranging in severity, inclusive of milder cases where the individual lives into adulthood (Agrawal et al., 2004; Saito et al., 2011; Schroder, Durling, & Laing, 2004).

Common congenital myopathy subtypes and pathological hallmarks

Five sub-classes of congenital myopathy have been associated with variants within *ACTA1*, with overlapping pathological features on skeletal muscle histology (Figure 2.2): (1) Nemaline myopathy is the most common congenital myopathy associated with *ACTA1* variants. Nemaline bodies are the identifying histological feature on muscle biopsy. Nemaline bodies are protein inclusions, often containing thin filament and Z-band proteins such as actin, α

actinin-2 and nebulin (Dubowitz & Sewry, 2007); (2) Intranuclear rod myopathy – rods are present within the myonuclei (Nowak et al., 1999); (3) Actin filament aggregate myopathy - abnormal aggregates of actin can be seen in sarcomeres of a muscle biopsy (Nowak et al., 1999); (4) Congenital fibre type disproportion - characterised by smaller type one fibres (Clarke, 2011); and (5) Core-rod myopathies - characterised by areas of sarcomeric disorganisation that lack mitochondria, as well as nemaline rods (Kaindl et al., 2004).

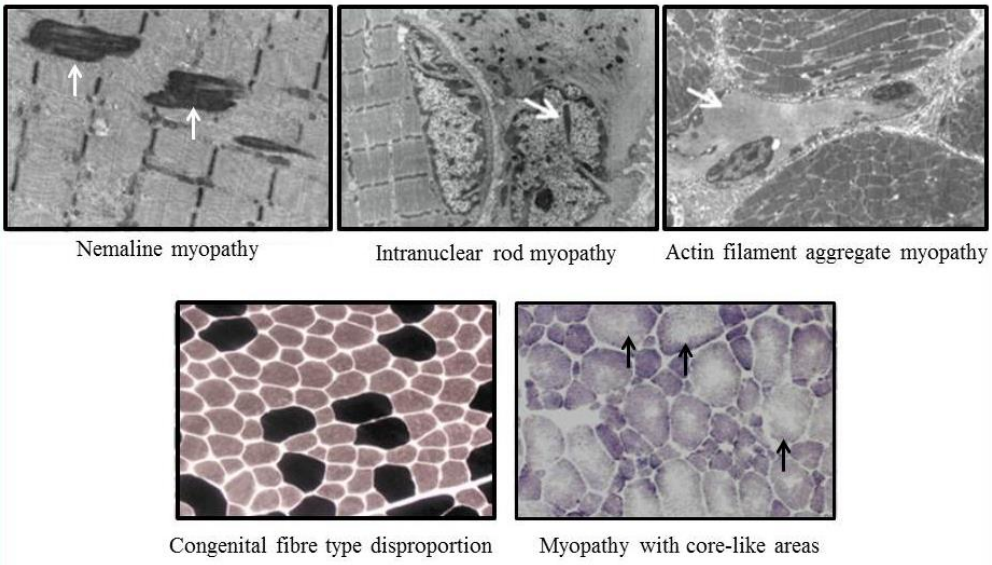

Figure 2.2: Overlapping skeletal muscle histological presentations caused by *ACTA1* variants. ***Upper panel*** **-** Electron microscopy images of nemaline bodies (left, white arrow); rods within the nucleus (middle, white arrow); and actin aggregates (right, white arrow). ***Lower panel*** **–** ATPase pH 10.4 stain showing small slow fibres in disproportion to fast fibres (left, pale – slow fibres, dark – fast fibres); and NADH stain showing core-like areas (right, black arrows) (Laing et al., 2009)

Molecular genetics of ACTA1 variants

Most *ACTA1* mutations are *de novo* dominant (~ 90% of cases) (Laing et al., 2009). Whilst there is little correlation between histological abnormalities, presumed functional consequence of the mutation and the clinical severity, the amount of mutant protein expressed correlates with age of onset (Ilkovski et al., 2004).

Recessive mutations make up ~ 10% of cases and typically occur in consanguineous families (Laing et al., 2009). To date, all recessive mutations have been functional null mutations (Costa et al., 2004; Laing et al., 2009; Nowak, Ravenscroft, & Laing, 2013; Nowak et al., 2007). The disease is caused by the absence of skeletal α-actin expression. Functional null mutations in skeletal actin are usually neonatally lethal. In patients that survive infancy, there is persistence of cardiac actin expression after birth in skeletal muscle which allows muscle function (Nowak et al., 2007). The more α-cardiac actin that is expressed, the milder the disease severity. Overall, there is little correlation between the histology and clinical severity, nor histology and the *ACTA1* mutation (type or function) (Feng & Marston, 2009).

Mapping of ACTA1 variants

Mapping of *ACTA1* variants on monomeric actin using molecular modelling programs allows hypotheses to be developed on how these mutations affect functionality of the thin filament. *ACTA1* mutations can be grouped into six categories by predicted functional outcomes: N-terminal processing, post-translational folding, polymerisation, interaction with the Z-band protein α-actinin and interaction with nebulin & structure of the contractile apparatus (Feng & Marston, 2009).

2.1.3 Aims of this project

Targeted parallel sequencing identified a novel homozygous missense variant in *ACTA1* within a muscular dystrophy patient with rigid spine. Our aim was to determine if the novel variant identified within *ACTA1* was pathogenic.

2.2 Part A: PAPER - Recessive *ACTA1* variant causes congenital muscular dystrophy with rigid spine

European Journal of Human Genetics (2015) 23, 883–886

www.nature.com/ejhg

SHORT REPORT

Recessive *ACTA1* variant causes congenital muscular dystrophy with rigid spine

Gina L O'Grady[1,2], Heather A Best[1,2], Emily C Oates[1,2], Simranpreet Kaur[1], Amanda Charlton[3], Susan Brammah[4], Jaya Punetha[5], Akanchha Kesari[5], Kathryn N North[1,2,6,7], Biljana Ilkovski[1,2], Eric P Hoffman[5] and Nigel F Clarke*[,1,2]

Variants in *ACTA1*, which encodes α-skeletal actin, cause several congenital myopathies, most commonly nemaline myopathy. Autosomal recessive variants comprise approximately 10% of *ACTA1* myopathy. All recessive variants reported to date have resulted in loss of skeletal α-actin expression from muscle and severe weakness from birth. Targeted next-generation sequencing in two brothers with congenital muscular dystrophy with rigid spine revealed homozygous missense variants in *ACTA1*. Skeletal α-actin expression was preserved in these patients. This report expands the clinical and histological phenotype of *ACTA1* disease to include congenital muscular dystrophy with rigid spine and dystrophic features on muscle biopsy. This represents a new class of recessive *ACTA1* variants, which do not abolish protein expression.
European Journal of Human Genetics (2015) **23,** 883–886; doi:10.1038/ejhg.2014.169; published online 3 September 2014

INTRODUCTION

Variants in the skeletal muscle α-actin gene (*ACTA1*) are a common cause of congenital myopathy with over 200 different variants now reported.[1] By far, the most frequent histological pattern associated is autosomal dominant nemaline myopathy; less common patterns include actin-accumulation myopathy, intranuclear rod myopathy and congenital fiber-type disproportion.[1] Approximately 10% of *ACTA1*-myopathy patients have autosomal recessive disease, and until now all such patients have had nemaline myopathy and a severe congenital phenotype associated with loss of α-skeletal actin expression.[1] We report a novel homozygous recessive missense variant (c.460G>C, *P.*(Val154Leu)) in two brothers with infantile-onset congenital muscular dystrophy with rigid spine, thus expanding the histological and clinical phenotypes associated with *ACTA1* variants and establishing a new class of *ACTA1* variants – recessive variants associated with expression of mutant actin and mild-to-moderate disease severity.

PATIENTS AND METHODS

Patients

We enrolled a large cohort of patients with limb-girdle weakness who lacked a genetic diagnosis in a whole-exome sequencing study, conducted with approval from the Human Research Ethics Committee of the Sydney Children's Hospitals Network (10/CHW/45).

Genetic analysis

DNA was extracted from blood leukocytes of Patient 1 using standard techniques. A QIAGEN (Melbourne, VIC, Australia) QIAamp DNA FFPE Tissue kit was used to extract DNA from formalin-fixed paraffin-embedded skeletal muscle of Patient 2.

Targeted next-generation sequencing of 45 neuromuscular disease genes was performed by emulsion PCR (RainDance, Billerica, MA, USA) of 1840 amplimers followed by sequence analysis (Illumina HiScan SQ). Data interpretation were performed using NextGene software. Confirmatory Sanger sequencing was carried out by the Australian Genome Research Facility, Sydney. The sequence was aligned on Sequencer 4.9 (Ann Arbor, MI, USA) with the reference sequence from NCBI, NM_001100.3. The variant is submitted to the Leiden Muscular Dystrophy *ACTA1* Mutation Database (www.LOVD.nl/ACTA1 (database ID ACTA1_00245)). Molecular modeling of the α-skeletal actin monomer was performed using DeepView/Swiss-Pdb Viewer (v 4.1.0, Basel, Switzerland), http://www.expasy.org/spdbv/[2] from the crystal structure solved by Kabsch *et al.*[3]

Muscle biopsy analysis

Muscle histology slides were stained using standard procedures. Frozen muscle biopsy sections were stained with antibodies to α-skeletal actin, cardiac actin and neonatal myosin. Western blot analysis was performed using antibodies to α-skeletal actin and cardiac actin. Glyceraldehyde 3-phosphate dehydrogenase was used as a loading control. See Supplementary methods for further details.

RESULTS

Clinical features

A Sri Lankan couple with possible distant consanguinity had two affected sons and four healthy children. The affected boys' prenatal and perinatal periods were uncomplicated and both walked at around

[1]Institute for Neuroscience and Muscle Research, Children's Hospital at Westmead, Sydney, New South Wales, Australia; [2]Discipline of Paediatrics and Child Health, Sydney Medical School, University of Sydney, Sydney, New South Wales, Australia; [3]Histopathology Department, The Children's Hospital at Westmead, Sydney, New South Wales, Australia; [4]Electron Microscope Unit, Concord Repatriation General Hospital, Sydney, New South Wales, Australia; [5]Research Center for Genetic Medicine, Children's National Medical Center, Washington, DC, USA; [6]Murdoch Childrens Research Institute, Melbourne, Victoria, Australia; [7]Faculty of Medicine, University of Melbourne, Melbourne, Victoria, Australia
*Correspondence: Associate Professor NF Clarke, Institute for Neuroscience and Muscle Research, Children's Hospital at Westmead, Locked Bag 4001, Sydney, New South Wales, Australia. Tel: +61 2 9845 1453; Fax: +61 2 9845 3078; E-mail: nigel.clarke@health.nsw.gov.au
Received 12 April 2014; revised 27 June 2014; accepted 12 July 2014; published online 3 September 2014

1 year of age. Neck weakness was noted in infancy in Patient 1 and by age 2 years, both were unable to run and fell frequently. Patient 1 had mild, stable, generalized weakness during childhood that progressed slowly from late teenage years. A mild thoracic kyphoscoliosis developed in adolescence. In early adulthood he developed mild dysphagia and mild restrictive lung disease. At age 25 years, forced vital lung capacity measured 44% of predicted. Nocturnal ventilation was not required. At age 34 years, he walked short distances and had a rigid spine (Figure 1a), generalized muscle wasting and a body mass index of 15. There was mild facial weakness, restricted jaw opening, scapular winging and generalized weakness in all limbs, worse in proximal muscles.

At age 5 years, Patient 2 was ambulant but used a wheelchair for longer distances. He had generalized weakness, more severe in proximal limb muscles with a positive Gowers' sign. He suffered recurrent pneumonia and died during one episode at age 6 years. Neither boy had ptosis, ophthalmoplegia, nor limb contractures.

Creatine kinase measures varied between 222and 1930 U/l. The electromyogram was myopathic in both siblings. Nerve conduction studies and echocardiograms were normal. Muscle MRI in Patient 1 at 34 years showed widespread muscle atrophy and fat infiltration (Figure 1b and c). At the mid thigh there was relative sparing of the vastus lateralis, vastus medialis, gracilis and sartorius muscles, while the posterior compartment and rectus femoris were more severely affected. In the lower leg there was mild to moderate generalized fatty infiltration, especially of soleus.

Genetic analysis

A missense variant (c.460G>C, *p.*(Val154Leu)) in *ACTA1* was identified in Patient 1. Sanger sequencing confirmed that both brothers were homozygous for the variant, with both parents heterozygous for the change. All unaffected siblings were either heterozygous or homozygous for the normal allele. A previously unreported, heterozygous missense variant in *SEPN1* (NM_020451.2: c.1162A>G, p.(Ser388Gly) (Leiden Muscular Dystrophy *SEPN1* Mutation Database (www.LOVD.nl/SEPN1 (database ID SEPN1_00115)) was also identified in Patient 1 but a second *SEPN1* variant was not found with Sanger sequencing or on a custom screen for exon deletions or duplications. No variants were found in other genes previously associated with a rigid spine phenotype (*CAPN3*, *COL6A1*, *COL6A2*, *COL6A3* or *LMNA*).

Molecular modeling showed that the Val154Leu variant alters a residue in subdomain 3 situated near the ATP-binding pocket and the hinge region (Figure 2h). The hinge region is responsible for relative movement of the domains in respect to each other, allowing molecules, including ATP, to bind in the clefts. As flexibility of the relative domains is essential for polymerization of the actin filament, the Val154Leu variant may influence polymerization by influencing the hinge region. The relative movement of the two domains may be changed such that ATP binds less efficiently.

Muscle biopsy analysis

A quadriceps muscle biopsy of Patient 1 at age 17 years 7 months showed increased fiber size variation, numerous internalized nuclei, fiber splitting, occasional degenerating and regenerating fibers (Figure 2b). Thirty-four percent of myofibers had at least one internal or central nucleus and 13% had two or more. The nicotinamide adenine dinucleotide tetrazolium reductase (NADH), cytochrome oxidase (COX) and succinic dehydrogenase (SDH) stains showed central lucencies and a 'moth-eaten appearance', suggestive of cores (Figure 2d). Similar findings, with prominent fatty infiltration, were present in a quadriceps biopsy from Patient 2 at age 5 years.

In both patients, electron microscopy (EM) showed smeared and accumulated Z-band material that typically spanned 1–2 sarcomeres in length, but extended across up to half the width of the fiber. The degree of accumulated Z-band material is unusual for minicores (Figure 2a). A single more typical minicore, lacking the accumulated Z-band material, was seen in the biopsy from Patient

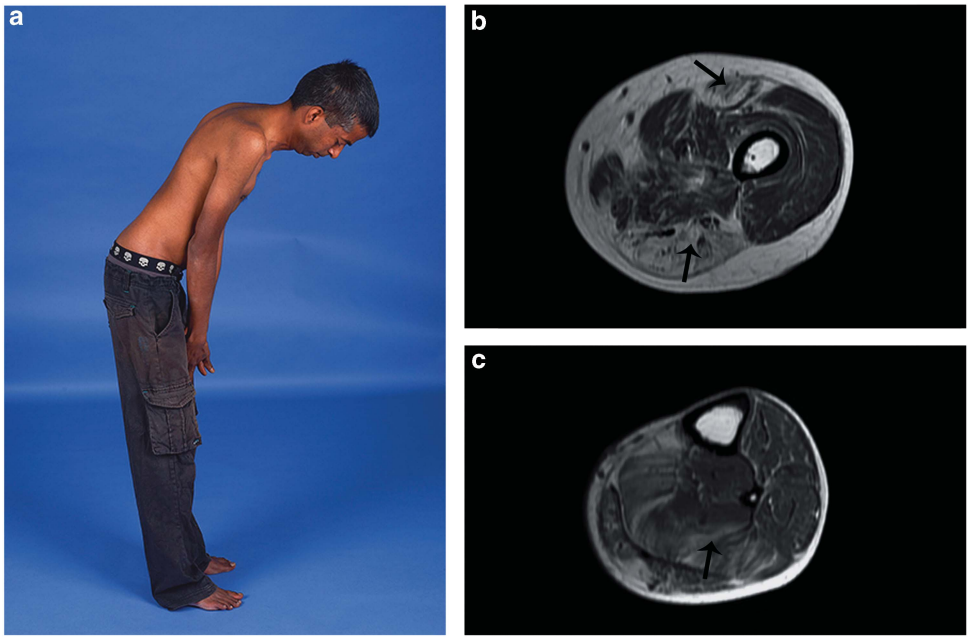

Figure 1 Clinical and radiological features associated with *ACTA1* variant Val154Leu. (**a**) Patient 1 at age 34 years demonstrating maximum forward flexion of the spine and neck. (**b** and **c**) Patient 1 muscle MRI of the left mid thigh (**b**) showing prominent fat infiltration in the rectus femoris and muscles of the posterior compartment (arrows), and left lower leg (**c**) showing particular involvement of the soleus (arrow).

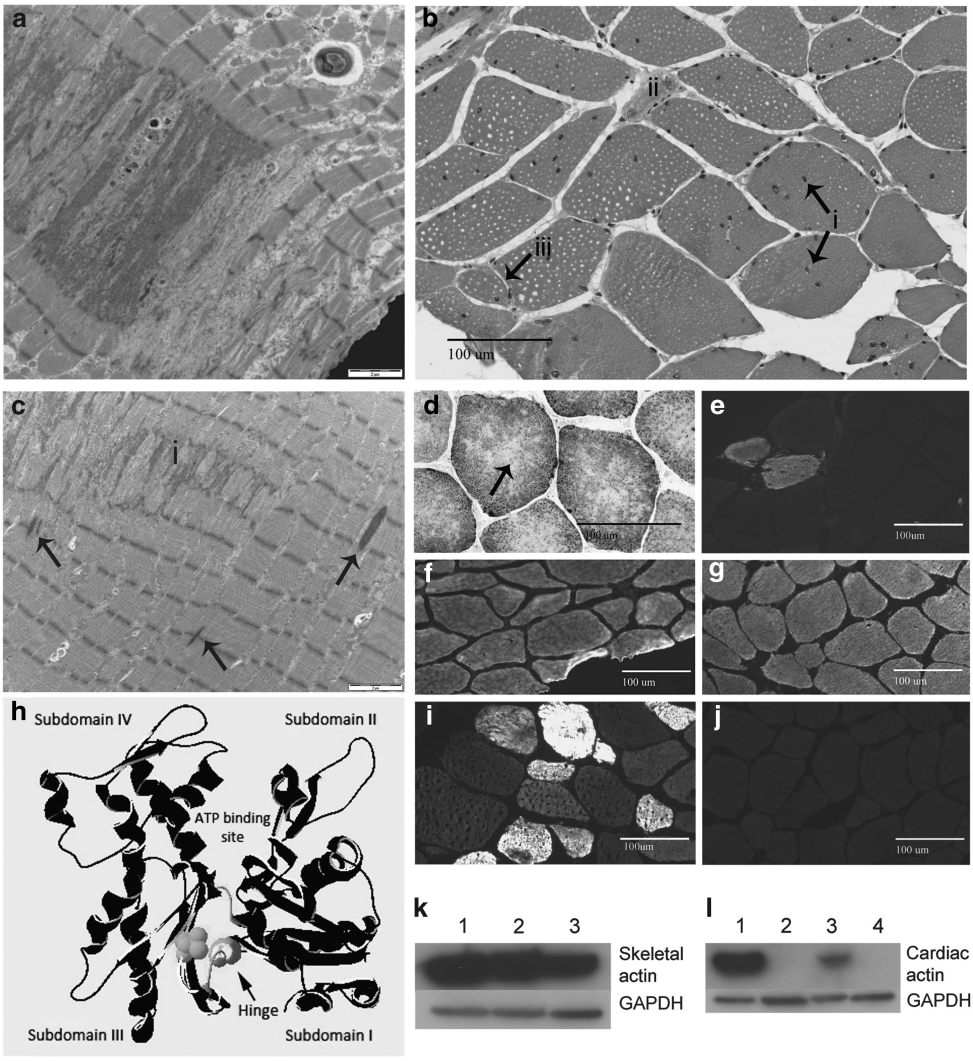

Figure 2 Histological features associated with *ACTA1* variant Val154Leu. (**a**) Electron microscopy of Patient 1's quadriceps muscle biopsy shows accumulated Z-band material. (**b**) Hematoxylin and eosin staining of Patient 1 quadriceps muscle shows multiple internalized nuclei (i), a regenerating fiber (ii) and a likely split fiber (iii). (**c**) Electron microscopy of Patient 1's quadriceps muscle biopsy shows streaming and accumulation (i) of Z-band material. Occasional small rods are also present (arrows). (**d**) COX SDH staining of Patient 1 quadriceps muscle biopsy demonstrating central lucencies and 'moth-eaten' areas suggestive of cores. (**e**) One percent of myofibers in Patient 1 was positive for neonatal myosin, supporting the presence of occasional regenerating fibers. (**f**) Immunohistochemistry for skeletal α-actin shows normal expression in all myofibers in muscle from Patient 1 at 17 years of age compared with adult control (**g**). (**h**) Molecular modeling of α-skeletal actin monomer in DeepView/Swiss-Pdb Viewer (v 4.1.0, http://www.expasy.org/spdbv/) from the crystal structure solved by Kabsch *et al*.[3] Valine154 is shown in yellow space fill, on actin depicted as a black ribbon structure. The two polypeptide chains making up the hinge region are shown in blue. (**i**) Immunohistochemistry of Patient 1 muscle demonstrates the presence of cardiac α-skeletal actin in 20% of myofibers of variable size and staining intensity, compared with adult control skeletal muscle (**j**). (**k** and **l**) Western blot analysis of Patient 1 muscle with glyceraldehyde 3-phosphate dehydrogenase shown as a loading control. (**k**) Normal levels of α-skeletal actin are present in Patient 1 muscle. Lanes 1 and 3 show adult control skeletal muscle, lane 2 contains patient skeletal muscle. (**l**) Cardiac actin is markedly upregulated in Patient 1 skeletal muscle compared with normal controls. Lane 1 contains baboon cardiac muscle, lanes 2 and 4 contain control adult skeletal muscle and lane 3 contains muscle from Patient 1. The full colour version of this figure is available at *European Journal of Human Genetics* online.

2. Occasional small nemaline rods were present (Figure 2c). These were too small and infrequent to be seen on light microscopy on Gomori trichrome, or with staining for cardiac and α-skeletal actin, or α-actinin.

Immunohistochemical staining for neonatal myosin on Patient 1 muscle showed 1% positive fibers (Figure 2e), consistent with the presence of occasional regenerating fibers. Cardiac α-actin was present in 20% of myofibers of variable size and fiber type, and with variable staining intensity (Figure 2i and j). Staining for α-skeletal actin showed normal levels of expression in all myofibers, indicating that mutant p.(Val154Leu) actin is expressed and is the predominant actin isoform in most myofibers (Figure 2f and g).

Western blot analysis of Patient 1 muscle showed normal levels of α-skeletal actin (Figure 2k). Cardiac actin was markedly upregulated compared with normal controls (Figure 2l).

DISCUSSION

The *ACTA1* gene is highly conserved throughout evolution and polymorphisms that alter the protein sequence are extremely rare in the general population, indicating that most changes to the actin

polypeptide sequence adversely affect protein function.[4] All previously described patients with recessive *ACTA1* disease (~10% of *ACTA1* patients) have had functional 'null' variants and make no α-skeletal actin.[1,4,5] All have had severe congenital nemaline myopathy and survival after birth is only possible due to persistence of cardiac α-actin in the skeletal muscle of these children.[5] We describe the first recessive *ACTA1* variant associated with expression of α-skeletal actin in skeletal muscle and survival well into adulthood. A limitation of this study is that we have not performed a comprehensive screen for other genetic variants that may influence the patient's phenotype. Nevertheless, the *ACTA1* recessive variants segregate with disease in the family and are predicted to be pathogenic by molecular modeling. As in other recessive *ACTA1* myopathies, cardiac actin was upregulated in patient muscle, but only in a subset of myofibers. Occasional cardiac actin-positive fibers may be regenerating fibers in which fetal sarcomeric isoforms, including cardiac actin and neonatal myosin, are expressed, but this explanation is unlikely to account for most cardiac actin-positive myofibers. We suspect cardiac actin is upregulated as a specific response to abnormalities in α-skeletal actin, as cardiac actin expression is unusual in congenital myopathies or dystrophies after the neonatal period, except in the context of myofiber regeneration.

The finding of mild dystrophic changes on muscle biopsy has not been previously reported in association with variants in *ACTA1* and expands the histological phenotype for *ACTA1*-related myopathies. Another notable histological feature was the presence of prominent internalized nuclei. Extensive Z-band streaming and the presence of occasional rods on EM may also provide a clue to the genetic diagnosis.

On clinical examination, spinal rigidity was a notable feature and the mild to moderately raised CK levels in both probands, together with the muscle biopsy findings led to a clinical diagnosis of congenital muscular dystrophy with spinal rigidity. Congenital muscular dystrophy with a rigid spine and variably elevated CK has been previously described in association with variants in *SEPN1*, *LMNA* and collagen VI genes, and we screened these genes for variants.[6] The lack of limb contractures in Patient 1 by adulthood is also atypical for *LMNA*- and *COLVI*-related myopathies, and almost all *SEPN1*-related myopathy patients develop nocturnal hypoventilation by this age. These clinical features and a different pattern of lower limb muscle involvement in our family may be useful clinical clues to identify additional patients with *ACTA1*-CMD.

This report extends the phenotypic spectrum of *ACTA1* myopathies to include congenital muscular dystrophy associated with rigid spine. Until recently, genetic testing has generally been limited to the analysis of disease genes known to be associated with the patient's phenotype and expense has been a major barrier to broad genetic screens. Advances in sequencing technologies now mean that testing of all known myopathy genes is widely available for patient diagnosis and there are many examples of when such testing has revealed unexpected genotype–phenotype associations.[7] Even though *ACTA1* was one of the first known congenital myopathy genes,[8] and *ACTA1* diagnostic sequencing has been available for over 14 years, the family we report raises the possibility that variants in *ACTA1* may be responsible for a much wider spectrum of disease than is currently appreciated.

CONFLICT OF INTEREST

The authors declare no conflict of interest.

ACKNOWLEDGEMENTS

This study was supported by National Health and Medical Research Council (Australia) grants 1022707, 1031893 & 1026933 (KNN, NFC), and 1056285 (GLO); National Institutes of Health (USA) 3R01 NS29525 (EPH); and The Australian Postgraduate Award, The University of Sydney (HAB).

AUTHOR CONTRIBUTIONS

GL O'Grady: Drafting/revising manuscript for content, analysis and interpretation of data. HA Best: Drafting/revising manuscript for content, analysis and interpretation of data. EC Oates: Drafting/revising manuscript for content, data generation, data interpretation. S Kaur: Data generation, data interpretation, manuscript revision. A Charlton: Revising manuscript for content, analysis and interpretation of data. S Brammah: Revising manuscript for content, analysis and interpretation of data. E Hoffman: Revising manuscript for content, study concept, analysis and interpretation of data. A Kesari: Experimental design, data generation, data interpretation, revising manuscript. J Punetha: Experimental design, data generation, data interpretation, revising manuscript. KN North: Drafting/revising manuscript for content, study concept and design, analysis and interpretation of data, study supervision, obtaining funding. Biljana Ilkovski: Drafting/revising manuscript for content, analysis and interpretation of data. NF Clarke: Drafting/revising manuscript for content, study concept and design, analysis and interpretation of data, study supervision, obtaining funding.

1 Nowak KJ, Ravenscroft G, Laing NG: Skeletal muscle α-actin diseases (actinopathies): pathology and mechanisms. *Acta Neuropathol* 2012; **125**: 19–32.
2 Guex N, Peitsch MC: SWISS-MODEL and the Swiss-Pdb Viewer: an environment for comparative protein modeling. *Electrophoresis* 1997; **18**: 2714–2723.
3 Kabsch W, Mannherz HG, Suck D, Pai EF, Holmes KC: Atomic structure of the actin: DNase I complex. *Nature* 1990; **347**: 37–44.
4 Laing NG, Dye DE, Wallgren-Pettersson C *et al*: Mutations and polymorphisms of the skeletal muscle α-actin gene (ACTA1). *Hum Mutat* 2009; **30**: 1267–1277.
5 Nowak KJ, Sewry CA, Navarro C *et al*: Nemaline myopathy caused by absence of α-skeletal muscle actin. *Ann Neurol* 2007; **61**: 175–184.
6 Mercuri E, Clements E, Offiah A *et al*: Muscle magnetic resonance imaging involvement in muscular dystrophies with rigidity of the spine. *Ann Neurol* 2010; **67**: 201–208.
7 Ceyhan-Birsoy O, Agrawal PB, Hidalgo C *et al*: Recessive truncating titin gene, TTN, mutations presenting as centronuclear myopathy. *Neurology* 2013; **81**: 1205–1214.
8 Nowak KJ, Wattanasirichaigoon D, Goebel HH *et al*: Mutations in the skeletal muscle alpha-actin gene in patients with actin myopathy and nemaline myopathy. *Nat Genet* 1999; **23**: 208–212.

Supplementary Information accompanies the paper on European Journal of Human Genetics website (http://www.nature.com/ejhg)

Recessive *ACTA1* mutation causes congenital muscular dystrophy with rigid spine

Supplementary Methods

PCR and Sequencing

A reaction volume of 20 µl was made up of 1 µl gDNA (20 ng), 10 µl Buffer D (Astral), 0.2 µl *Taq* DNA polymerase recombinase (5 units/µl), 6.8 µl DEPC water (Bioline), 1 µl forward (5'-CGCTGAGMGCCTAGCCTCGG-3') and 1 µL reverse primer (5'-TGCGGAGGGCAGAAGCAGGA-3') (10 µM, Sigma-Aldrich). PCR was carried out with a 33 cycle 2 x 3 step temperature gradient PCR. An initial 5 min activation at 95°C was followed by 14 cycles of: 94°C 30 sec, 68°C (-0.5°C/cycle), 72°C for 1 min; followed by 19 cycles of: 94°C for 30 sec, 60°C for 30 sec, 72°C for 1 min; and a terminal extension at 72°C for 10 mins. PCR for the FFPE gDNA was altered due to gDNA fragmentation. Four µl of gDNA (80ng) was used and the second PCR cycle increased to 26 to give 40 PCR cycles total. PCR products were run on a 1% agarose gel using hyperladder IV (Bioline). Prior to sequencing the PCR reactions were exosapped [0.3 µl Sap and 1 µl exo/tube (New England Biolabs); 37°C for 30 mins, 80°C for 20 mins]. The sequencing reactions were prepared (2 µL ExoSapped PCR reaction, 1 µl betaine, 1 µl reverse or forward primer, 10 µl DPEC water) and Sanger sequencing was carried out by Australian Genome Research Facility, Sydney. The sequence was aligned on Sequencer 4.9 with the reference sequence from NCBI, NM_001100.

Immunohistochemistry

Frozen muscle biopsy sections were cut at 8 µm, fixed with 3% paraformaldehyde (Sigma-Aldrich) for 3 min at room temperature and ice-cold methanol for 5 minutes -20°C, and stained with α-skeletal actin or cardiac actin. Primary antibodies used: polyclonal rabbit anti α-skeletal-actin, 1:100 (Sophie Clement, University of Geneva); monoclonal mouse cardiac
11 actin produced in a sheep, 1:250 (American Research Products); monoclonal mouse neonatal myosin, 1:20 (Novocastra). Secondary antibodes; Alexa Fluor® 488 donkey anti-rabbit IgG, 1:200 (Invitrogen); Alexa Fluor® 555 goat anti-mouse IgG, 1:200 (Invitrogen). The sections were imaged on an Olympus BX50 microscope linked to a SPOT™ digital imaging camera (Diagnostics Instruments Inc).

Western blot analysis

Frozen muscle biopsies were cut at 8 µm thickness to a total surface area of 200 mm^2 per sample. Solubilising solution [4% SDS (Sigma-Aldrich), 12 mM Tris pH 8.8, 20% glycerol (Astral Scientific), bromethol blue powder (Sigma-Aldrich) with the addition of 500 mM dithiothreitol (Biorad) and 1:500 protease inhibitor cocktail (Sigma-Aldrich) immediately prior to loading] was added at a ratio of 10 mm^2: 5 µl. Each sample was sonicated to

homogenise the muscle before heat inactivating at 94°C for three minutes and solubilising for 20 minutes on ice. Samples were separated on a 4-12% 1 mm, 10 well Biorad polyacrylamide gel by sodium dodecyl sulphate-polyacrylamide gel electrophoresis (SDS-PAGE) at 150 V constant voltage with 5 µl of Pageruler^{TM}Plus prestained protein ladder (Thermoscientific). A loading gel was used to determine equal loading based on myosin expression levels by coomassie staining. The experimental gel was transferred at 400 mA for one hour onto a PVDF membrane (Millipore) in transfer buffer (25 mM Tris, 192 mM glycine and 20% methanol, pH 8.3). Membranes were blocked for one hour in 5% skim milk diluted in phosphate buffer saline with 0.1% tween (PBST, Biochemicals) and probed with primary antibody diluted in 5% skim milk in PBST for 2 hours at room temperature [α-skeletal actin 1:2000, cardiac actin 1:1500, Glyceraldehyde 3-phosphate dehydrogenase 1:10,000 (GAPDH, Chemicon)]. Membranes were washed three times in PBST, blocked for 10 minutes and blotted with secondary antibody diluted 1:2000 in 5% skim milk in PBST at room temperature for 2 hours [α-skeletal actin probe with donkey anti-rabbit IgG HRP conjugate (GE Healthcare Biosciences) and cardiac actin & GAPDH probes with sheep anti-mouse IgG HRP conjugate, (VWR)]. The membrane was washed four times in PBST and developed with ECL Chemiluminescent reagents using Hyperfilm (VWR).

2.3 Part B: Molecular investigations into the ACTA1 Val154Leu variant

2.3.1 Results

2.3.1.1 ACTA1 c.460C>G variant segregates with disease

The *ACTA1* c.460C>G variant was identified by targeted next-generation sequencing in the older affected brother (II-3), causing a missense change Val154Leu. To determine if the identified variant segregated with disease, we carried out Sanger sequencing of *ACTA1* on the two probands, parents and four unaffected siblings. We identified the same homozygous variant, c.460C>G, in the younger affected brother (II-6) (Figure 2.3B, right chromatograms). By Sanger sequencing, the parents (I-1 and I-2) and two out of four unaffected siblings (II-1 and II-2) are heterozygous for c.460C>G (Figure 2.3, left chromatograms). Two out of four of the unaffected siblings (II-4 and II-5) are homozygous for wild type, c.460C, *ACTA1* (Figure 2.3, middle chromatograms). These results show recessive inheritance of the c.460C>G *ACTA1* variant segregates with congenital muscular dystrophy with rigid spine.

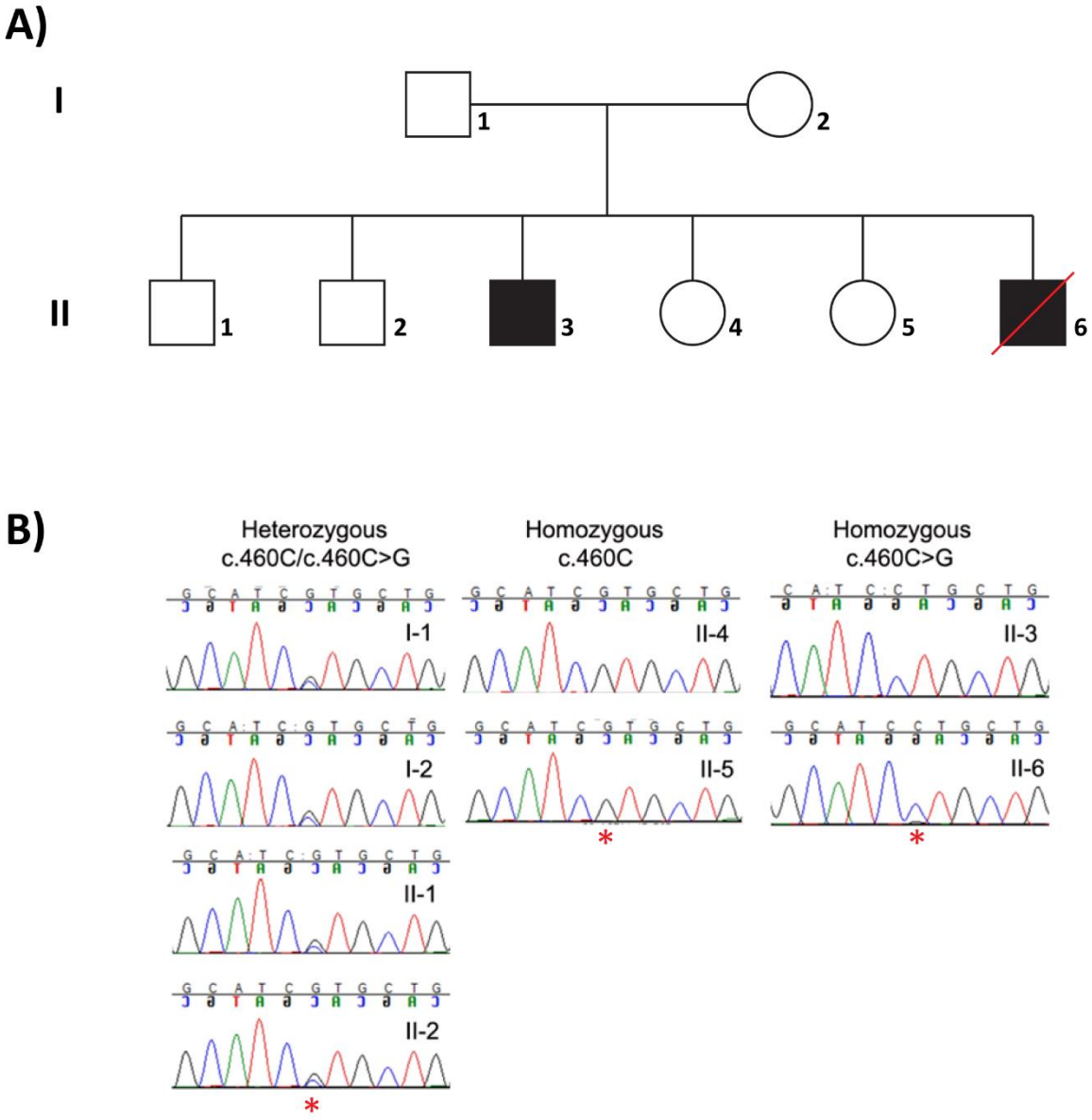

Figure 2.3: Sanger sequencing confirms *ACTA1* c.460C>G segregates with disease.
(A) Pedigree of affected family - Black fill indicates probands, red line indicates deceased. **(B)** Sanger sequencing chromatograms of *ACTA1* from position 455 to 465. Position 460 indicated with a red asterisk. Left chromatogram shows the unaffected parents, I-I & I-2, and two unaffected siblings, II-1 & II-2, are heterozygous for the *ACTA1* c.460C>G variant. The middle chromatogram shows two unaffected siblings, II-4 & II-5, do not carry the c.460C>G variant. The right chromatogram shows the two affected siblings, II-3 and II-6, are homozygous for the c.460C>G variant.

2.3.1.2 Levels and localisation of sarcomeric proteins within patient muscle

Protein levels

On histology, we observed protein aggregates which are structurally equivalent to nemaline bodies in the muscle of patient II-3. In order to determine whether the pathological pattern was similar to that described for other *ACTA1* NM patients, we carried out protein studies, particularly focusing on proteins commonly found in nemaline rods. Serial dilutions of skeletal muscle lysates of patient II-3 and a healthy age-matched control show upregulation of desmin, filamin, αβ-crystalin and α-actinin 2 in patient muscle (Figure 2.4).

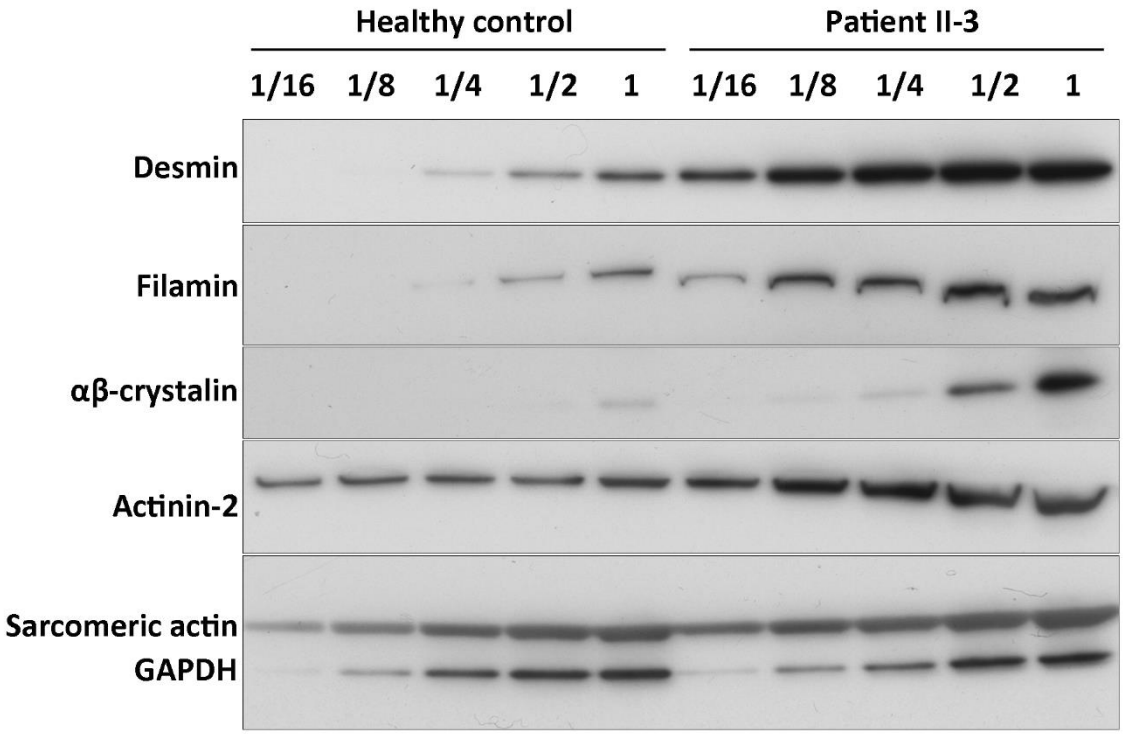

Figure 2.4: Patient muscle shows upregulation desmin, filamin, αβ-crystalin and α actinin-2. Western blot of skeletal muscle lysates. Loading is normalised to total myosin. Fractions indicate serial dilutions. Healthy muscle (17 years) and patient II-3 (17 years) were probed for desmin, filamin, αβ-crystalin and α actinin-2 levels. Sarcomeric actin and GAPDH were probed for as loading controls. Desmin, filamin, αβ-crystalin and α actinin-2 are upregulated in patient muscle.

Composition of inclusions

The adenosine triphosphatase reaction was carried out on patient II-3 muscle at pH 4.3 (ATPase 4.3) and showed inclusions within type I (slow twitch) fibres (Figure 2.5A, black arrows). We wanted to determine the protein composition of the inclusions seen within patient muscle. We stained patient II-3 muscle for proteins we found to be upregulated by western blot – desmin, filamin, αβ-crystalin, α-actinin-2 (Figure 2.5) and myotilin (result not shown). Inclusions consistent with those observed with the ATPase 4.3 reaction stained positively for myotilin and filamin (Figure 2.5B, white arrows). In addition, we observed aggregates positive for myotilin which differed in location, shape and size to those observed with the ATPase 4.3 reaction (Figure 2.5C, white arrows).

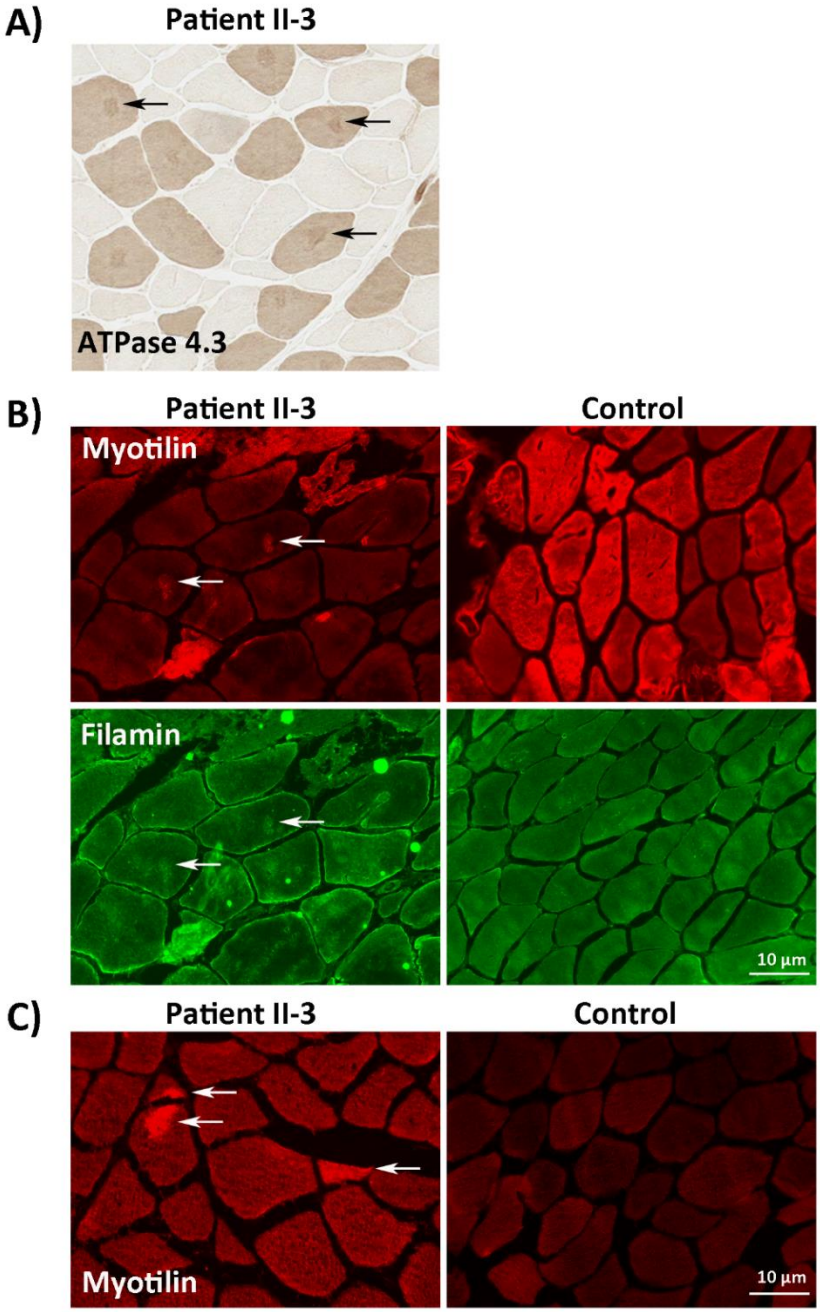

Figure 2.5: Patient inclusions contain myotilin and filamin. (A) The adenosine triphosphatase reaction was carried out at pH 4.3 (ATPase 4.3) on skeletal muscle of patient II-3 (17 years). Small, rounded inclusions near the centre of the myofibre were observed within type I fibres (black arrows). **(B, C)** Skeletal muscle of patient II-3 (17 years) and control (17 years) were stained for myotilin and filamin. Inclusions consistent in size, shape and location with those observed with ATPase 4.3 stained positively for myotilin and filamin (B, white arrows). Larger aggregates near the periphery of the myofibre of inconsistent shape stained positively for myotilin (C, white arrows). Note: Exposure times are 5s and 3.8s for panel B and C respectively. **The ATPase 4.3 reaction was carried out by the pathology department at the Children's Hospital at Westmead using standard procedures and imaged by Simranpreet Kaur on a Scanscope CS2 microscope (Aperio).**

2.3.1.3 Investigating the presence of cardiac actin

We established in Part A that the *ACTA1* c.460C>G variant is the first recessive variant within *ACTA1* where α-skeletal actin is made. Survival of *ACTA1*-myopathy patients who do not produce α-skeletal actin is due to the maintenance of cardiac actin expression within skeletal muscle beyond birth (Nowak et al., 2007). Similar to other recessive ACTA1 mutations, and thus in support of *ACTA1* c.460C>G being a pathogenic variant, we observed cardiac actin expression within a subset of skeletal muscle fibres of the elder affected son (Part A, Figure 2I). There was variation in the size and staining intensity of cardiac actin positive fibres.

The presence of cardiac actin within patient muscle can be a sign of either regeneration/degeneration or compensatory upregulation due to loss of functional skeletal actin. We further characterised cardiac actin positive fibres to determine the cause of cardiac actin expression within patient skeletal muscle.

Fibre typing cardiac actin positive fibres

To investigate if cardiac actin was produced selectively in fast or slow fibres we co-stained patient muscle with cardiac actin and slow-myosin (a marker of slow-twitch fibres) (Figure 2.6). Our results show that cardiac actin positive fibres within patient skeletal muscle is not restricted to fast or slow-twitch muscle fibres. However, only ~ 20% of cardiac actin positive fibres stained positively for slow myosin (Figure 2.4, white arrows). This differed from the Duchenne Muscular Dystrophy (DMD) positive control where ~50% of cardiac positive fibres stained positively for slow myosin (Figure 2.4, middle panel). This suggests ~80% of cardiac positive fibres within patient skeletal muscle are fast twitch fibres.

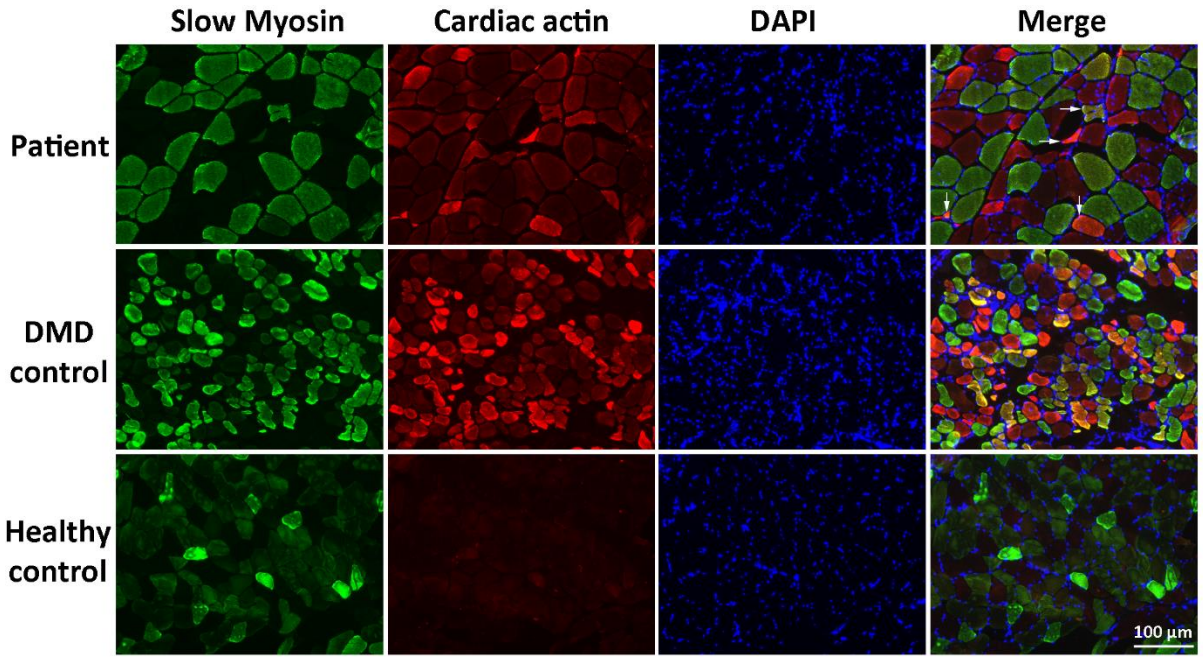

Figure 2.6: Slow twitch fibres are the minority of cardiac actin positive fibres. Skeletal muscle sections were co-stained with slow myosin (green), cardiac actin (red) and DAPI (blue). Patient II-3 (17 years) showed a small subset of cardiac actin positive fibres staining positive for slow myosin (white arrows). A Duchenne muscular dystrophy muscle biopsy (DMD, 2 years) was used as a positive control for cardiac actin. Approximately 50% of cardiac actin positive fibres within the DMD control stained positive for slow myosin. A muscle biopsy from a healthy adult (17 years) was used as negative control for cardiac actin, showing only background staining for cardiac actin.

Regenerating fibres within patient muscle

The foetal cardiac isoform, cardiac actin, is present within regenerating muscle fibres of dystrophic muscle (Dubowitz & Sewry, 2007). Therefore, we wanted to determine if the high proportion of cardiac actin positive fibres in patient muscle was attributed to regenerating fibres by co-staining sections with cardiac actin and markers for fibre regeneration (neonatal/developmental myosin, Figure 2.7A and B). Our results show the high proportion of cardiac actin positive fibres seen in patient muscle cannot be attributed to regenerating fibres. We do observe cardiac actin positive regenerating fibres – fibres staining positive for neonatal and/or developmental myosin (Figure 2.7, white arrows). However, we observe more cardiac positive non-regenerating fibres – fibres negative for developmental and neonatal myosin (Figure 2.7, white arrowhead). Interestingly, the non-regenerating cardiac actin positive fibres have a lower staining intensity than the regenerating cardiac actin positive fibres.

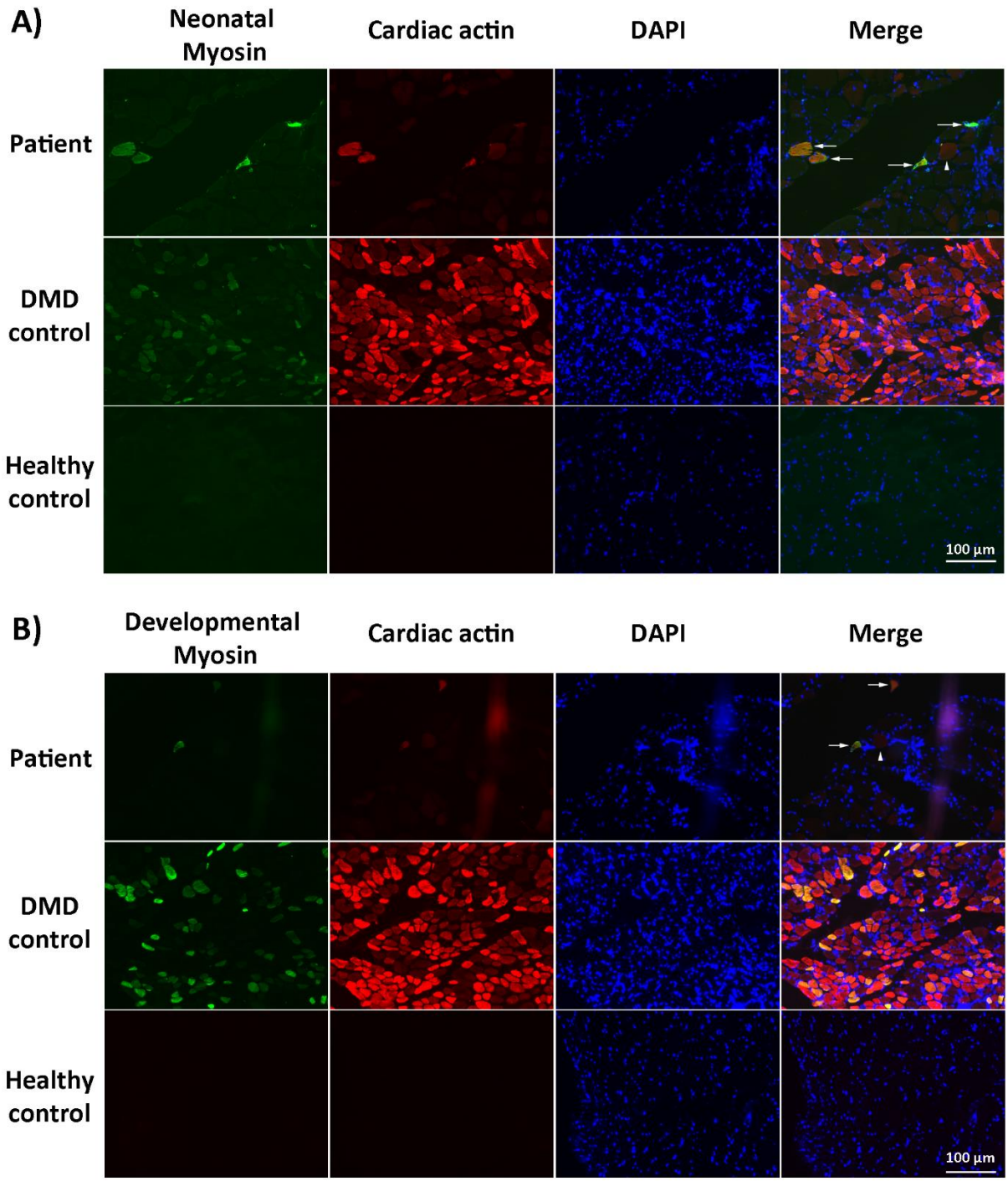

Figure 2.7: Regenerating fibres do not account for the majority of cardiac actin positive patient fibres. Sequential sections of skeletal muscle were co-stained with **(A)** neonatal or **(B)** developmental myosin (green), cardiac actin (red) and DAPI (blue). Fibres in Patient II-3 (17 years) strongly positive for cardiac actin, stained positively for neonatal and/or developmental myosin (white arrows). Fibres in Patient II-3 (17 years) weakly positive for cardiac actin, stained negatively for neonatal and/or developmental myosin (example - white arrowhead, same fibre). A Duchenne muscular dystrophy muscle biopsy (DMD, 2 years) was used as a positive control for regenerating fibres. A muscle biopsy from a healthy adult (17 years) was used as a negative control for regenerating fibres.

2.3.1.4 Molecular modelling of ACTA1 Val154Leu

Molecular modelling was used to investigate how ACTA1 Val154Leu may alter the function of α-skeletal actin and therefore cause disease. Molecular modelling suggests ACTA1 Val154Leu may compromise actin polymerisation.

The tertiary structure of α-skeletal actin was not predicted to be influenced by the Val154Leu variant. Substitution of valine with leucine at position 154 is a conservative change (Figure 2.8A) within a β-sheet of subdomain 3 of α-skeletal actin (Figure 2.8B, left). In silico analysis suggested the substitution of valine with leucine at position 154 does not alter this β-sheet structure (Figure 2.8B, right).

Interaction between α-skeletal actin and other sarcomeric proteins is not predicted to be influenced by the Val154Leu variant. Position 154, within subdomain 3, is in close proximity to the hydrophobic binding pocket, where many proteins bind to actin. However, subdomain 3 faces the interior of the filamentous actin structure and the Val154Leu variant is therefore unlikely to interact with sarcomeric proteins. We investigated amino acids within a 4Å radius of Val154Leu and changes in hydrogen bonding (Figure 2.8C, left and middle). All amino acids influenced by Val154Leu were internal and also unlikely to bind to sarcomeric proteins. Interestingly, three amino acids in the hinge region - Ser143, Leu144 and Met301 – were influenced by Val154Leu (Figure 2.8C, right).

The hinge region allows relative movement of the two domains. Movement of the two domains is required for ATP and a metal ion (calcium or magnesium) to bind in the ATP-binding pocket. ATP-ADP exchange is a crucial step for actin polymerisation. Therefore, if the Val154Leu variant influences the hinge region, ATP binding and/or ATP-ADP exchange may be compromised and in turn, polymerisation.

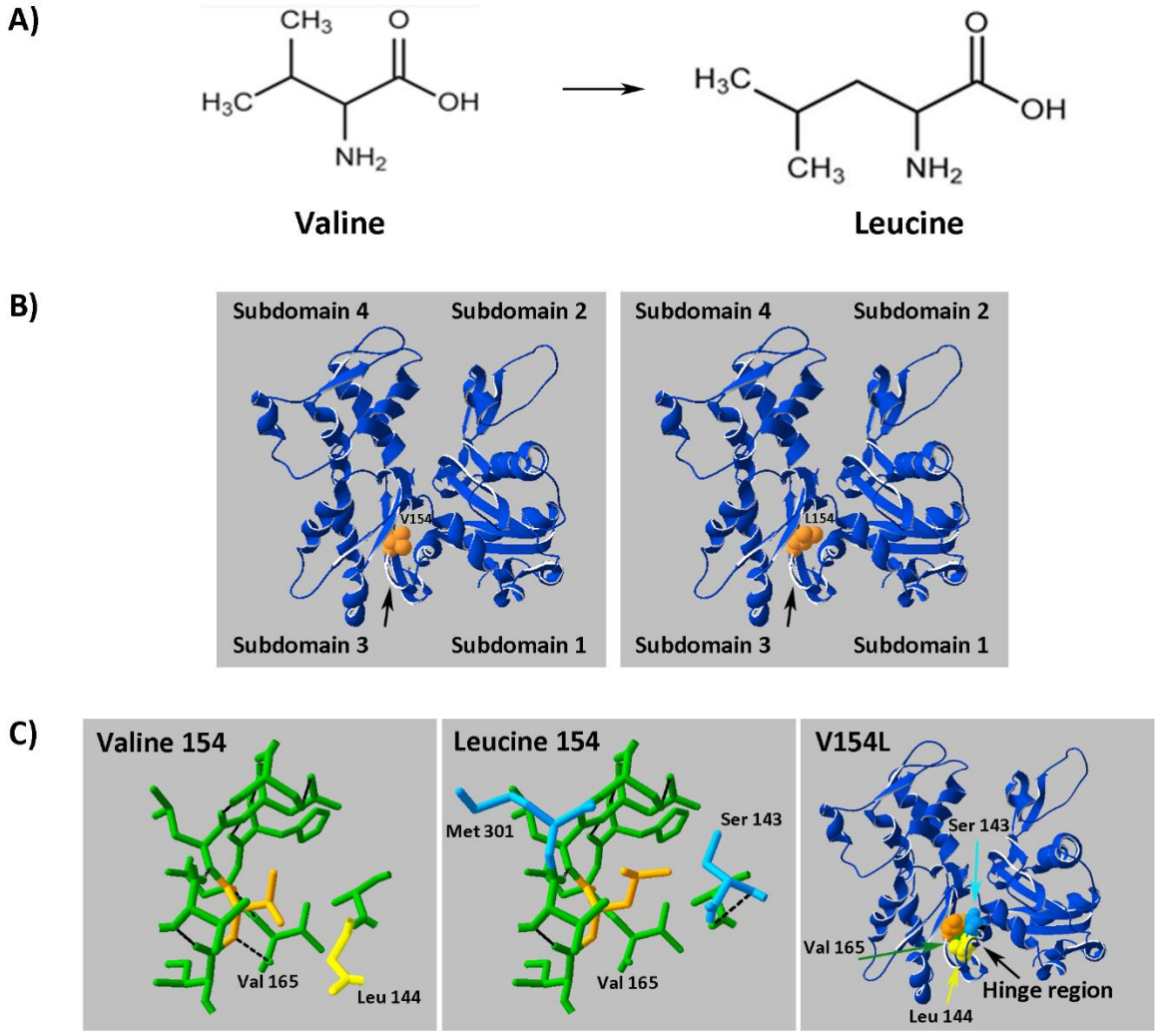

Figure 2.8: Molecular modelling predicts hinge region residues are influenced by the Val154Leu variant. (A) Valine to leucine is a conservative amino acid change. **(B)** Valine 154 is part of a β-sheet (black arrow) in subdomain 3. The change of valine to leucine at position 154 is not predicted to alter the secondary structure of α-skeletal actin. The β-sheet is maintained at position 154 (black arrow). **(C)** When valine (left) is changed to leucine (middle) at position 154 (orange) the residues and hydrogen bonding (black dashed lines) within a 4Å radius change. Leu144 (yellow) is lost, and Ser143 & Met299 are gained (light blue). The hydrogen bond with Val165 is lost. Leu144, Ser143 and Val165 are within the hinge region of α-skeletal actin (right). Molecular modelling of α-skeletal actin was carried out in DeepView/Swiss-Pdb Viewer (v 4.1.0) http://www.expasy.org/spdbv/(4) from the crystal structure solved by Kabsch et al. (1990).

2.3.2 Discussion

We have established the first recessive variant within *ACTA1* as the genetic cause of congenital muscular dystrophy with rigid spine. *ACTA1* variants typically present with a congenital myopathy pathology and severe clinical presentation. Dystrophic pathology (Wallgren-Pettersson & Laing, 2001) and stiffness (Jain et al., 2012) has been reported previously, but not in combination. The unique combination of clinical and histological presentation of our two patients expands the spectrum of *ACTA1* disease, and will help guide clinical care and future genetic diagnoses.

We observed upregulation of desmin, filamin, αβ-crystalin, myotilin and α-actinin 2 in patient muscle (Figure 2.4). The upregulation of filamin and myotilin can be readily explained by the presence of these proteins in aggregates within patient muscle (Figure 2.5). However, the degree of upregulation of filamin and myotilin is inconsistent with the number of inclusions/aggregates observed within the patient muscle. We did not find evidence of desmin, αβ-crystalin or α-actinin 2 within aggregates. Both affected brothers are homozygous for *ACTN3* R577X (previous diagnostic investigations, results not shown). *ACTN3* encodes α-actinin 3, a component of the Z-line. *ACTN3* R577X is a common polymorphism which results in an absence of α-actinin 3 (North et al., 1999). Patient II-3 muscle is absent for α-actinin 3 (previous diagnostic investigations, results not shown). Absence of α-actinin 3 results in compensatory upregulation of α-actinin-2 (MacArthur et al., 2007). Furthermore, the *Actn3* knockout mouse shows upregulation of desmin, filamin, αβ-crystalin and myotilin (Quinlan et al., 2010; Seto et al., 2011). Therefore, the *ACTN3* R577X polymorphism carried by both affected brothers may cause the upregulation of desmin, αβ-crystalin and α-actinin 2; and exacerbate the upregulation of myotilin and filamin, seen within patient muscle.

Chapter 3 - The link between *LMOD3* and *KLHL40*: two disease genes for nemaline myopathy

3.1 Introduction

3.1.1 Nemaline myopathy

Nemaline myopathy is a heterogeneous type of congenital myopathy first described in 1963 (Conen, Murphy, & Donohue, 1963; Shy, Engel, Somers, & Wanko, 1963) with an incidence of 1 in 50,000 live births (Sanoudou & Beggs, 2001). Nemaline myopathy is characterised by generalised muscle weakness and hypotonia (loss of muscle tone) as well as the presence of electron-dense protein aggregates, termed 'nemaline bodies', within skeletal muscle. *Nema* is the latin word for thread-like, explaining the etymology of the nomenclature, nemaline myopathy. While the presence of nemaline bodies are a requirement for a diagnosis of nemaline myopathy, the number and size of nemaline bodies within a muscle biopsy does not correlate with disease severity (Shimomura & Nonaka, 1989). The clinical spectrum of nemaline myopathy is broad, with sub-classification into six subtypes (Sanoudou & Beggs, 2001): Severe congenital, intermediate congenital, typical congenital, childhood onset, adult onset and Amish. Involvement of the respiratory muscles is common and can result in death due to respiratory insufficiency.

Nemaline myopathy is genetically heterogeneous and is associated with variants in thirteen genes to date. Ten of the thirteen genes linked with nemaline myopathy encode sarcomere thin filament proteins: Tropomyosin-3 (*TPM3*) (Laing et al., 1995), α-skeletal actin (*ACTA1*) (Nowak et al., 1999), troponin T1 (*TNNT1*) (Johnston et al., 2000), tropomyosin-2 (*TPM2*) (Donner et al., 2002), nebulin (*NEB*) (Lehtokari et al., 2006), cofilin-2 (*CFL2*) (Agrawal et al., 2007), leiomodin-3 (*LMOD3*) (Yuen et al., 2014), Myosin XVIIIB (*MYO18B*) (Malfatti et al., 2015), Myopalladin (*MYPN*) (Miyatake et al., 2017) and troponin T3 (*TNNT3*) (Sandaradura et al., 2017). This led nemaline myopathy to be considered a disease of the thin filament (Nance, Dowling, Gibbs, & Bonnemann, 2012). Three out of the thirteen genes linked with

nemaline myopathy are part of the kelch protein family: Kelch-like family member 40 (*KLHL40*) (Ravenscroft et al., 2013), kelch-like family member 41 (*KLHL41*) (Gupta et al., 2013) and kelch-repeat and BTB (POZ) domain containing 13 (*KBTBD13*) (Sambuughin et al., 2012). Our understanding of the role kelch proteins play in nemaline myopathy and their link to the thin filament is at its early stages and is reviewed in sections 3.1.3 and 3.1.4.

3.1.2 The leiomodin family

The leiomodin (LMOD) family is related to the tropomodulin (TMOD) family of actin capping proteins (Conley, Fritz-Six, Almenar-Queralt, & Fowler, 2001). The N-terminal two-thirds of the leiomodins share ~40% amino acid homology to the TMOD family. The LMOD family has a C-terminal extension which the TMODs lack (Conley et al., 2001). The LMOD family is made up of three members: leiomodin-1 (LMOD1), leiomodin-2 (LMOD2) and leiomodin-3 (LMOD3) (Nanda & Miano, 2012). The gene structure of *LMOD* is simple, each containing three exons, with the majority of the protein-coding region within exon 2 (Conley et al., 2001). *LMOD1* is predominantly expressed in smooth muscle, while *LMOD2* and *LMOD3* are predominantly expressed in striated muscle (Conley, 2001; Conley et al., 2001; Nanda & Miano, 2012).

In skeletal muscle, the LMOD and TMOD families play an important role in regulating actin turnover at the pointed end of the thin filament (reviewed in Fowler & Dominguez, 2017). The TMODs cap the pointed end of the thin filament, preventing actin monomer addition or dissociation (Weber, Pennise, Babcock, & Fowler, 1994). The LMODs are powerful actin filament nucleators, functioning both in the formation of new actin filaments (nucleation), and, in the addition of actin monomers to an established actin filament at the pointed end (polymerisation) (Boczkowska, Rebowski, Kremneva, Lappalainen, & Dominguez, 2015; Chereau et al., 2008). LMOD contains one tropomyosin binding domain (TM-h) and three actin

binding domains – A-H (Actin-binding helix), LRR (Leucine rich repeat) and WH2 (Wiskott-Aldrich-Syndrome protein homology 2 domain). LMOD can bind three G-actin monomers and form the 'nucleus' of a *de novo* actin filament. The interface of the nucleus is thought to be bound by the LRR, with the N-terminal wrapping around the nucleus positioning A-H to bind the first actin monomer and allowing TM-h to recruit tropomyosin. The C-terminal is thought to wrap around the nucleus, positioning the WH2 domain to bind the third actin monomer (Figure 3.1) (Fowler & Dominguez, 2017).

Variants within *LMOD* genes have been associated with disease in humans (Abbott et al., 2017; Berkenstadt et al., 2018; Halim et al., 2017; Yuen et al., 2014) and recapitulated in mouse models (Cenik et al., 2015; Halim et al., 2017; Tian et al., 2015). Loss of *LMOD1* is linked with megacystis microcolon intestinal hypoperistalsis (Halim et al., 2017). Our group established *LMOD3* as a disease gene for severe nemaline myopathy (Yuen et al., 2014), and mice deficient in *Lmod2* present with a lethal dilated cardiomyopathy (S. Li et al., 2016; Pappas et al., 2015).

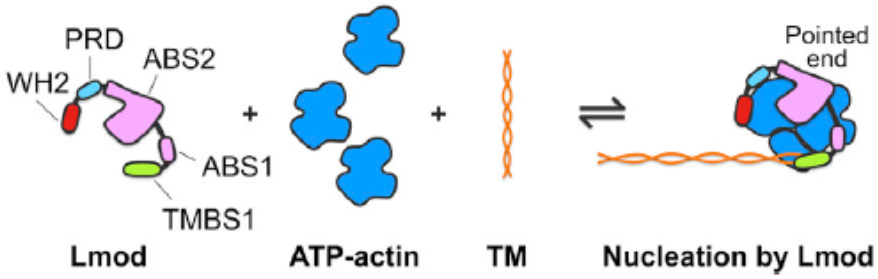

Figure 3.1: LMOD as a nucleator. LMOD contains a tropomyosin binding domain (TMBS1, green) and three actin binding domains (ABS1, purple; ABS2, purple; and WH2, red). LMOD can bind three G-actin monomers and form the 'nucleus' of a *de novo* actin filament. ABS2 is thought to bind at the interface of the actin nucleus. Reproduced from Fowler and Dominguez (2017). PRD – proline-rich domain.

3.1.3 Kelch-like superfamily

Kelch proteins

The kelch proteins are part of a large superfamily of genes defined by the presence of a kelch-repeat domain (Dhanoa, Cogliati, Satish, Bruford, & Friedman, 2013). Kelch proteins carry out a range of processes within the cell inclusive of actin binding, cell morphology and gene expression - but are best known for their role in the ubiquitin-proteasome pathway as ubiquitin ligase adaptor proteins (Adams, Kelso, & Cooley, 2000; Dhanoa et al., 2013; Shibata, Zhang, Puthumana, Stone, & Lifton, 2013). The kelch superfamily is made up of 63 protein-coding genes (plus three non-coding genes), divided into three families: (1) *KLHL* (42 members); (2) *KBTBD* (nine members); and (3) *KLHDC* (12 members) (Gupta & Beggs, 2014) (Figure 3.2A).

The different classes of kelch proteins are defined by the presence or absence of three domains: (1) BTB/POZ domain: **B**road complex, **t**ramtrack and **b**ric à brac (Zollman, Godt, Prive, Couderc, & Laski, 1994)/**po**xviruses and **z**inc finger (Bardwell & Treisman, 1994); (2) BACK domain: **B**TB **a**nd **C**-terminal **k**elch repeats (Stogios & Prive, 2004); and (3) a variable number of kelch-repeats.

KLHL proteins contain a BTB/POZ domain, BACK domain and kelch repeats (Dhanoa et al., 2013). KBTBD are similar to KLHL proteins but frequently lack the BACK domain. KLHDC proteins contain kelch repeats but typically lack BTB/POZ and BACK domains, and have other domains in their place (Figure 3.2B).

The BTB domain is involved in protein-protein interaction (Albagli, Dhordain, Deweindt, Lecocq, & Leprince, 1995) as well as self-dimerization (Zipper & Mulcahy, 2002). An important role of the BTB domain within kelch proteins is the interaction with the E3 ligase Cullin 3 (Cul3), mediating substrate-specific ubiquitination (Pintard, Willems, & Peter, 2004). The kelch-repeat domain is the region within kelch proteins which binds the specific substrate,

for example, KLHL37 binds actin (Adams et al., 2000). The kelch-repeat forms a β-propeller structure (Ito, Phillips, Yadav, & Knowles, 1994); each blade of the propeller is formed from a single kelch-motif folding into a four-stranded antiparallel β-sheet (Adams et al., 2000). The BACK domain has no known function to date, however, it is hypothesised to position the kelch-repeat-bound substrate in proximity to Cul3 (Stogios & Prive, 2004).

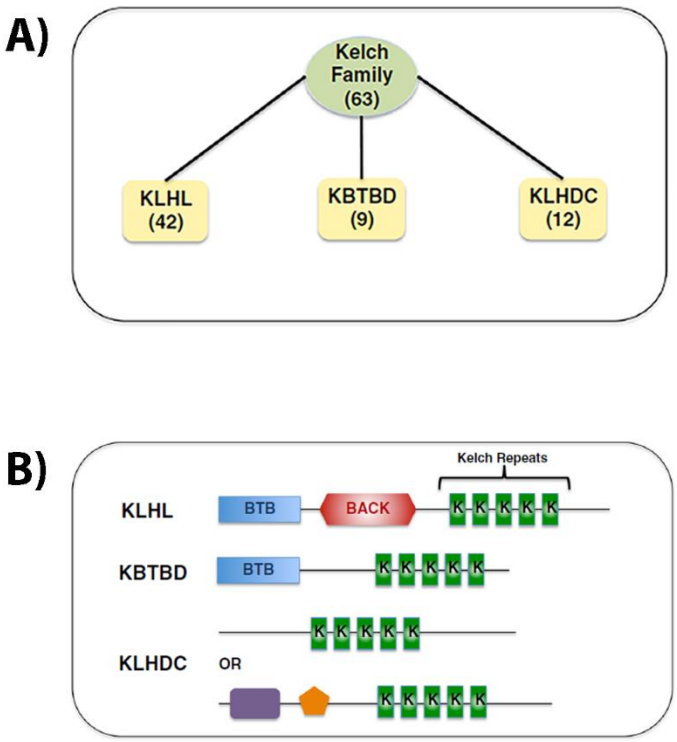

Figure 3.2: The kelch-like superfamily. (A) The kelch-like superfamily consisting of 63 proteins is sub-divided into three families: KLHL, KBTBD and KLHDC. **(B)** Typical domain organisation of KLHL, KBTBD and KLHDC families. KLHL consist of a BTB/POZ domain, a BACK domain and kelch repeats. KBTBD consist of a BTB/POZ domain and kelch repeats, typically missing the BACK domain. KLHDC contain kelch repeats with or without other domains (depicted in purple and orange) and typically lack the BTB/POZ and BACK domains. Reproduced from Gupta and Beggs (2014).

Ubiquitination

Ubiquitin (Ub) is an evolutionarily conserved 76-amino acid polypeptide present within eukaryotes (Pickart & Fushman, 2004). Ub forms an isopeptide bond with its substrate through Gly76 and most often a lysine (Lys) within the target substrate (Busch & Goldknopf, 1981; Hunt & Dayhoff, 1977; Orrick, Olson, & Busch, 1973). Substrate proteins may be mono-ubiquitinated or polyubiquitinated (Pickart & Fushman, 2004).

Ubiquitination occurs over three steps, catalysed by three enzymes (Hershko, Heller, Elias, & Ciechanover, 1983 and reviewed in Lecker et al., 2006): Ub-activating Enzyme 1 (E1), Ub-carrier proteins (E2) and Ub-ligases (E3) (Figure 3.3). Ub is activated by E1 in an ATP-dependent reaction, generating a highly reactive Ub thiolester. The activated Ub is then transferred to a sulfhydryl group of E2. E3 subsequently catalyses the transfer of Ub from E2 to a lysine within the substrate, and then a lysine within each additional Ub resulting in a polyubiquitinated substrate. In mammals, there is a single E1 per cell and 20-40 E2s, increasing ubiquitination specificity. E3s are the major source of specificity in the Ub-proteasome pathway, of which there are 500-1000 in mammals. Some E3s are able to bind Ub directly, mediating transfer to the substrate. Some E3 ligases bind both E2 and the substrate, bringing each into close proximity for Ub transfer. Other E3 ligases bind E2, and require an adaptor protein to bind the substrate. The Cullins are a subgroup of E3 ligases which require a substrate specific adaptor protein for ubiquitination. Kelch proteins act as adaptors for one cullin E3 ligase called Cullin-3 (Sarikas, Hartmann, & Pan, 2011).

Ubiquitination is responsible for a range of intracellular signals which differ based on the number of Ubs conjugated to the substrate, and through which lysine within Ub a polyubiquitin chain is formed (Pickart & Fushman, 2004). Polyubiquitination between Lys48 of Ub was the first discovered and is the most well studied (Chau et al., 1989; Finley et al., 1994). A single

polyubiquitin chain linked through Lys48 is sufficient to target a protein to the 26S proteasome for subsequent degradation. Lys68-linked polyubiquitin chains have been shown to be involved in ribosomal protein synthesis (Spence et al., 2000), protein trafficking (Hicke & Dunn, 2003), DNA damage tolerance (Ulrich, 2002) and inflammatory response (Sun & Chen, 2004). Monoubiquitination has been shown to be involved in protein trafficking (Hicke & Dunn, 2003). Lys29-linked polyubiquitination can target a protein for lysosomal degradation (Chastagner, Israel, & Brou, 2006), and kinases have been shown to be inhibited by polyubiquitination through Lys29 or Lys33 (Al-Hakim et al., 2008).

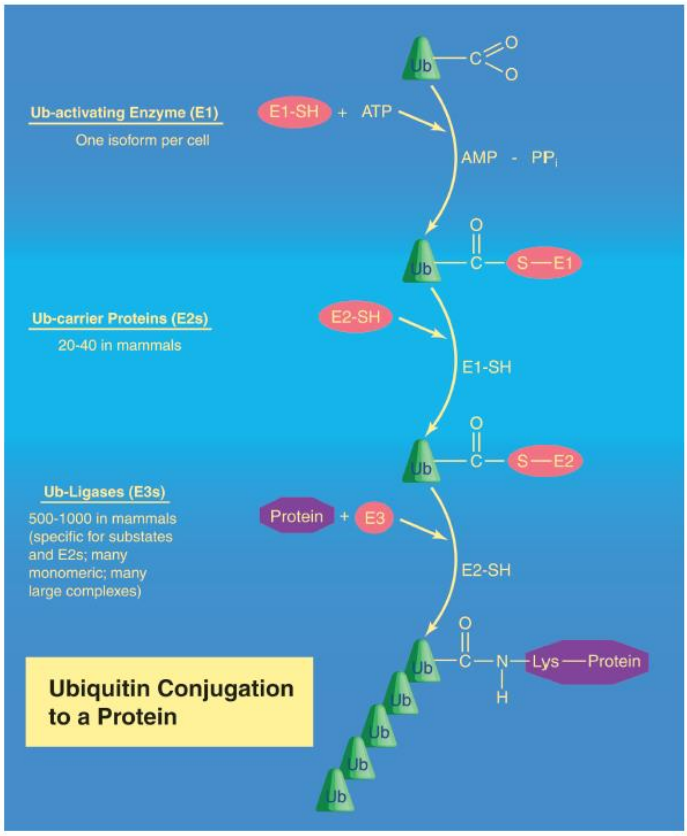

Figure 3.3: Protein ubiquitination. Three sequential steps are required to conjugate Ub onto a protein. E1 catalyses the activation of Ub which is subsequently transferred to E2 and the transfer of Ub onto the substrate is catalysed by E3. Reproduced from Lecker et al. (2006).

Kelch protein and disease

Variants within kelch proteins have been associated with a number of diseases (reviewed in Gupta & Beggs, 2014). Variants within *KLHL6, KLHL19, KLHL20* and *KLHL37* are linked with cancer (Q. K. Li, Singh, Biswal, Askin, & Gabrielson, 2011; Liang, Avraham, Jiang, & Avraham, 2004; Puente et al., 2011; Yuan et al., 2011). Variants within *KLHL1*, *KLHL9, KLHL16, KLHL40, KLHL41* and *KBTBD13* are linked with neuromuscular disease (Bomont et al., 2000; W. L. Chen et al., 2008; Cirak et al., 2010; Gupta et al., 2013; Ravenscroft et al., 2013; Sambuughin et al., 2010). Variants within *KLHL3, KLHL7* and *KLHL10* are a cause of pseudohypoalsosteronism type II (Louis-Dit-Picard et al., 2012), retinitis pigmentosa (Friedman et al., 2009) and oligozoospermia (Yatsenko et al., 2006), respectively.

Kelch proteins in skeletal muscle disease

To date, variants within genes encoding four kelch proteins have been identified as the cause of inherited skeletal muscle disorders in humans: *KLHL9* (Cirak et al., 2010), *KBTBD13* (Sambuughin et al., 2010), *KLHL40* (Ravenscroft et al., 2013) and *KLHL41* (Gupta et al., 2013). A dominant *KLHL9* pathogenic variant found within the BTB domain is associated with distal myopathy (Cirak et al., 2010; Furukawa, He, Borchers, & Xiong, 2003). Dominant variants within *KBTBD13* (Sambuughin et al., 2010) and recessive variants within *KLHL40* (Ravenscroft et al., 2013) and *KLHL41* (Gupta et al., 2013) cause nemaline myopathy. Interestingly, there is high amino acid homology between the kelch domains of KBTBD13, KLHL40 and KLHL41; with KLHL40 and KLHL41 being the most closely related (Gupta & Beggs, 2014). This suggests these proteins may bind the same, or related, substrates and be involved in the same or similar biological processes. In contrast to the proteins encoded by the ten other genes associated with nemaline myopathy, KBTBD13 and KLHL41 do not localise to the sarcomere thin filament (Garg et al., 2014; Gupta et al., 2013; Ravenscroft et al., 2013; Sambuughin et al., 2010). KLHL40, however, was reported to localise to the thin filaments

(Garg et al., 2014). Nemaline myopathy due to variants within kelch proteins may result from dysregulation of thin filament related pathways and kelch proteins may play a role in sarcomere maintenance. Human KLHL40 and mouse Klhl41 have been reported to bind thin filament proteins (Garg et al., 2014; Ramirez-Martinez et al., 2017). Mouse Klhl40 has been shown to be involved in the regulation of the MRTF/SRF pathway, which plays an important role in the transcriptional control of cytoskeletal proteins (Cenik et al., 2015). Klhl40 is considered to be a tight regulator of Lmod3 protein levels, this will be reviewed in detail in section 3.1.4.

Dominant *KBTBD13* pathogenic variants cause nemaline myopathy with cores, with variants thus far identified affecting residues within the kelch-repeats (Sambuughin et al., 2010). Pathogenic variants within *KLHL40* and *KLHL41* affect residues within the BTB, BACK and kelch-domains (Gupta et al., 2013; Ravenscroft et al., 2013). *KLHL40* mutations result in severe nemaline myopathy. A genotype-phenotype relationship was found for variants in *KLHL41*. Truncating variants cause a severe form of nemaline myopathy, whereas missense variants cause a mild or intermediate form of nemaline myopathy (Gupta et al., 2013).

The suggested disease mechanism for myopathies due to variants in *KLHL9, KBTBD13, KLHL40* and *KLHL41* is proposed to relate to protein ubiquitination and turnover (Cirak et al., 2010; Sambuughin et al., 2012; Sanoudou & Beggs, 2001). KLHL9, KBTBD13, KLHL40 and KLHL41 proteins have each been shown to form a complex with the Cul3 Ub E3 ligase (Canning et al., 2013; Sambuughin et al., 2012; Sumara et al., 2007; Zhang et al., 2005). KLHL9 and KLHL13 form a complex together with Cul3, Cul-KLHL9-KLHL13. The Cul3-KLHL9-KLHL13 complex has been shown to bind, and ubiquitinate, Aurora B (Sumara et al., 2007). Interestingly, KLHL41 (sarcosin) forms a complex with Cul3, which results in self-ubiquitination (Zhang et al., 2005).

3.1.4 The link between LMOD3 and KLHL40

Recent studies on the involvement of kelch proteins in nemaline myopathy provided a link between kelch and thin filament proteins (Cenik et al., 2015; Garg et al., 2014; Ramirez-Martinez et al., 2017). Mouse Klhl41 has been shown to associate with nebulin (Ramirez-Martinez et al., 2017). Garg et al. (2014) showed KLHL40 associated with two thin filament proteins – nebulin and LMOD3. *In vitro* studies suggest mouse Klhl40 interacts with mouse Lmod3 through the kelch repeat domain, and protects Lmod3 from Ub-dependent proteasome degradation.

Additionally, Garg et al. (2014) showed that co-transfection of a mouse *Lmod3* expression construct, together with an empty vector, resulted in no Lmod protein detected by western blot. Whereas, co-transfection of Lmod3 and a mouse Klhl40 expression construct resulted in robust detection of Lmod3 protein by western blot. Robust detection of Lmod3 protein could also be achieved when cells co-transfected with Lmod3 and an empty vector were treated with the proteasome inhibitor MG132. Further investigations suggested that when Lmod3 was co-transfected with an empty vector, higher levels of polyubiquitinated Lmod3 were observed, compared to when co-transfected with Klhl40. This study suggested polyubiquitin chains were conjugated through Lys48 (Garg et al., 2014); a signal able to target a protein to the proteasome (Chau et al., 1989; Finley et al., 1994). These results suggested Klhl40 protected Lmod3 from Ub-mediated proteasomal degradation.

Garg et al. (2014) also generated a *Klhl40* knock-out (KO) mouse, and showed that Klhl40 deficient muscle had reduced Lmod3 protein levels. They further utilised their cell transfection assay with Klhl40 deletion constructs, to refine the kelch repeat domains as being important in mediating a protective role upon Lmod3 protein levels. A paradigm of disease mechanism for severe *KLHL40*-nemaline myopathy was proposed, where KLHL40 either stabilises LMOD3

or protects it from degradation. The authors hypothesise that muscle weakness in severe *KLHL40*-nemaline myopathy patients may result from a secondary loss of LMOD3.

Cenik et al. (2015) showed Lmod3 and Klhl40 are involved in the feedforward loop that regulates the transcription of G-actin and other structural sarcomeric proteins in skeletal muscle (Figure 3.4). Studies carried out in transgenic mice, where the MEF2 or SRF consensus sites within *Lmod3* were fused to *LacZ,* demonstrated mouse *Lmod3* transcription is regulated by MRTF/SRF and MEF (myocardin-related transcription factors/ serum response factor and myocyte enhancer factor-2). *Klhl40* has previously been shown to be regulated by MEF2 (Liu et al., 2014). Cenik et al. (2015) used luciferase reporter assays to demonstrate Lmod3 and Klhl40 protein promote MRTF/SRF activity. Klhl40 alone was sufficient for MRTF reporter activity which was increased with the addition of Lmod3. Whereas Lmod3 alone was not sufficient for MRTF reporter activity. Furthermore, *Mrtfa* mRNA levels were reduced in the *Lmod3*-KO mice (Cenik et al., 2015). This study suggests loss of Lmod3 results in an accumulation of G-actin in the cytoplasm and reduced production of proteins essential for the contractile apparatus, resulting in nemaline myopathy.

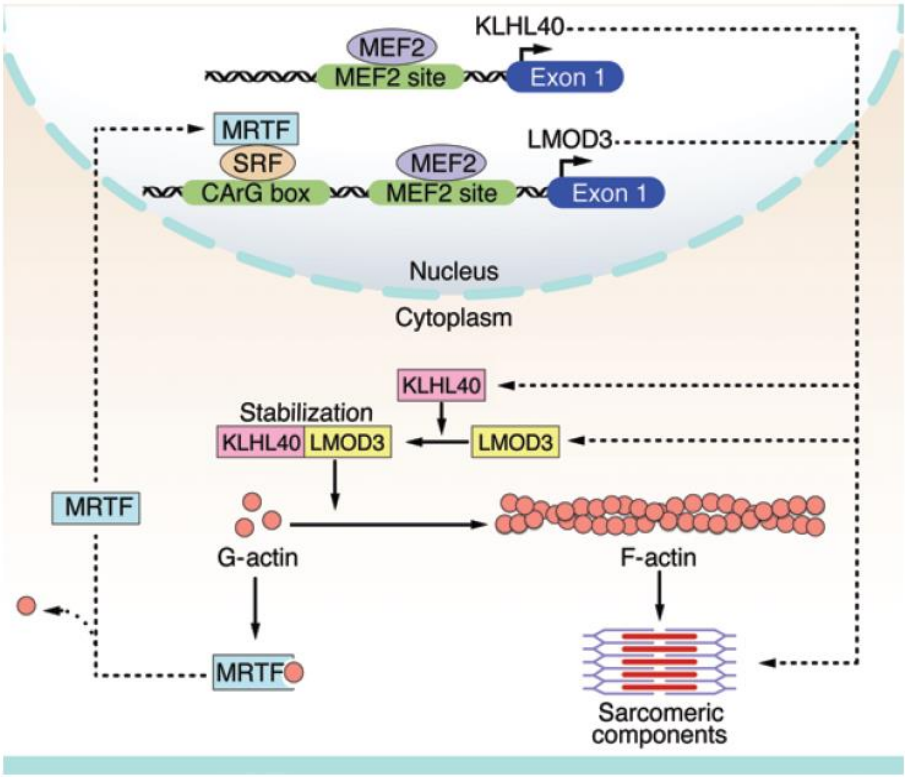

Figure 3.4: Proposed model for the promotion of MRTF/SRF dependent transcription by LMOD3 and KLHL40. MRTF (myocardin-related transcription factor) is sequestered in the cytoplasm when bound to G-actin. Polymerisation incorporates G-actin into F-actin, depleting the cytoplasmic G-actin pool and enabling MRTF to enter the nucleus where MRTF co-activates SRF (serum response factor). MRTF/SRF in combination with MEF (myocyte enhancer factor-2) regulates the transcription of genes crucial for the contractile apparatus, inclusive of *LMOD3* and *KLHL40*. KLHL40 and LMOD3 promote actin polymerisation, therefore depleting the G-actin pool and promoting translocation of MRTF to the nucleus. Reproduced from Cenik et al. (2015).

3.1.5 Study aims

The overarching goal of this part of my PhD was to lend insight into the pathogenesis of nemaline myopathy by: (1) Furthering our understanding of the LMOD family and their role as regulators of actin filament length; and (2) understanding the link between the Cul3-adapter kelch proteins (linked to proteasomal degradation) and LMOD proteins.

More specifically, we investigated the following aims:

PARTA: Investigating LMOD splice isoforms and tissue expression

Aim 1: Investigate expression of splice isoforms of *LMOD1*, *LMOD2* and *LMOD3* in mouse and human tissues.

PART B: Investigating the link between KLHL40 and LMOD proteins

Aim 2: Define regulation of LMOD protein expression by KLHL40:

(1) Determine if LMOD2 and LMOD3 developmental expression patterns correspond with KLHL40.

(2) Determine whether human LMOD3 protein levels are regulated by human KLHL40 (previously characterised in murine models).

(3) Define the region within LMOD3 that mediates regulation by KLHL40.

(4) Establish whether protein levels of LMOD1 and LMOD2 are similarly regulated by KLHL40.

3.2 Results

PART A: Investigating LMOD splice isoforms and tissue expression

3.2.1: Splice isoforms of *LMOD1, LMOD2* and *LMOD3* in mouse and human tissues

Our group established variants within *LMOD3* as a new genetic cause of a severe, lethal form of congenital nemaline myopathy and showed LMOD3 has an indispensable role for striated muscle function (Yuen et al., 2014). Preliminary western blot data collated during this project showed multiple bands on western blot analysis when tissues and cells were probed with antibodies recognising LMOD2 or LMOD3. This suggested additional LMOD isoforms may be expressed at the protein level, likely arising from alternate splice isoforms. To date, no studies have investigated the existence of alternatively spliced versions of LMOD proteins, or their potential function. The first focus of this chapter encompasses investigations into the tissue-specific expression of *LMOD* splice isoforms, as a correlation with data from protein biochemistry.

We utilised publicly-available data from the GTEx portal (https://www.gtexportal.org/home/) (Consortium, 2013) to investigate the tissue-specific expression of mRNA isoforms of human *LMOD1*, *LMOD2* and *LMOD3*. Mining GTEx data identified three putative mRNA isoforms for *LMOD1*, four putative mRNA isoforms for *LMOD2* and three putative mRNA isoforms for *LMOD3*. We used protein prediction programs and published data to compile known domains of the LMODs, and annotated the putative splice isoforms to lend insight into their potential different functions. Western blot was then carried out on a range of mouse and human tissues, to determine if these splice isoforms were detected at the protein level. Triplicate blots were probed with antibodies recognising each of the LMOD paralogues: LMOD1, LMOD2 or LMOD3.

LMOD1

Splice isoforms: The canonical isoform of *LMOD1* (NM_012134) is depicted in Figure 3.5A, and corresponds to the *LMOD1.1* isoform from the GTEx database. Canonical *LMOD1* is made up of three exons with the majority of the protein coding region encoded by exon 2. Exon 3 consists largely of a long 3' untranslated region (UTR). LMOD1.1 has a predicted molecular weight of 67 kDa (NM_012134). The second isoform of *LMOD1* described in GTEx, *LMOD1.2*, lacks a 152 bp from within exon 2 compared to *LMOD1.1* (encoding residues with no described feature or function to date), and has a shortened 5' and 3'UTR. LMOD1.2 has a predicted molecular weight of 62 kDa. The third isoform of LMOD1 described in GTEx, *LMOD1.3*, lacks a stop codon, suggesting mis-annotation of this isoform. All three *LMOD1* mRNA isoforms were annotated in GTEx as being expressed in smooth muscle-containing tissues (Figure 3.5B). *LMOD1.1* was the predominant mRNA isoform detected.

Protein studies: Western blots of a range of mouse tissues, as well as human cardiac and skeletal muscle were probed with an antibody against human LMOD1 (Abcam ab104858, antibody binding site within amino acids 2-51 of NP_036266). We identified a band migrating at 75 kDa, which likely corresponds to the canonical LMOD1 isoform (Figure 3.5C, red arrow, predicted molecular weight of 67 kDa). It is present at low levels in human skeletal muscle and was not detected in human heart. In murine tissues, Lmod1 was detected at high levels in smooth muscle-containing tissues – aorta, bladder, uterus and ovary, consistent with the published observation that *LMOD1* is expressed predominantly in smooth muscle (Conley, 2001; Conley et al., 2001; Nanda & Miano, 2012); and we detected lower levels in skeletal muscle, pancreas and testis.

We also observed a lower molecular weight band at ~65 kDa in most mouse tissues. This may plausibly correspond to LMOD1.2, with a predicted molecular weight of 62 kDa. However,

LMOD1.2 mRNA is not identified in GTEx as being expressed in many of the tissues shown to have a 65 kDa band on western blot (Figure 3.5B, green). Kidney, liver and pancreas, for example, show no reported expression of *LMOD1.2* (Figure 3.5B, green), but show a 65 kDa band on western blot (Figure 3.5C). In addition, a band of 27 kDa was observed recurrently in several tissues. We excluded that this 27 kDa band corresponds to endogenous immunoglobulin light chains, as it was not detected in the absence of the anti-LMOD1 primary antibody (when the membrane was probed with secondary antibody only, see Appendix Figure A.1). Additional bands were observed that do not correspond to any of the predicted mRNAs and are of unknown significance. Unfortunately, tissues from an *Lmod1* KO mouse were not available to establish the specificity of other bands recognised by the anti-LMOD1 antibody.

A)

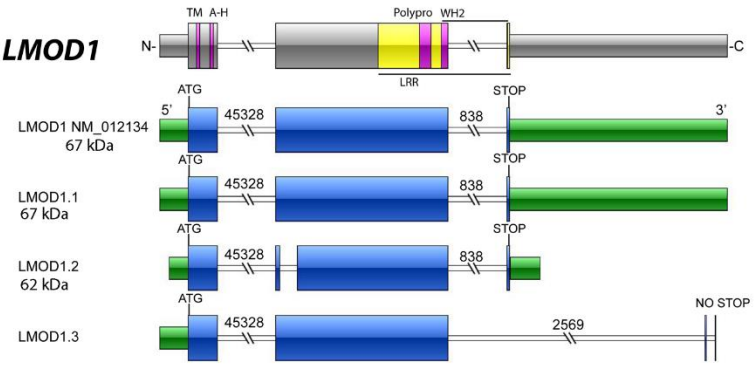
LMOD1
N-
-C
TM
A-H
Polypro
WH2
LRR
ATG
STOP
5'
3'
LMOD1 NM_012134
67 kDa
LMOD1.1
67 kDa
LMOD1.2
62 kDa
LMOD1.3
45328
838
2569
NO STOP

B)

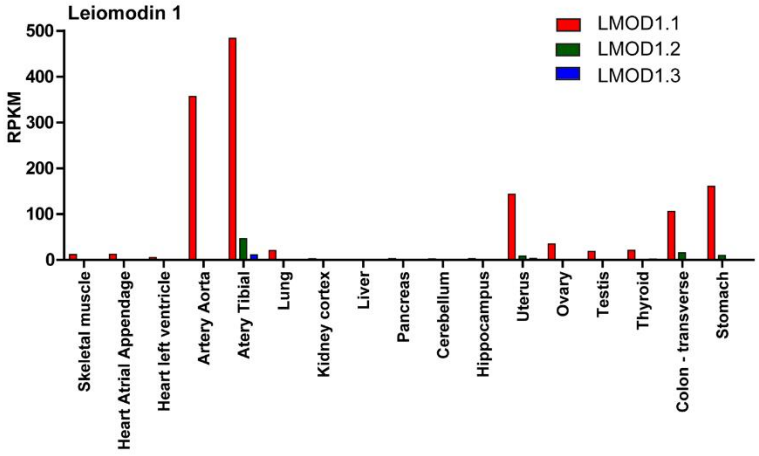
Leiomodin 1
LMOD1.1
LMOD1.2
LMOD1.3
RPKM
500
400
300
200
100
0
Skeletal muscle
Heart Atrial Appendage
Heart left ventricle
Artery Aorta
Atery Tibial
Lung
Kidney cortex
Liver
Pancreas
Cerebellum
Hippocampus
Uterus
Ovary
Testis
Thyroid
Colon - transverse
Stomach

C)

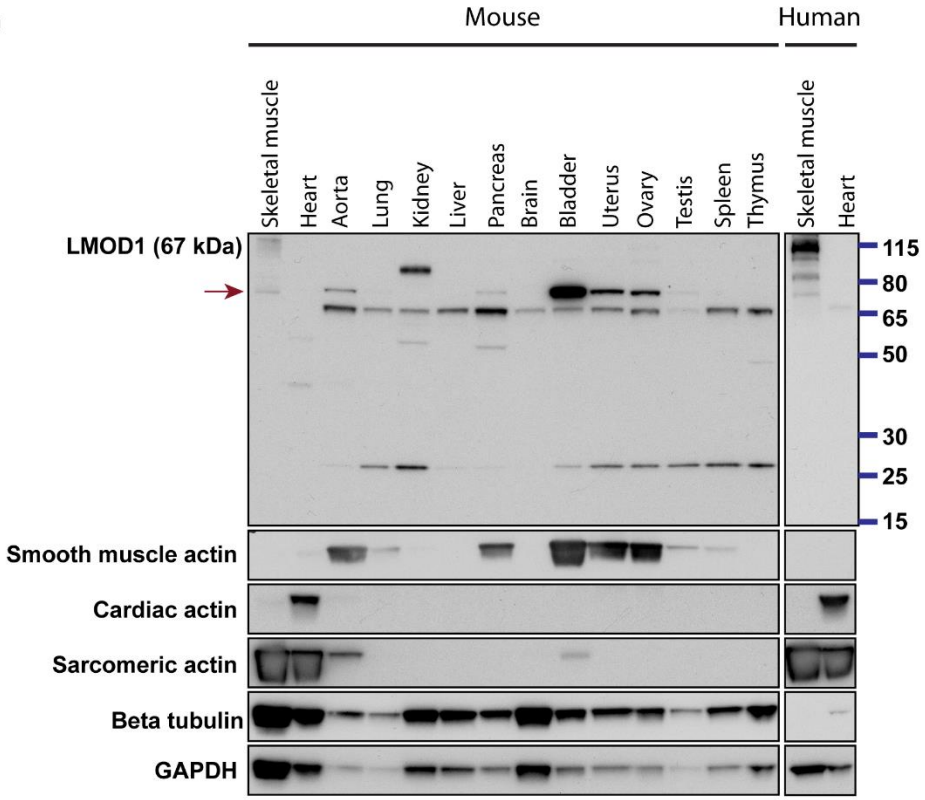
Mouse
Human
Skeletal muscle
Heart
Aorta
Lung
Kidney
Liver
Pancreas
Brain
Bladder
Uterus
Ovary
Testis
Spleen
Thymus
Skeletal muscle
Heart
LMOD1 (67 kDa)
115
80
65
50
30
25
15
Smooth muscle actin
Cardiac actin
Sarcomeric actin
Beta tubulin
GAPDH

Figure 3.5: Investigating LMOD1 splice isoforms. (A) Aligned genomic schematics (to scale) illustrating protein domains and genetic features of canonical *LMOD1* (NM_012134) and GTEx isoforms *LMOD1.1* (ENST00000367288), *LMOD1.2* (ENST00000412469) and *LMOD1.3* (ENST00000400965). Gene structure is annotated as per UCSC (https://genome.ucsc.edu/) and ENSEMBL (http://www.ensembl.org/index.html) entries. Genomic features are annotated as follows: Untranslated regions (green), exons (blue), introns (white), numerals refer to base pairs. Protein structure predictions were adapted from Uniprot (http://www.uniprot.org/), Chereau *et al.* (2008), Prosite (http://prosite.expasy.org/), InterProScan (http://www.ebi.ac.uk/interpro/search/sequence-search), COILS (https://npsa-prabi.ibcp.fr/cgi-bin/npsa_automat.pl?page=npsa_lupas.html), pfam (http://pfam.xfam.org/), ScanProsite (http://prosite.expasy.org/scanprosite/), SMART (http://smart.embl-heidelberg.de/) and LRR finder (http://www.lrrfinder.com/result.php) analysis and marked on the canonical isoform. Protein domains are indicated as follows: Tm – tropomyosin binding domain (pink), A-H - actin-binding helix (pink), LRR – Leucine rich repeat (yellow), Polypro – PolyProline rich region (pink), WH2 – Wiskott-Aldrich-syndrome protein homology 2 domain (pink); **(B)** Tissue expression of *LMOD1* mRNA isoforms from the GTEx database (https://www.GTExportal.org/home/). *LMOD1.1* (red), *LMOD1.2* (green) and *LMOD1.3* (blue). *LMOD1* mRNA is expressed in tissues consisting of smooth muscle. Isoforms are ranked based on mRNA expression (highest to lowest). RPKM – reads per kilobase per million; **(C)** Western blot of tissues harvested from a wild type C57BL/6J mouse (Lanes 1-14), human skeletal muscle (lane 15) and human heart (lane 16). Lmod1 is detected at high levels in mouse tissues with smooth muscle – aorta, pancreas, bladder, uterus, ovary and at low levels in the skeletal muscle and testis. LMOD1 is detected at low levels in human skeletal muscle; Smooth muscle actin, cardiac actin and sarcomeric actin were used as markers for smooth, cardiac and striated muscle respectively. β-tubulin and GAPDH served as loading controls. Red arrow indicates the canonical *LMOD1* (NM_012134) isoform.

LMOD2

Splice isoforms: The canonical isoform of *LMOD2* (NM_207163) is depicted in Figure 3.6A. The canonical *LMOD2* isoform is consistent with the *LMOD2.1* isoform from the GTEx database with additional sequence to the 3' UTR of *LMOD2.1*. LMOD2.1 protein has a predicted molecular weight of 62 kDa. The second LMOD2 isoform described in the GTEx database, LMOD2.2, lacks the C-terminal portion of the Glu-rich and polyproline regions, as well as shortened 5' and 3' UTRs. The LMOD2.2 isoform has a predicted molecular weight of 56 kDa. The third LMOD2 isoform described in the GTEx database, *LMOD2.3*, has a shortened 5'UTR, and lacks the majority of exon 2, including the C-terminal portion of the Glu-rich region and the entire PolyProline and PolyLys regions. *LMOD2.3* extends into intron 2 the majority of which becomes 3' UTR after an alternative stop codon. The LMOD2.3 isoform has a predicted molecular weight of 18 kDa. The fourth isoform described in the GTEx database, *LMOD2.4*, has a shortened 5'UTR and lengthened 3'UTR. LMOD2.4 lacks a portion of exon 2 inclusive of the C-terminal segment of the Glu-rich region. The LMOD2.4 isoform has a predicted molecular weight of 57 kDa. The mRNA isoforms of LMOD2 showed highest expression in skeletal muscle and heart tissue (Figure 3.6B).

Protein Studies: Western blots of a range of mouse tissues, as well as human cardiac and skeletal muscles, were probed with a polyclonal antibody against human LMOD2 (Santa Cruz Biotechnology sc-135493, antibody binding site near the N-terminus of human LMOD2). We identified the canonical isoform of LMOD2 (NM_207163, predicted molecular weight of 62 kDa) at a position corresponding to a size of approximately 70 kDa (as determined by the molecular weight marker) on western blot (Figure 3.6C, red arrow). LMOD2 was detected in human skeletal muscle and at higher levels in human heart. Lmod2 was detected at high levels in mouse heart and testis; and at lower levels in mouse thymus. Interestingly, we did not detect Lmod2 in mouse skeletal muscle (quadricep). This may suggest higher skeletal muscle

expression of LMOD2 in humans compared to mice or be due to higher LMOD2 expression in slow muscle fibres [which are more abundant in human than mouse skeletal muscle (Schiaffino & Reggiani, 2012)].

We observed a lower molecular weight band migrating at ~65 kDa in most mouse tissues and human heart, similar to that observed with the LMOD1 antibody (refer to Figure 3.5). The 65 kDa western blot band may plausibly correspond to LMOD2.2 (56 kDa) and/or LMOD2.4 (57 kDa). However, these mRNA transcripts are identified by GTEx as being expressed only in skeletal muscle and heart tissue (Figure 3.2B). Isoform LMOD2.3 (18 kDa) did not correspond to a band on western blot (Figure 3.2C). However, the LMOD2 antibody binding site is near the N-terminus (specific residues unknown) and therefore LMOD2.3 protein may not contain the LMOD2 antibody binding site for detection by western blot. We observed a ~45 kDa band in mouse and human skeletal muscle. Cross-reactivity of the anti-LMOD2 antibody for tropomodulin-4 migrating at 45 kDa was considered, and explored through western analyses with recombinant tropomodulin-4 protein (a generous gift from Prof Velia Fowler, see Appendix Figure A.2). Thus, cross-reactivity with tropomodulin-4 may explain the 45 kDa band observed with the anti-LMOD antibodies. Additional bands were observed which did not correspond to a detected mRNA and are thus of unknown origin and significance. Unfortunately, tissues from an *Lmod2* KO mouse were not available to establish the specificity of other bands recognised by the anti-LMOD2 antibody.

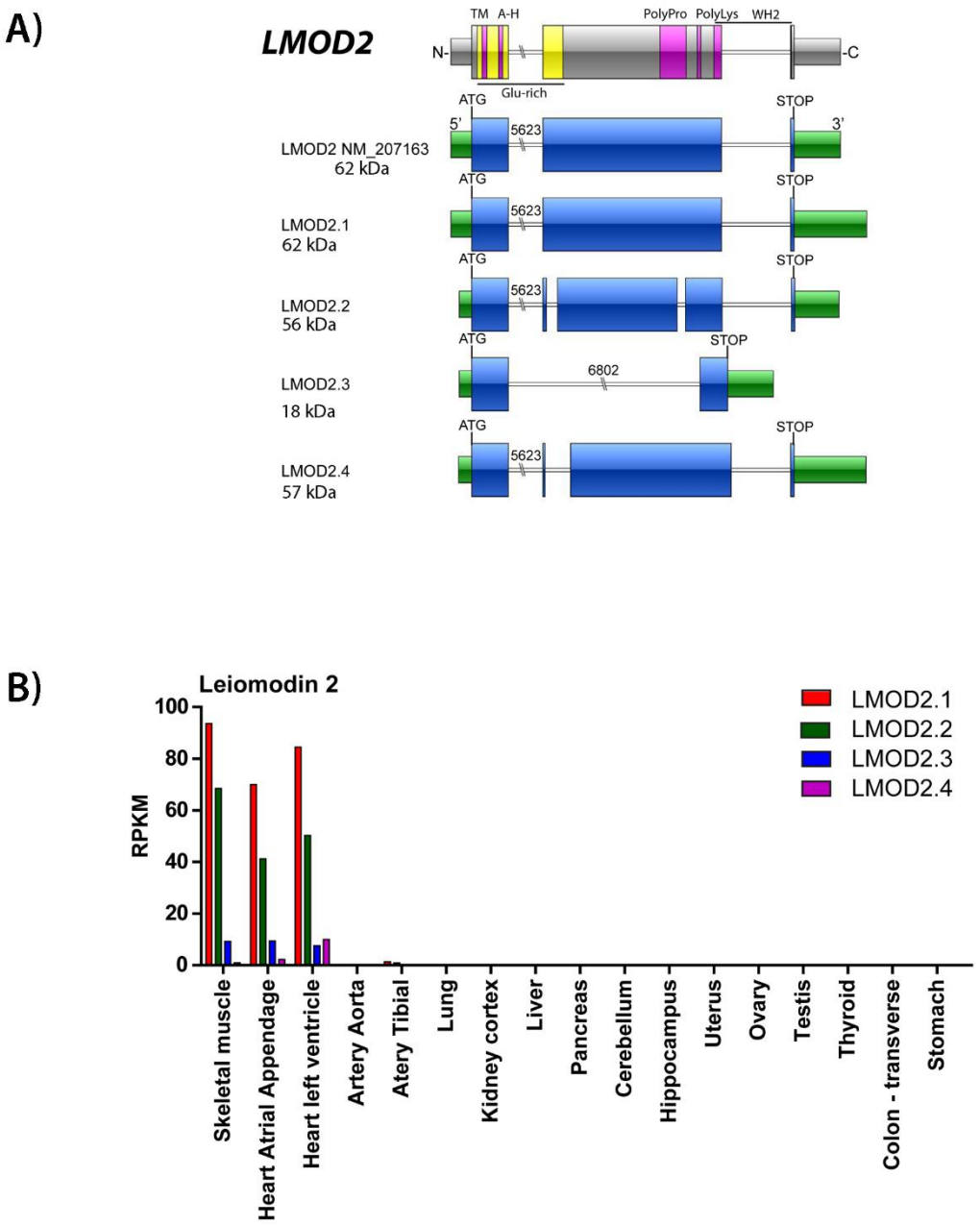

Figure 3.6: Investigating LMOD2 splice isoforms. Annotations, protein structure predictions and membrane probes were performed as described above (Figure 3.5) with additions: **(A)** Aligned genomic schematics (to scale) illustrating protein domains and genetic features of canonical LMOD2 (NM_207163) and GTEx isoforms LMOD2.1 (ENST00000458573.2), LMOD2.2 (ENST00000332074.7), LMOD2.3 (ENST00000456238.2), LMOD2.4 (ENST00000444702.1); Glu-rich – Glutamic acid-rich region (yellow) and polylys – Polylysine-rich region (pink) **(B)** Tissue expression of LMOD2 RNA isoforms from the GTEx database (https://www.GTExportal.org/home/). LMOD2 mRNA is expressed in the heart and at higher levels in skeletal muscle. Isoforms are ranked based on mRNA expression (highest to lowest).

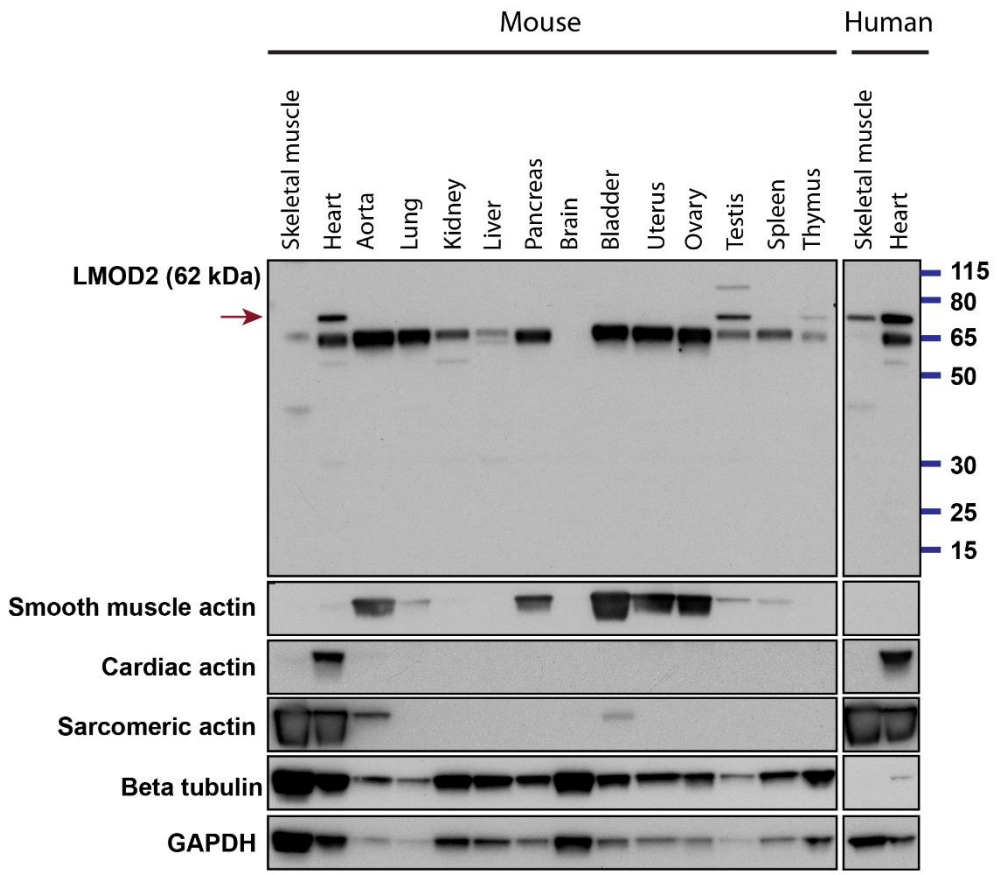

(C) Lmod2 is detected at high levels in mouse heart and testis, and at low levels in the thymus. LMOD2 is detected in human heart at lower levels in human skeletal muscle. Red arrow indicates canonical LMOD2 (NM_207163) isoform.

LMOD3

Splice isoforms: The canonical isoform of *LMOD3* (NM_198271) is depicted in Figure 3.7A. Interestingly, the three *LMOD3* isoforms detected by the GTEx database have the same coding region (CDS) which match the CDS of the canonical *LMOD3* (NM_198271) isoform and are predicted to result in a protein with a molecular weight of 65 kDa. The three isoforms differ only in the length of their 5' and 3' UTRs. None of the GTEx *LMOD3* isoforms exactly match the combination of 5'UTR and 3'UTR annotated in ENSEMBL for NM_198271. The first isoform of *LMOD3* described in GTEx, *LMOD3.1.1*, lacks a portion of the 5' UTR and has a shortened 3' UTR. The second isoform of *LMOD3* described in GTEx, *LMOD3.1.2*, is the closest match to the canonical *LMOD3* (NM_198271) isoform, but has a slightly shortened 5'UTR and slightly lengthened 3'UTR. The third *LMOD3* isoform detected in GTEx substitutes a portion of the 5' UTR for an upstream sequence, and has a shortened 3'UTR. The three *LMOD3* mRNA isoforms were reported by GTEx as being predominantly expressed in skeletal muscle and heart tissue (Figure 3.7B). In skeletal muscle, *LMOD3.1.1* is the highest expressed isoform. Whereas in heart tissue, *LMOD3.1.2* is the highest expressed isoform.

Protein Studies: Western blots of a range of mouse tissues, as well as human cardiac and skeletal muscles, were probed with a polyclonal antibody raised against human LMOD3 (Proteintech 14948-1-AP, BC039202). Our group has determined that this antibody is able to bind to a fragment consisting of the first 50 amino acids of LMOD3. The canonical isoform of LMOD3 (NM_198271) has a predicted molecular weight of 65 kDa and was detected on western blot at a position corresponding to approximately 75 kDa (Figure 3.7C, red arrow). LMOD3 was detected in human skeletal muscle and at slightly lower levels in human heart. Lmod3 was detected at high levels in mouse skeletal muscle and heart; and at lower levels in kidney, liver and pancreas. We again observed an abundant lower molecular weight band at ~65 kDa in most tissues, as well as a higher molecular weight band in kidney and brain.

Immunorecognition of proteins of this size could not be explained by isoforms detected in GTEx. Unfortunately, tissues from an *Lmod3* KO mouse were not available to verify the specificity of bands recognised by the anti-LMOD3 antibody.

A)

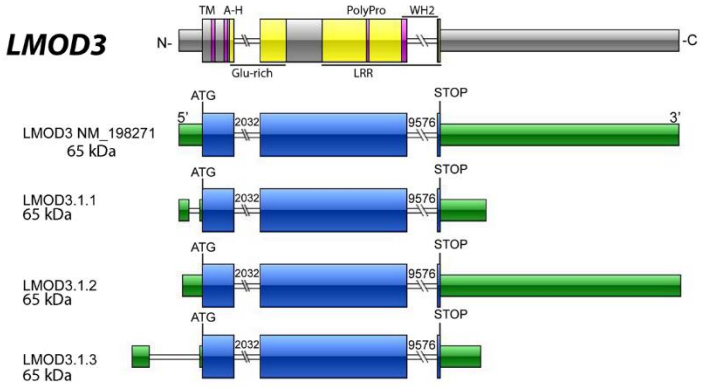
LMOD3
TM
A-H
PolyPro
WH2
N-
-C
Glu-rich
LRR
ATG
STOP
5'
3'
2032
9576
LMOD3 NM_198271
65 kDa
LMOD3.1.1
65 kDa
LMOD3.1.2
65 kDa
LMOD3.1.3
65 kDa

B)

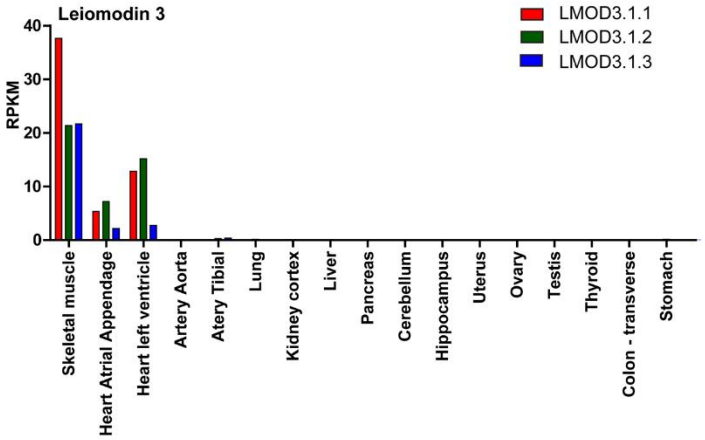
Leiomodin 3
LMOD3.1.1
LMOD3.1.2
LMOD3.1.3
RPKM
40
30
20
10
0
Skeletal muscle
Heart Atrial Appendage
Heart left ventricle
Artery Aorta
Atery Tibial
Lung
Kidney cortex
Liver
Pancreas
Cerebellum
Hippocampus
Uterus
Ovary
Testis
Thyroid
Colon - transverse
Stomach

C)

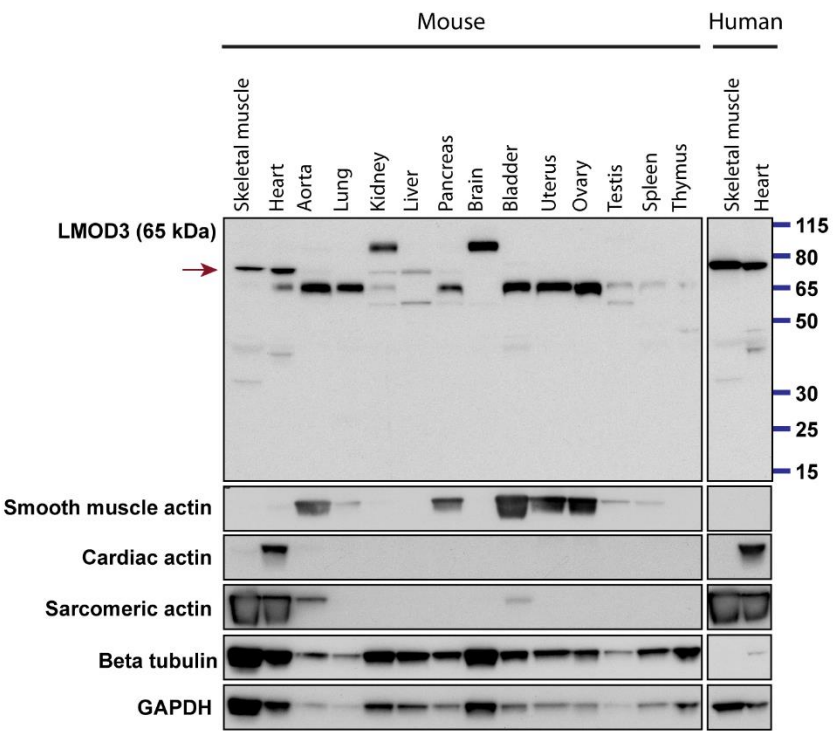
Mouse
Human
Skeletal muscle
Heart
Aorta
Lung
Kidney
Liver
Pancreas
Brain
Bladder
Uterus
Ovary
Testis
Spleen
Thymus
Skeletal muscle
Heart
LMOD3 (65 kDa)
115
80
65
50
30
25
15
Smooth muscle actin
Cardiac actin
Sarcomeric actin
Beta tubulin
GAPDH

Figure 3.7: Investigating LMOD3 splice isoforms. Annotations, protein structure predictions and membrane probes were performed as described above (Figure 3.5) with additions: **(A)** Aligned genomic schematics (to scale) illustrating protein domains and genetic features of canonical LMOD3 (NM_198271) and GTEx isoforms *LMOD3.1* (ENST00000489031.1), *LMOD3.2* (ENST00000420581.2) and *LMOD3.3* (ENST00000475434.1); Glu-rich – Glutamic acid-rich region (yellow); **(B)** Tissue expression of *LMOD3* mRNA isoforms from the GTEx database (https://www.GTExportal.org/home/). *LMOD3* mRNA is expressed highest in skeletal muscle followed by heart tissue. *LMOD3.1.1* is the dominant mRNA transcript in skeletal muscle. *LMOD3.1.2* is the dominant isoform in heart tissue. Isoforms are ranked based on mRNA expression (highest to lowest). Numbering of *LMOD3* refers to the identical CDS, followed by mRNA expression rank; **(C)** Lmod3 is detected at high levels in mouse skeletal muscle and heart, and at low levels in aorta, kidney, liver and pancreas. LMOD3 is detected at high levels in human skeletal muscle and slightly lower levels in human heart. Red arrow indicates canonical *LMOD3* (NM_198271) isoform.

PART B: Investigating the link between KLHL40 and LMOD proteins

This project required collaborative experimentation by three laboratory members; myself, Dr Michaela Yuen and research assistant Adam Bournazos. Dr Yuen and myself had collaborative roles in experimental concept and design as well as carrying out and interpreting experiments. Experimentation performed by Adam Bournazos is defined within the figure legends, and in these cases my role was in experimental concept, design and interpretation.

Synopsis

Garg et al. (2014) generated a *Klhl40* KO mouse that recapitulated the severe nemaline myopathy associated with *KLHL40* variants in humans. They observed dramatically reduced Lmod3 protein levels in the *Klhl40* KO mouse. *In vitro* studies showed KLHL40 can immunoprecipitate LMOD3 and the interaction between Klhl40 and Lmod3 was required in order for Lmod3 protein to be detected within transfected cells. Because expression of Lmod3 protein levels were 'rescued' following treatment with the proteasome inhibitor MG132, the authors proposed a mechanism whereby Klhl40 protected Lmod3 from ubiquitination and subsequent degradation by the proteasome in mice.

Garg et al. (2014) also examined LMOD3 protein levels in *KLHL40*-NM muscle biopsies. The study found two severe *KLHL40*-NM skeletal muscle biopsies, which showed a complete absence of KLHL40 protein, also had reduced levels of LMOD3 protein. Thus, Garg et al. (2014) proposed that the severe presentation of *KLHL40*-NM may be due mechanistically to secondary loss of LMOD3 protein in skeletal muscle (refer to Section 3.1.4).

This project explored whether the mechanistic paradigm proposed by Garg et al. (2014) was restricted to mice or was also true for humans, by determining whether human KLHL40 protects human LMOD3 from ubiquitination and subsequent proteasome degradation in cell

models. The aims of this chapter were originally: (1) To show human LMOD3 and KLHL40 are expressed at the same time in developing and differentiating skeletal muscle; (2) to show levels of human LMOD3 protein are regulated (i.e. stabilised) by human KLHL40 protein; (3) to define the region within human LMOD3 mediating regulation by human KLHL40; and (4) to determine if human KLHL40 also regulates human LMOD1 and/or LMOD2. However, we quickly accumulated convincing data that made us question the interpretation of results presented in Garg et al. (2014) and ultimately call into question the central paradigm of: 'the kelch protein KLHL40 protects LMOD3 from Ub-mediated proteasomal degradation'.

3.2.2 Do LMOD2 and LMOD3 developmental expression patterns correspond with KLHL40?

As a first step to investigating the biological relevance of findings from Garg et al. (2014) in humans, we wanted to establish if KLHL40, LMOD2 and LMOD3 protein were expressed at the same time in developing and differentiating human skeletal muscle. The domain and functional similarities between LMOD2 and LMOD3 lead us to consider that KLHL40 may plausibly also regulate LMOD2 protein levels.

Developing human muscle

Western blot was carried out on human skeletal muscle from healthy individuals or disease controls (without a known genetic neuromuscular condition), ranging from age 14 gestational weeks to 60 years. Triplicate membranes were probed with antibodies recognising LMOD2, LMOD3 and KLHL40 (Figure 3.8).

Two bands were detected with the LMOD2 antibody, 70 kDa and 65 kDa. A 70 kDa LMOD2 band (red arrow) was not clearly evident in muscle samples from early gestation (14 and 19 weeks), though observed in muscle samples from 25 gestational weeks onwards (although appears at lower levels in the 37 week, 21 years, 31 years and 60 years samples). The diffuse band at 65 kDa, is present in most gestational and childhood samples, though appears absent from adult samples (21 years, 31 years and 60 years). The 65kDa band does not correspond to splice isoforms described in section 3.2.1. The identity of this band is uncertain, though our later experiments raise a possibility this band may represent an LMOD2 protein from alternate initiation methionine(s) (to be discussed in further detail in Section 3.2.3). KLHL40 and LMOD3 were detected in human skeletal muscle samples at all developmental time points tested. Thus, expression of LMOD3 and KLHL40 appears to precede that of LMOD2 in human skeletal muscle.

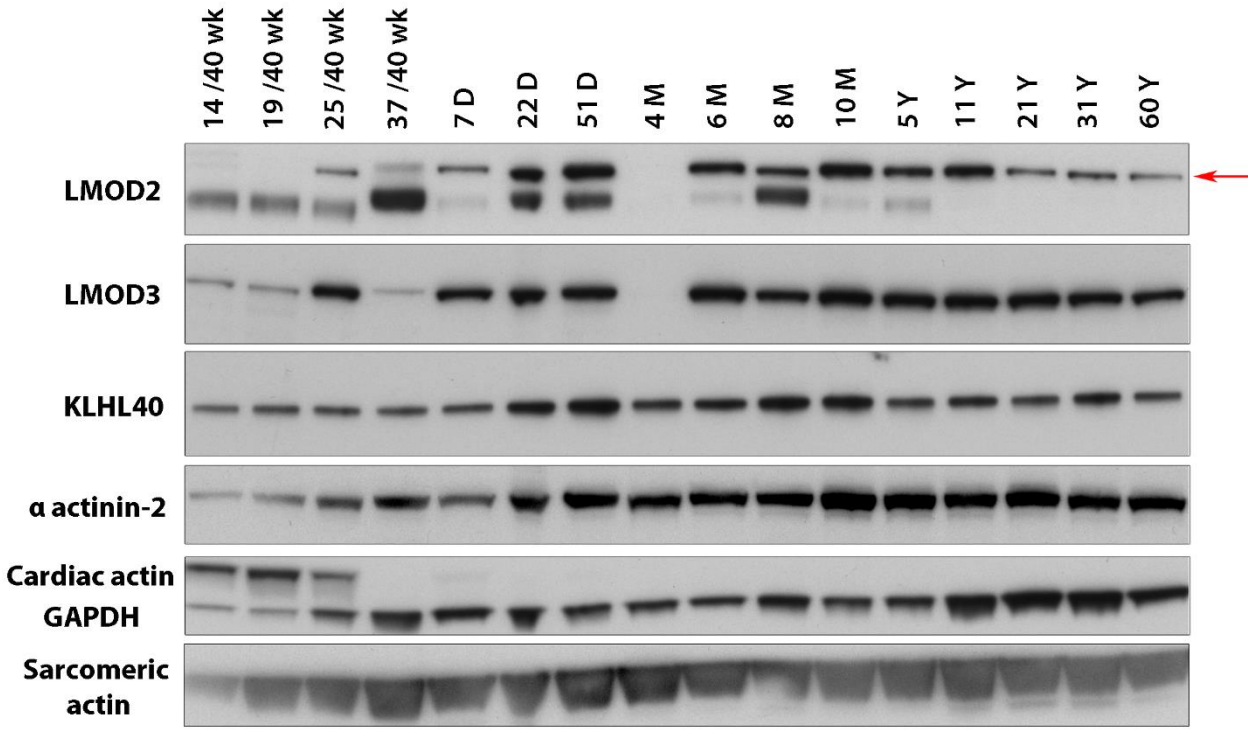

Figure 3.8: Human LMOD3 and KLHL40 are expressed throughout skeletal muscle development. Western blot of human skeletal muscle through development from 14/40 weeks gestation to 60 years of age. LMOD2 (red arrow) is detected from 25/40 weeks gestation to 60 years of age. LMOD3 and KLHL40 are detected from 14/40 weeks gestation to 60 years of age. It is unclear why LMOD2 and LMOD3 cannot be detected in one sample (4 month). Cardiac actin was used as a control for pre-natal skeletal muscle; GAPDH was used as a loading control; sarcomeric actin and α-actinin 2 were used as loading controls for skeletal muscle. W - weeks of gestation, D - days, M - months, Y - years.

Differentiating human myoblasts

Western blot was carried out on differentiating primary human myoblasts from day 0 to day 8 of differentiation, and triplicate membranes were probed for antibodies recognising LMOD2, LMOD3 and KLHL40 (Figure 3.9). An LMOD2 band was detected from differentiation day 3, increasing in levels with differentiation day. An LMOD3 band was detected weakly at differentiation day 0, and at higher levels from differentiation day 1. The KLHL40 antibody detected three bands in primary human myoblasts. The red arrow denotes the band most likely representing KLHL40 (corresponds to the molecular weight of an untagged KLHL40 expression construct, refer to section 3.2.3), and is detected from differentiation day 3, and increasing in levels. Higher (65 kDa) and lower (55kDa) bands were also detected throughout differentiation. It is unclear if the higher and lower molecular weight bands are KLHL40 or non-specific bands. Uniprot predicts a KLHL40 isoform of 53 kDa which may correspond to the 55 kDa band.

In summary, our collective results suggest expression of LMOD3 precedes that of LMOD2 and KLHL40 in differentiating human myoblasts.

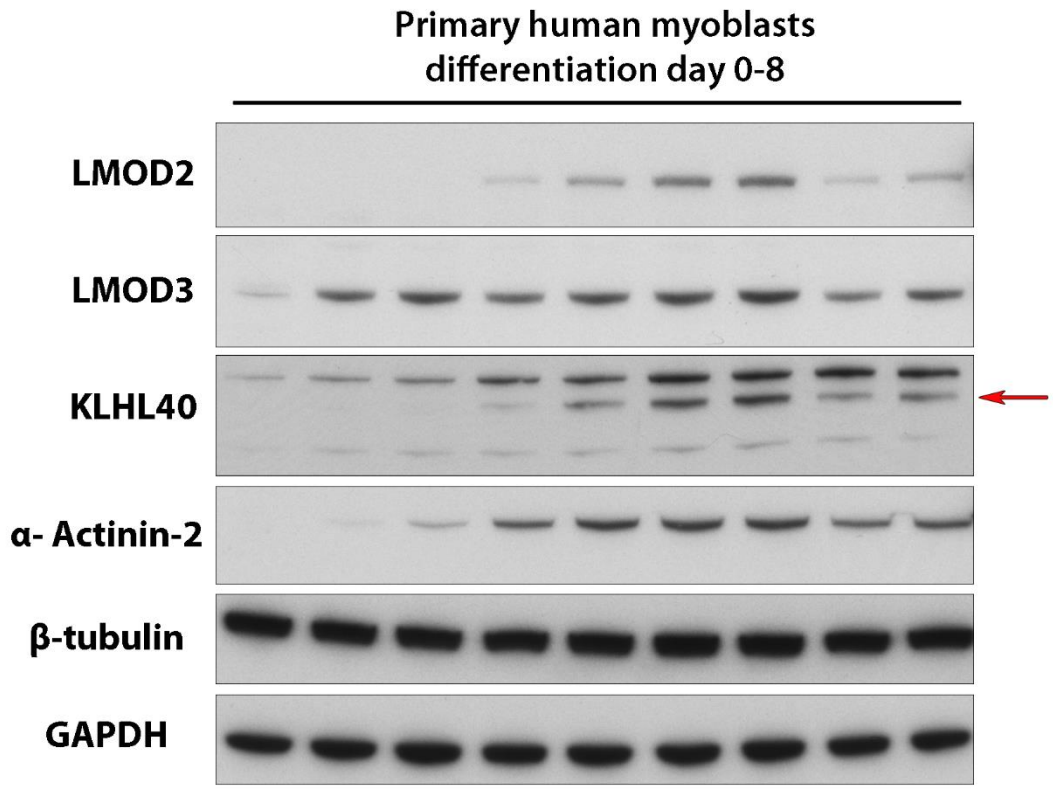

Figure 3.9: Human KLHL40 mimics LMOD2 expression in differentiating primary human myoblasts. Western blot of primary human myoblasts differentiating into myotubes from day 0 through to day 8. KLHL40 (red arrow) and LMOD2 are expressed from differentiation day 3. LMOD3 is expressed from differentiation day 0. LMOD2 expression mirrors that of KLHL40, being expressed at low levels at differentiation day 3 and then increasing. LMOD3 expression is seen weakly at differentiation day 0, increasing sharply at day 1 LMOD3 levels remain relatively constant from day 1 to day 8.

KLHL40 expression in fast and slow fibres

We wanted to further define protein expression of KLHL40 within skeletal muscle to determine whether KLHL40 and LMOD3 were present in the same muscle fibres in humans, allowing them to interact as suggested by Garg et al. (2014). We determined levels of LMOD3 and KLHL40 in fast and slow fibres by single fibre western blot (Figure 3.10). We found LMOD3 and KLHL40 were expressed in both fast and slow fibres, with slightly higher LMOD3 and KLHL40 protein levels in slow fibres.

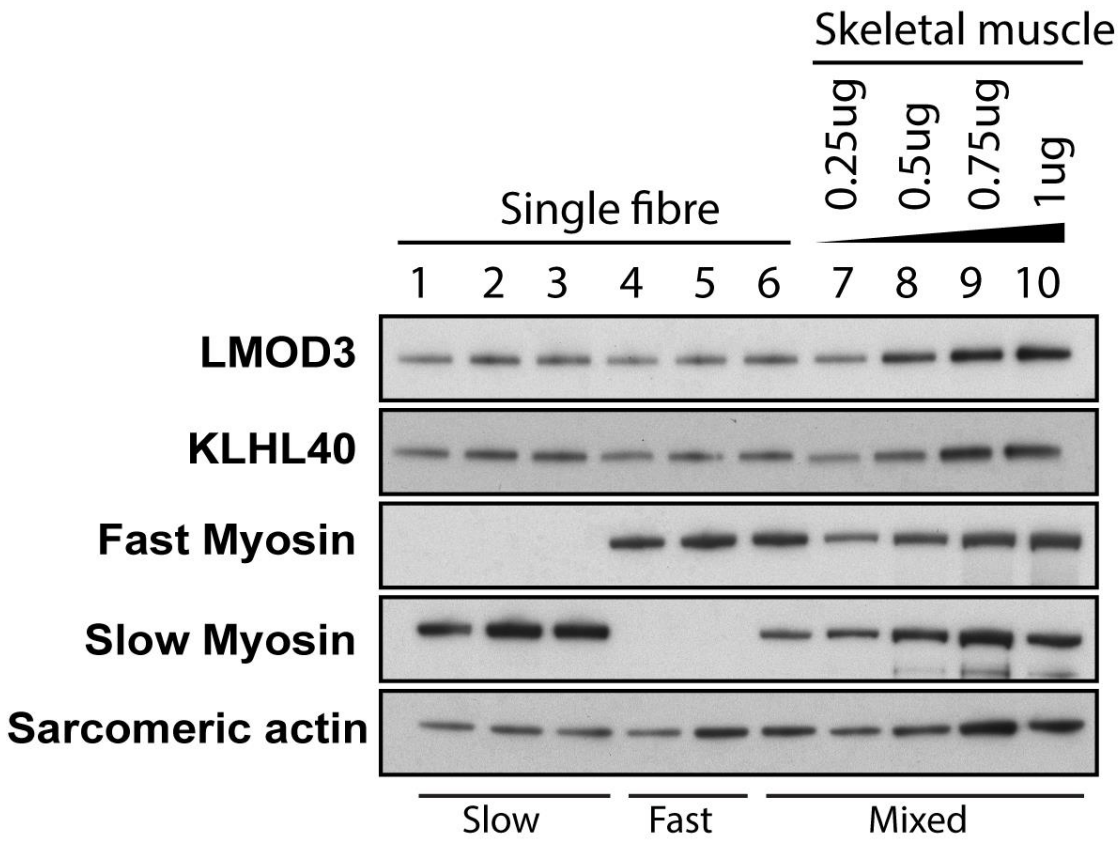

Figure 3.10: KLHL40 and LMOD3 protein levels are slightly higher in slow twitch muscle fibres. Western blot of control human single skeletal muscle fibres (Lanes 1-6 – 0.25 µg loaded) and whole muscle lysates (Lanes 7-10 – loading amounts indicated). Triplicate blots were probed for LMOD3 and KLHL40. Fast myosin and slow myosin were probed for to determine fibre type (fast and slow, respectively). Sarcomeric actin was probed for as a loading control. Serial dilutions of skeletal muscle lysate indicate 0.25 µg of total protein is within the linear range of detection for the LMOD3 and KLHL40 antibodies. KLHL40 and LMOD3 protein levels are slightly higher in slow twitch muscle fibres (Lanes 1-3).

3.2.3 Defining the regulation of LMOD protein levels by KLHL40

Reproducing published results with human LMOD3

The Olsen laboratory (Department of Molecular Biology, University of Texas Southwestern Medical Center, Dallas, United States) generously provided us with the panel of mouse Lmod3 and mouse Klhl40 expression constructs (mLmod3 and mKlhl40 respectively) reported in Garg et al. (2014). The Laing laboratory (Centre for Medical Research, The University of Western Australia & the Harry Perkins Institute of Medical Research, Perth, WA, Australia) generously provided us with the human KLHL40 expression construct (hKLHL40). We performed transfection experiments with mLmod3 or human LMOD3 (hLMOD3) expression constructs, with and without co-transfection of hKLHL40 or mKlhl40 constructs. We reproduced results in transfected Cos-7 cells published by Garg et al. (2014) with both mLmod3 and hLMOD3 (Figure 3.11). Namely, co-transfection of pcDNA3.1-hLMOD3 or pcDNA3.1-mLmod3$_{MycHis}$ with pEGFP-NI-Empty produced scant levels of hLMOD3 or mLmod3 (Lane 7 and 8 hLMOD3; Lane 13 mLmod3). Co-transfection with mKlhl40 rescued protein levels of hLMOD3 and mLmod3 (Lanes 11 and 12 hLMOD3; Lane 15 mLmod3). However, co-transfection with hKLHL40 in pEGFP-N1 (GFP was not expressed due to the presence of a stop codon), did <u>not</u> rescue levels of hLMOD3 or mLmod3 protein (Lanes 9 and 10 hLMOD3, Lane 14 mLmod3). Interestingly, when hLMOD3 was expressed within pMT3 with an N-terminal FLAG tag (pMT3-$_{FLAG}$hLMOD3) normal levels of hLMOD3 protein were detected when co-transfected with pEGFP-NI-Empty (Lanes 1 and 2), hKLHL40 (Lanes 3 and 4) or mKLHL40 (Lanes 5 and 6).

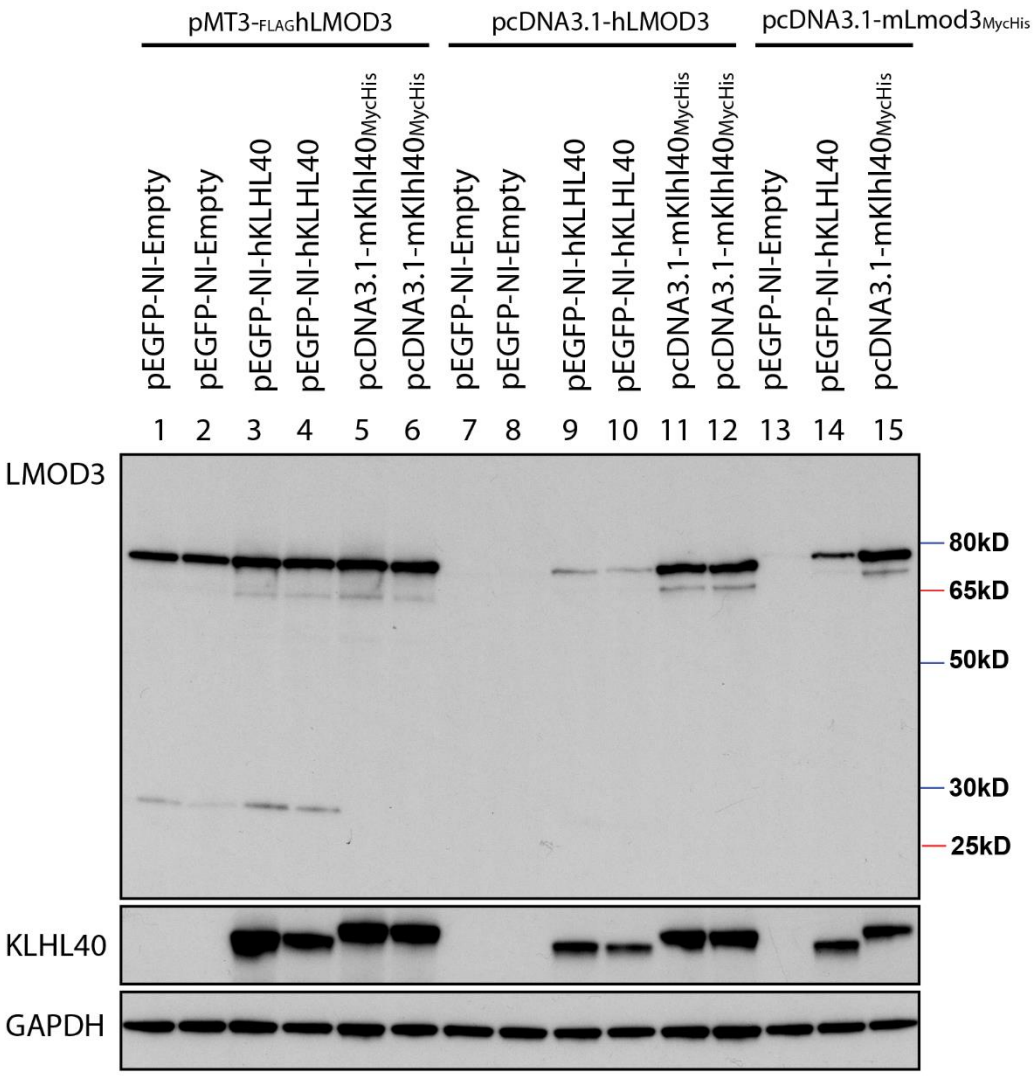

Figure 3.11: hLMOD3 is stable in the absence of hKLHL40 or mKLHL40 when expressed within the pMT3 expression vector. Western blot of Cos-7 cells co-transfected with hLMOD3 with an N-terminal FLAG tag in the pMT3 vector (pMT3-FLAGhLMOD3), hLMOD3 untagged in the pcDNA3.1 vector (pcDNA3.1-hLMOD3.1) or mLmod3 in pcDNA3.1 with C-terminal MycHis tags with empty pEGFP-NI (pEGFP-NI-Empty), hKLHL40 untagged in the pEGFP-NI vector (pEGFP-NI-hKLHL40) or mKlhl40 with C-terminal Myc and His tags in the pcDNA3.1 vector (pcDNA3.1-mKlhl40MycHis). pMT3-FLAG-hLMOD3 is detected when co-transfected with pEGFP-NI-Empty, pEGFP-NI-hKLHL40 or pcDNA3.1-mKlhl40MycHis. pcDNA3.1-hLMOD3 and pcDNA3.1-mLmod3MycHis protein is not detected when co-transfected with pEGFP-NI-Empty, weakly detected when co-transfected with pEGFP-NI-hKLHL40 and strongly detected when co-transfected with pcDNA3.1-mKlhl40MycHis. Duplicate western blots were probed for LMOD3 and KLHL40 with GAPDH probed for as a loading control.

The 'necessity' for Klhl40 disappears in the absence of the pEGFP-NI vector

Surprisingly, when we carried out a single transfection of pcDNA3.1-hLMOD3, we detected normal hLMOD3 protein levels (Figure 3.12, Lane 2), with hLMOD3 protein levels unchanged or slightly increasing when treated with MG132 (Lane 3). When pcDNA3.1-hLMOD3 was co-transfected with pEGFP-NI-Empty, low levels of hLMOD3 protein levels were detected (Lane 4), with hLMOD3 protein levels increasing slightly with MG132 treatment (Lane 6). These results strongly suggest a factor within the pEGFP-NI vector reduces pcDNA3.1-hLMOD3 protein levels, which is partially rescued by MG132 treatment.

Despite having a very good antibody to the N-terminus of LMOD3, we did not detect breakdown products of mLmod3, nor hLMOD3 with or without MG132, as might be expected if mLmod3 or hLMOD3 protein is very rapidly degraded by the proteasome when mKlhl40 or hKLHL40 is not present. We also did not observe higher-migrating polyubiquitinated mLmod3, or hLMOD3 with or without treatment of MG132. However, we consistently observed a lower migrating band of ~65 kDa (similar to the band identified in mouse and human tissues in Section 3.2.1), for both hLMOD3 and mLmod3, over many experiments. This lower migrating band will be discussed later in this section. We now suspect this band corresponds to an LMOD3 protein translated via use of an alternate downstream start methionine.

The regulation of mLmod3 and hLMOD3 in cell models may be at the transcription, translation or protein surveillance level. It is unlikely to be at the transcription level as: (1) Garg et al. (2014) carried-out quantitative PCR and showed mouse *Lmod3* mRNA levels did not differ between samples where mLmod3 protein was and was not detected; and (2) the expression vectors all used a CMV promotor and thus should similarly drive transcription of mLmod3 and hLMOD3. Experiments with MG132 did not provide any consistent evidence for proteasomal

surveillance. Therefore, we investigated whether an artefact of transient transfections was influencing post-transcriptional regulation of hLMOD3 and complicating result interpretation.

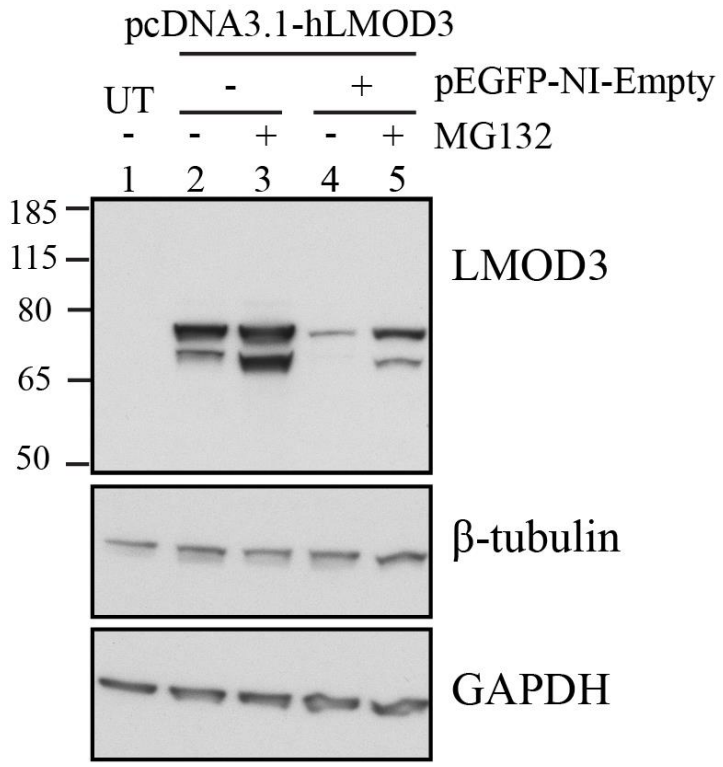

Figure 3.12: The pEGFP-NI vector reduces pcDNA3.1-hLMOD3 protein levels which are partially 'rescued' by MG132. Western blot of Cos-7 cells treated with MG132 or DMSO (vehicle control) and untransfected (UT), transfected with full length hLMOD3 untagged in the pcDNA3.1 vector (pcDNA3.1-hLMOD3) or co-transfected with pcDNA3.1-hLMOD3 and pEGFP-NI-Empty. As a single transfection, pcDNA3.1-hLMOD3 protein is robustly detected at equal levels with and without MG132 treatment. When pcDNA3.1-hLMOD3 is co-transfected with pEGFP-NI-Empty LMOD3 protein levels are low and are partially 'rescued' with MG132. GAPDH and β-tubulin were probed for as loading controls. This experiment was performed by Adam Bournazos.

Proposed double-stranded RNA interference from the pEGFP-NI vector suppressing LMOD3 translation

Reviewing the literature revealed published evidence linking co-transfection of pEGFP-CI (same backbone sequence as pEGFP-NI) to double-stranded RNA (dsRNA) interference and suppression of translation of transiently transfected (sensitive) cDNAs (Nejepinska, Malik, Moravec, & Svoboda, 2012; Nejepinska, Malik, Wagner, & Svoboda, 2014). pEGFP-C1 (and N1) are reported to produce dsRNA due to bidirectional transcription of genes within the vector backbone. dsRNA activates cellular defence pathways linked to activation of Phosphokinase-R (PKR), which in turn phosphorylates the eukaryotic initiation factor 2 (eIF2-α), inhibiting translation.

Translational inhibition of transiently transfected genes through dsRNA and PKR has been reported previously for numerous genes including chloramphenicol acetyltransferase, neomycin phosphotransferase and dihydrofolate reductase (Kalvakolanu, Bandyopadhyay, Tiwari, & Sen, 1991; Kaufman, 1997; Kaufman, Davies, Pathak, & Hershey, 1989). Importantly, dsRNA induced translational suppression is not observed on endogenous genes, or exogenous genes integrated into the genome (Nejepinska, Malik, Filkowski, et al., 2012; Nejepinska, Malik, Moravec, et al., 2012; Terenzi et al., 1999). The Kanamycin/neomysin resistance cassette within the pEGFP-CI backbone is one source of spurious sense and anti-sense RNA, which complements to form dsRNA (Nejepinska, Malik, Moravec, et al., 2012; Nejepinska et al., 2014).

It is therefore possible that the vectors used in co-transfection experiments reported in Garg et al. (2014) also generated dsRNA and suppressed translation of mLMOD3. To test this, we generated empty pcDNA3.1 and pCMV10 vectors and performed co-transfections. Scant levels of hLMOD3 protein were detected when pcDNA3.1-hLMOD3 was co-transfected with

pcDNA3.1-Empty (Figure 3.13, lane 5) or pCMV10 (-Kan^R)-Empty (Lane 9) which were 'rescued' with MG132 treatment (Lanes 6 and 10 respectively).

This suggests co-transfection of empty pEGFP-N1, pcDNA3.1 or pCMV10 activates the dsRNA interference response, likely suppressing translation of transiently transfected genes sensitive to this interference – resulting in only low levels of translation of hLMOD3.

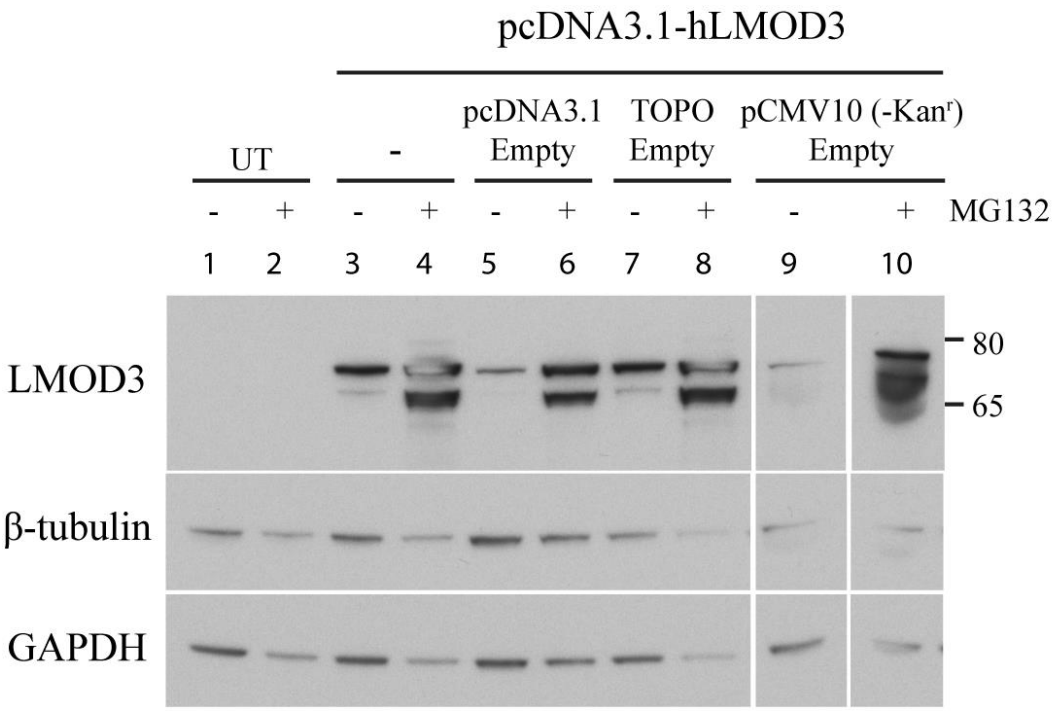

Figure 3.13: Low pcDNA3.1-hLMOD3 protein levels are detected when co-transfected with pcDNA3.1-Empty or pCMV10 (-Kan^R). Western blot of Cos-7 cells treated with MG132 or DMSO (vehicle control). Cells were left untransfected (UT), singularly transfected with hLMOD3 untagged in the pcDNA3.1 vector (pcDNA3.1-hLMOD3) or co-transfected with pcDNA3.1-hLMOD3 and pcDNA3.1-Empty, TOPO-Empty (used as a neutral vector) or empty pCMV10 with the kanamycin resistance cassette removed (pCMV10(-Kan^r)-Empty). pcDNA3.1-hLMOD3 protein is readily detected when singularly transfected, or co-transfected with TOPO-Empty with no change in hLMOD3 protein levels with MG132 treatment. Low levels of hLMOD3 protein are detected when pcDNA3.1-hLMOD3 is co-transfected with either pcDNA3.1-Empty or pCMV10(-Kan^r)-Empty, with hLMOD3 protein levels returning to normal with MG132 treatment. GAPDH and β-tubulin were probed for as loading controls. This experiment was performed by Adam Bournazos.

pEGFP-NI reduces protein levels of hLMOD2 and hLMOD3 but not hLMOD1

We asked whether the proposed double-stranded RNA interference from the pEGFP-NI vector also suppressed hLMOD1 and hLMOD2 translation, or if this was specific to hLMOD3. hLMOD1 protein was readily detected when untagged hLMOD1 in pcDNA3.1 (pcDNA3.1-hLMOD1) was co-transfected with pEGFP-NI-Empty (Figure 3.14, Lane 1). Whereas, only low levels of hLMOD2 protein were detected with co-transfection of untagged hLMOD2 in pcDNA3.1 (pcDNA3.1-hLMOD2) and pEGFP-NI-Empty (Lane 4) - hLMOD3 protein was virtually undetectable with co-transfection of pcDNA3.1-hLMOD3 with pEGFP-NI-Empty (Lane 7). Protein levels of each hLMOD slightly increased when co-transfected with pEGFP-NI-hKLHL40 (Lanes 2, 5 and 8), and were robust when co-transfected with pcDNA3.1-mKlhl40$_{MycHis}$ (Lanes 3, 6 and 9). An additional lower molecular weight band was observed for hLMOD3 when co-transfected with pcDNA3.1-mKlhl40$_{MycHis}$ (Lane 9), the significance of this is unclear. These results suggest that hLMOD2 and hLMOD3, but not hLMOD1, are sensitive to the dsRNA interference response elicited by the pEGFP-NI vector, resulting in reduced hLMOD2 and hLMOD3 protein levels in the presence of pEGFP-NI.

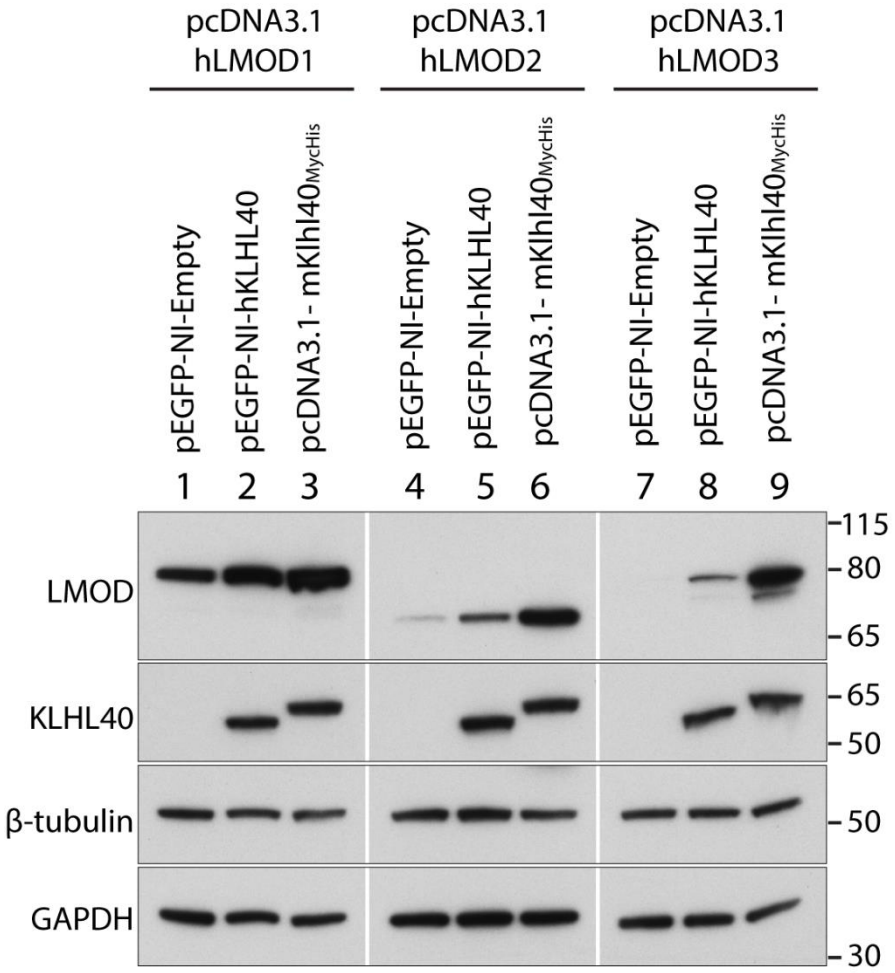

Figure 3.14: pcDNA3.1-hLMOD1 protein is detected and pcDNA3.1-hLMOD2 protein is detected weakly when co-transfected with pEGFP-NI-Empty. Western blot of Cos-7 cells co-transfected with hLMOD1 untagged in the pcDNA3.1 vector (pcDNA3.1-hLMOD1), hLMOD2 untagged in the pcDNA3.1 vector (pcDNA3.1-hLMOD2) or hLMOD3 untagged in the pcDNA3.1 vector (pcDNA3.1-hLMOD3) and empty pEGFP-NI (pEGFP-NI-Empty), hKLHL40 untagged in the pEGFP-NI vector (pEGFP-NI-hKLHL40) or mKlhl40 with C-terminal Myc and His tags in the pcDNA3.1 vector (pcDNA3.1-mKlhl40$_{MycHis}$). pcDNA3.1-hLMOD1 protein is detected when co-transfected with pEGFP-NI-Empty with levels slightly increased with co-transfection of pEGFP-NI-hKLHL40 and levels are higher again with co-transfection of pcDNA3.1-mKlhl40$_{MycHis}$. pcDNA3.1-hLMOD2 protein is detected weakly when co-transfected with the pEGFP-NI-Empty with levels slightly increased with co-transfection with pEGFP-NI-hKLHL40 and levels are robust with co-transfection of pcDNA3.1-mKlhl40$_{MycHis}$. pcDNA3.1-hLMOD3 protein is not detected when co-transfected with pEGFP-NI-Empty with levels slightly increased when co-transfected with pEGFP-NI-hKLHL40 and robust when co-transfected with pcDNA3.1-mKlhl40$_{MycHis}$. Quadruplicate western blots were probed for LMOD1, LMOD2, LMOD3 and KLHL40 with β-tubulin and GAPDH probed for as a loading controls. This experiment was performed by Adam Bournazos.

LMOD3 has signals for poor translation in vivo

We next wanted to determine why LMOD3 protein levels were susceptible to co-expression with pEGFP-NI. There are five main structural features of mRNAs that influence the efficiency of translation initiation (reviewed in (Kozak, 1991a, 1991c)): (1) the presence of a 7-methylguanylate cap; (2) the sequence surrounding the AUG codon, ie. the strength of the Kozak sequence; (3) position of the initiating AUG codon; (4) length of the 5' UTR; and (5) secondary structure 5' and 3' of the ATG.

Analysing the sequences of the three *LMOD3* mRNA isoforms (refer to Figure 3.3) revealed three structural features typical of poor translation: (1) A weak Kozak sequence. The Kozak sequence of all *LMOD3* isoforms is AAAATAATGT. The absence of a G at position +4 (where the A of ATG is +1) weakens the strength of the Kozak sequence of *LMOD3* (Kozak, 1997); (2) The 5'UTR length of each *LMOD3* isoform is beyond the efficient translation range of 17-80 nucleotides (Kozak, 1991b): *LMOD3.1.1* – 155 bp; *LMOD3.1.2* – 180 bp; and *LMOD3.1.3* – 184 bp; and (3) All 5'UTRs of the *LMOD3* isoforms are predicted to have hairpins within the first 12 nucleotides (http://rtools.cbrc.jp/). Hairpins within the first 12 nucleotides of the 5'UTR stalls translation by interfering with 40s ribosome binding (Kozak, 1989). Thus, *in silico* analyses suggested that *LMOD3* mRNA may be subject to inefficient translation.

Possible LMOD3 protein translated via use of an alternate downstream start methionine

During *in silico* analysis we found a second methionine within *LMOD3* at position 39 preceded by a strong Kozak sequence. If translation initiated at methionine 39, the predicted molecular weight of LMOD3 would decrease by 4.4 kDa. The predicted shift in molecular weight corresponds to the lower molecular weight band consistently detected by our LMOD3 antibody. We made a deletion construct removing amino acids 1-38 (pMT3-hLMOD3Δ1-38) which ran at approximately the same molecular weight as the consistently detected lower molecular weight band (Figure 3.15, red arrow), with protein levels increasing with MG132 treatment as previously observed. Furthermore, when duplicate blots of pMT3-FLAGhLMOD3 were probed with an antibody against FLAG one band was observed which matched the upper band detected by our LMOD3 antibody (Figure 3.15 Lanes 1 and 2, green asterisks). These results suggest: (1) The consistently detected lower molecular weight band is an LMOD3 protein; and (2) this LMOD3 protein may be produced through the use of an alternate start codon.

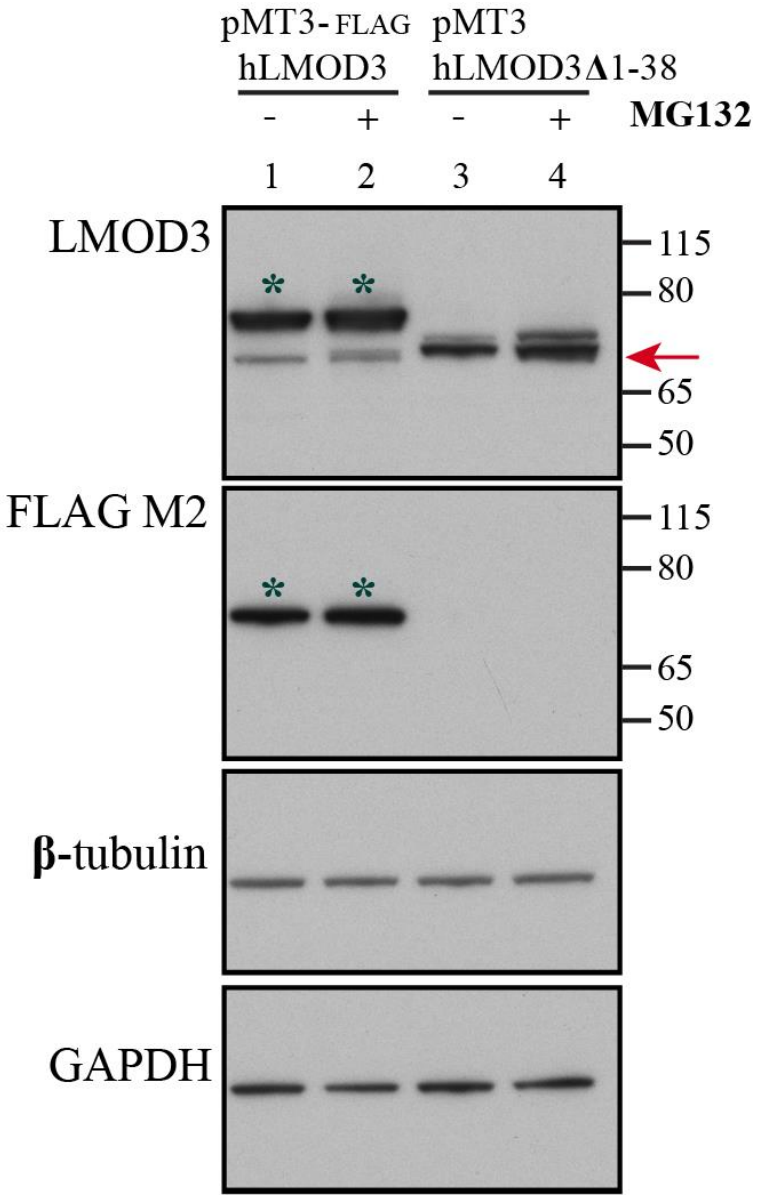

Figure 3.15: Consistently detected lower molecular weight band is LMOD3 and likely the result of an alternate start codon. Western blot of Cos-7 cells treated with MG132 or DMSO (vehicle control) and transfected with full length hLMOD3 with an N-terminal tag in pMT3 (pMT3-FLAGhLMOD3) or hLMOD3Δ1-38 untagged in pMT3 (pMT3-hLMOD3Δ1-38). Duplicate membranes were probed with antibodies raised against LMOD3 and FLAG. The FLAG antibody detected one band which matched the upper band detected by the LMOD3 antibody (green asterisks). The pMT3-hLMOD3Δ1-38 construct ran at a similar molecular weight to the lower band detected by the LMOD3 antibody (red arrow) with protein levels slightly increasing with MG132 treatment. GAPDH and β-tubulin were probed for as loading controls. This experiment was performed by Adam Bournazos.

The influence of the FLAG tag and Kozak sequence of the pMT3 vector on 'rescuing' proposed inefficient translation of LMOD3

We hypothesised that if *LMOD3* mRNA is translated inefficiently, that the coding sequence of *LMOD3* present within expression vectors would be susceptible to poor translation signals. We observe normal hLMOD3 protein levels when pMT3-$_{FLAG}$hLMOD3 protein is co-transfected with pEGFP-NI-Empty however, pcDNA3.1-hLMOD3 protein is not detected when co-transfected with pEGFP-NI-Empty (refer to Figure 3.11). This suggests that a component within the pMT3 vector, lacking from the pcDNA3.1 vector, is rescuing translational suppression of hLMOD3 elicited from the pEGFP-NI vector.

Upon analysing each vector sequence, we found a weak Kozak in the pcDNA3.1 vector, and a strong Kozak sequence preceding the N-terminal FLAG tag in pMT3-$_{FLAG}$hLMOD3 (Figure 3.16A). We hypothesised that in the presence of the pEGFP-NI vector: (1) LMOD3 is translated inefficiently when in the pcDNA3.1 vector due to a weak translation initiation signal (weak Kozak sequence); and (2) LMOD3 is translated efficiently in the pMT3 vector due to a strong translation initiation signal (strong Kozak sequence).

We sub-cloned the Kozak sequence and FLAG tag from the pMT3-$_{FLAG}$hLMOD3 vector into the pcDNA3.1-HumanLMOD3 vector. Protein levels of pcDNA3.1-$_{FLAGKOZAK}$hLMOD3 and pcDNA3.1-hLMOD3 were low when co-transfected with pEGFP-NI-Empty (Figure 3.16B, Lanes 1 and 3) and readily detected when co-transfected with pcDNA3.1-MouseKlhl40$_{MycHis}$ (Lanes 2 and 4). This suggests the Kozak sequence and FLAG tag from pMT3 are insufficient to rescue LMOD3 protein levels.

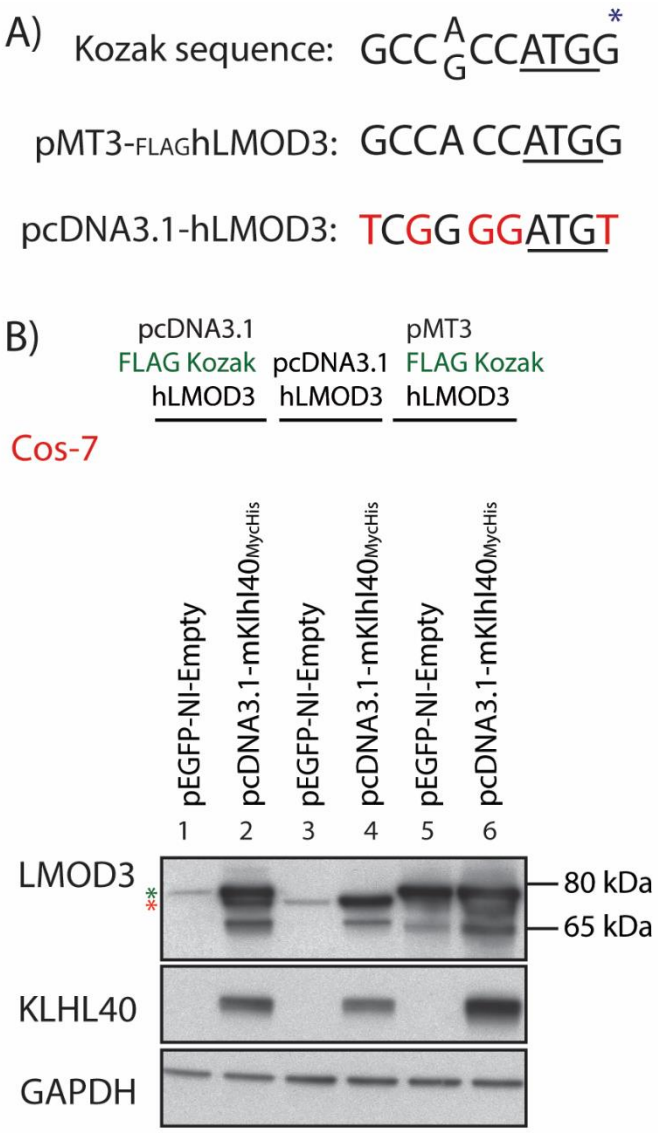

Figure 3.16: A strong Kozak sequence is insufficient to restore LMOD3 protein levels in pcDNA3.1 in the presence of pEGFP-NI. (A) Kozak sequence - proposed optimal sequence for translation initiation (Kozak, 1987), position +4 indicated with a blue asterisks. Six base pairs 5' and one base pair 3' flanking the initiating ATG of pMT3-FLAGhLMOD3 and pcDNA3.1-hLMOD3. Red letters indicate alterations from the Kozak sequence. pMT3-FLAGhLMOD3 has a strong Kozak sequence and pcDNA3.1-hLMOD3 has a weak Kozak sequence**; (B)** Western blot of Cos-7 cells co-transfected with hLMOD3 in pcDNA3.1 with the Kozak sequence and FLAG epitope tag from pMT3-FLAGhLMOD3 (pcDNA3.1-FLAGKozak-hLMOD3), LMOD3 in pcDNA3.1 (pcDNA3.1-hLMOD3) or LMOD3 in pMT3 (pMT3-FLAGKozak-hLMOD3) and empty pEGFP-NI (pEGFP-NI-Empty) or mKlhl40 with C-terminal Myc and His tags in pcDNA3.1 (pcDNA3.1-mKlhl40MycHis). LMOD3 in pcDNA3.1 is weakly detected when co-transfected with pEGFP-NI-Empty and readily detected when co-transfected with pcDNA3.1-mKlhl40MycHis irrespective of the presence of the Kozak sequence and FLAG tag from the pMT3 vector. Duplicate western blots were probed for LMOD3 and KLHL40 with GAPDH probed for as a loading control. This experiment was performed by Adam Bournazos.

The influence of the VA segment within pMT3 on 'rescuing' proposed inefficient translation of LMOD3.

The pMT3 vector was generated by modifying the pMT2 vector (Kaufman et al., 1989). The pMT2 vector contains an adenoviral VA sequence absent from the pcDNA3.1 vector. The VA segment has high sequence homology to the human integrated adenovirus 2 virus associated (VA) RNA (Figure 3.17A). VA is a short mRNA, with internal transcriptional control regions, involved in supressing translation inhibition resulting from an anti-viral defence (Mathews & Shenk, 1991). Adenovirus virus-associated RNAs I and II (VAI and VAII) are used in expression vectors to enhance translation of exogenous genes (Kaufman & Murtha, 1987). We hypothesised that: (1) The VA sequence within pMT3 rescues the inefficient translation of hLMOD3 in the presence of the pEGFP-NI vector; and (2) How VA mRNA acts to enhance hLMOD3 translation may be related to the mechanism by which pEGFP-NI inhibits hLMOD3 translation.

Translation begins with the initiating Met-tRNA being transferred to the initiating AUG, mediated by eIF2-α-GTP (Baird & Wek, 2012). Transfer of Met-tRNA to the initiating methionine metabolises eIF2-α-GTP to eIF2-α-GDP. After the transfer of Met-tRNA, eIF2α-GDP leaves the ribosome complex. The guanosine nucleotide exchange factor (GEF) then exchanges GDP with GTP, allowing eIF-2α-GTP to initiate further rounds of translation. Phosphorylation of eIF2-α at Ser51 prevents the exchange of GDP with GTP by GEF and therefore halts further translation. A very modest increase in p-eIF2-α can have detrimental effects on translation of proteins. Phosphorylation of eIF2-α can be carried out by the double-stranded RNA-activated inhibitor (DAI) also named Phosphokinase R (PKR). DAI is activated by binding to double-stranded RNA and has antiviral properties. VA has been shown to inhibit DAI (Aparicio, Razquin, Zaratiegui, Narvaiza, & Fortes, 2006). We hypothesised that LMOD3 translation is inhibited due to high levels of phosphorylated eIF2-α, elicited by dsRNA

produced from the pEGFP-NI vector, and VA can overcome translational suppression by preventing the phosphorylation of eIF2-α, resulting in robust detection of hLMOD3 (Figure 3.17B).

We sub-cloned the VA segment from the pMT3 vector into the TOPO shuttle vector. The TOPO vector does not contain a mammalian promotor and therefore VA could only be produced from its internal promoter sequences. We carried out co-transfections in Cos-7 cells and determined hLMOD3 protein levels by western blot (Figure 3.17C). hLMOD3 protein was readily detected when pcDNA3.1-hLMOD3 was co-transfected with pMT3-Empty (Lane 4) and at slightly lower levels when co-transfected with the VA element in the TOPO shuttle vector (TOPO-VA, Lane 5). This correlated with lower levels of phosphorylated eIF2-α (p-eIF2-α) when compared to co-transfecting with pEGFP-NI-Empty (Figure 3.17C, Lane 3 and Figure 3.17D, red asterisk). These results suggest that the pEGFP-NI vector is increasing levels of p-eIF2-α, suppressing translation of hLMOD3 and resulting in reduced hLMOD3 protein levels. Further, that phosphorylation of eIF2-α is diminished by the VA segment, but this is not sufficient to fully restore hLMOD3 protein levels.

A)

```
Adenovirus 2 VA     ------------GGGCACTCTTCCGTGGTCTGGTGGATAAATTCGCAAGGGTATCATGGC    48
PMT2                GAGCCTGTAAGCGGGCACTCTTCCGTGGTCTGGTGGATAAATTCGCAAGGGTATCATGGC    60
                    ************************************************

Adenovirus 2 VA     GTGGACGACCGGGGGTTCGAACCCCGGATCC-----------GTGATCCATGCGGTTACCG    97
PMT2                --GGACGACCGGGGGTTCGAACCCCGGATCCGGCCGTCCGCCGTGATCCATGCGGTTACC-    117
                    ***************************          ******************

Adenovirus 2 VA     TCCGCCGCCCGTGCGTCGAACCCAGGTGTGCGACGTCAGACAACGGGGGAGCGCTCCTT-    156
PMT2                ------GCCCGCGTGTCGAACCCAGGTGTGCGACGTCAGACAACGGGGGAGCGCTCCTTT    171
                          ***** * ********************************************

Adenovirus 2 VA     -------------------- 156
PMT2                TGGCTTCCTTCCAGGCGCGG 191
```

B)

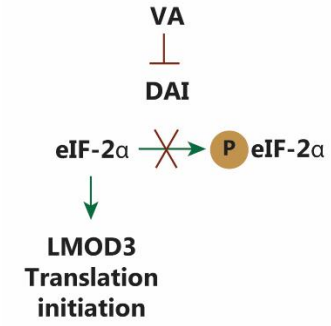

C)

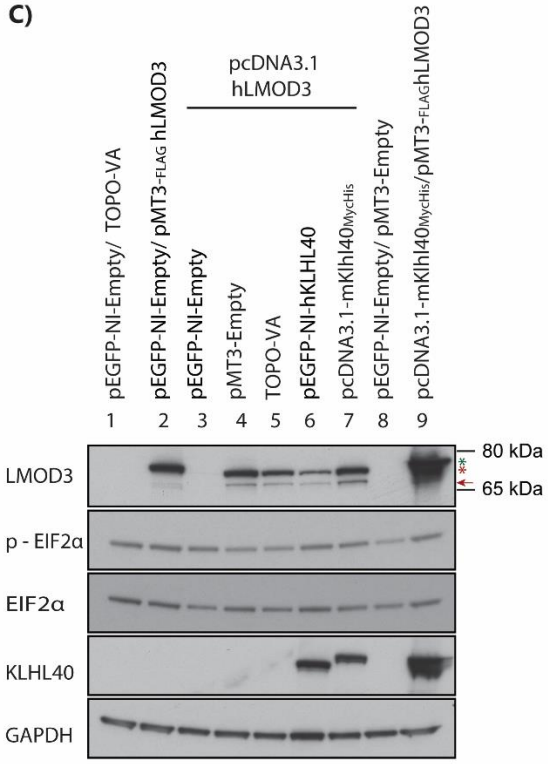

D)

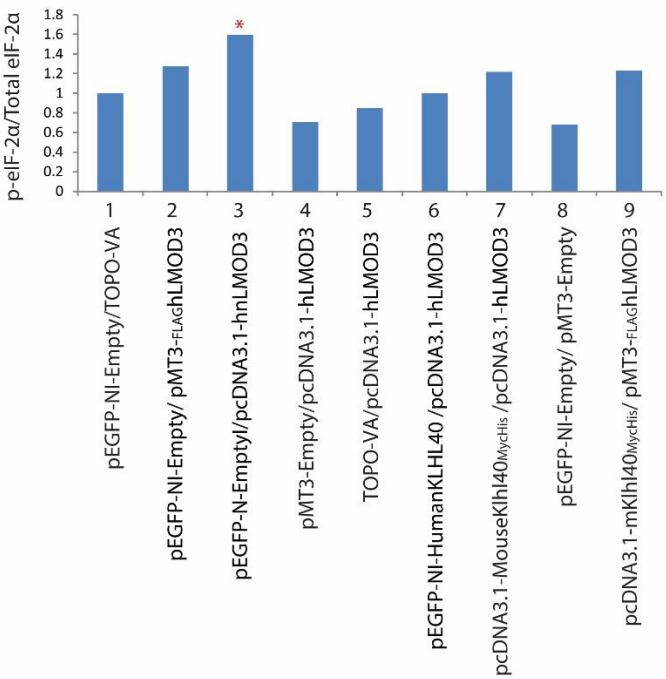

Figure 3.17: pcDNA3.1-hLMOD3 protein is readily detected when co-transfected with the pMT3-Empty or the VA element within the TOPO vector. (A) Alignment of human integrated adenovirus 2 VA RNA (M3596.1) and pMT2 showing high sequence homology; **(B)** Hypothesis schematic of VA inhibiting DAI and in turn allowing the translation of LMOD3 through un-phosphorylated eIF-2α; **(C)** Western blot of Cos-7 cells co-transfected as indicated. hLMOD3 levels are detected when pcDNA3.1-hLMOD3 is co-transfected with TOPO-VA, and slightly higher when co-transfected with pMT3-Empty; **(D)** Densitometry (ImageJ) of (C). Levels of p-eIF2-α are reduced when pcDNA3.1-hLMOD is co-transfected with pMT3-Empty or TOPO-VA. Levels of p-eIF2-α are highest when pcDNA3.1-hLMOD3 is co-transfected with pEGFP-NI-Empty (red asterisk). This experiment was performed by Adam Bournazos.

Overall, our results suggest the data published by Garg et al. (2014) have been mis-interpreted, due to:

1) Sensitivity of Lmod3 translation to the double-stranded RNA response elicited by co-transfection of certain vector backbones. In particular, pEGFP-N1 has previously been reported to evoke a powerful dsRNA response that can silence initiation of translation of sensitive transiently co-transfected cDNAs (Nejepinska, Malik, Moravec, et al., 2012; Nejepinska et al., 2014). Our results suggest this effect is also seen with the vector backbones pcDNA3.1 and pCMV10 used in Garg et al. (2014).

2) The wide-ranging roles of the proteasome and MG132. In addition to protein surveillance, the proteasome plays a role in transcription by degrading the inhibitor of the transcription factor NF-κβ (Palombella, Rando, Goldberg, & Maniatis, 1994);. MG132 has been shown to induce JNK-dependent apoptosis (Meriin, Gabai, Yaglom, Shifrin, & Sherman, 1998), prevent cleavage of β-secretase (Steinhilb, Turner, & Gaut, 2001), suppress global protein synthesis by increasing the phosphorylation of eIF2α (Yerlikaya, Kimball, & Stanley, 2008) and reprogram translation following cellular stress (Cowan & Morley, 2004). It is possible that MG132 overcomes the translational suppression of hLMOD3 induced by the dsRNA response. This hypothesis required further investigation.

Overall, our results do not support the hypothesis that KLHL40 is required for the stability of LMOD3 by binding to and protecting LMOD3 from ubiquitination and subsequent degradation by the proteasome. We propose instead, that LMOD3 coding sequences are sensitive to dsRNA pathways that act to suppress initiation of translation. Our experiments are consistent with LMOD3 protein not being translated, rather than being 'unstable' and proteolytically degraded. Whilst caveats of *in vitro* expression systems abound, our research may have also elucidated

pathways relevant to regulation of the LMOD family of proteins *in vivo*. Namely: LMOD3 transcripts are subject to multiple layers of translational regulation.

3.3 Discussion

Taken together, our results suggest LMOD3 is tightly regulated at the level of translation. Three *LMOD3* mRNA isoforms are reported with the same CDS; alternative splicing within the 5'UTRs and several structural features within the 5'UTRs and CDS are indicative of inefficient translation. Each *LMOD3* mRNA isoform varies in the length of the 3'UTR, the longer transcripts may be regulated by nonsense-mediated decay. We observe reduced hLMOD3 protein levels when hLMOD3 is co-transfected with the following vectors: pEGFP-NI, pcDNA3.1 and pCMV10. Our results are consistent with translational suppression elicited from the dsRNA response originating from transiently co-transfected vectors. Our preliminary results with hLMOD2 indicate similar regulation at the level of translation, which is not observed with hLMOD1. This suggests tight translational regulation is specific to the striated muscle LMODs.

3.3.1 Alternate LMOD isoforms

We used gencode v12 annotated mRNA transcripts of *LMOD1*, *LMOD2* and *LMOD3* from the GTEx database to investigate the presence of alternate splice isoforms within the *LMODs.* However, the predicted molecular weight of these isoforms did not correlate well with protein bands detected by western blot, using antibodies recognising LMOD1, LMOD2 and LMOD3. Additional bands were observed which do not correspond to any of the isoforms within GTEx and are of unknown significance, acknowledging that there may be splice isoforms of the *LMODs* other than those annotated in gencode v12. Unfortunately, we did not have access to biospecimens from *LMOD* KO animals to show these bands indeed correspond to LMOD isoforms (or breakdown products) to warrant further investigation. Of note, the LMOD proteins run ~10 kDa higher than their predicted molecular weight. This may be due to a post-translational modification, a structural feature, or an influence from the highly acidic regions

within LMOD proteins on the stoichiometric binding of SDS. It has been shown previously that hairpins can cause a protein to migrate between -10% to +30% of their predicted molecular weight on SDS-PAGE (Rath, Glibowicka, Nadeau, Chen, & Deber, 2009) and charge can influence the migration of a protein through SDS-PAGE (Shi et al., 2012).

Regulation of LMOD3 by alternative UTRs

GTEx detects three mRNA transcripts for *LMOD3* with the same CDS, each with a unique 5' UTR, and varying length of the 3' UTR. Each transcript is reported to be expressed in human skeletal muscle and heart, however, the dominant transcript expressed differs between striated muscle tissues. The expression of multiple isoforms with different UTRs from a single gene is not uncommon, and alternate 5'UTRs often result from alternate promoter use for example, nine isoforms with alternate 5'UTRs have been described for neuronal nitric oxide synthase (nNOS) and relate to transcriptional initiation in different tissues through alternate promoter use (Y. Wang et al., 1999). Tissue-specific transcripts have also been shown to influence protein expression by the effect of the 5'UTRs on translation efficiency. For example, Axin-2 has three mRNA isoforms with alternate 5'UTRs that structurally influence the translation efficiency of Axin-2 (Hughes & Brady, 2005). In contrast, varying lengths of 3'UTRs have been shown to influence transcript stability. Specifically, long extended 3'UTRs are linked to regulation of transcript (and protein) levels via deployment of nonsense mediated decay, as shown in immunoglobulin-μ (Buhler, Steiner, Mohn, Paillusson, & Muhlemann, 2006). Incorrect expression of alternate UTRs can lead to disease highlighting the functional importance of alternative UTRs. For example, MDM2 protein is increased in soft tissue tumours (Brown, Mize, Pineda, George, & Morris, 1999), T-cell receptor zeta chain protein is reduced in systemic lupus erythematosus (Chowdhury et al., 2005) and BRCA1 protein is reduced in breast and ovarian cancer (Sobczak & Krzyzosiak, 2002) due to incorrect alternate UTR expression. Alternate *LMOD3* transcripts expressed in skeletal muscle and heart may

influence the different protein levels observed in these tissues (Yuen et al., 2014), and possibly the location of LMOD3. Yuen et al. (2014) observed LMOD3 at the pointed ends as well as along the thin filament.

Alternate start AUG used in LMOD

Reproducible recognition of a band migrating at ~65 kDa with antibodies probing for LMOD1, LMOD2 and LMOD3 was observed on western blot of tissues and cells. We also observed a second band with mLmod3 and hLMOD3 expression constructs, running ~5 kDa lower than the dominant mLmod3 and hLMOD species on western blot. Analysis of the *LMOD3* sequence showed the presence of a methionine at position 39 with a strong Kozak sequence. Use of the methionine at position 39 as the initiating methionine is predicted to form a protein ~5 kDa smaller than full length LMOD3, correlating to the bands observed on western blot. Importantly, this band is absent when probed with an antibody against the N-terminal epitope tag. This raises the possibility that the western blot band detected by the LMOD antibodies migrating at ~65 kDa is the result of alternate start codon use within the LMODs.

Initiation at the first and second AUGs of eukaryotic genes has been described previously within the same reading frame, generating two functionally similar protein products (Makela, Saksela, & Alitalo, 1989; Soldati, Schafer, & Perriard, 1990). Interestingly, use of two AUGs generating two protein products that are functionally distinct are predominately found in viruses (Kozak, 1991a). The use of an alternate AUG in the above cases is due to an unfavourable Kozak sequence surrounding the first AUG. This leads to the first AUG being occasionally skipped, and the translational machinery reading the second AUG as the initiation codon. The first AUG of LMOD3 is surrounded by an unfavourable Kozak sequence with the second AUG surrounded by a favourable Kozak. This supports the hypothesis that the first

AUG within LMOD3 is occasionally skipped, and the second AUG is used for translation initiation.

An LMOD protein lacking amino acids 1-38 effectively disrupts the N-terminal tropomyosin binding domain, shown to encompass residues 27-38 of LMOD2 (Chereau et al., 2008) and 29-40 of LMOD3 (Yuen et al., 2014). The tropomyosin binding domain of LMOD2 has been shown to be important for its nucleation activity and localisation to the pointed ends of the thin filament (Ly et al., 2016; Skwarek-Maruszewska et al., 2010). Therefore, an LMOD3 protein with a loss of, or disruption to, tropomyosin binding would likely confer a different role. Of note, inhibiting the proteasome with MG132 increases detection of the ~65 kDa band more so than the canonical ~70 kDa band. This suggests a susceptibility of the ~65 kDa protein to proteasomal degradation.

Several factors of genomic *LMOD3* DNA show features consistent with poor translation – a weak Kozak sequence, long 5'UTR and strongly predicted secondary structure within the 5'UTR. A 5'UTR burdened with secondary structure is common in cytoskeletal genes, and is proposed that poor translation is a requirement for regulation of these proteins (Kozak, 1991a). While further experiments are required to confirm if *LMOD3* uses the second AUG as an initiating codon, we speculate it would be a secondary effect of poor translation used in LMOD3 protein regulation.

3.3.2 Regulation of LMOD translation by dsRNA

Caveats associated with transient transfection of expression vectors

Transient transfections are a common molecular biology tool, though, as with all experimental approaches, holds potential artefacts originating from the expression vector (Nejepinska, Malik, Moravec, et al., 2012). Many backbones of expression vectors commonly used today were generated decades ago, when the current technologies did not permit detailed

investigations of the plasmids (Chalfie, Tu, Euskirchen, Ward, & Prasher, 1994; de Wet, Wood, DeLuca, Helinski, & Subramani, 1987; Lorenz et al., 1996). Peer-reviewed studies of vector artefact are decades old and infrequently cited, making them difficult to source (Farr & Roman, 1992; Sorscher & Cordeiro-Stone, 1994). Collective analysis of our research data and the published literature support translation of hLMOD2 and hLMOD3 (but not hLMOD1) is strongly silenced by the double-stranded RNA cellular defence mechanism. Our study illuminates the layers of complexity arising from transient co-transfection artefact, and highlights the necessity of stringent vector controls in transient co-transfection assays.

Proposed regulation of LMOD by dsRNA in vivo.

It has been reported previously that specific cDNA sequences are more sensitive to vector artefact if the process is already occurring *in vivo* for example, transcripts containing a premature stop codon (inducing nonsense-mediated decay (NMD)) expressed within the pIREShyg2 vector are sensitised to NMD induced by structural features within the vector (Shikama et al., 2010). This raises the possibility that LMOD2 and LMOD3 coding sequences are more sensitive to the dsRNA response *in vitro* due to natural regulation of expression of LMOD2 and LMOD3 by dsRNA *in vivo*. Hairpins are evident within the UTRs and CDS of *LMOD2* and *LMOD3*. The hairpins within *LMOD2* and *LMOD3* transcripts are a source of dsRNA. While translational suppression from the cellular response to dsRNA (generated from a plasmid) is specific to exogenous genes (Nejepinska, Malik, Moravec, et al., 2012; Nejepinska et al., 2014; Terenzi et al., 1999), translational suppression of genes within genomic DNA by dsRNA is observed during a viral attack (reviewed in (Mathews & Shenk, 1991)). We therefore speculate that the dsRNA generated by *LMOD2* and *LMOD3* may be used to regulate the translation of LMOD2 and LMOD3 *in vivo*.

3.3.3 Regulation of the Lmod3 and LMOD3 by kelch-like proteins

Alternate interpretation of Garg et al. (2014)

We show that pcDNA3.1-hLMOD3 protein levels are low when co-transfected with pEGFP-NI-Empty, pcDNA3.1-Empty or pCMV10(-Kan^{R})-Empty compared to a single transfection or co-transfection with TOPO-Empty. We hypothesise that the pEGFP-NI, pcDNA3.1 and pCMV10 vectors generate dsRNA that supresses translation of mLmod3 and hLMOD3. The source of dsRNA from the pEGFP-NI vector has been linked previously to the kanamycin resistance cassette (Nejepinska, Malik, Moravec, et al., 2012; Nejepinska et al., 2014). However, we removed this cassette within the pCMV10 vector in our control 'empty vector' experiments. We therefore hypothesise that the source of the dsRNA from the pcDNA3.1 and pCMV10 vectors is the SV40 promoter sequence, present in both vectors, and shown previously to be a source of spurious RNA transcription (Nejepinska, Malik, Moravec, et al., 2012).

As previously published, we also observe increased pcDNA3.1-hLMOD3 protein levels when co-transfected with a kelch protein (mKlhl40 or hKLHL40) expressed within pEGFP-NI or pcDNA3.1. We speculate that the presence of a gene within these vectors reduces the amount of spurious dsRNA produced (and therefore, a reduction on translational suppression), due to the transcriptional machinery 'focusing' on the inserted gene.

Garg et al. (2014) generated a *Klhl40* KO mouse and showed Lmod3 protein levels were reduced 3-fold at postnatal day 1. This demonstrates that while Lmod3 protein levels are reduced, Lmod3 is detectable by western blot in the absence of Klhl40. At postnatal day 8, Lmod3 protein levels were reduced ten-fold, suggesting the levels of Lmod3 protein in the *Klhl40* KO mouse reduces over time. Cenik et al. (2015) showed LMOD3 and KLHL40 promote activity of the transcription factors MRTF/SRF which in turn coactivate the

transcription of cytoskeletal proteins, including *LMOD3* and *KLHL40*. Their work demonstrated that LMOD3 alone was not sufficient to activate MRTF/SRF however, KLHL40 alone was sufficient, and MRTF/SRF activity was enhanced with the addition of LMOD3. An alternate explanation to reduced levels of Lmod3 protein over time in the *Klhl40* KO mouse, and in human *KLHL40*-NM samples, is the loss of a player in the feedforward loop. Over time, loss of Klhl40 would reduce the transcription of *Lmod3,* as well as other cytoskeletal proteins. Reduced Lmod3 protein would reduce actin filament polymerisation, therefore increasing the amount of actin monomers in the cytoplasm. Actin monomers sequester MRTF in the cytoplasm, preventing activation of MRTF/SRF dependent genes, including *Lmod3* (Cenik et al., 2015). Therefore, a reduction in Lmod3 protein would indirectly reduce the transcription of *Lmod3* further. This would result in Lmod3 protein in the *Klhl40* KO mouse at a very young age, but reduced Lmod3 protein levels over time. This may also explain why *KLHL40*-NM patients who express some KLHL40 protein have normal levels of LMOD3 protein. Collectively, our data and published work suggest the mechanism of *KLHL40*-NM would not be targeted with proteasome-inhibitors. Instead, we support the therapeutic target proposed by Cenik et al. (2015) of enhancing the MRTF/SRF pathway to treat *KLHL40*-NM, *LMOD3*-NM and possibly other types of nemaline myopathy caused by disease genes regulated by the MRTF/SRF pathway.

Proposed role of KLHL40 in LMOD3 ubiquitination and localisation

Many members of the kelch family are substrate adaptor proteins for the E3 ligase Cul3, mediating monoubiquitination (Beck et al., 2013; Jin et al., 2012; Werner et al., 2015) or polyubiquitination of specific substrates (Kasahara et al., 2014; Yanagiya et al., 2012), and in some cases autoubiquitination of the Kelch adaptor protein itself (Lin et al., 2016; Zhang et al., 2005). Our data strongly suggests KLHL40 does not protect LMOD3 from ubiquitination and subsequent degradation by the proteasome. However, due to the large number of kelch proteins

characterised as mediating the ubiquitination of the substrates they bind, it is highly likely that KLHL40 ubiquitinates LMOD3. Cul3-Kelch mediated ubiquitination results in various outcomes for the ubiquitinated protein inclusive of localisation, degradation and protein interactions (Beck et al., 2013; Kasahara et al., 2014; Werner et al., 2015). While the most common lysine linking Ub in a polyubiquitin chain is Lys48, targeting a protein for Ub-mediated proteasome degradation (Pickart & Fushman, 2004), Cul3-kelch has been shown to link Ub through alternative lysines. For example, Cul3-KLHL20 polyubiquitinates Coronin 7, linking Ub through Lys33 and targeting Coronin 7 to the trans-golgi network (Yuan et al., 2014).

We propose KLHL40 mono- or polyubiquitinates LMOD3 where Ub is linked through a lysine other than Lys48 – most likely resulting in a different fate for LMOD3 than Ub-mediated proteasome degradation (Pickart & Fushman, 2004). Monoubiquitination or the lysine linking polyubiquitin is correlated with the fate of the ubiquitinated protein and the cellular process it is involved in, which may lend insight into how KLHL40 regulates LMOD3. Alternatively, we suggest, if LMOD3 is polyubiquitinated through Lys48 that this will not target LMOD3 to the proteasome for degradation, but result in a proteolysis-independent fate for LMOD3. This has been shown previously with the transcription factor Met4 (Flick et al., 2004). One approach to determine if KLHL40 ubiquitinates LMOD3, the number of ubiquitins and through which lysine they are linked would be mass spectrometry. We speculate that ubiquitination of LMOD3 targets LMOD3 to the pointed ends of the thin filament, influencing actin polymerisation and the MERF/SRF pathway.

3.3.4 Conclusions and Future directions

Additional LMOD protein products

Our work suggests *LMOD* mRNA isoforms detected on the GTEx database are not translated into protein, and instead represent regulation of *LMOD* at the level of translation. Preliminary results suggest the *LMODs* may use an additional start AUG and this is likely a secondary effect of poor translation of the *LMODs in vivo.* Additional bands were observed on western blot which do not correspond to any of the predicted mRNAs investigated and are of unknown significance. An important next step is to use tissues from *Lmod1*, *Lmod2* and *Lmod3* KO mice as controls to determine if this lower molecular weight band are also absent, providing further evidence they represent LMOD proteins. If these bands are specific to the LMODs it will be important to investigate their origin and if they perform distinct functions, inclusive of regulatory roles, within the cell.

Translational suppression of LMOD2 and LMOD3 by dsRNA generated by vector backbones

Our results strongly suggest that translation of hLMOD3 in co-transfection models is suppressed due to the dsRNA response elicited by the pEGFP-NI vector. It will be important to determine whether dsRNA mechanisms regulate levels of LMOD2 and LMOD3 *in vivo.*

We also show reduced hLMOD3 protein levels in the presence of pcDNA3.1 and pCMV10 vectors and hypothesis that this originates from spurious dsRNA from these vectors. Garg et al. (2014) used the pcDNA3.1 and pCMV10 vectors to conclude mKlhl40 binds to and protects mLmod3 from Ub-mediated proteasome degradation. It will be important to determine if these vectors also generate dsRNA leading to translational suppression of mLmod3. A sign of dsRNA editing is the presence of A/G conversions (Nejepinska, Malik, Filkowski, et al., 2012). Therefore, analysing pcDNA3.1 and pCMV10 sequences for A/G conversions should flag if any regions generating dsRNA and warrant further investigation. It is also plausible that the

discrepancies between results presented in Garg et al. (2014) and our results are due to differences between mouse and human orthologues. It will be important to determine which of the two hypotheses are true to: (1) Elucidate the functional consequences of interaction between mKlhl40 and mLmod3; and (2) to understand the differences between mLmod3 & mKlhl40 and the human paralogues.

To determine if each of the pEGFP-NI, pcDNA3.1 and pCMV10 vectors influence hLMOD3 and mLmod3 protein levels through dsRNA mediated translational suppression several approaches should be taken. Co-transfections of hLMOD3 or mLmod3 with serial dilutions of each vector complemented with a 'neutral' vector (does not elicit an artefact on transiently co-transfected genes, to normalise for transfected DNA concentrations) should be used to confirm the involvement of each vector in hLMOD3 and mLmod3 protein levels. This should also be carried out with a three-way co-transfection of hLMOD3 or mLmod3, empty vector and serial dilutions of hKLHL40 or mKlhl40 to determine if this kelch protein is involved in rescuing hLMOD3 and/or mLmod3 from translational suppression. To determine if hLMOD3 and mLmod3 are influenced by dsRNA co-transfections should be carried out with vectors designed to generate dsRNA (antisense/sense DNA sequences). Lastly, to determine if PKR and eIF2-α are the mechanism by which hLMOD3 and mKlhl40 translation is suppressed, rescue of hLMOD3 and mLmod3 protein detection should be tested by: (1) treating co-transfected cells with 2-aminopurine, an inhibitor of PKR phosphorylation (Farrell, Balkow, Hunt, Jackson, & Trachsel, 1977); (2) serial dilutions of TOPO-VA; and (3) serial dilutions of a mutant eIF2-α (serine to alanine) construct that cannot be phosphorylated (Kaufman et al., 1989).

Chapter 4 - PYROXD1: A novel, previously unstudied early-onset myopathy gene - essential for life and a key to unlock how oxidative distress impacts muscle pathology.

Prologue

As part of the INMR translational genomics program, we identified variants within the oxidoreductase *PYROXD1* as a new genetic cause of early-onset myopathy. This was a large inter-disciplinary collaboration providing the first characterisation of *PYROXD1*-myopathy, and establishes oxidative distress as a primary mechanistic pathway in the myopathies. I hold joint first author in this published work, presented in Part A. Part A functions as the introduction to this chapter.

My contribution to this article was in the genetic and molecular functional studies of PYROXD1 in healthy and diseased states. PYROXD1 had not been previously characterised, therefore, a large part of this work involved establishing tools in our lab to study PYROXD1. During this process we uncovered cellular, molecular and biochemical properties of PYROXD1 that were vital to enable the characterisation of PYROXD1 and *PYROXD1*-myopathy, but were not included in our publication. These studies are presented as Part B of this chapter.

To further investigate the role of PYROXD1 in fundamental biology and disease we established two mouse models. These studies are presented in Part C of this chapter.

4.1 Part A: PAPER - Variants in the oxidoreductase PYROXD1 cause early-onset myopathy with internalized nuclei and myofibrillar disorganisation

ARTICLE

Variants in the Oxidoreductase PYROXD1 Cause Early-Onset Myopathy with Internalized Nuclei and Myofibrillar Disorganization

Gina L. O'Grady,[1,2,3,25] Heather A. Best,[1,2,25] Tamar E. Sztal,[4,25] Vanessa Schartner,[5,26] Myriam Sanjuan-Vazquez,[6,26] Sandra Donkervoort,[7,26] Osorio Abath Neto,[5] Roger Bryan Sutton,[8] Biljana Ilkovski,[1] Norma Beatriz Romero,[9,10] Tanya Stojkovic,[10] Jahannaz Dastgir,[7] Leigh B. Waddell,[1] Anne Boland,[11] Ying Hu,[7] Caitlin Williams,[4] Avnika A. Ruparelia,[4] Thierry Maisonobe,[10] Anthony J. Peduto,[12] Stephen W. Reddel,[13] Monkol Lek,[14,15] Taru Tukiainen,[14,15] Beryl B. Cummings,[14,15] Himanshu Joshi,[1] Juliette Nectoux,[16,17] Susan Brammah,[18] Jean-François Deleuze,[11] Viola Oorschot Ing,[19] Georg Ramm,[19,20] Didem Ardicli,[21] Kristen J. Nowak,[22] Beril Talim,[21] Haluk Topaloglu,[21] Nigel G. Laing,[22] Kathryn N. North,[1,23] Daniel G. MacArthur,[14,15] Sylvie Friant,[6] Nigel F. Clarke,[1,2] Robert J. Bryson-Richardson,[4] Carsten G. Bönnemann,[7] Jocelyn Laporte,[5,24,27] and Sandra T. Cooper[1,2,27,*]

This study establishes *PYROXD1* variants as a cause of early-onset myopathy and uses biospecimens and cell lines, yeast, and zebrafish models to elucidate the fundamental role of *PYROXD1* in skeletal muscle. Exome sequencing identified recessive variants in *PYROXD1* in nine probands from five families. Affected individuals presented in infancy or childhood with slowly progressive proximal and distal weakness, facial weakness, nasal speech, swallowing difficulties, and normal to moderately elevated creatine kinase. Distinctive histopathology showed abundant internalized nuclei, myofibrillar disorganization, desmin-positive inclusions, and thickened Z-bands. PYROXD1 is a nuclear-cytoplasmic pyridine nucleotide-disulphide reductase (PNDR). PNDRs are flavoproteins (FAD-binding) and catalyze pyridine-nucleotide-dependent (NAD/NADH) reduction of thiol residues in other proteins. Complementation experiments in yeast lacking glutathione reductase *glr1* show that human PYROXD1 has reductase activity that is strongly impaired by the disease-associated missense mutations. Immunolocalization studies in human muscle and zebrafish myofibers demonstrate that PYROXD1 localizes to the nucleus and to striated sarcomeric compartments. Zebrafish with *ryroxD1* knock-down recapitulate features of PYROXD1 myopathy with sarcomeric disorganization, myofibrillar aggregates, and marked swimming defect. We characterize variants in the oxidoreductase *PYROXD1* as a cause of early-onset myopathy with distinctive histopathology and introduce altered redox regulation as a primary cause of congenital muscle disease.

Introduction

Myopathies are a group of genetically heterogeneous conditions characterized by muscle weakness, with overlap in the clinical presentation and histopathological features of different genetic subtypes.[1] Within this group, congenital myopathies are most commonly characterized by hypotonia and weakness, often from birth, commonly with the presence of facial weakness, with or without ptosis and ophthalmoplegia. There are 25 recognized genetic causes of congenital myopathy (see GeneTable in Web Resources); currently a genetic diagnosis is achieved in only ~50% of

[1]Institute for Neuroscience and Muscle Research, Kid's Research Institute, Children's Hospital at Westmead, Sydney, NSW 2145, Australia; [2]Discipline of Paediatrics and Child Health, Faculty of Medicine, University of Sydney, Sydney, NSW 2006, Australia; [3]Paediatric Neurology Service, Starship Children's Health, Auckland 1023, New Zealand; [4]School of Biological Sciences, Monash University, Melbourne, VIC 3800, Australia; [5]Institut de Génétique et de Biologie Moléculaire et Cellulaire (IGBMC), 67400 Illkirch, France; [6]Department of Molecular and Cellular Genetics, UMR7156, Université de Strasbourg, CNRS, Strasbourg 67081, France; [7]National Institute of Neurological Disorders and Stroke Neurogenetics Branch, Neuromuscular and Neurogenetic Disorders of Childhood Section, NIH, Bethesda, MD 20892-1477, USA; [8]Department of Cell Physiology and Molecular Biophysics, and Center for Membrane Protein Research, Texas Tech University Health Sciences Center, Lubbock, TX 79430, USA; [9]Sorbonne Universités, UPMC Univ Paris 06, INSERM UMRS974, CNRS FRE3617, Center for Research in Myology, GH Pitié-Salpêtrière, 47 Boulevard de l'hôpital, 75013 Paris, France; [10]Centre de Référence de Pathologie Neuromusculaire Paris-Est, Institut de Myologie, GHU La Pitié-Salpêtrière, Assistance Publique-Hôpitaux de Paris, 7503 Paris, France; [11]Centre National de Génotypage, Institut de Génomique, CEA, CP5721, 91057 Evry, France; [12]Department of Radiology, Westmead Hospital, Western Clinical School, University of Sydney, Sydney, NSW 1024, Australia; [13]Department of Neurology, Concord Clinical School, University of Sydney, Sydney, NSW 2139, Australia; [14]Analytic and Translational Genetics Unit, Massachusetts General Hospital, Boston, MA 02114, USA; [15]Broad Institute of Harvard and Massachusetts Institute of Technology, Cambridge, MA 02142, USA; [16]Service de Biochimie et Génétique Moléculaire, HUPC Hôpital Cochin, Paris 75014, France; [17]INSERM, U1016, Institut Cochin, CNRS UMR8104, Université Paris Descartes, Paris 75014, France; [18]Electron Microscope Unit, Concord Repatriation General Hospital, Concord, NSW 2139, Australia; [19]The Clive and Vera Ramaciotti Centre for Structural Cryo-Electron Microscopy, Monash University, Melbourne, VIC 3800, Australia; [20]Department of Biochemistry and Molecular Biology, Monash University, Melbourne, VIC 3800, Australia; [21]Department of Pediatric Neurology, Hacettepe University Children's Hospital, 06100 Ankara, Turkey; [22]Centre for Medical Research, The University of Western Australia & the Harry Perkins Institute of Medical Research, Perth, WA 6009, Australia; [23]Murdoch Children's Research Institute, The Royal Children's Hospital, Flemington Road, Parkville, VIC 3052, Australia; [24]Université de Strasbourg, 67081 Illkirch, France
[25]These authors contributed equally to this work
[26]These authors contributed equally to this work
[27]These authors contributed equally to this work
*Correspondence: sandra.cooper@sydney.edu.au
http://dx.doi.org/10.1016/j.ajhg.2016.09.005.

patients,[2,3] driving ongoing gene discovery. The introduction of next-generation sequencing technologies has seen a rapid acceleration in the identification of new genetic causes of neuromuscular disorders.[4,5]

Through international whole-exome sequencing programs in Australia, France, the United States, and Turkey, we identified five families (nine probands) with four different recessive variants (missense and splicing variants) in *PYROXD1*. *PYROXD1* is located at 12p12.1 and encodes pyridine nucleotide-disulfide oxidoreductase domain-containing protein 1, a 500 amino acid protein previously undescribed in published literature. Pyridine nucleotide-disulphide reductases (PNDRs) are flavoproteins (FAD-binding) and catalyze the pyridine nucleotide (NAD/NADH)-dependent reduction of cysteine residues in their substrates.[6] PNDRs catalyze complex reduction reactions and use several steps of electron transfer via their enzymatic co-factors FAD and NAD. Although functionally uncharacterized, PYROXD1 is classified as a class 1 oxidoreductase and bears two putative enzymatic domains: a pyridine nucleotide-disulphide oxidoreductase domain (amino acids 39–361) and a NADH-dependent nitrite reductase domain (amino acids 447–494) (see Figure 3).

Herein we establish PYROXD1 as a nuclear-cytoplasmic oxidoreductase that underlies an early-onset myopathy characterized by generalized weakness with multiple internalized nuclei and myofibrillar aggregates on biopsy.

Subjects and Methods

Genetic Analysis

Family A was the index family identified through whole-exome sequencing of a large cohort of undiagnosed myopathy and dystrophy patients (367 individuals from 193 families) recruited from The Institute for Neuroscience and Muscle Research (Sydney, Australia). No further families were identified in this cohort with PYROXD1-related disease. Exome sequencing was performed on gDNA from both brothers and their unaffected parents at the Broad Institute using the XBrowse bioinformatics platform as described previously.[7] Family B was identified through the French Myocapture project (1,000 exomes from 397 families with myopathies or dystrophies). Exome sequencing was performed for both affected brothers and their parents at Centre National de Génotypage (CNG, Evry, France). Common variants (>1%) found in dbSNP, 1000 Genomes, Exome Variant Server, and an internal database of 1,550 exomes including ethnically matched individuals were filtered out. The Varank pipeline was used for variants scoring and ranking.[8] Data were filtered for homozygous recessive variants based on the known consanguinity of the family. Family B was the only family identified with recessive *PYROXD1* variants in the Myocapture cohort. For family C, exome sequencing was performed through the NIH Intramural Sequencing Center (NISC) on genomic DNA obtained from both affected siblings. Data were analyzed using a custom analysis program, MPG (Most Probable Genotype) based on a probabilistic Bayesian algorithm.[9] For families D and E, exome sequencing was performed on gDNA from both siblings and unaffected parents at the Theragen Etex Bio Institute. ANNOVAR was used to functionally annotate genetic variants.[10] Table S1 provides a list of recessive variants shown to segregate with disease for each family.

Phylogenetic Analysis and Calculation of the PYROXD1 Homology Model

PYROXD1 sequence alignments were performed using CLUSTAL.[11] Identity and similarity were calculated using Sequence Manipulation Suite.[12,13] Modeler[14] was used to compare the primary sequence of PYROXD1 with homologous proteins in the PDB database. The primary sequence of PYROXD1 was aligned with eight of the most similar protein sequences determined from Modeler using Promals3D:[15] *Shewanella* PV-4 NADH-dependent persulfide reductase (PDB: 3NTD), *Staphylococcus* Coenzyme A-disulfide reductase (PDB: 1YQZ), *Bacillus* Coenzyme A-disulfide reductase (PDB: 3CGC), *Novosphingobium* ferredoxin reductase (PDB: 3LXD), *Rhodopseudomonas* ferredoxin reductase (PDB: 3FG2), *Pseudomonas p.* putidaredoxin reductase (PDB: 1Q1R), *Pseudomonas sp.* ferredoxin reductase (PDB: 2GQW), and *Enterococcus* NADH peroxidase (PDB: 1NHQ). Modeler was used to compute the homology model of human PYROXD1 using information from all eight homologous crystal structures. The resulting model with the lowest energy was further refined using Modrefiner.[16] FAD binding residues were determined via the 3DLigandSite server.[17] Figures were generated with Pymol (The PyMOL Molecular Graphics System, v.1.8, Schrödinger, LLC).

Western Blot

Western blot of skeletal muscle and skin fibroblasts was carried out as described in Yuen et al.[18] Primary antibodies used were anti-PYROXD1 (1:1,000; Abcam cat# ab122458; RRID: AB_11129858), β-tubulin (1:1,000; E7, Developmental Studies Hybridoma bank), GAPDH (1:10,000; Millipore cat# MAB374; RRID: AB_2107445), Emerin (NCL 1:300, Novocastra), and sarcomeric alpha-actinin (EA-53 1:2,500, Sigma-Aldrich). For zebrafish, embryos were deyolked and protein extracted as described.[19] 13 μL of protein sample was reduced using NuPAGE Reducing Agent (Thermo Fisher) and equal amounts loaded onto a NuPAGE 4%–12% Bis-Tris Gel using MES SDS running buffer (Thermo Fisher). Membranes were blocked and probed with antibodies diluted in 1× phosphate-buffered saline, 0.1% Tween20 (Sigma-Aldrich), and 5% skim milk. Primary antibodies used were 1:1,000 anti-Ryroxd1-C (Abmart), 1:1,000 anti-GFP (Abcam cat# ab137827), and 1:2,000 α-tubulin (Sigma-Aldrich cat# T6074; RRID: AB_477582). The secondary antibody used was 1:10,000 HRP-conjugated mouse IgG (Southern Biotech) and developed using chemiluminescent detection (GE Life Sciences). For yeast, total yeast extracts were obtained by NaOH lysis followed by TCA precipitation. The equivalent of 1.5 OD_{600nm} unit of yeast cells were resuspended in 50 μL of 2× Laemmli buffer plus Tris Base. Samples were incubated 5 min at 37°C and analyzed by 10% SDS-PAGE followed by immunoblotting with anti-PYROXD1 (1:500), polyclonal R3500 produced in rabbit with human PYROXD1 immunogen amino acid 488–500 (Cys Leu Leu Asp Pro Asn Ile Asp Ile Glu Asp Tyr Phe Asp). Images were acquired with the ChemiDoc Touch Imaging System (Bio-Rad).

Immunostaining and Microscopy

For skeletal muscle, 8 μm muscle cryosections were fixed in 3% paraformaldehyde for 15 min, extracted with cold methanol for

10 min, and probed with primary antibodies diluted in 2% BSA/PBS for 16 hr at 4°C: PYROXD1 (1:50; Abcam cat# ab122458 or ab204560; RRID: AB_11129858), desmin (1:50; NCL-Des, Novacastra), myosin (1:20; RS034, Novacastra), and lamin A/C (1:80; NCL-LAM-A/C, Novacastra). After washing in PBS, samples were incubated with secondary antibody for 1 hr at room temperature, washed, and mounted with ProLong Gold with DAPI antifade reagent (Life Technologies). Goat anti-rabbit $IgG^{Alexa555}$ goat anti-mouse $IgG^{Alexa488}$ (H+L) (1:200, A21428 and A110018, Life Technologies). Specimens were imaged on a Leica SP5 confocal microscope. For zebrafish, 4% paraformaldehyde (PFA)-fixed 2 dpf whole-mount or 4 dpf whole-mount and vibratome-sectioned embryos were stained as described.[19] Antibodies used were α-actinin2 (Sigma clone A7811, 1:100) and an AlexaFluor-labeled-488 secondary antibody (Molecular Probes, 1:200) and rhodamine-Phalloidin (Molecular Probes, 1:200). Imaging was performed with an LSM 710 confocal microscope (Zeiss), using a 20× 1.0 numerical aperture water-dipping objective.

For yeast, living cells expressing EGFP C-terminal-tagged PYROXD1, PYROXD1-Asn155Ser, or -Gln372His were imaged on a fluorescence Axio Observer D1 microscope (Zeiss) using GFP filter and DIC optics with 100×/1.45 oil objective (Zeiss). Images were captured with a CoolSnap HQ2 photometrix camera (Roper Scientific).

Cell Culture, Constructs, cDNA Synthesis, and Transfections

HEK293 cells were cultured and transfected as described.[20] Cos-7 cells and primary human fibroblasts were cultured in DMEM/F12 with 10% FBS and 1:200 gentamycin (all from Life Technologies). Cos7 cells were transfected with Lipofectamine LTX (15338-100, Life Technologies) as per the manufacturer's instructions in 10 cm^2 dishes. Human *PYROXD1* cDNA (GenBank: NM_024854) was cloned into pEGFP-CI (Genscript) via BspE1/Sal1. GFP was then removed via AgeI/BspEI. RNA extraction of primary human fibroblasts was carried out using TRIzol (Invitrogen) and alcohol precipitation. cDNA was synthesized using random primers $p(dn)_6$ (Roche 11043921) or $Oligo(dt)_{20}$ primers (Invitrogen 55063) and Superscript III reverse transcriptase (Invitrogen 56575) according to the manufacturer's instructions. Primers used for PCR of *PYROXD1* cDNA were exon 1 F: 5′-AGGGAAGTTCGTGGTGGTC-3′; exon 6 R: 5′-TGGCCCAAATCACTTCACAG-3′; exon 12 R: 5′-AGGACGAGAATACATCAAAGTCG-3′.

Plasmids, Strains, Media, and Methods for Yeast Cells

The PYROXD1 and missense mutants p.Asn155Ser or p.Gln372His cDNA sequences were cloned into pDONR221 entry vector (Invitrogen) and then into yeast destination vectors (Addgene) via the Gateway (Invitrogen) method to obtain the pAG415-promGPD-PYROXD1, p.Asn155Ser or p.Gln372His (pSF371 to pSF373) and pAG415-promGPD-PYROXD1-EGFP, p.Asn155Ser or p.Gln372His (pSF374 to pSF376) plasmids. Plasmid sequences were verified (GATC Biotech). *S. cerevisiae* strains used were BY4742 WT (*MATα leu2Δ0 ura3Δ0 his3Δ0 lys2Δ0*) and *glr1Δ* (BY4742 *glr1:kanMX*). Yeast were grown in YPD-rich medium (1% yeast extract, 2% peptone, 2% glucose) or in Synthetic Medium (SD): 0.67% yeast nitrogen base (YNB) without amino acids, 2% glucose, and the appropriate –Leu dropout mix to maintain the plasmid. Yeast cells were transformed using the modified lithium acetate method.[21]

Zebrafish

Production of Transgenic Constructs, Morpholino Injections, and RNA Rescue Experiments

Zebrafish were maintained according to standard protocols.[22] Transgenic constructs were assembled with the modular tol2 kit. N-terminal eGFP-tagged wild-type or mutant PYROXD1 constructs were created using p5E-actc1b,[23] p5E-SP6-CMV,[24] p3E-pA, and pDEST-Tol2-pA2. Transgenic constructs used were actc1b-h2afv-mCherry[24] and actc1b-actinin3-mCherry.[25] For morpholino injections, ryroxd1 morpholinos (splice MO: 5′-TCGATGGTTTCTTACCTGTTCTGCA-3′, 0.25 mM and ATG MO: 5′-CCATTGAACTTCAGCACATGGAGAT-3′, 0.25 mM) and GFP morpholino (5′-GTTCTTCTCCTTTACTCAGGATC-3′, 0.5 mM) were diluted in distilled water and co-injected with Cascade Blue-labeled dextran (Molecular Probes) into one-cell embryos. For RNA rescue experiments, wild-type PYROXD1-eGFP RNA, lacking the morpholino binding site, was synthesized using the mMessage mMachine SP6 Transcription Kit (Ambion). RNA was co-injected at a concentration of either 0.5 or 1 ng/μL into one-cell stage embryos with Cascade Blue. Injected embryos were sorted for Cascade Blue labeling prior to analysis.

In Situ Hybridization

Whole-mount in situ hybridization was carried out as described previously.[26] Probes were constructed using specific gene primers (F: 5′-AGAAACCGAAGATGGTCAGAGA-3′ and R: 5′-GAGCGAAGACGCTTCTCTTCTA-3′). Imaging was performed with an Olympus SZX16 stereomicroscope.

cDNA Synthesis and Quantitative PCR

Total RNA was extracted using TRIzol reagent (Invitrogen Life Technologies) and cDNA was synthesized using Protoscript first strand cDNA synthesis kit (New England Biosciences). Quantitative PCR (qPCR) was performed on a Roche Lightcycler instrument using β-actin as a reference gene. Primers for qPCR are β-actin (F: 5′-GCATTGCTGACCGTATGCAG-3′ and R: 5′-GATCCACATCTGCTGGAAGGTGG-3′) and ryroxd1 (F: 5′-TCAATGGCTTCAGAGAAACAAG-3′ and R: 5′-CTGTTCTGCACAAGTGACACC-3′).

Swimming Assays

Touch-evoked response assays and analysis were performed on 48 hr post fertilization zebrafish as per Sztal et al.[19]

Electron Microscopy

Zebrafish were fixed in 2.5% gluteraldehyde, 2% paraformaldehyde in 0.1 M sodium cacodylate buffer, with post-fixation in 1% OsO_4 1.5% K3Fe(III)(CN)6 in 0.065 M sodium cacodylate buffer. Samples were dehydrated through an ethanol series and embedded in Epon 812. 80 nm sections were stained with Uranyl acetate and lead citrate before imaging using a Hitachi H-7500. Muscle biopsies were fixed in 2.5% glutaraldehyde in 0.1 M sodium cacodylate buffer and processed routinely for electron microscopy. Ultrathin sections were examined in an FEI Tecnai Spirit Biotwin.

Study Approval

Ethical approval for this research was obtained from the Human Research Ethics Committees of the Children's Hospital at Westmead, Australia (10/CHW/45), The University of Western Australia, the Comité de Protection des Personnes Est IV (DC-2012-1693), France, the Institutional Review Board of the National Institute of Neurological Disorders and Stroke, NIH (12-N-0095), and Ethical Committee of Hacettepe University, Faculty of Medicine. Written informed consent was obtained from participants for genetic testing, biobanking of DNA, muscle, and fibroblasts,

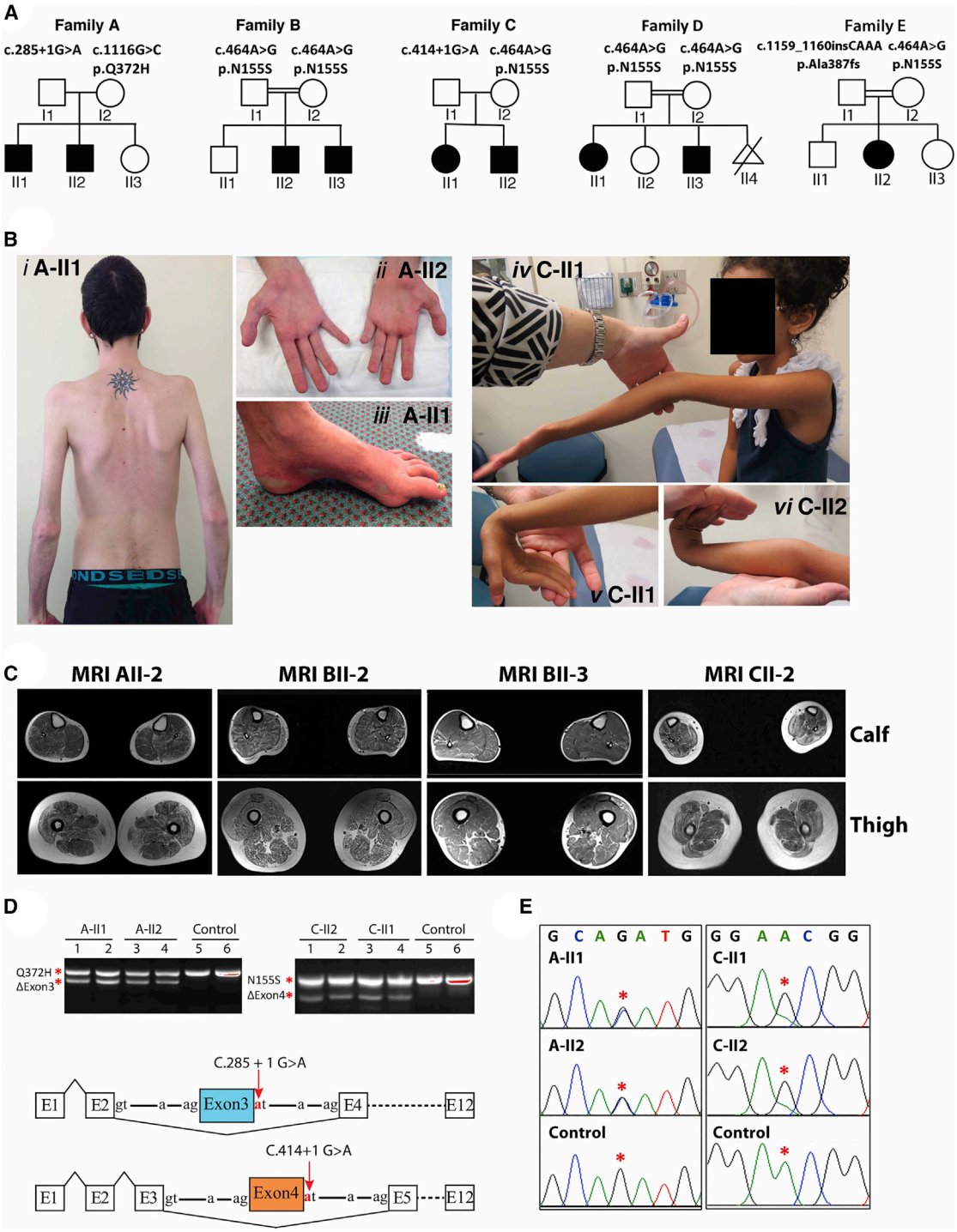

Figure 1. Clinical Features of *PYROXD1*-Related Myopathy

(A) Pedigrees of the five affected families.

(B) Posterior view of A-II1 (*i*) demonstrating generalized reduction of muscle bulk and prominent scapulae. Hands of A-II2 (*ii*) demonstrating marked wasting of the thenar and hypothenar eminence. Foot of A-II1 (*iii*) showing pes cavus and skin discoloration. C-II1 (*iv*) demonstrating hyperextension of the elbow and reduced muscle bulk. C-II1 (*v*) wrist hyperextension. C-II2 (*vi*) hand and wrist hyperextension.

(C) Axial T1 muscle MRI of calf and thigh of individuals A-II2, B-II2, B-II3, and C-II2. In all individuals, the thigh shows generalized reduction in muscle, atrophy, and fatty marbling. There is relative sparing of rectus femoris relative to vastus lateralis. The calf of individuals in family B is more mildly affected.

(D) Top: Agarose gel of PCR products of fibroblast cDNA from two affected siblings from family A (left) and family C (right). For both families, sequencing of the lower band established in-frame skipping of exon 3 in family A and exon 4 in family C. Sequencing of the upper band in family A identified only transcripts bearing the maternal c.1116 G>C (p.Gln372His) missense variant. Sequencing

(legend continued on next page)

and publishing of photographs of affected individuals. Fish maintenance and handling were carried out as per standard operating procedures approved by the Monash Animal Services Ethics Committee.

Results

Recessive *PYROXD1* Variants Cause Early-Onset Myopathy with Combined Histopathology of Multiple Internalized Nuclei and Myofibrillar Disorganization

Clinical Features of PYROXD1 Myopathy

Nine affected individuals from five families presented with childhood-onset muscle weakness (infancy to 8 years) (Figure 1A; Table 1). Perinatal history and early gross motor milestones were largely within normal limits. All affected individuals walked between 9 and 20 months of age. Two probands had poor head control in infancy (family C, II1 and II2). Weakness was slowly progressive. All affected individuals were still ambulant at 7–31 years but had difficulty with running and stairs. A-II1 required a cane for support and was unable to climb stairs from 24 years. All individuals had generalized reduction in muscle bulk (Figure 1B) and displayed symmetrical proximal weakness of the upper and lower limbs. Triceps brachii power was disproportionally reduced in three affected individuals. Distal weakness of the upper and lower limbs was also present in families A, B, C, and E. A-II1 and A-II2 showed marked wasting of distal musculature, in particular the thenar and hypothenar muscles (Figure 1B, *ii*), with abductor digiti minimi strength graded 3/5 and abductor pollicus brevis 0/5 in A-II2.

Neck weakness and mild scapular winging (5/9) were present (Figure 1B, *i*). Deep tendon reflexes were reduced or absent. Moderate joint laxity was present in families A and C (Figure 1B, *iv*–*vi*) but had resolved in family A by adulthood. Joint contractures did not occur, with the exception of mild tendoachilles contractures in A-II1. Mild scoliosis was seen in 2/9, pectus excavatum in 2/9, and thoracolumbar rigidity in family C. All affected individuals had mild to moderate facial weakness and mild ptosis was present in 3/9. A high arched palate and dental malocclusion were present in 7/9. Nasal speech was present in all individuals, swallowing difficulties in 6/9, fatigue with chewing in 2/9, and A-II2 required surgery for velopharyngeal incompetence. Ophthalmoplegia was not present.

Cognition was normal, except A-II1 who had mild, specific learning difficulties. Mild restrictive lung disease was present in the teenage years, but no individual had nocturnal hypoventilation. Frequent respiratory infections were seen in 4/9. Cardiac evaluations were normal, except for A-II1 who had developed abnormal septal wall motion and a low normal ejection fraction (50%) on his most recent assessment at 27 years of age.

Creatine kinase levels ranged from normal to moderately elevated (up to 1,051 IU/L). Electromyography (EMG) was myopathic in all individuals tested. Electrophysiological studies are summarized in Table S2. Nerve conduction studies in A-II1 and A-II2, the oldest affected individuals (26 and 29 years of age), found compound muscle action potential (CMAP) amplitudes reduced to 1%–10% of normal, absent peroneal CMAPs, reduced sural sensory potentials, but normal upper limb sensory amplitudes, suggestive of a mild length-dependent axonal neuropathy. Muscle MRI imaging of family A showed diffuse muscle atrophy and fatty marbling with relative sparing of rectus femoris relative to vastus lateralis in the thigh. In family B, only mild changes were seen, with vastus lateralis most affected in the upper leg and gastrocnemius in the lower leg (Figure 1C).

Histopathological Features of PYROXD1 Myopathy

Muscle biopsies were available from five affected individuals (Table 1). Haemotoxylin and eosin staining showed marked variation in fiber size and multiple internalized nuclei, commonly occurring in clusters (Figure 2A, *i*, *v*, *ix*, and see EM in Figure 2B, *i* and *vi*). Occasional degenerating and regenerating fibers were seen, with a moderate increase in interstitial connective tissue. Oxidative stains showed large central core-like zones devoid of mitochondrial activity (Figure 2A, *ii*, *vi*, *x* NADH). Immunohistochemical staining of skeletal muscle demonstrated large myofibrillar inclusions positive for desmin (Figure 2A, *iii*, *vii*, and *xi*), myotilin (Figure 2A, *iv* and *viii*), alpha-actin (Figure 2A, *xii*), and αB crystallin (not shown). Electron microscopy showed extensive sarcomeric disorganization, with small atrophied fibers showing complete loss of sarcomeric architecture, absence of aligned thick filaments, and accumulation of thin filaments (Figure 2B, *i*, *iii*, *iv*, *vi*, *vii*, *viii*). In some small fibers, electron-dense thickened z-line remnants or small nemaline rods were also present (Figure 2B, *iv* and *vii*). Large fibers showed multiple areas of Z-band streaming and large, focal zones of sarcomeric disorganization (Figure 2B, *ii*), devoid of mitochondria and organelles (Figure 2B, *v*). Thus, PYROXD1 myopathy

of the upper band in family C identified only transcripts bearing the maternal c.464A>G (p.Asn155Ser) variant. Bottom: Schematic of *PYROXD1* exon skipping events in family A and family C (not to scale).
(E) Sequencing chromatogram of the total PCR mixture using exon 1 forward and exon 12 reverse primers. Family A shows equal peak heights for the paternal wild-type and maternal missense variant c.1116 G>C (p.Gln372His) (red asterisks), suggesting approximately equal abundance of exon 3 skipped transcripts and missense c.1116 G>C (p.Gln372His) transcripts among the total mRNA pool. In contrast, family C shows evidence for maternal allele bias, with a lower peak height of the paternal c.464A relative to maternal c.464G variant (red asterisks).
Collective data (D, right and E, right) suggest that the paternal exon 4-skipped transcripts are less abundant than the maternal c.464A>G (p.Asn155Ser) among the total mRNA pool.

Table 1. Clinical Characteristics of Affected Individuals with PYROXD1 Variants

ID	Family A-II1	Family A-II2	Family B-II2	Family B-II3	Family C-II1	Family C-II2	Family D-II1	Family D-II3	Family E-II2
Gender, current age	male, 29 y	male, 26 y	male, 31 y	male, 21 y	female, 9 y	male, 7 y	female, 22 y	male, 17 y	female, 15 y
Ethnicity; consanguinity	European descent; no	European descent; no	Turkish; yes	Turkish; yes	Persian Jewish; no	Persian Jewish; no	Turkish; yes	Turkish; yes	Turkish; yes
PYROXD1 variants	c.285+1G>A (chr12: g.21598401G>A), c.116G>C (p.Gln372His, chr12: g.21615796G>C)	c.285+1G>A (chr12: g.21598401G>A), c. 0.116G>C (p.Gln372His, chr12: g.21615796G>C)	Hom. c.464A>G (p.Asn155Ser, chr12: g.21605064A>G)	Hom. c.464A>G (p.Asn155Ser, chr12: g.21605064A>G)	c.414+1G>A (chr12: g.21602626G>A), c.464A>G (p.Asn155Ser, chr12: g.21605064A>G)	c.414+1G>A (chr12: g.21602626G>A), c.464A>G (p.Asn155Ser, chr12: g.21605064A>G)	Hom. c.464A>G (p.Asn155Ser, chr12: g.21605064A>G)	Hom. c.464A>G (p.Asn155Ser, chr12: g.21605064A>G)	c.464A>G (p.Asn155Ser, chr12: g.21605064A>G), c.1159_1160insCAAA, chr12: g.21620457_21620458insCAAA)
Onset/progression	onset 5 y, difficulty running; slowly progressive weakness from 20 y; unable to climb stairs from 24 y; slow walk with a cane	onset 8 y; stable in childhood; mild progression from teenage years; increasing difficulty with stairs	onset 10 y; ambulant with difficulty ascending stairs	onset 10 y; ambulant	congenital onset; hypotonia; mild gross motor delay; walked age 20 mo; weakness from 6 y; increasing difficulty with stairs	infantile onset with hypotonia; walked age 13 mo; stable strength; difficulty with stairs	onset 2 y; ambulant; difficulty running and climbing; frequent falls; slowly progressive weakness from 20 y	onset 2.5 y; ambulant; difficulty climbing; stable in childhood	onset 4 y; easy fatigue; frequent falls; difficulty on stairs; slowly progressive; increasing difficulty with stairs
Pattern of limb weakness (HP:0001324)	symmetrical; UL, LL, axial; P, D	symmetrical; UL, LL, axial; P, D	symmetrical; UL, LL, axial; P UL, D LL	symmetrical; UL, LL, axial; P	symmetrical; UL, LL, axial	symmetrical; UL, LL, axial	symmetrical; UL, LL, axial; P	symmetrical; UL, LL, axial; P	symmetrical: UL, LL; P, D
Severity of limb weakness	all 4− and 4/5, except deltoid 2/5, shoulder abduction 1/5	all 4+ and 5/5, except deltoid 2/5, ADM 3/5, APB 0/5; lower limbs 4/5 except hip flex 3/5	–	–	all 4+ and 4−/5, except shoulder abd. 3/5, wrist flex 3+/5, neck flex 2/5, hip abduction 3/5	all 4 and 4−/5, except deltoid 3+/5, finger spread 3+/5, neck flex 2/5; hip extension 5−/5	proximal 4−, distal 4+/5, lower limbs more affected	proximal 4+ and 5−/5, distal 5/5	proximal 4− and 4+/5; hip flexion 3/5; thenar wasting
Hyporeflexia (HP:0001265)	reduced or absent	reduced or absent	reduced or absent	reduced or absent	reduced or absent	reduced or absent	reduced or absent	reduced or absent	reduced or absent
Achilles contractures (HP:0001771)	yes	no	no	no	yes	no	no	no	no
Joint contracture 5th finger (HP:0009183)	yes	no	no	no	yes	no	no	no	no
Joint hypermobility (HP:0001382)	distal laxity, resolved with age	distal laxity, partial patella subluxations	no	no	elbow and MCP joints	mild at elbow, wrist, and MCP joints	no	no	no
Facial weakness (HP:0002058)	yes	yes	yes	yes	yes	yes	yes	yes	yes
Ptosis (HP:0000508)	no	no	no	mild	no	no	mild	mild	no

(*Continued on next page*)

Table 1. ***Continued***

ID	Family A-II1	Family A-II2	Family B-II2	Family B-II3	Family C-II1	Family C-II2	Family D-II1	Family D-II3	Family E-II2
Ophthalmoplegia (HP:0000602)	no	no	no	no	no	no	no	no	no
High arched palate (HP:0000218)	yes	yes	no	no	yes	yes	yes	yes	yes
Additional facial features	dental malocclusion (HP:0000689), elongated face	dental malocclusion (HP:0000689), elongated face	no	micrognathia and retrognathia (HP:0000308)	int. exotropia, surgical correction (HP:0000577)	no	elongated face (HP:0000276)	elongated face (HP:0000276)	no
Dysphagia (HP:0002015)	present from 12 y; improved	yes, plus nasal regurgitation from 9 y; surgery for VPI	yes	no	no	no	yes	yes	yes
Chewing difficulties (HP:0030193)	no	no	no	no	yes	yes	no	no	no
Nasal speech (HP:0001611)	yes	yes	yes	yes	yes	yes	yes	yes	yes
Scoliosis (HP:0002650)	mild thoracic scoliosis from 20 y	no	no	no	mild scoliosis from 7 y	no	no	no	no
Spinal rigidity (HP:0003306)	no	no	no	no	thoracolumbar rigidity	thoracolumbar rigidity	no	no	no
Pectus excavatum (HP:0000767)	yes	no	no	no	yes	no	no	no	no
Scapular winging (HP:0003691)	yes	no	mild	mild	mild	mild, asymmetric	no	no	no
Pes cavus (HP:0001761)	yes	no	no	no	no	no	no	no	no
Pes planus (HP:0001763)	no	yes	yes	yes	no	no	yes	yes	no
Restrictive lung disease (HP:0002091)	yes, from 15 y	no	no	yes	no	no	no	no	no
Recurrent infections (HP:0002783)	no	no	no	no	yes	yes	yes	no	yes
Cardiac disease	abnormal septal motion and low normal ejection fraction at 27 y	no	no	no	mild to moderate pulmonic insufficiency	no	no	no	mild mitral and tricuspid insufficiency (HP:0001653)
Elevated CK (IU/L) (HP:0040081)	no (148–262)	yes (118–1,051)	yes (500–700)	yes (700–800)	no	no	yes (400–700)	no (290–376)	no

(*Continued on next page*)

Table 1. *Continued*

ID	Family A-II1	Family A-II2	Family B-II2	Family B-II3	Family C-II1	Family C-II2	Family D-II1	Family D-II3	Family E-II2
Histology	11 y	not performed	not performed	16 y	not performed	4 y	not performed	13 y	10 y
Internalized nuclei	yes	–	–	yes	–	yes	–	yes (>50% of fibers)	yes
Central cores	yes	–	–	yes	–	yes	–	yes on NADH and SDH stains	yes
Myofibrillar inclusions[a]	yes	–	–	yes	–	yes	–	EM not performed	EM not performed
Sarcomeric disorganization	yes	–	–	yes	–	yes	–	–	–
Thin filament accumulations	yes	–	–	yes	–	–	–	–	–
Nemaline rods	yes	–	–	yes	–	–	–	–	–

Abbreviations are as follows: UL, upper limb; LL, lower limb; P, proximal; D, distal; ADM, abductor digiti minimi; APB, abductor pollicus brevis; MCP, metocarpophalyngeal; VPI, velopharyngeal insufficiency; CMAP, compound muscle action potential; EMG, electromyography; NCS, nerve conduction studies; NCV, nerve conduction velocity; y, year; mo, month.
[a]Myofibrillar inclusions were positive to desmin, myotilin, alpha-actin, and αB crystallin.

has a distinctive histopathology that combines features seen in central and minicore disease, centronuclear, myofibrillar, and nemaline myopathies.

Genetic Analyses

Exome sequencing in five unrelated families identified compound heterozygous variants in *PYROXD1* (GenBank: NM_024854.3) in families A, C, and E and the same homozygous recessive missense variant in consanguineous Turkish families B and D (Figures 1A and 3). Sanger sequencing confirmed all variants and familial segregation was consistent with autosomal-recessive inheritance. DNA was not available for D-II2 or D-II4.

In family A, a paternally inherited essential splice site variant, c.285+1G>A (chr12: g.21598401G>A), was identified. The variant is found at low frequency in the heterozygous state in the Exome Aggregation Consortium (ExAC) database (allele frequency 4.295×10^{-5}).[27] cDNA analysis performed on muscle from A-II1 (not shown) and fibroblasts from A-II1 and A-II2 (Figure 1D) confirmed disruption of the donor splice site, with in-frame skipping of exon 3 a common consequence of the splice variant (Figure 1D, left gel, approximately equal levels of normal splicing [upper band] and exon 3 skipping [lower band]). PCR using exon 1 forward and intron 3 reverse primers did not provide evidence for increased frequency of exon 3 extension in family A relative to control fibroblasts (not shown). A second maternally inherited missense variant, c.1116G>C (p.Gln372His; chr12: g.21615796G>C), was not found in the ExAC database.[27] In silico predictions support pathogenicity (PolyPhen-2 score 1.0 = probably damaging;[28] Provean score −4.68 = deleterious;[29] MutationTaster score 0.999 = disease causing[30]). c.1116 G>C is the terminal 3′ base of exon 10, but cDNA analyses revealed no obvious consequence for splicing (Figures 1D and 1E) and approximately equal levels of the c.1116 G>C (p.Gln372His) variant on cDNA (Figure 1E, family A; equal peak heights at position c.1116G>C are asterisked).

In families B and D, exome sequencing identified a homozygous missense variant c.464A>G (p.Asn155Ser; chr12: g.21605064A>G) in the affected siblings (B-II2 and B-II3 and D-II1 and D-II3, Figure 1A). The variant was found at very low frequency in the ExAC database and always in the heterozygous state (allele frequency 7.157×10^{-5}).[27] In silico predictions support pathogenicity (PolyPhen-2 score 1.0 = probably damaging;[28] SIFT score 0.74 = tolerated; Provean score −4.97 = deleterious;[29] MutationTaster score 0.999 = disease causing[30]).

Families C and E (Figure 1A) had compound heterozygous variants including the c.464A>G (p.Asn155Ser; chr12: g.21605064A>G) missense variant described in family B and D. In family C an essential splice site variant c.414+1G>A (chr12: g.21602626G>A) was paternally inherited. The c.414+1G>A variant is present in the heterozygous state at very low frequency in ExAC (allele frequency 4.295×10^{-5}).[27] The c.414+1G>A (chr12: g.21602626G>A) variant is predicted to disrupt the donor splice site of exon 4.[30] cDNA analysis on skin fibroblasts

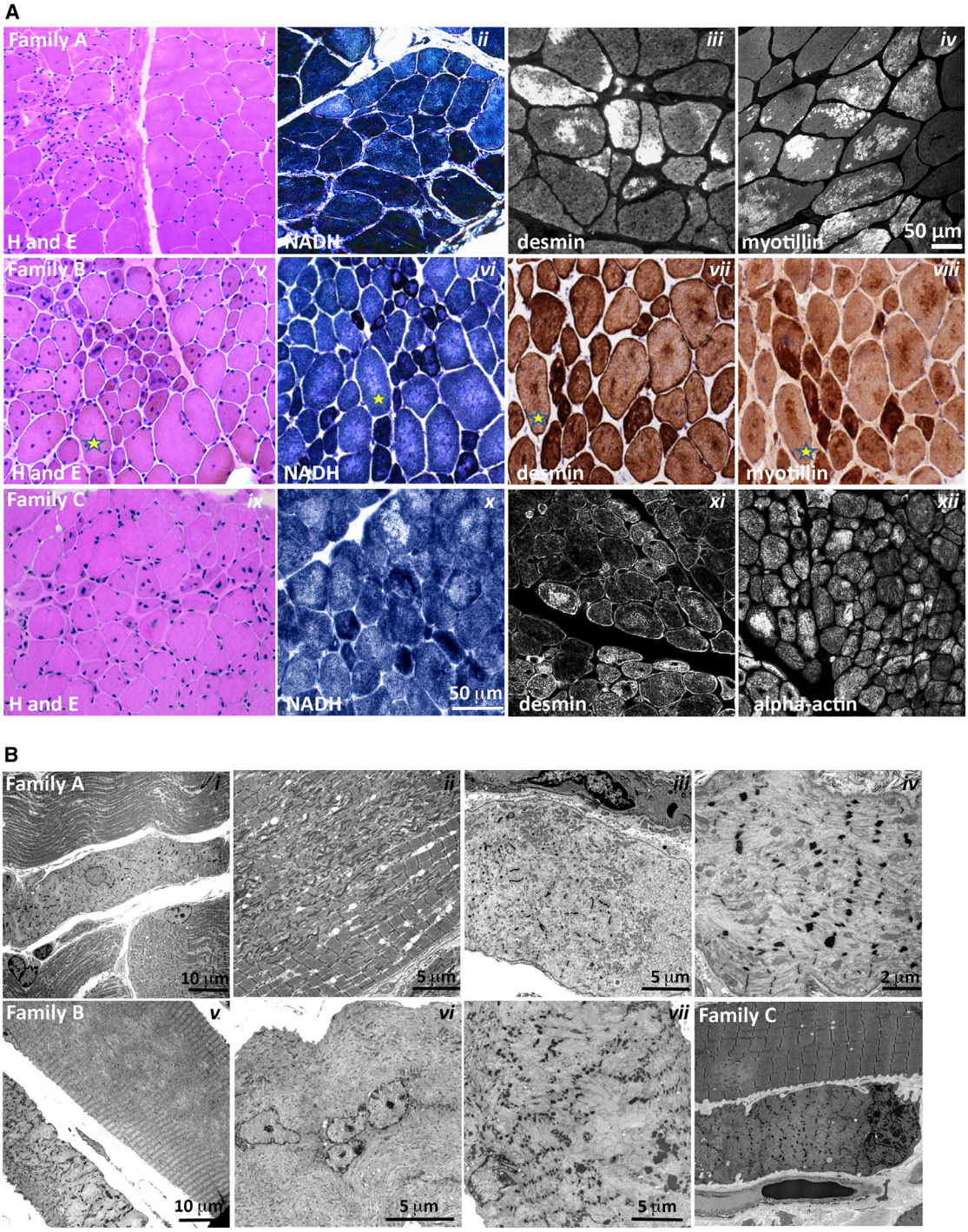

Figure 2. Histopathological Findings in PYROXD1 Myopathy

(A) Histopathological findings in skeletal muscle sections from family A (A-II1, quadriceps biopsy at 11 years of age), family B (B-II3, quadriceps biopsy at 16 years of age), and family C (C-II2, quadriceps biopsy at 4 years of age). Haemotoxylin and eosin (H&E) staining of muscle biopsy specimens from each family shows variation in fiber size, multiple internalized nuclei, and increased fibrous connective tissue. Immunofluorescent staining of skeletal muscle from A-II1 and C-II2 and immunoperoxidase staining from B-II3 demonstrate inclusions highly immunoreactive to desmin, myotillin, and alpha-actin (and αB-crystallin, not shown). H&E and immunoperoxidase images are provided via Hospital Pathology without a scale bar. Fibers in sequential sections of B-II3 are marked with a yellow star.

(B) Electron microscopy of muscle biopsy specimens. Family A: (*i*) small atrophic fiber with a central nucleus and loss of sarcomeric organization; (*ii*) large region of Z-band streaming with only occasional areas of normal sarcomeric register; and (*iii*, *iv*) atrophic fibers showing total loss of sarcomeric register, loss of thick filaments, and prominent Z-bands sometimes forming small nemaline bodies. Family B: (*v*) Large fibers show large central minicore-like regions devoid of normal myofibrillar structure and lacking mitochondria and organelles, with adjacent small fibers showing total loss of sarcomeric structure, accumulations of thin filaments, and loss of thick

(legend continued on next page)

from C-II1 and C-II2 confirmed that the c.414+1G>A splice site variant disrupts normal splicing, effecting in-frame skipping of exon 4 in a subset of transcripts (Figure 1D, right gel: normal splicing [upper gel], exon 4 skipping [lower gel]). PCR was also performed with exon 1 forward and intron 3 or intron 4 reverse primers. Family C fibroblast cDNA showed higher levels of exon 3 extension, relative to controls; no evidence for exon 4 extension was observed (not shown). Sanger sequencing of cDNA across the c.464A>G (chr12: g.21605064A>G) maternal variant showed some evidence for maternal allele bias (Figure 1E, family C, note lower peak height of the paternal c.464A relative to maternal c.464G variant, red asterisks). Collectively, our data suggest at least two outcomes from the c.414+1G>A donor splice variant; in-frame skipping of exon 4 and ectopic inclusion of intron 3 sequences that create a premature stop codon after 97 amino acids and may be subject to nonsense-mediated decay.

In family E the second variant was a heterozygous 4 bp insertion, c.1159_1160insCAAA (p.Ala387fs*13; chr12: g.21620457_21620458insCAAA), which was paternally inherited. This frameshift variant will encode a truncated protein lacking the conserved NADH-nitrile reductase domain and bearing 13 ectopic amino acids downstream of Ala387 before an early termination codon.

Families B, D, and E are Turkish. SNP markers in the region of the c.464A>G (chr12: g.21605064A>G) variant are consistent with a shared minimal confirmed haplotype between the three families of at least 348 Kb, from chr12: 21,331,987 to 21,680,609 (Table S3).

PYROXD1 Belongs to an Ancient Family of Oxidoreductases

PYROXD1 (pyridine nucleotide-disulphide oxidoreductase [PNDR] domain-containing protein 1) is classified as a class I pyridine nucleotide-disulphide oxidoreductase by neXtprot and UniProtKB. PNDRs are an ancient family of enzymes that regulate the redox state of other proteins. Unlike the five other human class I PNDRs—dihydrolipoamide dehydrogenase (DLD [MIM: 238331]), glutathione reductase (GSR [MIM: 138300]), and thioredoxin reductases 1, 2, and 3 (TXNRD1 [MIM: 601112], TXNRD2 [MIM: 606448], TXNRD3 [MIM: 606235])—PYROXD1 does not bear a consensus redox active site within the oxidoreductase domain (Gly Gly Thr Cys Val Asn Val Gly Cys in GSR and thioredoxin reductases, Gly Gly Thr Cys Leu Asn Val Gly Cys in DLD; reactive cysteine disulphide underlined). Moreover, PYROXD1 does not bear a conserved C-terminal dimerization domain identified in all other class I PNDRs, and instead bears a highly evolutionarily conserved nitrile reductase domain (69% identity and 85% similar in *Dictyostelium*). Though apparently divergent to other class I PNDRs, PYROXD1 is highly evolutionarily conserved, with 63% identity (78% similarity) of human PYROXD1 to zebrafish PYROXD1 and 39% identity (54% similarity) to *Dictyostelium* PYROXD1 (slime mold). Structural modeling of PYROXD1 using eight homologous solved crystal structures derived from other PNDRs support a predicted FAD-binding site (Figure 3B) that is vital for oxidoreductase activity of the PNDR family.[6]

The amino acids affected by the p.Gln372His and p.Asn155Ser substitutions are both highly evolutionarily conserved (Figure 3C), and removal of amino acids encoded by exon 3 (family A) or exon 4 (family C) (see Figures 3A and 3B) appears likely to significantly impact tertiary folding and abolish FAD binding and enzymatic function.

Missense Variants in Human PYROXD1 Impair Reductase Activity in Yeast

Redox activity of PYROXD1 was not previously reported, so we established a complementation assay in yeast to test the reductase activity of human PYROXD1 and the impact of identified missense variants. Replacing the yeast gene by its human counterpart is a powerful approach to help decipher the role of the human protein.[31,32] *Saccharomyces cerevisiae* has two overlapping oxidoreductase pathways, a cytoplasmic and a mitochondrial thioredoxin system, sharing some enzymes. To determine the localization of exogenous human PYROXD1 in yeast, GFP-tagged constructs were expressed in wild-type (WT) *S. cerevisiae* (Figure 3D). Fluorescent imaging of GFP-tagged PYROXD1 revealed widespread cytosolic localization, with wild-type, p.Asn155Ser, and p.Gln372His missense mutants showing similar, high expression in transformed *S. cerevisiae* by western blot (Figure 3F). Among the cytoplasmic yeast oxidoreductases, the Grl1 glutathione reductase localizes to the cytoplasm and mitochondria and is required for survival under oxidative stress.[33] Expression of non-tagged human PYROXD1 in *glr1Δ* mutant yeast that are hypersensitive to H_2O_2 due to lack of oxidoreductase activity rescued the growth defect of the *glr1Δ* mutant strain (Figure 3E), with wild-type and missense mutants showing similar, high protein levels in transformed *S. cerevisiae* by western blot (Figure 3F). Conversely, p.Asn155Ser and p.Gln372His PYROXD1 mutants failed to complement *glr1Δ* (Figure 3F). These data show that human PYROXD1 has a reductase activity that is strongly impaired by both identified missense variants.

Individuals with *PYROXD1* Variants Show Near-Normal or Reduced Levels of PYROXD1 Protein in Muscle, Fibroblasts, or Myoblasts

Western blot analysis of PYROXD1 protein levels showed a marked reduction in primary skin fibroblasts of A-II1 and

filaments; (*vi*) many large fibers have multiple internalized nuclei, often in clusters; and (*vii*) fibers show thin filament accumulations with electron-dense aggregates that resemble thickened z-lines and small nemaline bodies. Family C: (*viii*) Small atrophic fiber with loss of sarcomeric register. A large fiber shows multiple areas of Z-band streaming and a minicore-like region with absence of normal myofibrillar structure.

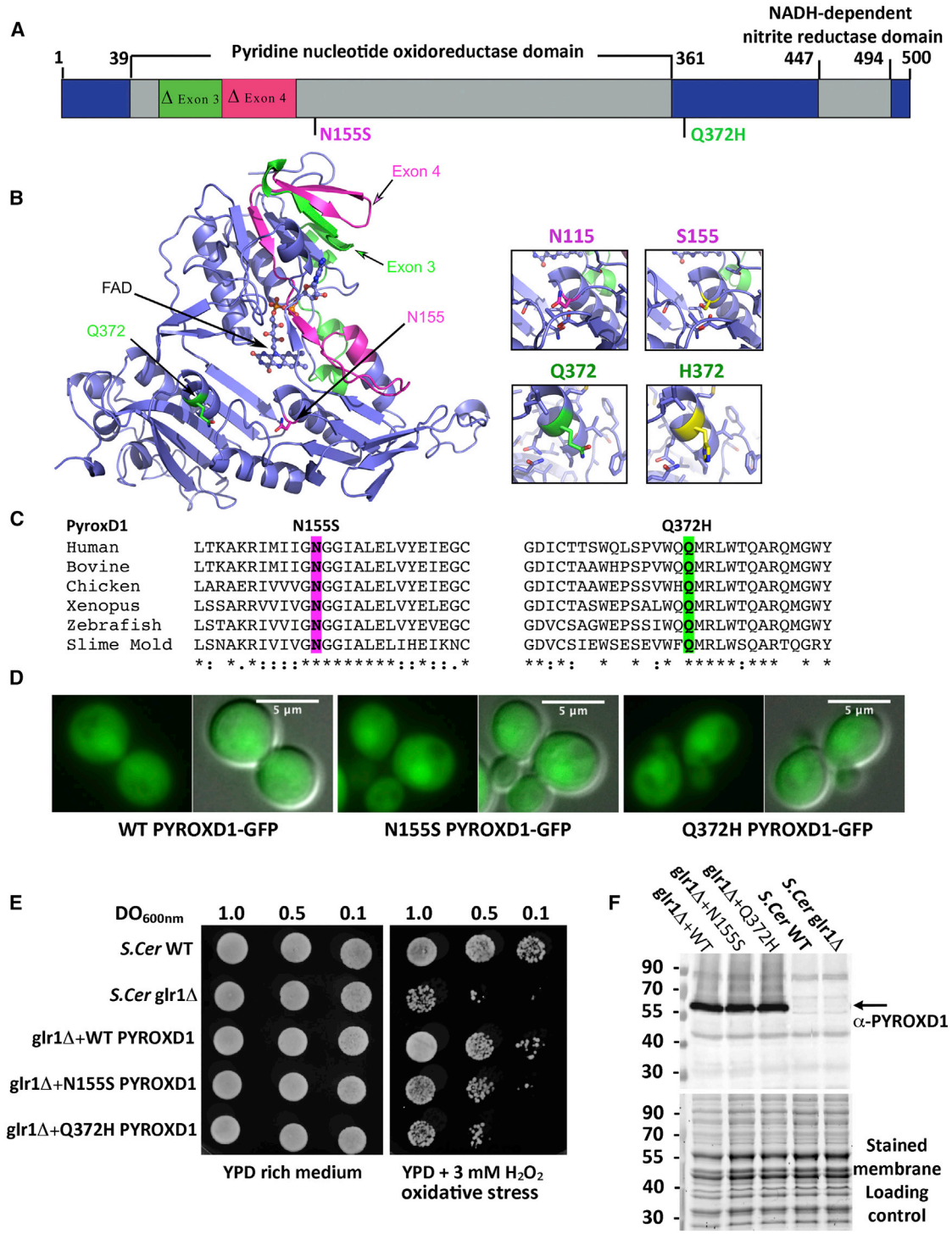

Figure 3. PYROXD1 Is an Oxidoreductase

(A) A schematic of PYROXD1 with functional domains and identified missense variants created using DOG 2.0.[35] Family A, Δexon3 and p.Gln372His (Q372H, green); families B and D, p.Asn155Ser (N155S); family C, Δexon4 and p.Asn155Ser (N155S, red).

(B) PYROXD1 homology model derived from eight homologous crystal structures (see Subjects and Methods). A co-ordinated FAD co-factor and the position of each identified variant on the crystal structure of PYROXD1 are highlighted in green (family A, Δexon3 and Q372H) and pink (family C: Δexon4 and N155S) as in (A).

(C) The identified missense variants p.Asn155Ser and p.Gln372His are evolutionarily conserved to primitive eukaryotes (Uniprot identifiers): human (Q8WU10), bovine (A7YVH9), chicken (F1NPI8), *Xenopus* (B1WAU8), *Danio rerio* (Q6PBT5), *Dictyostelium* (Q54H36).

(D) Living wild-type (WT, BY4742) yeast cells expressing human PYROXD1-GFP, PYROXD1-N155S-GFP, or PYROXD1-Q372H-GFP were observed by fluorescence microscopy with GFP filters and DIC optics. The merge represents the merge between the GFP and DIC images.

(legend continued on next page)

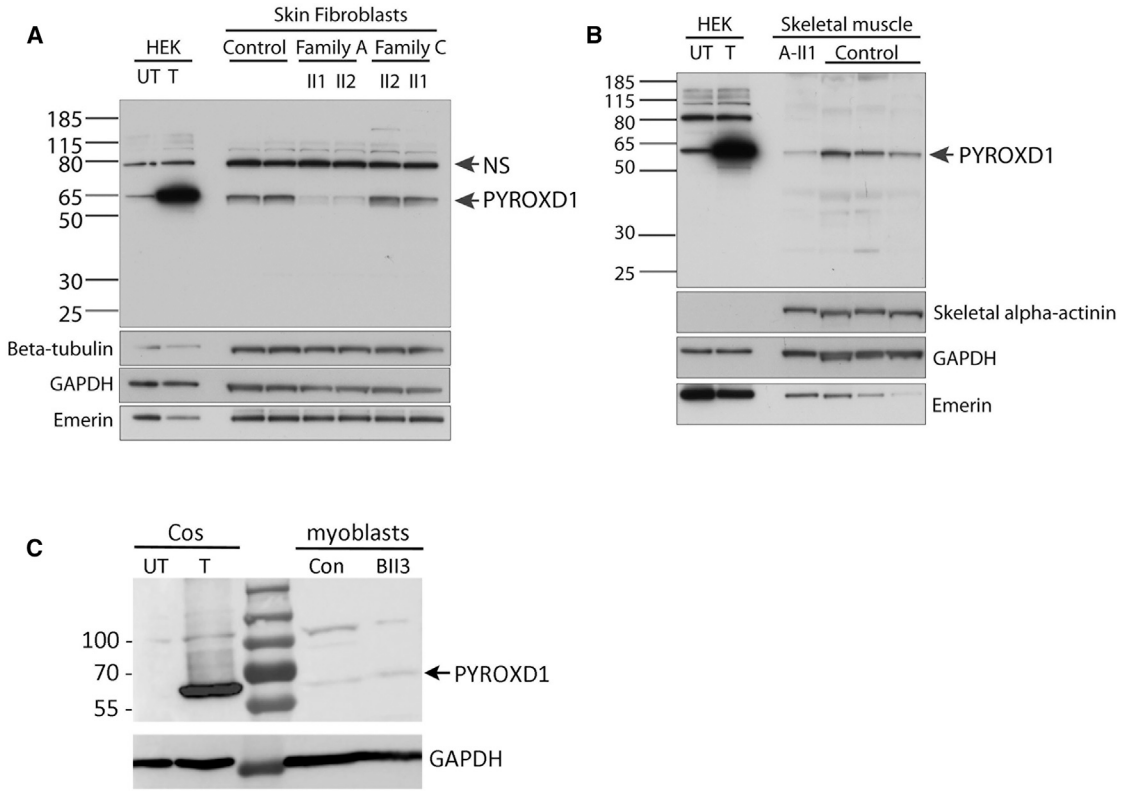

Figure 4. Affected Individuals with *PYROXD1* Variants Show Reduced or Near-Normal Levels of PYROXD1
(A) Western blot of skin fibroblasts from two controls (42 and 46 years of age) and affected siblings from family A (29 and 26 years) and family C (6 and 8 years). HEK293 cells transfected with a plasmid encoding human PYROXD1 establishes the apparent molecular weight of PYROXD1 at ~60 kDa (UT, untransfected; T, transfected). A non-specific (NS) band is indicated by an arrow. Levels of PYROXD1 are reduced in family A but not different to control levels in family C.
(B) Western blot of A-II1 triceps (11 years) (Abcam cat# ab122458; RRID: AB_11129858) shows reduced levels of PYROXD1 relative to three age-matched control biopsy specimens (quadriceps 11 years, 10 years, 15 years). Loading controls: β-tubulin and GAPDH control for overall protein content, with one cytoskeletal and one cytoplasmic marker; emerin controls for the number of nuclei; skeletal α-actinin controls for myofibrillar content.
(C) Western blot of myoblasts extracts from control subject and B-II3. Extracts from COS-1 cells transfected with the 500 aa human PYROXD1 cDNA (GenBank: NM_024854.3) was used as size control.

A-II2 (collected at 29 and 26 years of age) (Figure 4A, family A: ΔExon 3 and p.Gln372His), with no significant change in PYROXD1 levels in skin fibroblasts from C-II1 or C-II2 (8 and 6 years) (family C ΔExon 4 and p.Asn155Ser). In-frame deletion of exon 3 or exon 4 is predicted to remove 4.4 kDa or 4.7 kDa, respectively. Using two different anti-PYROXD1 antibodies (Abcam cat# ab122458 or ab204560; RRID: AB_11129858), we were unable to detect evidence for a lower molecular weight species, even with long exposures. Thus, our results suggest that in-frame deletions of exon 3 or exon 4 do not produce a stable protein. Western blot analyses of skeletal muscle specimens from A-II1 (collected at 11 years of age) similarly demonstrate reduced levels of PYROXD1 (Figure 4B), consistent with results in skin fibroblasts. Western blot analysis of family B (B-II3) cultured myoblasts detected low levels of PYROXD1 that did not appear altered compared to control (Figure 4C). Together, our data indicate that the splice variants lead to unstable proteins that are not detected by western blot, PYROXD1-Asn155Ser appears to have normal stability and protein levels (family B and C), whereas PYROXD1-Gln372His is detected at reduced levels (family A).

PYROXD1 Is a Nuclear-Cytoplasmic Oxidoreductase

Figure 5A demonstrates the localization of PYROXD1 in control human skeletal muscle longitudinal sections, lightly stretched (10% passive stretch) prior to fixation to facilitate resolution of thin and thick filaments. PYROXD1 protein shows a distinct nuclear localization and also

(E) Cultures of non-transformed wild-type (WT) or *glr1*Δ yeast, or *glr1*Δ yeast transformed with expression plasmids bearing wild-type, N155S-, or Q372H-PYROXD1 were spotted at the indicated concentration (OD_{600nm}) on rich (YPD) or on solid medium containing 3 mM H_2O_2. Plates were incubated at 30°C and observed after 48 hr.
(F) Western blot of non-transformed wild-type (WT) and *glr1*Δ, as well as *glr1*Δ yeast transformed with PYROXD1 expression vectors. The black arrow indicates PYROXD1 and the lower panel shows the protein-stained membrane used as loading control.

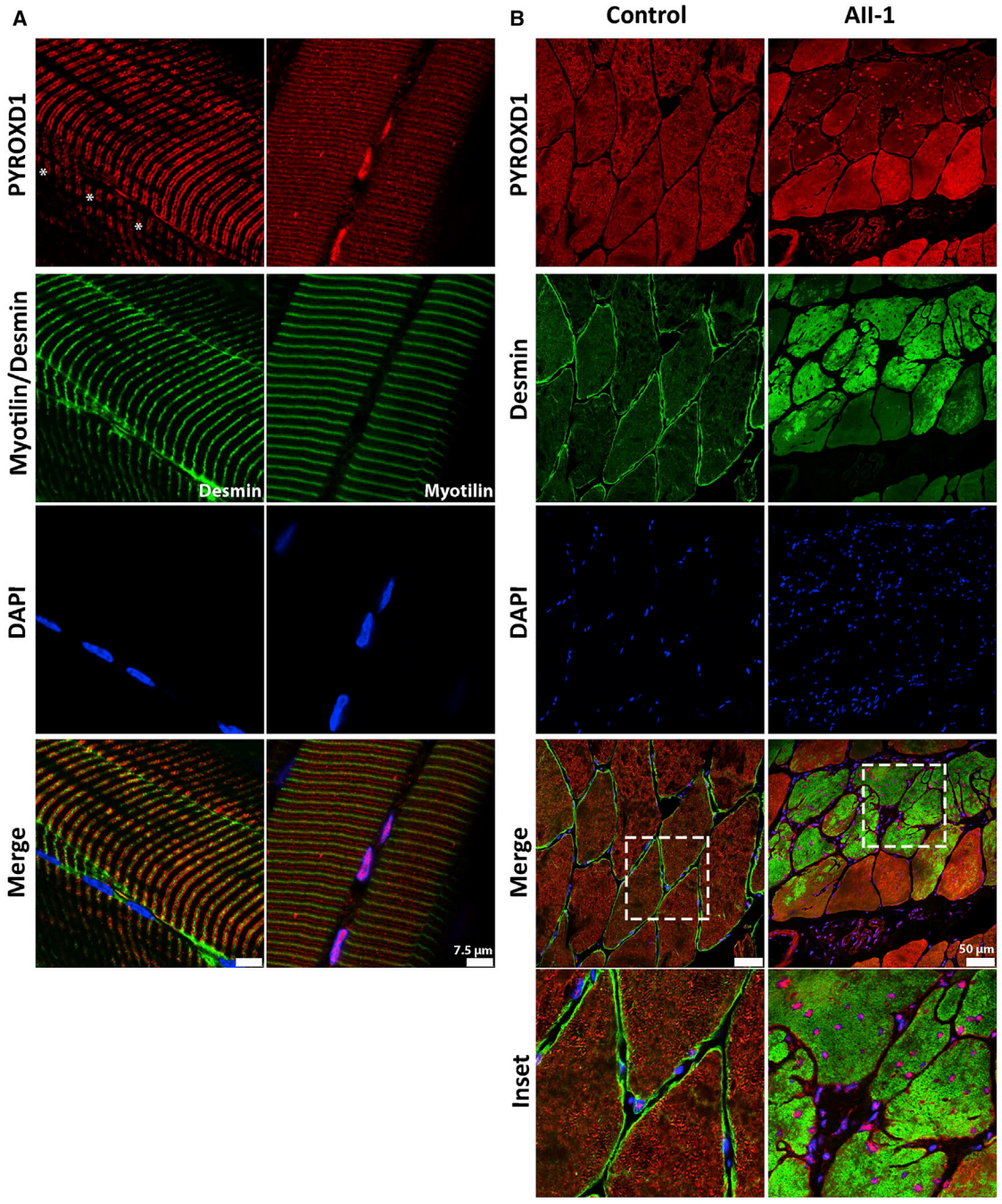

Figure 5. PYROXD1 Shows Both Nuclear and Striated Immunolocalization in Human Muscle
(A) Control stretched human skeletal (quadriceps) muscle co-stained with α-PYROXD1 (red), myotilin or desmin (green), and DAPI (blue). PYROXD1 intensely labels peripheral myonuclei, as well as showing two different patterns of striated labeling. Right: In this fiber, PYROXD1 brightly labels consecutive myonuclei and shows cytoplasmic striated labeling that aligns with desmin (Z-band region) and interdigitates between Z-bands (M-line region). Left: PYROXD1 does not brightly label myonuclei (asterisks show the position of DAPI-labeled nuclei) and shows a broader banding of striated labeling spanning the breadth of the I-band.
(B) Control and AII-1 tricep cross-sectioned human skeletal muscle co-stained with α-PYROXD1 (red), α-desmin (green), and DAPI (blue). The triceps muscle from AII-1 bears large inclusions that positively label for desmin, split fibers, and multiple internalized nuclei that brightly label for PYROXD1. Coverslips were imaged on a Leica SP5 confocal and single Z-planes are presented.

striated labeling (Figure 5A). PYROXD1 labels some peripheral nuclei more intensely than other nuclei (Figure 5A, left, asterisks show nuclei negative for PYROXD1). The sarcomeric compartment labeled by anti-PYROXD1 antibodies varied in different muscle specimens. Images presented show the two main types of striated labeling observed. The right panel of Figure 5A shows striations aligning both with the Z-band *and* interdigitating between Z-lines (near the M-band). The left panel shows a broader band of PYROXD1 labeling spanning the breadth of the

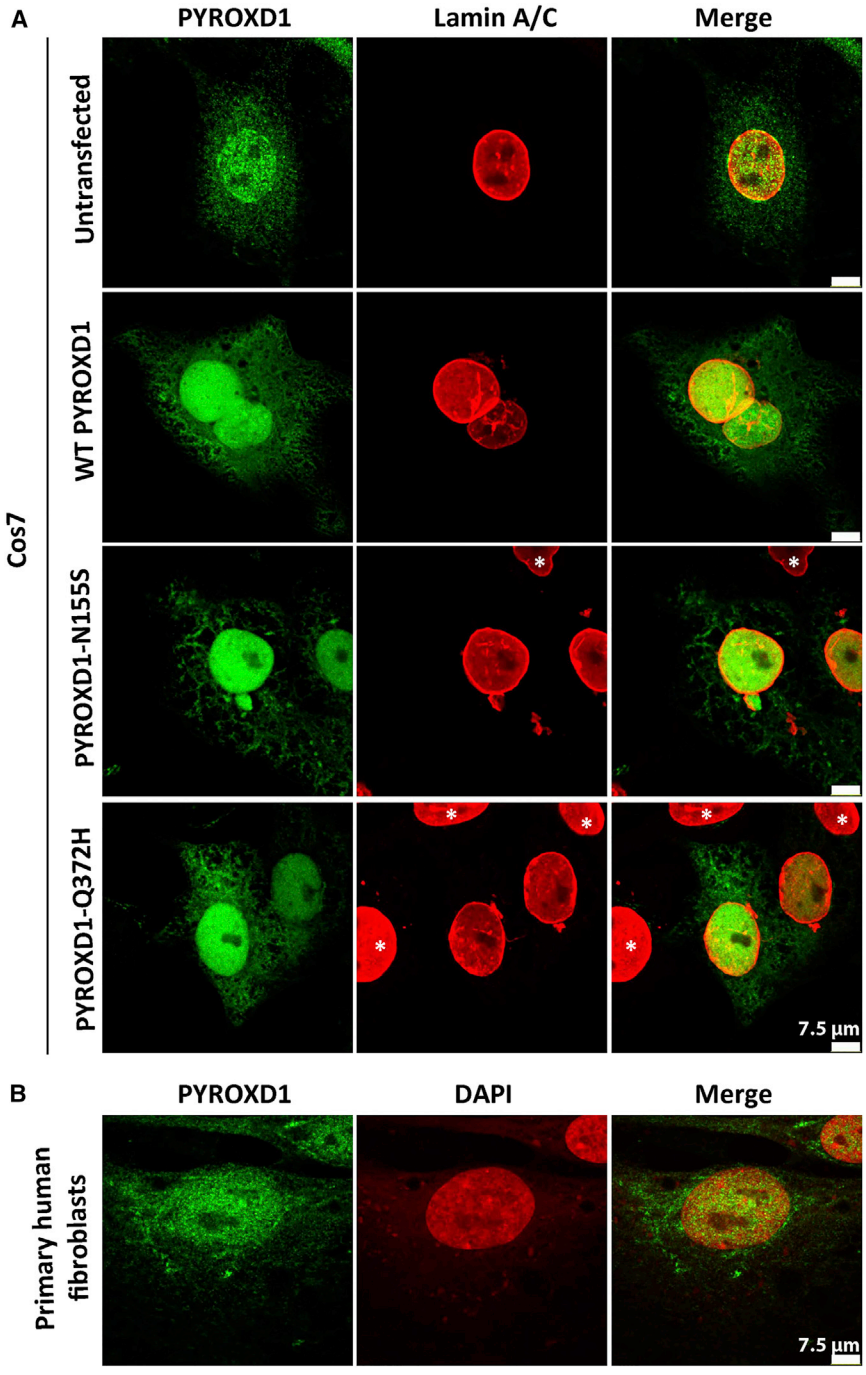

Figure 6. PYROXD1 Shows Nuclear Localization in Human Skin Fibroblasts and Transfected Cos-7 Cells

(A) Untransfected Cos-7 cells (top row) and Cos-7 cells transfected with human wild-type, p.Asn155Ser (N155S)-, or p.Gln372His (Q372H)-PYROXD1 expression constructs co-stained for PYROXD1 (green) and lamin A/C (red) shows enriched labeling for PYROXD1 within the nucleus, as well as labeling of cytoplasmic networks. For transfected Cos-7 cells (bottom three rows), asterisks demark untransfected cells within the field, with much lower levels of PyroxD1, that show very weak labeling under optimum capture conditions for transfected cells.

(B) Nuclear-cytoplasmic labeling is observed for endogenous PYROXD1 in primary human fibroblasts.

I-band. These data establish that PYROXD1 localizes to the nucleus and to sarcomeric/sarcoplasmic compartments.

Immunohistochemistry of control human skeletal muscle in cross section similarly shows dual localization of PYROXD1 in peripheral myonuclei as well as intramyofibrillar labeling throughout the contractile apparatus (Figure 5B). Levels of PYROXD1 in the triceps of A-II1 were lower relative to control muscle, and higher capture conditions are presented in order to portray key findings. As observed in the quadriceps of A-II1 (Figure 2A, *i*), the triceps muscle has large inclusions that label positively for desmin (Figure 5B, desmin, green) and multiple internalized nuclei (Figure 5B, DAPI, blue) that label positively for PYROXD1-Gln372His (Figure 5B, PYROXD1, red). Levels of cytoplasmic PYROXD1 appear brighter in myofibers *without* myofibrillar aggregates (Figure 5B, PYROXD1, red, enlarged inset). Thus, our results suggest that the equilibrium of cytoplasmic versus nuclear PYROXD1 is shifted to more predominant nuclear localization in muscle fibers burdened with myofibrillar aggregates.

Dual nuclear-cytoplasmic localization of PYROXD1 is supported by immunostaining of untransfected and transfected Cos-7 fibroblasts and primary human fibroblasts (Figure 6). Heterologous transfection of expression constructs encoding wild-type, p.Asn155Ser, or p.Gln372His PYROXD1 into Cos-7 fibroblasts showed a similar distribution of nuclear and cytoplasmic localization (Figure 6); similar patterns of staining for wild-type and PYROXD1 missense variants were also observed in transfected C2C12 myoblasts and immortalized human myoblasts (not shown). Moreover, no overt changes in PYROXD1 localization were observed in primary fibroblasts from two siblings from family A or two siblings from family C relative to fibroblasts from two age-matched controls (not shown).

PYROXD1 Shows Nuclear-Cytoplasmic Localization in Mature Zebrafish Myofibers, with Evidence for Aggregates Induced by Expression of p.Asn155Ser and p.Gln372His Mutant Constructs

To determine the localization of PYROXD1 within the skeletal muscle, we overexpressed eGFP-tagged wild-type and mutant (p.Asn155Ser and p.Gln372His) human PYROXD1 within zebrafish muscle using the muscle-specific *actc1b*

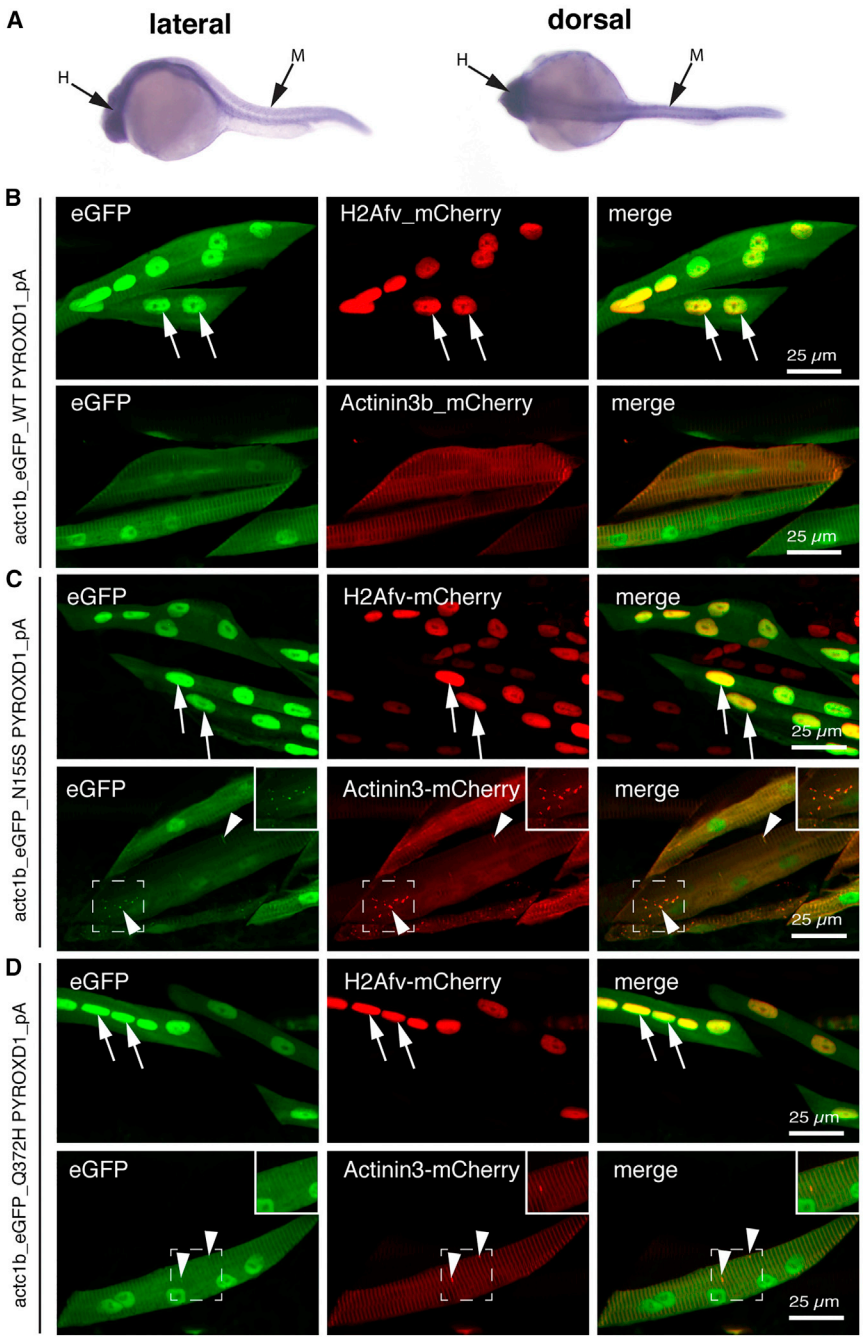

Figure 7. PYROXD1 Shows Nuclear-Cytoplasmic Localization in Zebrafish Myofibers, with Aggregates Induced by Expression of Asn155Ser and Gln372His Variants

(A) In situ hybridization on 24 hpf zebrafish shows widespread *ryroxd1* expression including the trunk musculature (M) in both lateral and dorsal views.

(B–D) Immunolabeling of vibratome-sectioned embryos 4 days post fertilization (dpf) expressing eGFP-conjugated human PYROXD1, either wild-type (B), p.Asn155Ser (C; N155S), or p.Gln372His (D; Q372H) via a muscle-specific actin promoter (*actc1b*) together with the Z-disk marker Actinin3-mCherry or nuclear marker histone H2A-mCherry. PYROXD1 localizes to myonuclei and shows striated labeling of sarcomeres. Small regions of thickening and sarcomeric disruption (arrowheads and inset) were observed after heterologous expression of N155S- or Q372H-PYROXD1, but not with wild-type PYROXD1.

promoter. All PYROXD1 constructs show dual nuclear and striated labeling aligning with the Z-disk, as evidenced by co-localization with actc1b:actinin3-mCherry and actc1b:H2Av-mCherry (Figure 7B, arrows). We also observed an occasional thickening of the Z-disk at 48 hpf when p.Asn155Ser and p.Gln372His PYROXD1 isoforms were overexpressed (Figures 7C and 7D, actinin3-mCherry arrowheads).

Zebrafish with Knockdown of RyroxD1 Show Sarcomeric Disorganization, Myofibrillar Aggregates, and a Defect in Swimming

We identified a single *PYROXD1* ortholog in zebrafish, *ryroxd1*, which is expressed throughout the developing embryo, including the skeletal muscle (Figure 7A). To study the function of Ryroxd1, we analyzed the effects of *ryroxd1* knockdown during early embryogenesis (Figure 8). Both quantitative PCR (qPCR) and western blot analyses confirm reduction of Ryroxd1 when *ryroxd1* ATG and exon2 splice morpholinos were used singularly and in combination (Figures 8A–8C).

To determine the effect of Ryroxd1 knockdown, we examined the swimming performance of the morpholino-injected embryos. Ryroxd1 single (ATG) and double (ATG and splice) morphants show a significant reduction in maximum acceleration in a touch-evoke response assay at 2 dpf compared to GFP morpholino-injected control zebrafish (Figure 8C). Co-injection of eGFP-tagged human wild-type PYROXD1 mRNA (wtPYROXD1-eGFP) with both Ryroxd1 morpholinos rescued the reduction in swim performance, demonstrating that the effect was due specifically to reduction of Ryroxd1 (Figure 9D).

Examination of zebrafish muscle through antibody labeling for Actinin2 and phalloidin shows no obvious defects in Ryroxd1 splice and ATG single morphants (Figure S1), but disrupted sarcomeric structure is evident in Ryroxd1 double morphants (Figure 8D). By 96 hpf, Actinin2 and phalloidin-positive aggregates are observed in Ryroxd1 ATG morphants (Figure S1). However, RyroxD1 double morphants show severe disruption of the musculature

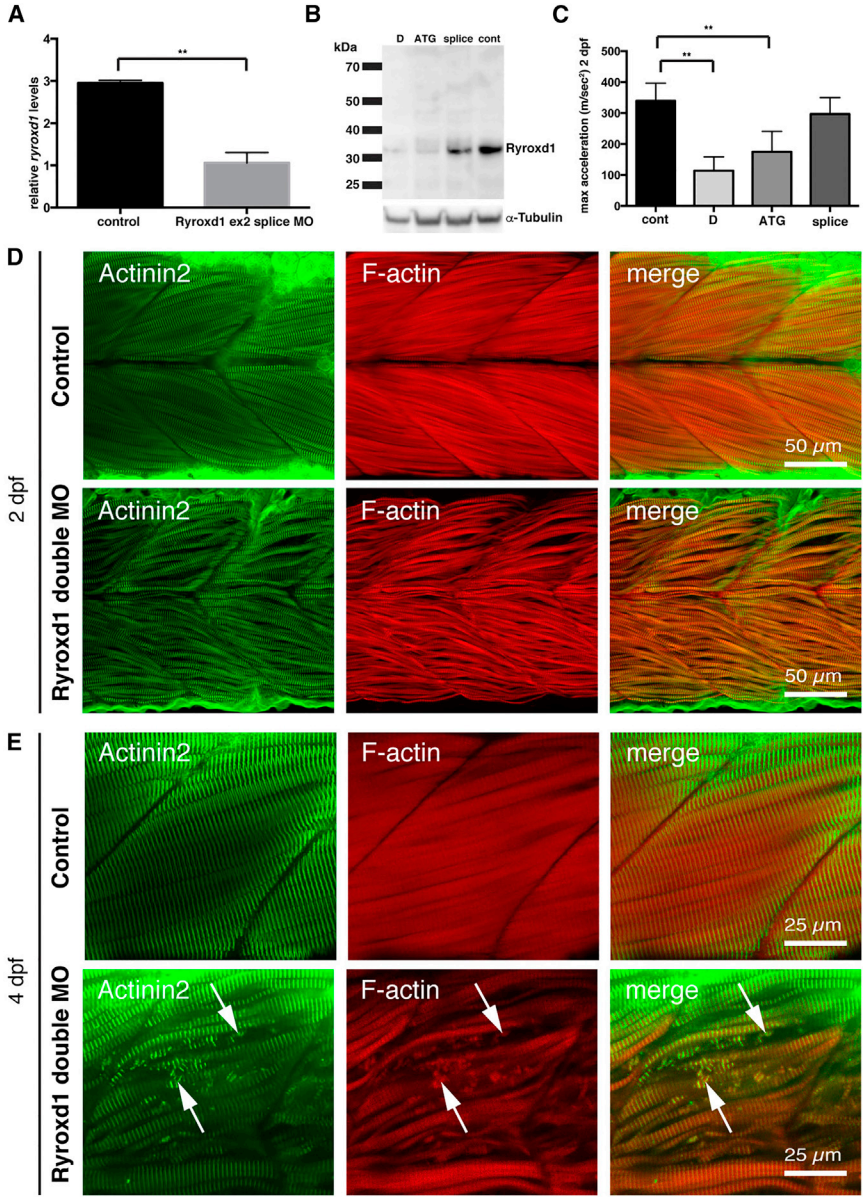

Figure 8. Zebrafish Deficient for RyroxD1 Show Sarcomeric Disorganization, Myofibrillar Aggregates, and a Defect in Swimming

(A) Quantitative PCR for *ryroxd1* mRNA levels in control (uninjected) and Ryroxd1 morpholino-injected (Ryroxd1 ex2 splice MO) zebrafish at 2 dpf.

(B) Western blot for Ryroxd1 protein and α-tubulin loading control in control (uninjected) and Ryroxd1 morpholino-injected zebrafish (D = Ryroxd1 double morpholino, ATG = Ryroxd1 ATG morpholino, and splice = Ryroxd1 splice-site targeting morpholino) at 48 hpf demonstrates effective reduction of Ryroxd1.

(C) Ryroxd1 ATG-single and ATG/splice double morphants show a significant reduction, of 48% and 73% respectively, in maximum acceleration in a touch-evoke response assay at 2 dpf compared to control zebrafish injected with a GFP targeting morpholino (Cont).

(D and E) Antibody labeling of Ryroxd1 double morphants at 48 hpf (D) and 96 hpf (E) for Actinin2 and phalloidin show disruption of muscle structure compared to uninjected controls.

(E) At 96 hpf, Ryroxd1 double morphants show severe disruption of the musculature with remnants of fragmented muscle fibers evident (arrows).

For (A) and (C), error bars represent SEM for three independent replicate experiments comprising 15 fish in each, $^{**}p < 0.01$.

with fragmentation of the muscle fibers (Figure 8E) and, in some cases, loss of fiber integrity and accumulation of actin at the myosepta (Figure 9A). Consistent with the improvement in muscle performance, the severity of structural muscle defects was significantly reduced by co-injection of Ryroxd1 double morphants with wtPYROXD1-eGFP mRNA (Figure 9A), demonstrating that the phenotype is due to reduction of Ryroxd1.

To further investigate the muscle phenotype observed in the morphant embryos, we examined the muscle structure using electron microscopy. In morphant embryos, but not uninjected controls, we observed disintegration of the myofibrils with mitochondrial infiltration of the resulting space, loss of Z-disk structures, and the formation of electron dense, nemaline-like, bodies reminiscent of those observed in the human muscle biopsies (Figure 9E).

Discussion

This publication describes the oxidoreductase function of *PYROXD1* and identifies recessive variants in *PYROXD1* as a cause of early-onset myopathy characterized histologically by a combination of multiple internalized nuclei, with large zones of sarcomeric disorganization—often devoid of mitochondria and organelles, accumulations of thin filaments, thickened Z-bands, and desmin-positive inclusions (Figure 2). All affected individuals presented in infancy or early childhood (1–8 years) with slowly progressive symmetrical weakness affecting both proximal and distal muscles, with normal to moderately elevated creatine kinase. Mild facial weakness, a high palate, nasal speech, and swallowing difficulties were typical features, mild restrictive lung disease was common, and evidence of cardiac involvement was present in the eldest individual, now aged 27. Thus, we emphasize the need for respiratory and cardiac surveillance in individuals with PYROXD1 myopathy. Nerve conduction studies in family A in the third decade showed a mild length-dependent axonal sensory neuropathy. These findings were present only in family A, so the significance is uncertain, but raises the possibility that different

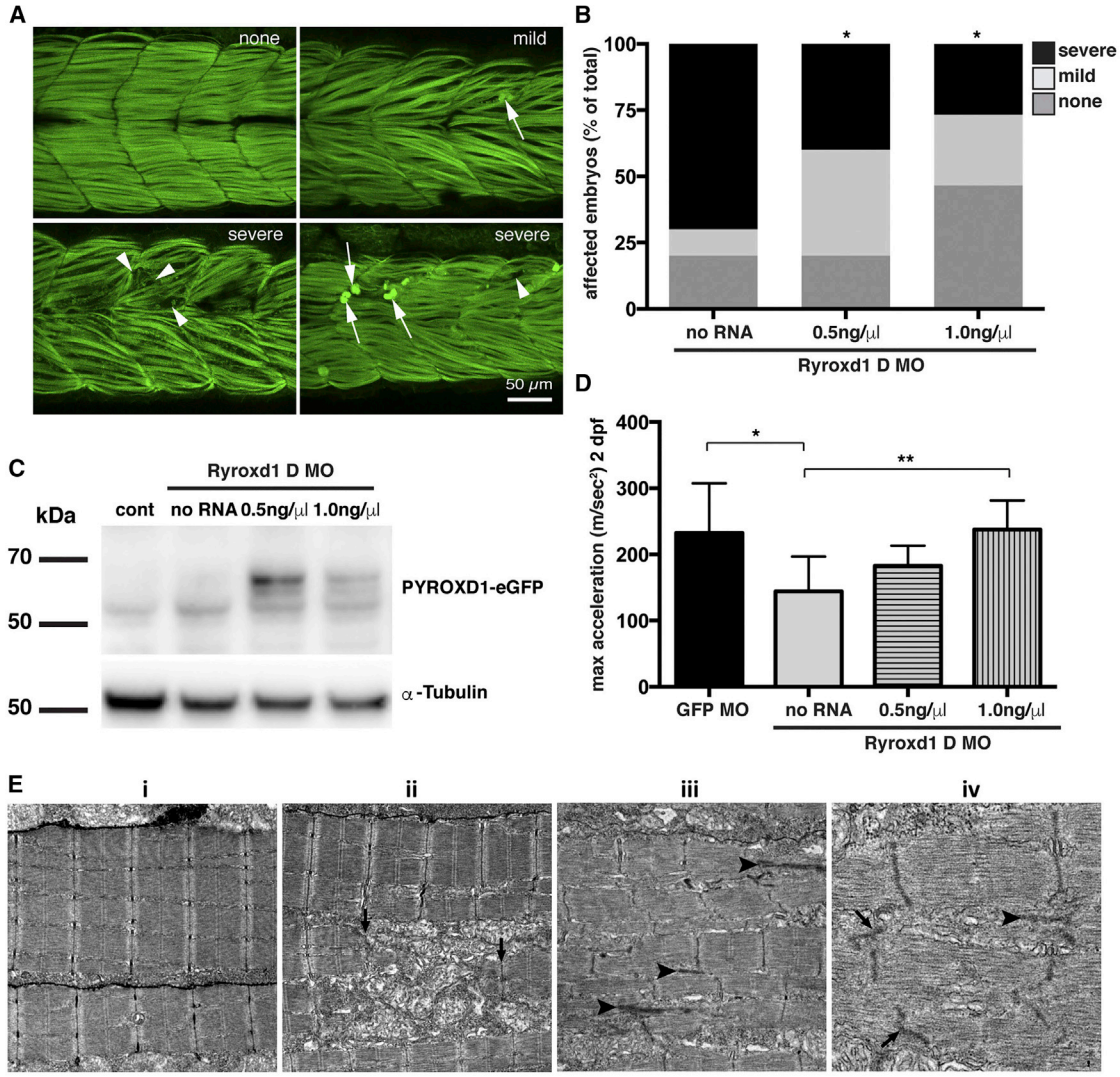

Figure 9. Human PYROXD1 Rescues Muscle Pathology and Swimming Defects in Ryroxd1 Morphants and EM of Zebrafish Muscle Pathology

(A) Representative images depicting the range of severity of muscle defects in Ryroxd1 double morphants. No obvious phenotype (none), embryos displaying occasional broken fibers and actin accumulation (mild, arrows), severe fragmentation of muscle fibers (severe, arrowheads), severe loss of fiber integrity and accumulation of actin at the myosepta (severe, arrows).

(B) Quantification of phenotypes (as in A) observed in Ryroxd1 double morphants (Ryroxd1 D MO) injected with either 0.5 ng/μL or 1.0 ng/μL wild-type (wt) wtPYROXD1-eGFP RNA compared to Ryroxd1 double morpholino injection alone (no RNA). 15–20 animals were scored per condition, *$p < 0.05$.

(C) Western blot for GFP and α-tubulin in GFP morpholino-injected control embryos (cont), Ryroxd1 double morpholino-injected zebrafish (no RNA), and Ryroxd1 double morpholino-injected zebrafish co-injected with either 0.5 ng/μL or 1.0 ng/μL wtPYROXD1-eGFP RNA, demonstrating translation of the injected mRNA.

(D) Ryroxd1 double morphants injected with human wtPYROXD1-eGFP mRNA show dose-dependent rescue in a touch-evoke response assay at 2 dpf. Ryroxd1 double morphants injected with 1.0 ng/μL human wtPYROXD1-eGFP show a 61% increase in maximum acceleration compared to Ryroxd1 double morphants (no RNA), achieving similar levels of maximum acceleration to wild-type embryos injected with a control GFP targeting morpholino (GFP MO).

(E) Electron micrograph of muscle (*i*) in a wild-type uninjected 96 hpf zebrafish embryo; examination of Ryroxd1 double morphant embryos (*ii–iv*) demonstrates myofibrillar fragmentation (*ii*, arrows) with mitochondrial infiltration, small nemaline-like bodies (*iii*, black arrowheads), and Z-disk fragmentation and loss (*iii–iv*; black arrowheads).

Scale bar represents 1 μm. Error bars represent SEM for three independent replicate experiments comprising 15 animals in each replicate experiment, *$p < 0.05$, **$p < 0.01$.

PYROXD1 variants may eventually predispose to the development of a neuropathy with increasing age.

All families identified in this study for which muscle, myoblasts, or fibroblasts were available exhibited either normal levels or reduced levels of PYROXD1; no individual showed absence of PYROXD1. Analysis of splice variants identified in *PYROXD1* in family A and family C revealed a subset of transcripts with in-frame deletion of amino acid sequences encoded by exon 3 (family A) or exon 4 (family C). However, we could not find evidence for

expression of truncated proteins, suggesting that the resulting protein products are unstable and degraded. The two substitutions p.Asn155Ser and p.Gln372His strongly impair the oxidoreductase activity of PYROXD1 in a yeast heterologous expression system. Importantly, no affected individuals described to date possess two predicted loss-of-function variants or exhibited complete loss of PYROXD1 in skin fibroblasts or skeletal muscle specimens. Thus, our findings suggest that myopathy results from partial loss of PYROXD1 function. Of note, targeted deletion of *PYROXD1* in murine models results in embryonic lethality (our own studies and confirmed by the International Mouse Phenotyping Consortium). This suggests that recessive loss-of-function variants in *PYROXD1* may result in a severe-lethal presentation in humans. Our current studies are defining the tissue-specific and developmental expression of PYROXD1, together with determination of the consequences of PYROXD1 deficiency, using a PYROXD1 conditional knock-out and LacZ reporter mouse-model.

PYROXD1 mRNA is ubiquitously expressed at low levels (GTex Portal). *PYROXD1* is highly evolutionarily conserved to unicellular eukaryotes, with functional FAD-dependent oxidoreductase and NADH-dependent nitrile reductase domains present in prokaryotic enzymes. Thus, PYROXD1 has an ancient biology not yet understood. In contrast to PYROXD1, the five other class I PNDRs are well characterized and play significant roles in regulation of cellular redox: glutathione reductase (*GSR*), thioredoxin reductases 1, 2, and 3 (*TXNRD1*, *TXNRD2*, and *TXNRD3*), and mitochondrial dihydrolipoyl dehydrogenase (*DLD*).[6] Recessive variants in *DLD* cause dihydrolipoamide dehydrogenase deficiency (DLDD [MIM: 246900]), a metabolic disorder characterized by lactic acidosis and neurological dysfunction. Dihydrolipoamide dehydrogenase is the E3 component of several vital mitochondrial enzyme complexes, including pyruvate dehydrogenase and ketoglutarate dehydrogenase, affecting oxidative metabolism via both the citric acid cycle and fatty acid biosynthesis.[6]

In addition to the reducing capabilities of their enzyme co-factors (FAD and NAD), PNDRs typically bear an intrinsic "redox active site" that catalyzes the final step to reduce their substrate, most commonly a conserved redox-reactive disulphide motif. Many PNDRs form enzymatic homodimers via a C-terminal conserved motif and are grouped into two classes (class 1 and class 2), according to characteristics related to nucleotide and flavin binding sites, the type of non-flavin redox active site, and the structural features of their dimer interface.[34] Although PYROXD1 is classified as a class 1 PNDR, it does not contain a conserved redox active disulphide within the oxidoreductase domain, nor a classical C-terminal dimerization motif, and thus appears a divergent member of the class I PNDR family.

Importantly, using a heterologous complementation assay in yeast, we showed that human PYROXD1 exhibits a reductase activity that can rescue the H_2O_2 sensitivity of yeast cells lacking the glutathione reductase *glr1*. As the two missense variants impair this activity, it supports that the myopathy observed in affected individuals arises, at least in part, from a defect in oxidoreductase activity. Future work will need to identify what are the substrate(s) of PYROXD1 to better understand the pathophysiology.

Immunolocalization studies in human skeletal muscle, skin fibroblasts, and zebrafish myofibers show that PYROXD1 localizes to both the nucleus and cytoplasmic/sarcomeric compartments. Knockdown of the zebrafish ortholog Ryroxd1 produced embryos with abnormal musculature and marked sarcomeric disorganization within individual myofibrils, including Z-disk loss and fragmentation and the presence of electron-dense bodies, reminiscent of findings observed in human muscle biopsies. In addition to the pathological features observed, Ryroxd1 morphants also performed poorly in a touch-evoked swim assay, consistent with impaired muscle function.

In summary, we describe PYROXD1 as a nuclear-cytoplasmic oxidoreductase conserved through evolution and important for human skeletal muscle biology. Recessive variants in *PYROXD1* cause an early-onset myopathy characterized by slowly progressive limb and facial weakness, nasal speech, and swallowing difficulties. PYROXD1 myopathy histopathology is distinctive in that it combines multiple pathological hallmarks characteristic of different myopathies: central core and minicore disease, centronuclear, myofibrillar, and nemaline myopathies. Although one or two of these histopathological features can often exist in combination, it is rare to observe core-like zones, multiple internal nuclei, extensive myofibrillar disorganization, myofibrillar accumulations, and small nemaline-like bodies all within a single biopsy specimen. Thus, our discovery of PYROXD1 myopathy introduces altered redox regulation as a primary disease mechanism in congenital myopathy and raises the provocative possibility that several pathological endpoints in the myopathies may be linked ultimately to altered cellular redox.

Supplemental Data

Supplemental Data include five case reports, one figure, and three tables and can be found with this article online at http://dx.doi.org/10.1016/j.ajhg.2016.09.005.

Acknowledgments

This study was supported by the following funding: The Australian National Health and Medical Research Council (NHMRC) 1080587 (S.T.C., N.F.C., D.G.M., K.N.N., R.B.R., K.J.N., N.G.L.), 1022707 and 1031893 (K.N.N., N.F.C., and N.G.L.), 1048816 (S.T.C.), and 1056285 (G.L.O.), Muscular Dystrophy New South Wales (G.L.O.), Royal Australasian College of Physicians (G.L.O.), Australian Research Council FT100100734 (K.J.N.), National Human Genome Research Institute of the NIH (D.G.M., Medical Sequencing Program grant U54 HG003067 to the Broad Institute principal investigator, Lander), Division of Intramural

Research of the National Institutes of Neurological Disorders and Stroke, France Génomique National infrastructure grant Investissements d'Avenir and Agence Nationale pour la Recherche (ANR-10-INBS-09 and ANR-11-BSV1-026), Fondation Maladies Rares "Myocapture" sequencing project, Association Française contre les Myopathies (AFM-15352 and AFM-16551), Muscular Dystrophy Association (MDA-186985), Myotubular Trust and IDEX-Université de Strasbourg PhD fellowship (M.S.-V.), and intramural funds of the NINDS/NIH (C.G.B. and S.D.).

We thank Sarah Sandaradura for recruitment and consent of family A, Meganne E. Leach for clinical review of family C, Goknur Haliloglu for clinical review of family D, Xavière Lornage and Christine Kretz for help with experiments for family B, Pierre Bouche and Gisèle Bonne for sequence analysis in family B, Roberto Silva Rojas for help with yeast experiments, and Maud Beuvin, Guy Brochier, and Dr. Edoardo Malfatti from the Morphological Unit of the Myology Institute (Paris).

Received: April 27, 2016
Accepted: September 7, 2016
Published: October 13, 2016

Web Resources

Clustal Omega, http://www.ebi.ac.uk/Tools/msa/clustalo/
dbSNP, http://www.ncbi.nlm.nih.gov/projects/SNP/
ExAC Browser, http://exac.broadinstitute.org/
GenBank, http://www.ncbi.nlm.nih.gov/genbank/
GeneTable of Neuromuscular Disorders, http://www.musclegenetable.fr/
GTEx Portal, http://www.gtexportal.org/home/gene/PYROXD1
Human Phenotype Ontology (HPO), http://www.human-phenotype-ontology.org/
International Mouse Phenotyping Consortium, http://www.mousephenotype.org/data/genes/MGI:2676395#section-associations
Knockout Mouse Project (KOMP) Repository, https://www.komp.org/
neXtprot, https://www.nextprot.org/term/FA-00613/
NHLBI Exome Sequencing Project (ESP) Exome Variant Server, http://evs.gs.washington.edu/EVS/
OMIM, http://www.omim.org/
RCSB Protein Data Bank, http://www.rcsb.org/pdb/home/home.do
RRID, https://scicrunch.org/resources
seqr, https://seqr.broadinstitute.org/
Sequence Manipulation Suite, http://www.bioinformatics.org/sms2/ident_sim.html
UniProt, http://www.uniprot.org/

References

1. Nance, J.R., Dowling, J.J., Gibbs, E.M., and Bönnemann, C.G. (2012). Congenital myopathies: an update. Curr. Neurol. Neurosci. Rep. *12*, 165–174.
2. Amburgey, K., McNamara, N., Bennett, L.R., McCormick, M.E., Acsadi, G., and Dowling, J.J. (2011). Prevalence of congenital myopathies in a representative pediatric united states population. Ann. Neurol. *70*, 662–665.
3. Chae, J.H., Vasta, V., Cho, A., Lim, B.C., Zhang, Q., Eun, S.H., and Hahn, S.H. (2015). Utility of next generation sequencing in genetic diagnosis of early onset neuromuscular disorders. J. Med. Genet. *52*, 208–216.
4. Ng, S.B., Buckingham, K.J., Lee, C., Bigham, A.W., Tabor, H.K., Dent, K.M., Huff, C.D., Shannon, P.T., Jabs, E.W., Nickerson, D.A., et al. (2010). Exome sequencing identifies the cause of a mendelian disorder. Nat. Genet. *42*, 30–35.
5. Ng, S.B., Nickerson, D.A., Bamshad, M.J., and Shendure, J. (2010). Massively parallel sequencing and rare disease. Hum. Mol. Genet. *19* (R2), R119–R124.
6. Argyrou, A., and Blanchard, J.S. (2004). Flavoprotein disulfide reductases: advances in chemistry and function. In Progress in Nucleic Acid Research and Molecular Biology (Academic Press), pp. 89–142.
7. Ghaoui, R., Cooper, S.T., Lek, M., Jones, K., Corbett, A., Reddel, S.W., Needham, M., Liang, C., Waddell, L.B., Nicholson, G., et al. (2015). Use of whole-exome sequencing for diagnosis of limb-girdle muscular dystrophy: outcomes and lessons learned. JAMA Neurol. *72*, 1424–1432.
8. Geoffroy, V., Pizot, C., Redin, C., Piton, A., Vasli, N., Stoetzel, C., Blavier, A., Laporte, J., and Muller, J. (2015). VaRank: a simple and powerful tool for ranking genetic variants. PeerJ *3*, e796.
9. Teer, J.K., Bonnycastle, L.L., Chines, P.S., Hansen, N.F., Aoyama, N., Swift, A.J., Abaan, H.O., Albert, T.J., Margulies, E.H., Green, E.D., et al.; NISC Comparative Sequencing Program (2010). Systematic comparison of three genomic enrichment methods for massively parallel DNA sequencing. Genome Res. *20*, 1420–1431.
10. Wang, K., Li, M., and Hakonarson, H. (2010). ANNOVAR: functional annotation of genetic variants from high-throughput sequencing data. Nucleic Acids Res. *38*, e164.
11. Thompson, J.D., Higgins, D.G., and Gibson, T.J. (1994). CLUSTAL W: improving the sensitivity of progressive multiple sequence alignment through sequence weighting, position-specific gap penalties and weight matrix choice. Nucleic Acids Res. *22*, 4673–4680.
12. Dereeper, A., Audic, S., Claverie, J.-M., and Blanc, G. (2010). BLAST-EXPLORER helps you building datasets for phylogenetic analysis. BMC Evol. Biol. *10*, 8.
13. Dereeper, A., Guignon, V., Blanc, G., Audic, S., Buffet, S., Chevenet, F., Dufayard, J.-F., Guindon, S., Lefort, V., Lescot, M., et al. (2008). Phylogeny.fr: robust phylogenetic analysis for the non-specialist. Nucleic Acids Res. *36*, W465-9.
14. Webb, B., and Sali, A. (2002). Comparative protein structure modeling using MODELLER. In Current Protocols in Bioinformatics (John Wiley & Sons, Inc.).
15. Pei, J., Kim, B.-H., and Grishin, N.V. (2008). PROMALS3D: a tool for multiple protein sequence and structure alignments. Nucleic Acids Res. *36*, 2295–2300.
16. Xu, D., and Zhang, Y. (2011). Improving the physical realism and structural accuracy of protein models by a two-step atomic-level energy minimization. Biophys. J. *101*, 2525–2534.
17. Wass, M.N., Kelley, L.A., and Sternberg, M.J.E. (2010). 3DLigandSite: predicting ligand-binding sites using similar structures. Nucleic Acids Res. *38*, W469-73.
18. Yuen, M., Sandaradura, S.A., Dowling, J.J., Kostyukova, A.S., Moroz, N., Quinlan, K.G., Lehtokari, V.-L., Ravenscroft, G., Todd, E.J., Ceyhan-Birsoy, O., et al. (2014). Leiomodin-3 dysfunction results in thin filament disorganization and nemaline myopathy. J. Clin. Invest. *124*, 4693–4708.
19. Sztal, T.E., Zhao, M., Williams, C., Oorschot, V., Parslow, A.C., Giousoh, A., Yuen, M., Hall, T.E., Costin, A., Ramm, G., et al.

(2015). Zebrafish models for nemaline myopathy reveal a spectrum of nemaline bodies contributing to reduced muscle function. Acta Neuropathol. *130*, 389–406.
20. Redpath, G.M.I., Sophocleous, R.A., Turnbull, L., Whitchurch, C.B., and Cooper, S.T. (2016). Ferlins show tissue-specific expression and segregate as plasma membrane/late endosomal or trans-Golgi/recycling ferlins. Traffic *17*, 245–266.
21. Gietz, D., St Jean, A., Woods, R.A., and Schiestl, R.H. (1992). Improved method for high efficiency transformation of intact yeast cells. Nucleic Acids Res. *20*, 1425.
22. Westerfield, M. (2007). The Zebrafish Book. A Guide for the Laboratory Use of Zebrafish (*Danio rerio*), Fifth Edition (Eugene: University of Oregon Press).
23. Higashijima, S., Okamoto, H., Ueno, N., Hotta, Y., and Eguchi, G. (1997). High-frequency generation of transgenic zebrafish which reliably express GFP in whole muscles or the whole body by using promoters of zebrafish origin. Dev. Biol. *192*, 289–299.
24. Sztal, T.E., Sonntag, C., Hall, T.E., and Currie, P.D. (2012). Epistatic dissection of laminin-receptor interactions in dystrophic zebrafish muscle. Hum. Mol. Genet. *21*, 4718–4731.
25. Ruparelia, A.A., Oorschot, V., Ramm, G., and Bryson-Richardson, R.J. (2016). FLNC myofibrillar myopathy results from impaired autophagy and protein insufficiency. Hum. Mol. Genet., ddw080.
26. Ruparelia, A.A., Zhao, M., Currie, P.D., and Bryson-Richardson, R.J. (2012). Characterization and investigation of zebrafish models of filamin-related myofibrillar myopathy. Hum. Mol. Genet. *21*, 4073–4083.
27. Lek, M., Karczewski, K., Minikel, E., Samocha, K., Banks, E., Fennell, T., O'Donnell-Luria, A., Ware, J., Hill, A., Cummings, B., et al. (2015). Analysis of protein-coding genetic variation in 60,706 humans. bioRxiv http://dx.doi.org/10.1038/nature19057.
28. Adzhubei, I.A., Schmidt, S., Peshkin, L., Ramensky, V.E., Gerasimova, A., Bork, P., Kondrashov, A.S., and Sunyaev, S.R. (2010). A method and server for predicting damaging missense mutations. Nat. Methods *7*, 248–249.
29. Kumar, P., Henikoff, S., and Ng, P.C. (2009). Predicting the effects of coding non-synonymous variants on protein function using the SIFT algorithm. Nat. Protoc. *4*, 1073–1081.
30. Schwarz, J.M., Rödelsperger, C., Schuelke, M., and Seelow, D. (2010). MutationTaster evaluates disease-causing potential of sequence alterations. Nat. Methods *7*, 575–576.
31. Amoasii, L., Bertazzi, D.L., Tronchère, H., Hnia, K., Chicanne, G., Rinaldi, B., Cowling, B.S., Ferry, A., Klaholz, B., Payrastre, B., et al. (2012). Phosphatase-dead myotubularin ameliorates X-linked centronuclear myopathy phenotypes in mice. PLoS Genet. *8*, e1002965.
32. Kachroo, A.H., Laurent, J.M., Yellman, C.M., Meyer, A.G., Wilke, C.O., and Marcotte, E.M. (2015). Evolution. Systematic humanization of yeast genes reveals conserved functions and genetic modularity. Science *348*, 921–925.
33. Trotter, E.W., and Grant, C.M. (2005). Overlapping roles of the cytoplasmic and mitochondrial redox regulatory systems in the yeast *Saccharomyces cerevisiae*. Eukaryot. Cell *4*, 392–400.
34. Kuriyan, J., Krishna, T.S.R., Wong, L., Guenther, B., Pahler, A., Williams, C.H., Jr., and Model, P. (1991). Convergent evolution of similar function in two structurally divergent enzymes. Nature *352*, 172–174.
35. Liu, W., Xie, Y., Ma, J., Luo, X., Nie, P., Zuo, Z., Lahrmann, U., Zhao, Q., Zheng, Y., Zhao, Y., et al. (2015). IBS: an illustrator for the presentation and visualization of biological sequences. Bioinformatics *31*, 3359–3361.

4.2 Part B: Characterisation of the oxidoreductase PYROXD1 in health and disease

4.2.1 Results

4.2.1.1 Establishing molecular biology tools to study PYROXD1

The Pyridine nucleotide disulphide reductase (PNDR) family of redox enzymes have previously been studied with several members having a plethora of literature available on their characterisation, such as glutathione (Couto, Wood, & Barber, 2016) and thioredoxin (Mustacich & Powis, 2000) reductases. However, *PYROXD1* was previously undescribed in the published literature, and thus no validated molecular biology tools were available to enable investigations into the possible pathogenicity of *PYROXD1* variants.

Thus, we optimised three commercially available antibodies against PYROXD1, each raised using immunogens representing a different region of the PYROXD1 protein sequence (Figure 4.1). In combination, these antibodies would enable detection of each patient variant, taking into consideration the deletion of amino acids 56-95 (Δexon 3, Family A, c.285+1G>A) and amino acids 96-138 (Δexon 4, Family C, c.414+1G>A) from one allele, and the positions of the missense variants on the second allele, Q372H (c.1116G>C, Family A) and N155S (c.464A>G, Family C).

To test these antibodies for the desired experimental applications (western blotting, immunocytochemistry and immunohistochemistry) we generated expression constructs of wildtype human PYROXD1, and two patient missense variants, N155S and Q372H. We generated constructs without epitope tags to optimise western blotting, as well as GFP-PYROXD1 fusion constructs to optimise immunocytochemistry.

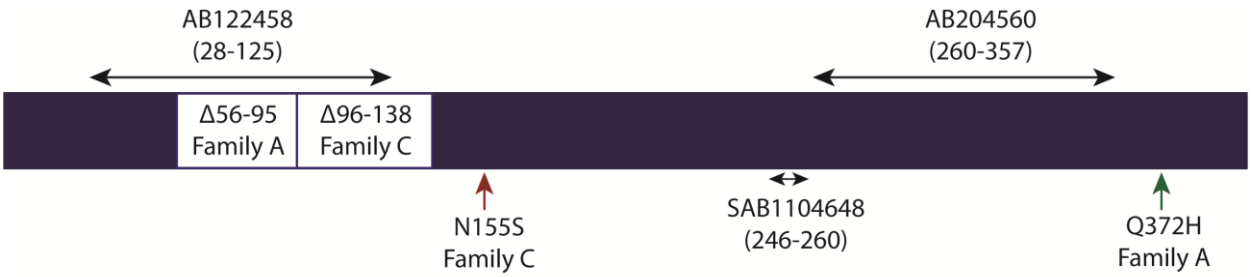

Figure 4.1: PYROXD1 antibody immunogen regions and predicted changes to patient protein indicated on the PYROXD1 protein. To-scale schematic representing the 500 amino acid human PYROXD1 (NM_024854) protein. Immunogens used to generate three commercial antibodies against human PYROXD1 are annotated with the respective antibody and amino acid span in brackets. Protein changes within Pyroxd1 patients from Family A and C are annotated.

Optimisation of Pyroxd1 antibodies for western blot

To allow optimal protein extraction we tested two solubilisation methods: Extraction with (1) RIPA buffer (RadioImmunoPrecipitation Assay) and (2) Sodium dodecyl sulphate (SDS) lysis buffer. The lysis buffer used for protein solubilisation prior to separation by SDS polyacrylamide gel electrophoresis (PAGE) is dependent on the localisation and biochemical properties of the protein. Mild extraction with RIPA is commonly used for cell and tissue protein extractions. Whereas more harsh extraction by SDS lysis buffer is required when the protein in question is a structural protein or binds to the cytoskeleton. As PYROXD1 had not been previously studied, the ideal extraction method was unknown.

We carried out protein extraction on human control skeletal muscle and primary human fibroblasts with RIPA or SDS lysis buffer (Figure 4.2). We found a light extraction with RIPA resulted in no detectable PYROXD1 from skeletal muscle and very low levels of PYROXD1 from primary human fibroblasts by western blot. Extraction with SDS better enabled detection of PYROXD1. Based on *PYROXD1* mRNA levels in GTEx (Figure 4.3), we had expected similar protein levels in fibroblasts and skeletal muscle. However, we detected higher levels of PYROXD1 in primary human fibroblasts compared to skeletal muscle despite the skeletal muscle manifestation of PYROXD1 mutations (Figure 4.3).

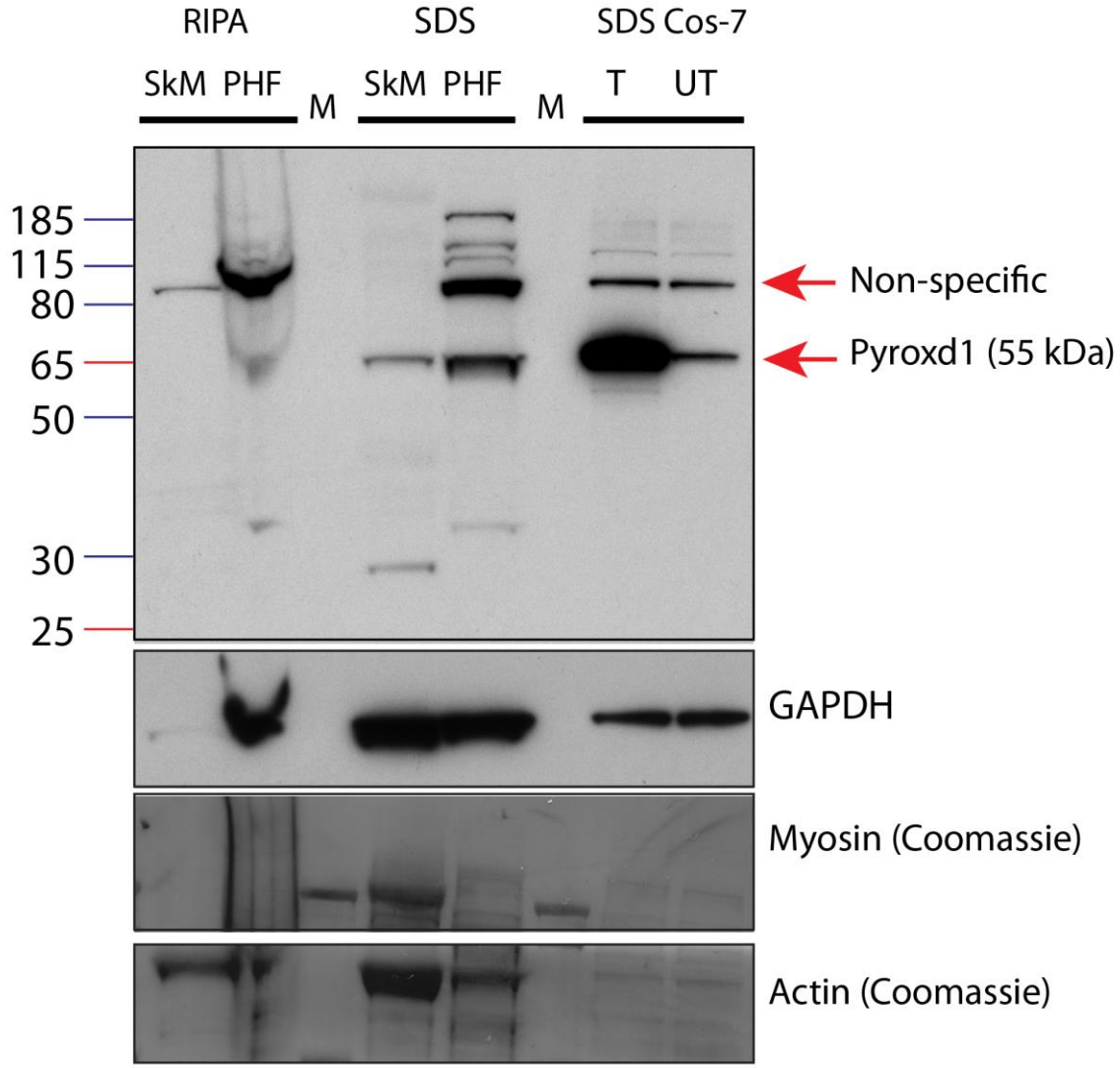

Figure 4.2: SDS lysis results in the best extraction of PYROXD1 protein from skeletal muscle and fibroblast samples. Western blot of 20 µg control human skeletal muscle (SkM), control primary human fibroblast (PHF) and 5 µg Cos-7 cell lysates with protein extracted with RIPA or SDS lysis buffer probed for PYROXD1 and GAPDH. Cos-7 cells transfected (T) with wild type human PYROXD1 extracted with SDS were used as a positive control where a protein band immunoreactive to an anti-PYROXD1 antibody (AB122458) runs at ~65 kDa and is stronger than that seen in untransfected (UT) Cos-7 cells. Skeletal muscle protein extracted with RIPA does not contain enough PYROXD1 to be detected by western blot and PYROXD1 is weakly detected in primary human fibroblasts. Skeletal muscle protein extracted with SDS lysis buffer contains enough PYROXD1 to be detected by western blot with a stronger PYROXD1 band observed in primary human fibroblasts. Coomassie of myosin and actin were used as positive controls for SDS extraction of skeletal muscle. M- Molecular weight marker.

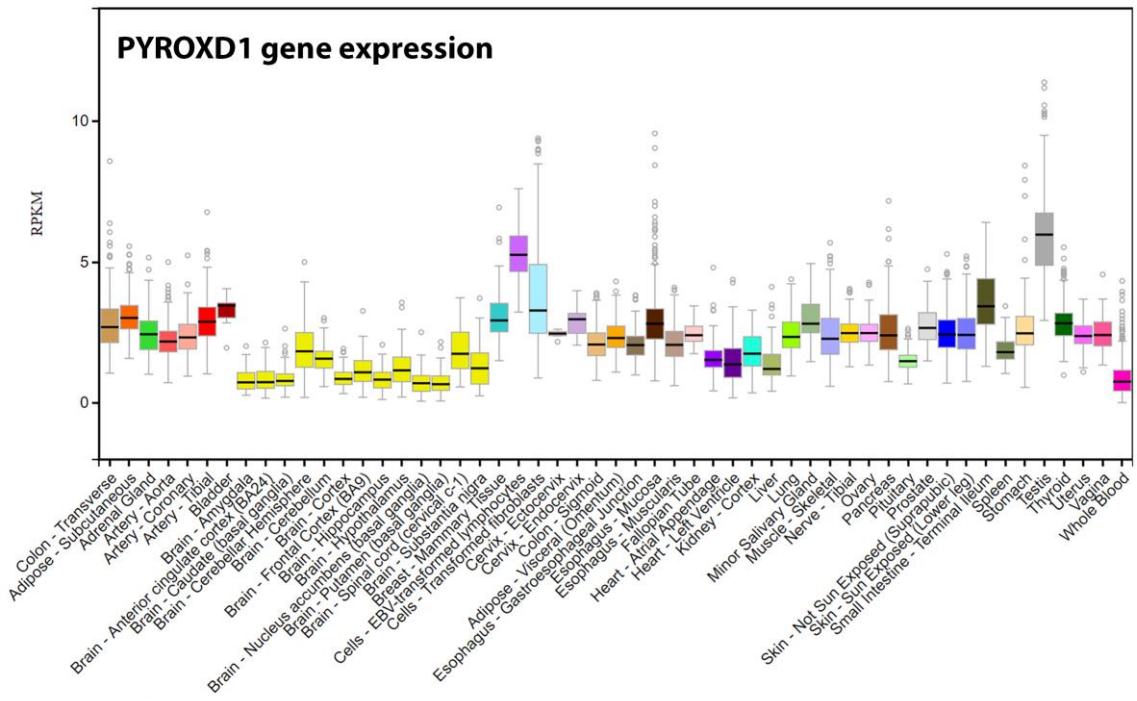

Figure 4.3: *PYROXD1* RNA is expressed ubiquitously and at low levels. *PYROXD1* RNA expression in 53 human tissues from 544 donors. *PYROXD1* RNA is detected in all 53 tissues. RPKM – Reads per kilobase per million. These images were adapted from the GTEx portal (https://www.gtexportal.org/home/).

Optimisation of Pyroxd1 antibodies for immunocytochemistry and immunohistochemistry

We utilised the GFP-fused PYROXD1 expression construct (GFP-PYROXD1) to determine localisation of PYROXD1 in transfected cells and optimise PYROXD1 antibodies for immunocytochemistry by comparing the predicted staining pattern. As PYROXD1 is predicted to be a soluble enzyme present at low levels, we were mindful that harsh permeabilisation techniques such as high concentrations of triton and saponin as well as alcohol permeabilisation might extract PYROXD1 from fixed cells, so we tested a number of permeabilisation techniques and compared the results.

Light permeabilisation: Cos-7 cells were transfected with GFP-PYROXD1, permeabilised with 0.015% saponin and stained separately with two PYROXD1 antibodies, AB122458 and SAB1104648 (Figure 4.4). GFP staining was dominantly nuclear, with lower levels of staining evident within the cytoplasm. We observed a lack of correlation between GFP fluorescence and staining from the AB122458 PYROXD1 antibody (Left panel, green arrows). Furthermore, staining of endogenous PYROXD1 (negative for GFP fluorescence) differed for each antibody. The AB122458 PYROXD1 antibody showed an intense signal in a cluster to the periphery of the nucleus (left panel, red arrow). Whereas the SAB1104648 PYROXD1 antibody showed weak cytoplasmic staining, with intense signal observed within the nucleus (Right panel, yellow arrow) and in a cluster to the periphery of the nucleus (Right panel, red arrow). While weak GFP fluorescence was observed to the periphery of the nucleus, the intensity of the signal was inconsistent with the staining intensities observed with the PYROXD1 antibodies. Permeabilisation with 0.01% triton, 0.1% triton and 0.15% saponin showed similar staining patterns (data not shown).

The lack of correlation between GFP fluorescence and PYROXD1 antibody staining seen with saponin or triton permeabilisation suggested detergent was unlikely to provide optimal

permeabilisation conditions for detection of PYROXD1. Therefore, we next tried alcohol permeabilisation.

Alcohol permeabilisation: We permeabilised Cos-7 cells transfected with GFP-PYROXD1 with methanol, acetone or methanol:acetone v:v and stained with anti-PYROXD1 AB122458 (Figure 4.5). Each condition showed good correlation between GFP-PYROXD1 fluorescence, and fluorescent labelling with anti-PYROXD1 AB122458 (and also for anti-PYROXD1 AB204560 and SAB1104648, not shown). Thus, alcohol extraction was determined to provide the best revelation of PYROXD1 immunogens for labelling. Our data also suggest, anecdotally, that PYROXD1 may not exist as a freely diffusable soluble enzyme in the nucleoplasm or cytoplasm, but is bound to other proteins or tethered to the cytoskeleton, and thus resistant to alcohol extraction.

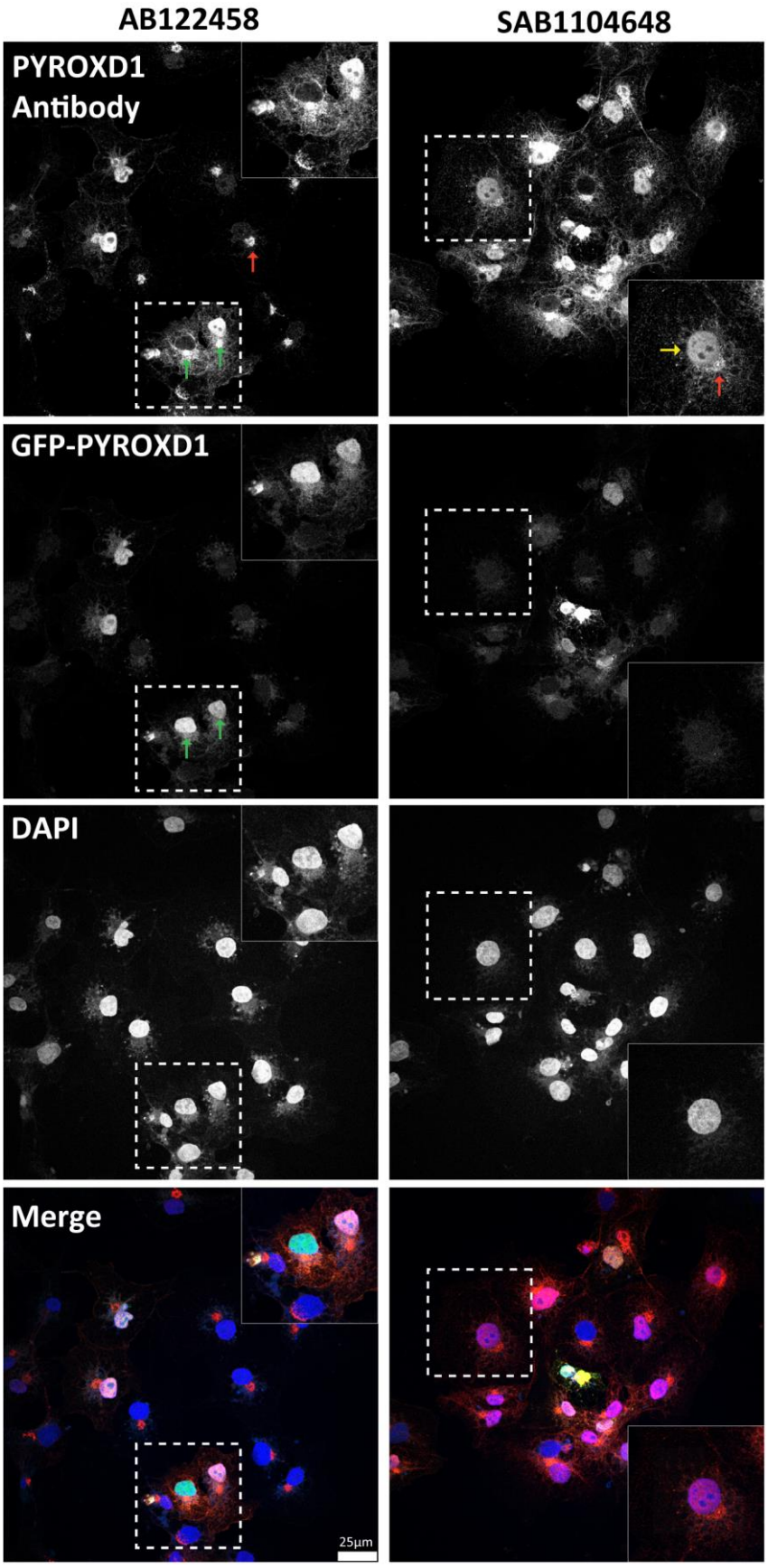
AB122458
SAB1104648
PYROXD1
Antibody
GFP-PYROXD1
DAPI
Merge
25µm

Figure 4.4: Localisation of GFP-PYROXD1 and antibody labelling differ when permeabilised with saponin. Cos-7 cells transfected with GFP-PYROXD1 stained with anti-PYROXD1 AB122458 (left panel) or SAB1104648 (right panel) and DAPI. GFP-PYROXD1 is predominately localised to the nucleus with lower levels detected in the cytoplasm. AB122458 inconsistently stains the GFP-PYROXD1 construct (Green arrows) with staining of endogenous PYROXD1 seen in cytoplasmic clusters (red arrow). SAB1104648 consistently stains the GFP-PYROXD1 construct with staining of endogenous PYROXD1 predominately localised to the nucleus (yellow arrow) and additionally, to cytoplasmic clusters (red arrow). PYROXD1 – red, GFP – green, DAPI – blue.

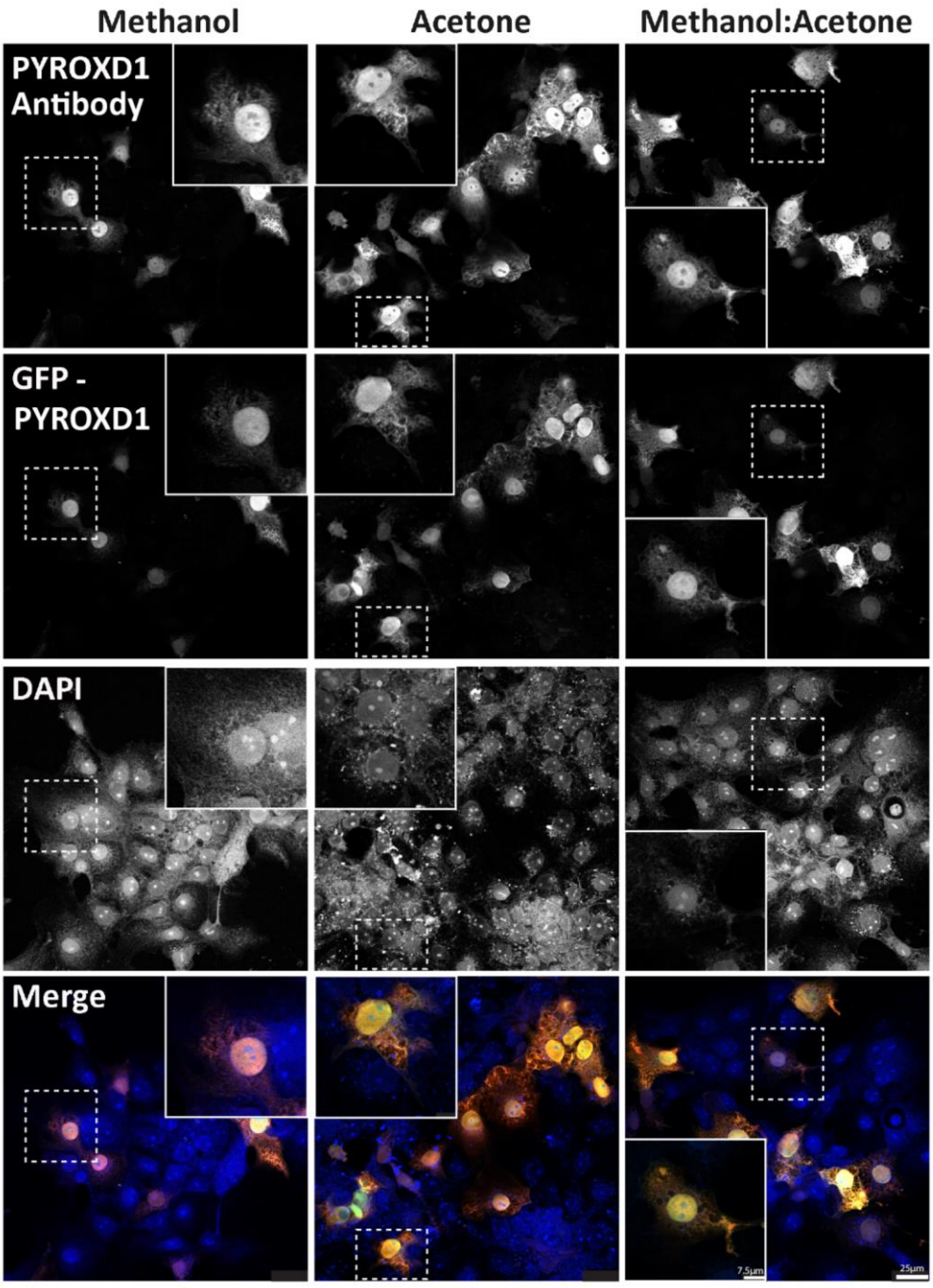

Figure 4.5: Alcohol permeabilisation results in consistent and specific detection of PYROXD1 by immunocytochemistry. Cos-7 cells transfected with GFP-PYROXD1 permeabilised with methanol (left panel), acetone (centre panel), or methanol:acetone v:v (right panel) and stained with anti-PYROXD1 AB122458. In each permeabilisation condition the PYROXD1 antibody consistently and specifically stains the GFP-PYROXD1 construct. PYROXD1 – red, GFP – green, Dapi – blue.

4.2.1.2 Cell & molecular biology and biochemistry of PYROXD1

***Nuclear localisation and export signals within* Pyroxd1**

In Figures 5A and 6 of Part A, we established PYROXD1 as a nuclear-cytoplasmic oxidoreductase. Observing that PYROXD1 localised to the nucleus in some cells, but not in all cells; results suggest PYROXD1 may dynamically shuttle between the nucleus and cytoplasm. *PYROXD1*-patient skeletal muscle showed increased PYROXD1 expression within internalised nuclei coupled with reduced cytoplasmic expression in fibres burdened with aggregates, fibre splitting and internalised nuclei (Figure 5B), in comparison to staining intensities observed in control skeletal muscle.

We used predictive programs to determine whether PYROXD1 contained nuclear localisation sequences (NLS) and nuclear export sequences (NES) (Figure 4.6). cNLS mapper (http://nls-mapper.iab.keio.ac.jp/cgi-bin/NLS_Mapper_form.cgi) discovered 8 sequences within PYROXD1 predicted to target PYROXD1 to both the nucleus and the cytoplasm (Figure 4.6A). NetNes 1.1 (http://www.cbs.dtu.dk/services/NetNES/) predicted a nuclear export sequence inclusive of leucine 476 as the hydrophobic residue. Collectively, these results support the hypothesis that PYROXD1 is a dynamic enzyme capable of translocating between the nucleus and cytoplasm. This has led to further investigations into the translocation of PYROXD1 under oxidative distress, beyond the scope of this thesis – and now the topic of investigation for another PhD student within our group.

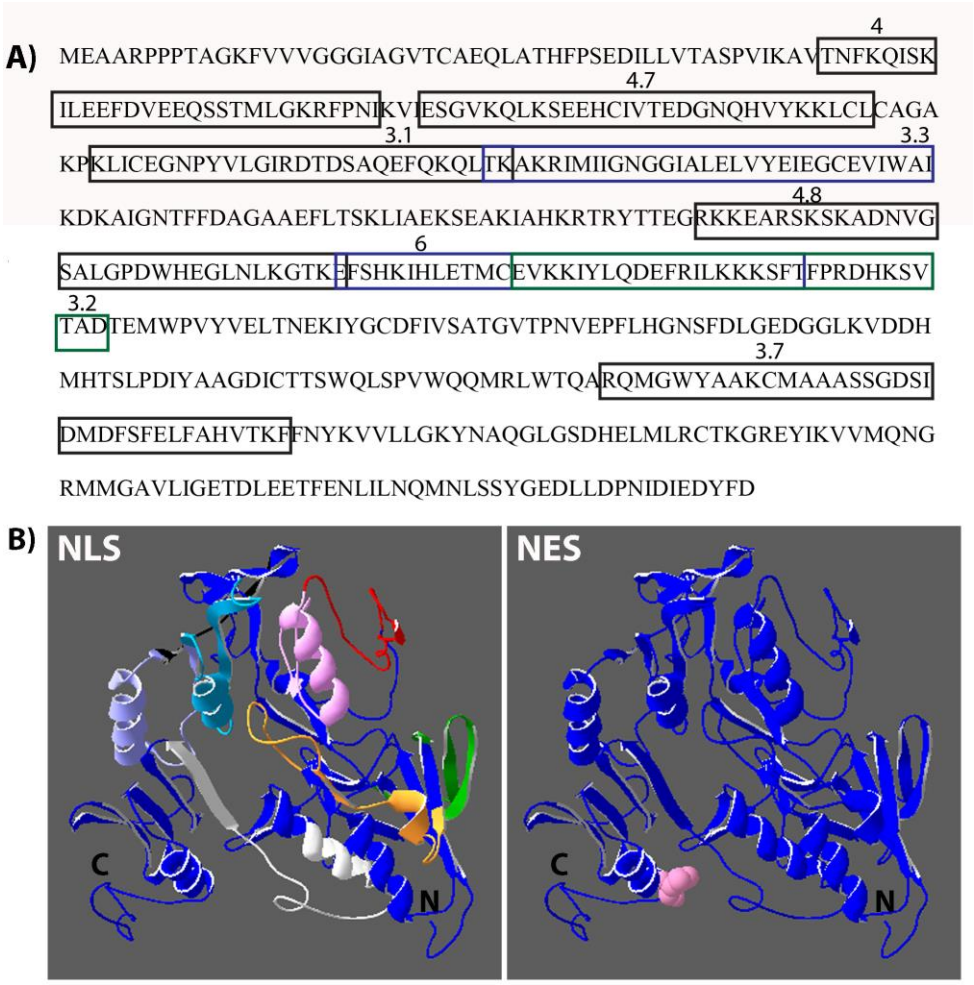

Figure 4.6: PYROXD1 contains predicted NLS and NES.

(A) Predicted NLS within human PYROXD1 predicted by cNLS Mapper and marked on the PYROXD1 (NM_024854) sequence. Scoring: The localisation of a GUS-GFP protein fused to a sequence with a score of: 1-2, cytoplasm; 3-5, nucleus and cytoplasm; 7-8 nucleus partially; 8-10, nucleus **(B)** DeepView/Swiss-Pdb viewer (v 4.1.0, http://www.expasy.org/spdbv/) was used for molecular modelling of the PYROXD1 homology model generated by A/Prof Roger Bryan Sutton. Left panel - NLS from (A) highlighted in: orange, green, pink, red, cyan, lilac, black and white from N- to C- terminal; Right panel – NES predicted by NetNes 1.1 indicated by leucine 476 highlighted in pink.

PYROXD1 protein levels within human skeletal muscle and mouse tissues

To determine PYROXD1 protein levels within skeletal muscle during development, we performed western blot of human skeletal muscle samples from a cross-section of ages. We detected a ~55 kDa PYROXD1 protein in all tested ages (14/40 weeks gestation to 58 years; Figure 4.7). We then explored PYROXD1 protein levels during *in vitro* myogenic differentiation of primary human myoblasts into myotubes. Western blot detected a ~55 kDa PYROXD1 protein in myoblasts and myotubes (day 0 - day 8 of differentiation; Figure 4.8). We also observed additional bands with the PYROXD1 AB122458 antibody which do not correspond to known isoforms. From the late perinatal period we consistently see a 32 kDa band (Figure 4.7) and in differentiating myoblasts we see an 80 kDa band (Figure 4.8) band. These bands may be isoforms, degradation products, posttranslational modification or non-specific binding of the antibody.

The GTEx database suggested ubiquitous expression of PYROXD1 mRNA (refer to Figure 4.2). To explore protein levels of PYROXD1, we performed western blot on mouse tissues and myoblasts, probing membranes with the AB122458 PYROXD1 antibody. We observed a ~55 kDa Pyroxd1 protein in mouse brain, bladder, kidney, testis, uterus, skeletal muscle (Figure 4.9, left blot, red arrow) and differentiating mouse myoblasts (right blot, red arrow).

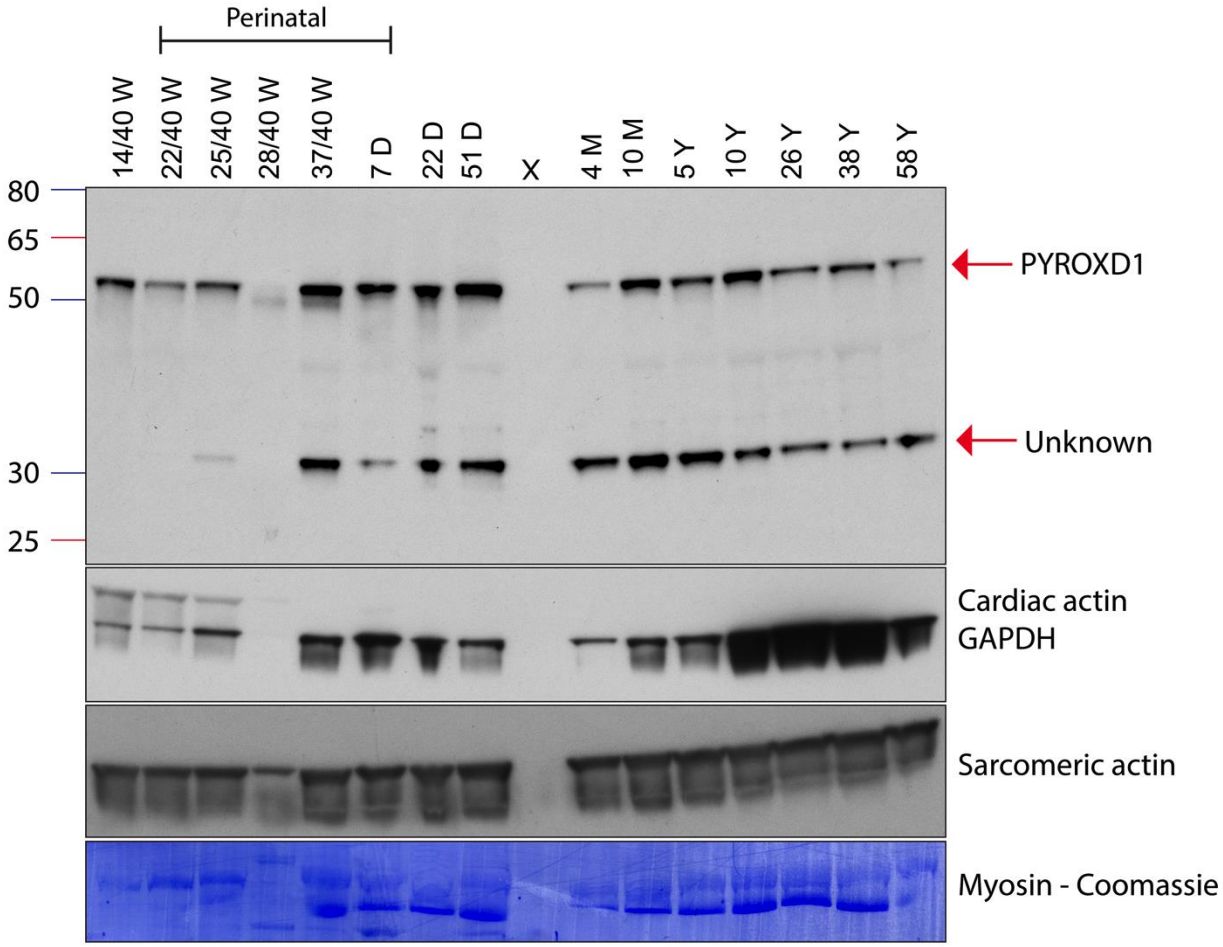

Figure 4.7: PYROXD1 is expressed throughout skeletal muscle development.

Western blot of whole human skeletal muscle lysates through development probed with an anti-PYROXD1 antibody (AB122458). PYROXD1 (55 kDa) is detected in all ages tested (14/40 weeks gestation to 58 years of age). A 32 kDa band is detected consistently from the late perinatal period, the relevance of this band is unknown. Cardiac actin was used as a control for pre-natal skeletal muscle; GAPDH was used as a loading control; sarcomeric actin and myosin were used as loading controls for skeletal muscle. W - weeks of gestation, D - days, M - months, Y – years, X-empty lane.

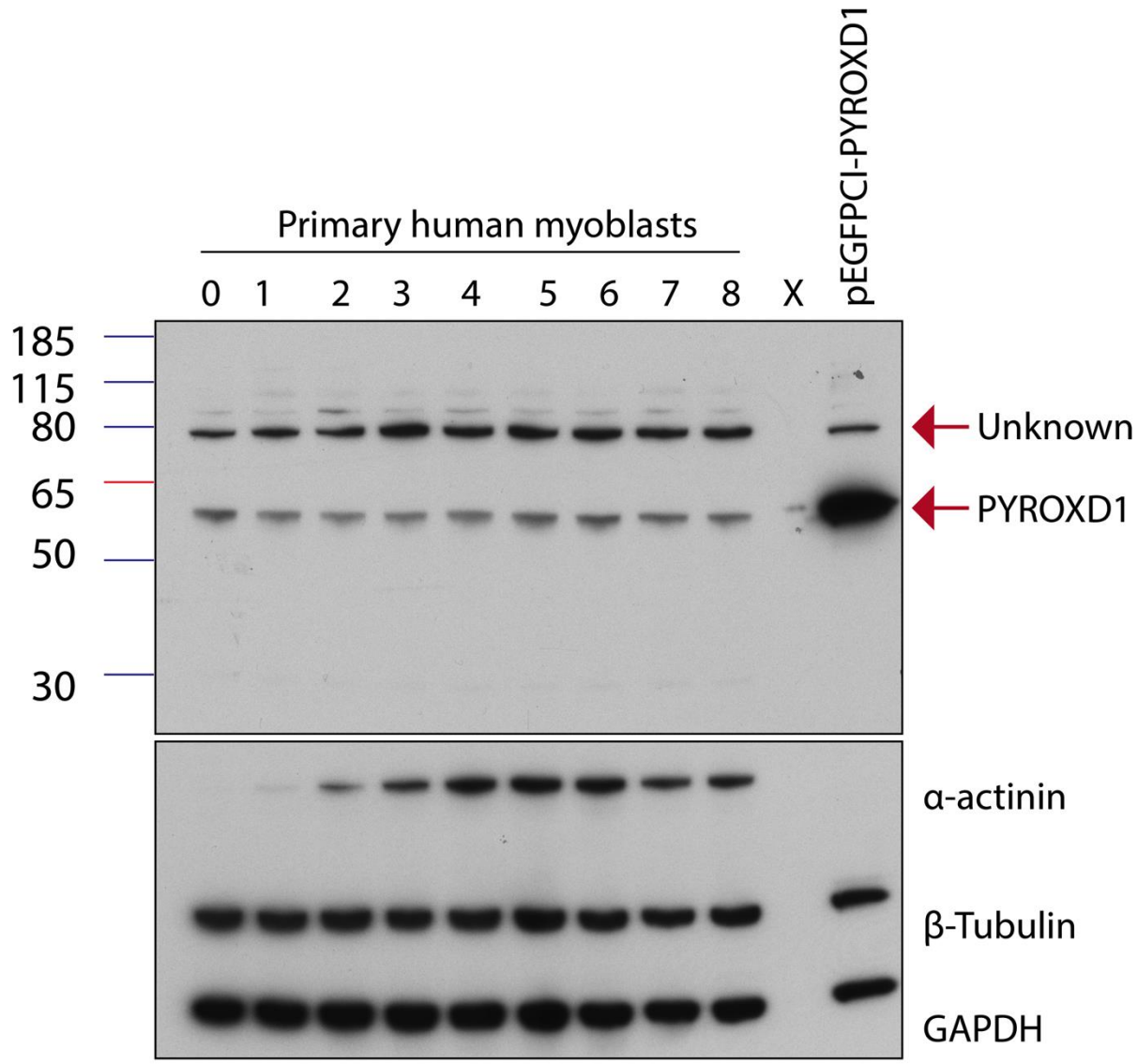

Figure 4.8: PYROXD1 is expressed consistently throughout differentiating primary human myoblasts. Western blot on whole cell lysates of primary human myoblasts differentiated for 8 days and probed for PYROXD1 (AB122458). Cell lysate from HEK293T cells transfected with EGFP-CI human PYROXD1 (untagged) was used as a positive control (55 kDa). PYROXD1 is detected consistently from day 0 to day 8 of myoblast differentiation, in comparison to the muscle protein alpha-actinin which is detected weakly from differentiation day 1 with expression increasing with differentiation age. An 80 kDa band is consistently detected in all samples, the relevance of this band is unknown. GAPDH and β-tubulin were used as loading controls. X- empty lane.

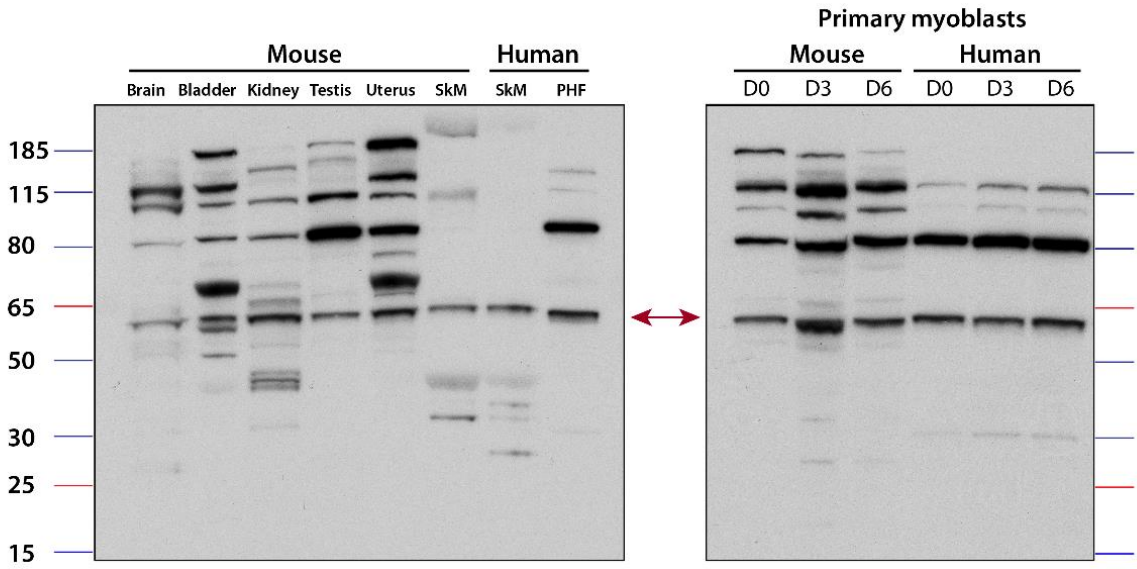

Figure 4.9: Pyroxd1 protein is detected in adult mouse tissues and differentiating mouse myoblasts. Western blot of: ***Left blot*** **-** whole tissue lysates from C57BL/6J wild type mouse brain, bladder, kidney, testis, uterus and skeletal muscle (SkM); and human skeletal muscle, primary human fibroblasts (PHF); ***Right blot*** **–** whole cell lysates from mouse and human primary myoblasts differentiated for 0, 3 and 6 days. Membranes were probed with an antibody against PYROXD1 (AB122458). Red arrow – mouse Pyroxd1/human PYROXD1.

Investigating disulphide bond formation within **PYROXD1**

Evolutionary analysis identifies PYROXD1 within a class of oxidoreductases (Class I PNDRs) which have the characteristic feature of a redox-active disulphide bond, utilised in the first electron transfer step of substrate reduction (Argyrou & Blanchard, 2004). We carried out reducing and non-reducing western blots on HEK293T cells transfected with GFP-PYROXD1 and PYROXD1 constructs. Formation of one or more intramolecular disulphide bridges between the 11 cysteines within PYROXD1 should result in a more globular secondary structure, enabling progression through the polyacrylamide gel at an apparent lower molecular weight.

GFP-PYROXD1-WT, GFP-PYROXD1-N155S and GFP-PYROXD1-Q372H constructs ran at 80 kDa (Figure 4.10B, green arrow). PYROXD1-WT, PYROXD1-N155S & PYROXD1-Q372H ran at 55 kDa (Red arrow). A non-specific band was evident at 80 kDa in all samples, and endogenous PYROXD1 at 55 kDa. When these samples were separated on a non-reducing gel (Figure 4.10B, right blot), we observe an additional lower molecular weight band at 70 kDa (green asterisks), only in samples transfected with GFP-PYROXD1. This suggests PYROXD1 forms an intramolecular disulphide bond with GFP. GFP contains two cysteines - at amino acids 49 and 71. There are two amino acids between PYROXD1 and GFP - serine and glycine. This places GFP within close proximity to PYROXD1, making a disulphide bond with one of the 11 cysteines within PYROXD1 a possibility. However, we could find no evidence supporting the existence of a covalent intramolecular disulphide within PYROXD1 itself.

We also carried out reducing and non-reducing western blots on primary human fibroblasts from controls and patients of Family A & C, and skeletal muscle from Family A. We observed no difference in banding patterns between reducing and non-reducing western blots (Figure 4.11B). This suggests PYROXD1 does not form intramolecular disulphide bonds with

cysteines within PYROXD1 that differ between patients and controls, detectable by this technique.

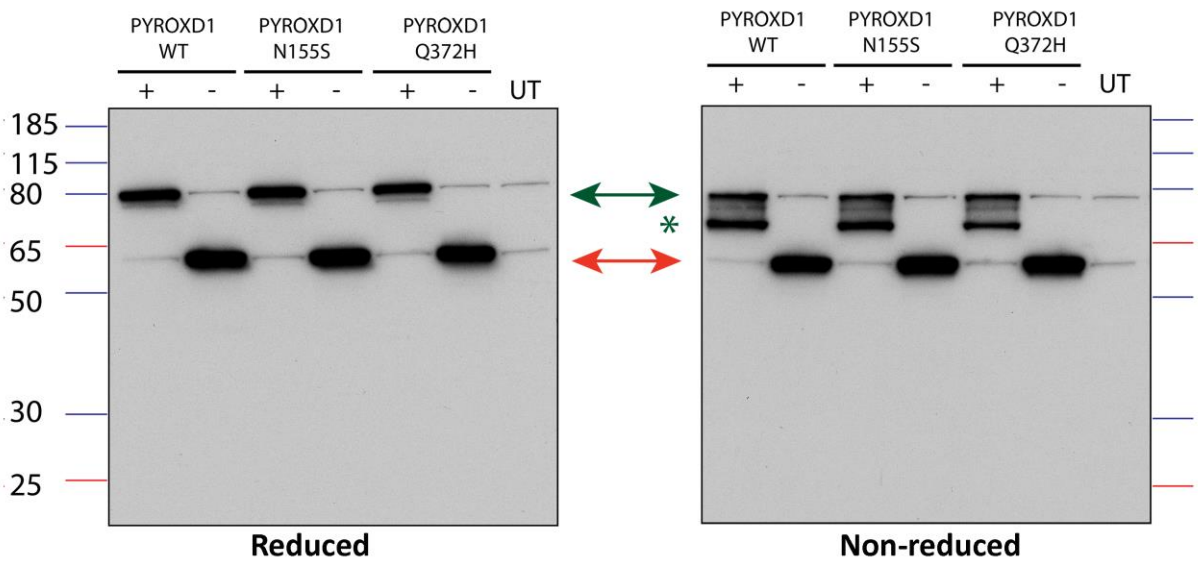

Figure 4.10: Exogenous PYROXD1 forms an intramolecular disulphide bond with N-terminally fused GFP. HEK293T cells were transfected with PYROXD1-WT, N155S or Q372H with (+) or without (-) an N-terminally fused GFP tag. Reducing (left) and non-reducing (right) western blots were carried out on cell lysates solubilised in the presence of N-Ethylmaleimide to quench free thiols and probed for PYROXD1 (AB122458). GFP-PYROXD1 constructs run at 80 kDa (green arrow) with a non-specific band at the same molecular weight seen in all remaining samples. Non-GFP fused constructs run at 55 kDa (red arrow). In the non-reducing western blot we observe a 70 kDa band (green asterisks) only in samples transfected with GFP-fused PYROXD1.

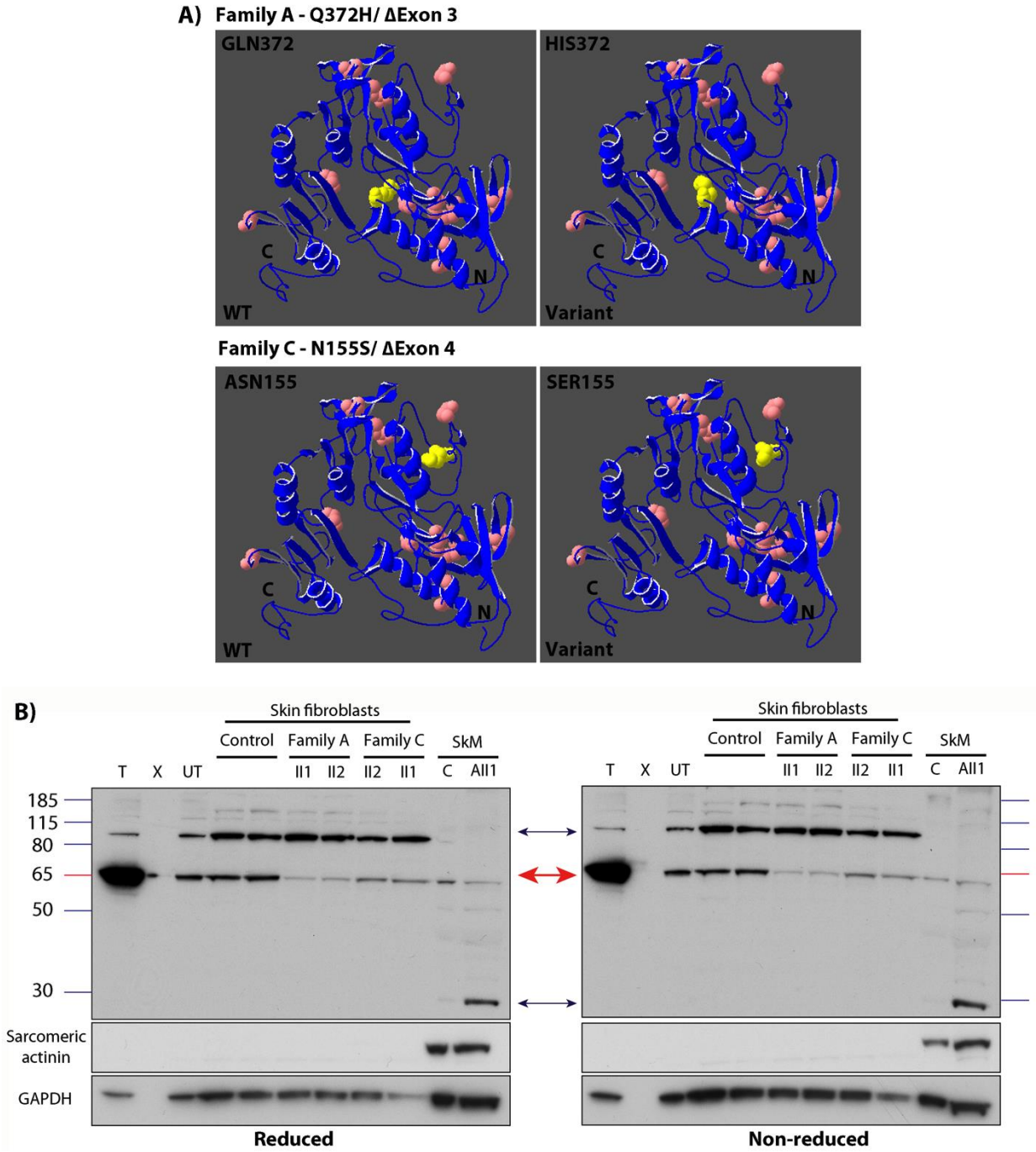
A)
Family A - Q372H/ ΔExon 3
GLN372
HIS372
C
N
WT
Variant
Family C - N155S/ ΔExon 4
ASN155
SER155
B)
Skin fibroblasts
Control
Family A
Family C
SkM
T X UT
II1 II2 II2 II1 C AII1
185
115
80
65
50
30
Sarcomeric actinin
GAPDH
Reduced
Non-reduced

Figure 4.11 Endogenous wildtype and patient PYROXD1 do not show evidence of intramolecular disulphide bond formation. (A) Cysteines within PYROXD1 are highlighted in pink. Patient variants from Family A (upper panel) and Family C (lower panel) are highlighted in yellow with the missense variants denoted with the wild type amino acid in the left model and the missense variant in the right model. DeepView/Swiss-Pdb viewer (v 4.1.0, http://www.expasy.org/spdbv/) was used for molecular modelling of the PYROXD1 homology model generated by A/Prof Roger Bryan Sutton; **(B)** Reducing (left) and non-reducing (right) western blots were carried out on lysates solubilised in the presence of N-Ethylmaleimide to quench free thiols and probed for PYROXD1 (AB122458). HEK293T cells were transfected (T) with PYROXD1-WT untagged which runs at approximately 65 kDa with a weaker band evident in untransfected (UT) HEK293T cells at the same molecular weight (red arrow, endogenous PYROXD1). PYROXD1 is detected in primary skin fibroblasts from controls (42 and 46 years), Family A (29 and 26 years) and Family C (6 and 8 years) at 65 kDa with a non-specific band at 85 kDa (top blue arrow). PYROXD1 is detected in skeletal muscle (SkM) from a healthy control (C – age 11 years) and Family AII-1 (11 years) at 65 kDa with a non-specific band at 25 KDa (lower blue arrow). No additional bands were observed on the non-reducing gel. Sarcomeric actinin was used as loading control for skeletal muscle and GAPDH as a loading control for HEK293T cells and primary human fibroblasts.

4.2.1.3 Patient *PYROXD1* variants and *PYROXD1* in muscle disease

Protein levels of patient splice site variants

PYROXD1-patients showed normal or reduced levels of PYROXD1 protein (Part A, Figure 4A and B). The anti-PYROXD1 antibody AB122458 recognises an immunogen encoded by amino acids 28-125 of PYROXD1 (NM_024854). Western blot using AB122458 did not reveal evidence for truncated protein products resulting from the splice site variants identified in Family A and C – shown previously to cause in-frame skipping of exon 3 (Family A) or exon 4 (Family C) (Part A, Figure 1D). However, deletion of exon 3 (corresponding to amino acids 56-95) or exon 4 (corresponding to amino acids 96-138) may remove the antibody binding site.

To confirm the observed results were not due to removal of the antibody binding site, we probed the same samples with a second PYROXD1 antibody, AB204560. AB204560 recognises an immunogen encoded by amino acids 260-357 (NM_024854). Therefore, the antigen recognised by PYROXD1 AB204560 antibody could not be removed by the patient splice-site variants. (Refer to Figure 4.1 for antibody immunogen schematics).

A duplicate western blot probed with AB204560 (Figure 4.12, upper panel) showed results consistent with AB122458 (Figure 4.12, lower panel). The Q372H missense variant harboured by Family A was expressed at reduced levels, and the N155S missense variant carried by Family C was expressed at normal levels, compared to controls. Thus, collective results suggest the in-frame deletion of residues encoded by exon 3 (Family A) or exon 4 (Family C) does not produce a stable protein detectable by western blot.

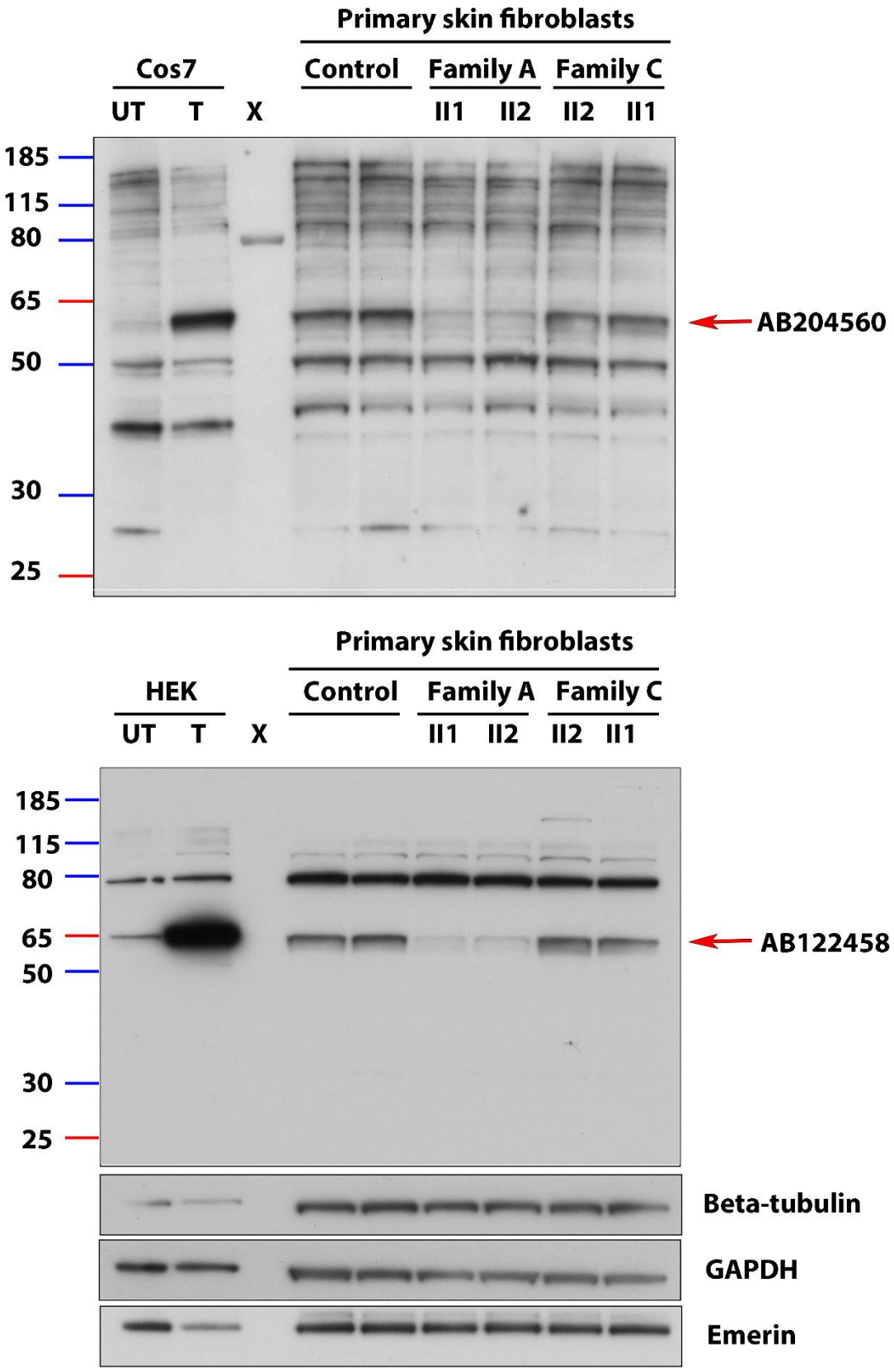
Primary skin fibroblasts
Cos7
Control
Family A
Family C
UT
T
X
II1
II2
II2
II1
185
115
80
65
50
30
25
AB204560
Primary skin fibroblasts
HEK
Control
Family A
Family C
UT
T
X
II1
II2
II2
II1
185
115
80
65
50
30
25
AB122458
Beta-tubulin
GAPDH
Emerin

Figure 4.12: Patient splice site variants causing in-frame exon deletions do not produce a protein detectable by western blot. Cos-7 or HEK cells were transfected (T) with PYROXD1-WT as a positive control. PYROXD1-WT runs at approximately 60 kDa, with a weak band present at the same molecular weight in untransfected Cos-7 or HEK cells (UT). PYROXD1 is detected in primary skin fibroblasts from controls (42 and 46 years), Family A (29 and 26 years) and Family C (6 and 8 years) at 55 kDa (red arrow). Lower levels of PYROXD1 are detected in Family A with no lower molecular weight bands seen uniquely in patients corresponding to expression of PYROXD1 absent of exon 3 (Family A, 4.4 kDa) and exon 4 (Family C, 4.7 kDa). Upper blot – probed with anti-PYROXD1 AB204560; Lower blot re-presented from Figure 4 Part A – probed with anti-PYROXD1 AB122458. Beta-tubulin, GAPDH and emerin were used as loading controls. X – lane containing the molecular weight ladder.

Intron retention within PYROXD1

Essential splice site variants identified within Family A and Family C caused in-frame skipping of exon 3 and 4 respectively (refer to Figure 1D & E, Part A). These transcripts do not contain a premature termination codon (PTC), and therefore should not activate nonsense-mediated decay (NMD). Interestingly, we cannot detect protein product of patient splice site variants by western blot (refer to Figure 4.12). However, intron retention was also a plausible outcome from the essential splice site variants. Intron retention would generate a premature stop codon, triggering nonsense-mediated decay - possibly explaining the absence of protein on western blot. We designed additional PCRs to test for relative levels of intron-3 or intron-4 retention in Family A or Family C (respectively), versus controls.

I extracted mRNA from control and patient primary skin fibroblasts and synthesised cDNA. I carried out PCR amplification of the cDNA using primer pairs to detect intron 3 and intron 4 retention (Figure 4.13). Unexpectedly, I found evidence for exon-3 extension in fibroblast cDNA from controls (C1 and C2), both siblings from Family A (who bear the intron 3 variant), and Family C (who bear the intron 4 variant) (Figure 4.13A). This data suggests a level of innate leakiness at this splice site in controls. I also found evidence for intron-4 retention in fibroblast cDNA from controls, both siblings from Family A and both siblings from Family C. This data suggests, as with Exon 3, that there is an innate leakiness at this splice site in controls. Collectively, these data suggest intron retention and subsequent NMD does not explain the absence of truncated PYROXD1 proteins encoded by patient splice-site variants.

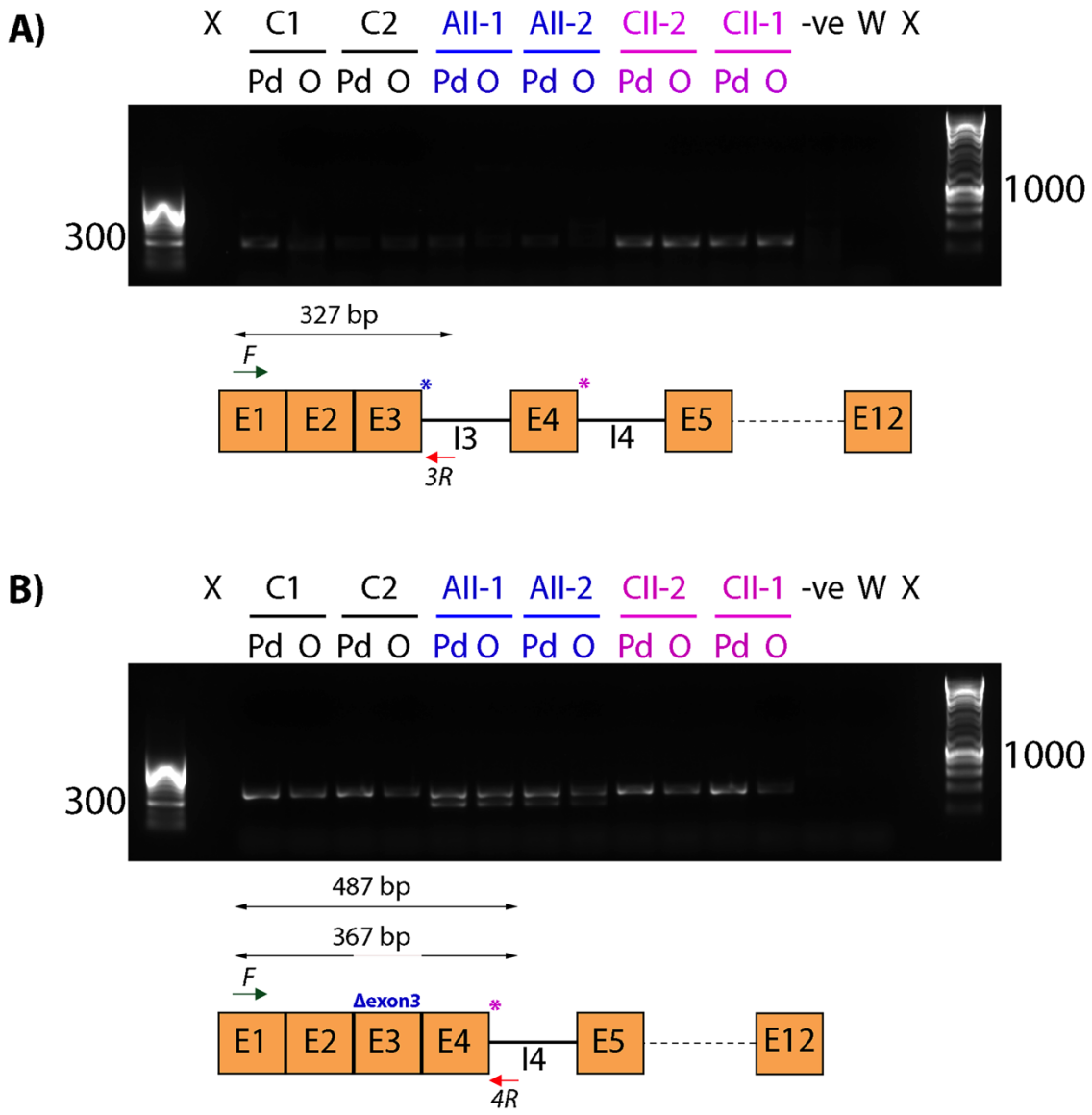

Figure 4.13: Extension of exon 3 and exon 4 of PYROXD1 is evident in controls. mRNA was extracted from skin fibroblasts of controls (C1, C2), Family A (blue - AII-1, AII-2) and Family C (pink- CII-2, CII-1). cDNA was synthesised using random PdN(6) (P) or $OligoDT_{20}$ (O) primers. Control gDNA was used as the negative DNA control (-ve) and water (W) as a negative control. E – Exon, I – Intron, X – blank lane. **(A)** PCR was carried out with primers within exon 1 (F, green arrow) and intron 3 (3R, red arrow) to detect extension of exon 3. Low levels of exon 3 extension were detected as a 327 bp band in controls and Family A with higher levels detected in Family C. Family A splice site variant - blue asterisks, Family C splice site variant - pink asterisks. **(B)** PCR was carried out with primers within exon 1 (F, green arrow) and intron 4 (4R, red arrow) to detect extension of exon 4. Exon 4 extension was detected in all samples as a 487 bp band. The 367 bp band detected within Family A is consistent with the deletion of exon 3 caused by their splice site variant (blue, Δexon3). Family C splice site variant -pink asterisks.

Proteasome degradation of PYROXD1 patient variants

Next, we hypothesised the variant forms of PYROXD1 (namely, lacking residues encoded by exon 3 or exon 4) were unstable and were being targeted for ubiquitin-mediated proteasomal degradation. To investigate this hypothesis, we treated control and patient primary skin fibroblasts with the proteasome inhibitor MG132, and determined protein levels by western blot. We did not observe a lower molecular weight band corresponding with the in-frame deletion of exon 3 (reduction by 4.4 kDa) in Family A, nor a noticeable difference in expression of PYROXD1 Q372H (Figure 4.14A). Thus, we were unable to confirm active degradation of misfolded protein products by the proteasome, and these experiments were not further pursued.

Similarly, treatment of fibroblast cultures from Family C siblings with MG132 showed no significant difference in levels of PYROXD1 expression. This result suggests N155S is not influenced by the proteasome. A weak lower molecular weight band corresponding to protein product from c.414+G>A (reduction by 4.7 kDa) was observed with MG132 treatment (Figure 4.14B, red asterisk). This result suggests, PYROXD1 protein harbouring the c.414+G>A variant, causing in-frame deletion of exon 4, is made at very low levels and degraded by the proteasome. Collectively, these results are consistent with the equal levels of cDNA expression observed from each allele in Family A, and a biased towards N155S in Family C (Figure 1E, Part A).

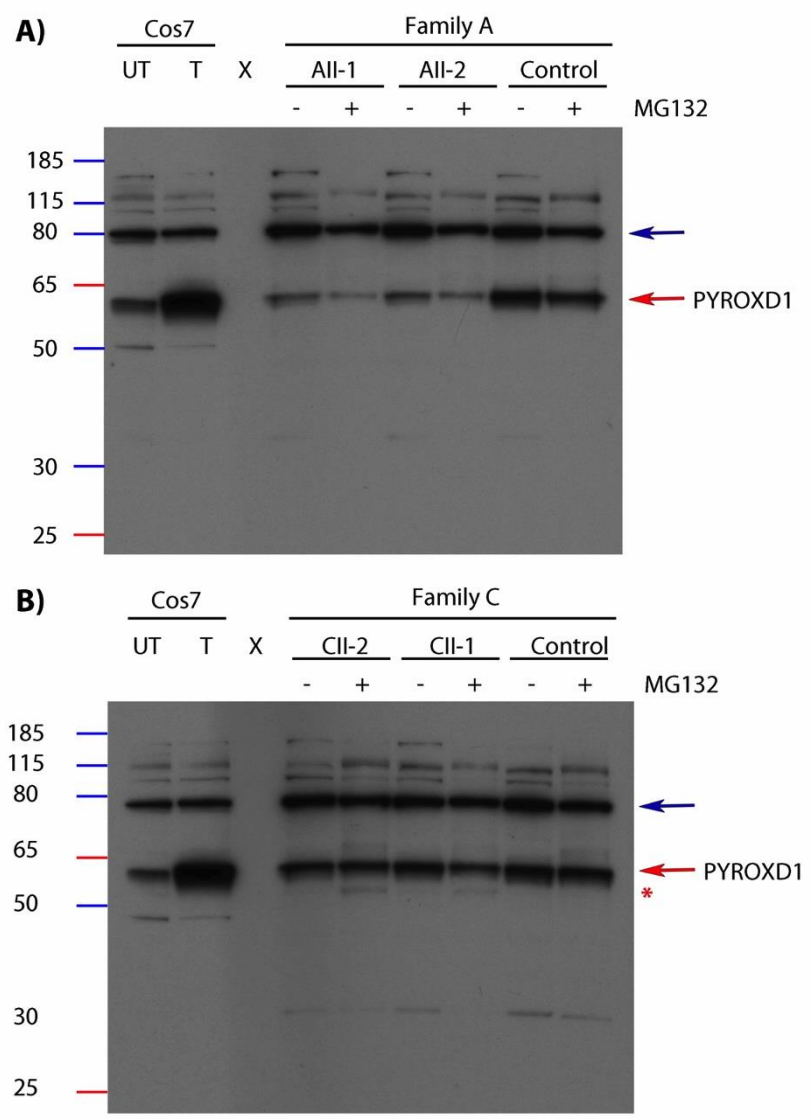

Figure 4.14: MG132 treatment mildly rescues the protein expression of splice site variant within Family C but not Family A. Cos-7 cells were transfected (T) with PYROXD1-WT as a positive control running at approximately 60 kDa (red arrow) with a weaker band present at the same molecular weight in untransfected Cos-7 cells (UT, endogenous PYROXD1). Primary skin fibroblasts were treated with the proteasome inhibitor MG132 (+) or vehicle control DMSO (-) and run on a reducing western blot. PYROXD1 is detected in all primary skin fibroblasts at 60 kDa. **(A)** Family A shows a lower level of PYROXD1 expression with no lower molecular weight bands detected unique to patient samples; **(B)** Family C shows a normal level of PYROXD1 expression with a faint lower molecular weight band in MG132 treated samples (red asterisks) corresponding to the molecular weight of PYROXD1 containing the patient's splice site variant and absence of exon 4 (decrease of 4.7 kDa). A non-specific band is detected at 80 kDa (blue arrow).

PYROXD1 ***levels in dystrophic muscle***

The Australian index case (Family A) had an initial clinical diagnosis of muscular dystrophy, due to dystrophic features observed in patient muscle. To determine whether PYROXD1 protein was also involved in the pathogenesis of other types of dystrophies we investigated PYROXD1 protein levels in: (1) Duchenne muscular dystrophy (*DMD*) (2) Limb girdle muscular dystrophy type 2B (*DYSF*); and (3) Limb girdle muscular dystrophy type 2A (*CAPN3*), caused by variants within calpain 3.

Skeletal muscle lysates were loaded so total actin levels were equal between samples. Dystrophic muscle contains an increased number of nuclei (Dubowitz, Sewry, & Oldfors, 2013). We rationalised PYROXD1 levels should be analysed in comparison to a nuclear marker, due to PYROXD1 predominantly localising within the nucleus (Part A, Figure 6). When PYROXD1 levels were normalised to emerin, PYROXD1 protein levels did not differ between dystrophic and healthy muscle (Figure 4.15).

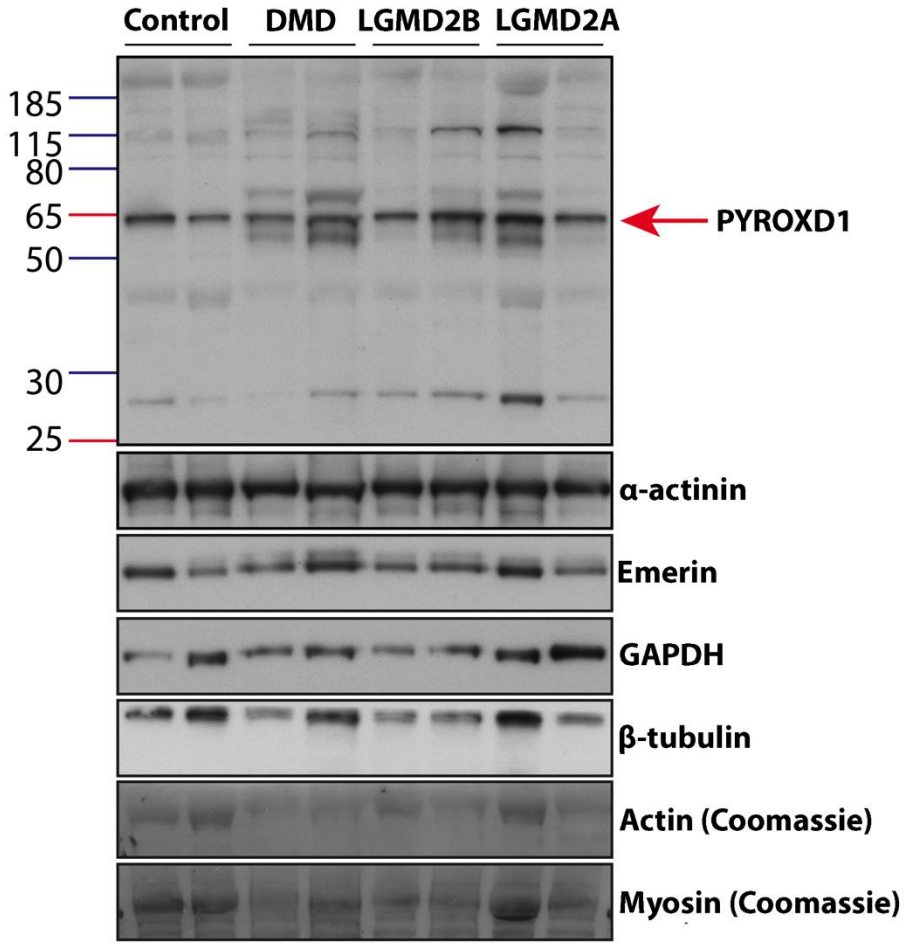

Figure 4.15: Skeletal muscle PYROXD1 expression in muscular dystrophy patients does not differ to controls. Western blot of whole muscle lysates from healthy controls (5 and 21 years), duchenne muscular dystrophy caused by variants within dystrophin (8 and 5 years), limb girdle muscular dystrophy type 2B caused by variants within dysferlin (22 and 20 years) and limb girdle muscular dystrophy type 2A caused by variants within calpain 3 (18 and 17 years). Actin & myosin coomassie and α-actinin probe were used as loading controls for skeletal muscle. GAPDH and β-tubulin were used as markers for fat and connective tissue infiltration in diseased muscle. Emerin was used as a nuclei marker. PYROXD1 expression levels match those of emerin and when this is taken into account, PYROXD1 expression within dystrophic muscle does not differ to that within controls.

Localisation of **PYROXD1** *in patient fibroblasts*

Protein localisation studies showed exogenous PYROXD1 missense variants did not alter the localisation of PYROXD1 (refer to Figure 6, Part A). Here, we investigated the localisation of endogenous PYROXD1 in primary human fibroblasts. Figure 4.16 shows consistent localisation patterns between patients of Family A & C and controls - predominant nuclear localisation with diffuse cytoplasmic staining.

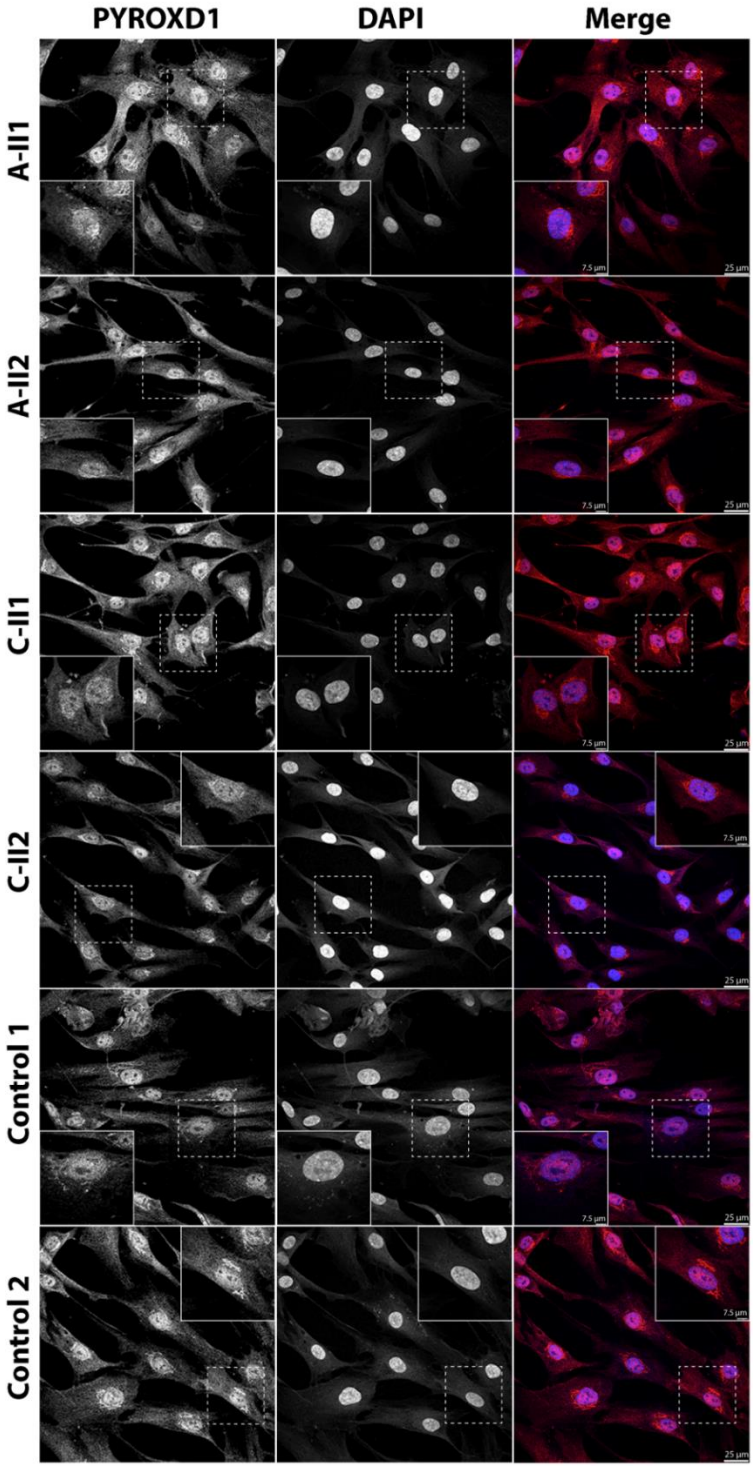

Figure 4.16: PYROXD1 localisation in patient primary skin fibroblasts does not differ to controls. Primary human fibroblasts were co-stained with PYROXD1 (AB122458) and DAPI. *PYROXD1*-patient fibroblasts from Family A (AII-1 & AII-2) and Family C (CII-1 & CII-2) show predominant PYROXD1 staining within the nucleus and diffuse cytoplasmic staining coupled with stronger staining to the periphery of the nucleus. Control primary human fibroblasts match the staining patterns observed in our patients. PYROXD1 – red, DAPI – blue. Note: Exposure times were higher for patient compared to control fibroblasts to observe perinuclear staining.

Parallels between PYROXD1-myopathy and neurodegeneration

Collectively, our data suggests oxidative distress caused by perturbed PYROXD1 activity is only evident within long lived cells. The dominant clinical presentations of our patients are muscular. In addition, our eldest *PYROXD1*-patient (AII-1), is beginning to present with a peripheral neuropathy. The pathological features of *PYROXD1*-myopathy share similarities with neurodegenerative disease – mitochondrial dysfunction, cellular atrophy and cellular aggregates (Rothstein, 2009). Variants within *TDP-43* cause motor neuron disease, as well as being a component of skeletal muscle aggregates in myofibrillar myopathy (Olive et al., 2009; Rothstein, 2009). We have shown a link between *PYROXD1*-myopathy and myofibrillar myopathy. Therefore, we wanted to investigate the link between PYROXD1 and neurodegeneration.

We stained *PYROXD1*-patient muscle for the neuronal aggregate markers αβ-crystalin and TDP-43. We found aggregates within *PYROXD1*- patient muscle stained for αβ-crystalin and TDP-43 (Figure 4.17). Furthermore, when we stained myofibrillar myopathy skeletal muscle, we found skeletal muscle aggregates also stained for PYROXD1 (Figure 4.18). These results draw a parallel between *PYROXD1*-myopathy and neurodegeneration. Further studies need to be carried out, to determine if similar pathways are involved in the pathogenesis and if similar mechanistic therapies may be successful.

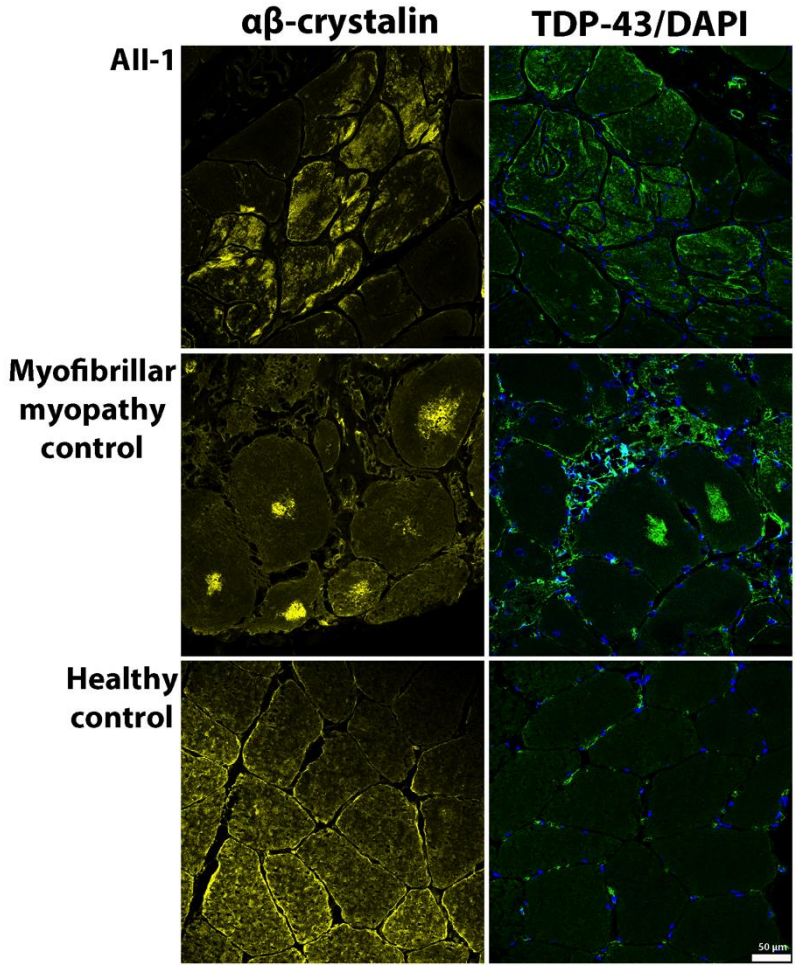

Figure 4.17: Neuronal aggregate markers αβ-crystalin and TDP-43 stain aggregates within PYROXD1 patient muscle. Sequential sections of skeletal muscle (quadricep) from *PYROXD1*-patient AII-1 (15 years), a myofibrillar myopathy patient (45 years) and a healthy control (38 years) stained for DAPI (blue) and the neuronal aggregate markers αβ-crystalin (yellow) & TDP-43 (green). In healthy control muscle αβ-crystalin stains the centre of the myofibre and TDP43 stains the peripheral nuclei. In myofibrillar myopathy control and *PYROXD1*-patient AII-1 muscle αβ-crystalin and TDP-43 stain myofibril aggregates.

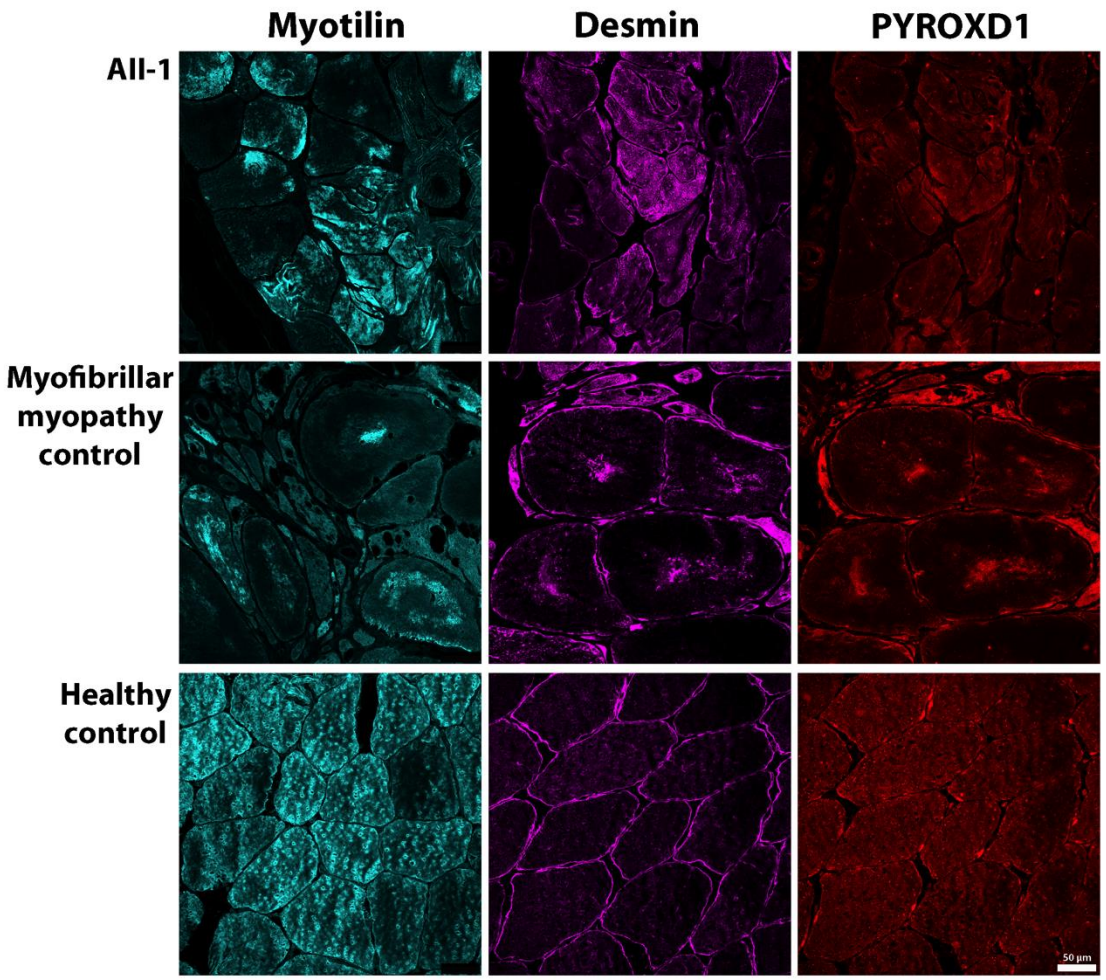

Figure 4.18: PYROXD1 labels aggregates within myofibrillar myopathy patient muscle. Sequential sections of skeletal muscle (quadricep) from *PYROXD1*-patient AII-1 (15 years), a myofibrillar myopathy patient (45 years) and a healthy control (38 years) stained for myotilin (cyan) and co-stained for desmin (purple) and Pyroxd1 (red – AB122458). In healthy control muscle myotilin stains the centre of the myofibre, desmin stains the periphery of the myofibre and PYROXD1 predominantly stains the peripheral nuclei with lower levels of staining seen within the centre of the myofibre. In *PYROXD1*-patient AII-1 and myofibrillar myopathy control muscle myotilin, desmin and PYROXD1 stain myofibril aggregates.

4.3 PART C: Generating mouse models to gain insight into PYROXD1 biology and disease

4.3.1 Introduction

4.3.1.1 The international Knockout Mouse Consortium

The International Knockout Mouse Consortium (IKMC) formed in 2006, aims to generate a null-reporter mouse for each protein-encoding gene, and make these available to the scientific community to study gene function (Collins, Finnell, Rossant, & Wurst, 2007). The IKMC is made up of three knock-out programs: (1) KnockOut Mouse Project (KOMP), (2) European Conditional Mouse Mutagenesis Program (EUCOMM), and (3) North American Conditional Mouse Mutagenesis Project (NorCOMM) ("A Mouse for All Reasons," 2007). The IKMC chose to use the C57BL/6 mouse strain as the background mouse strain for the generation of mutant alleles ("A Mouse for All Reasons," 2007). The C57BL/6 is one of the best characterised mouse strains, applicable to many fields of research, and C57BL/6J was the reference strain used to first sequence the mouse genome (Mouse Genome Sequencing et al., 2002). A C57BL/6 embryonic stem cell line with robust germline transmission was established for the international mouse knockout program - JM8 from the C57BL/6N mouse strain (Pettitt et al., 2009). A combination of gene-trapping and gene-targeting technologies were used in C57BL/6N embryonic stem (ES) cells to generate a conditional knockout resource for the scientific community (Skarnes, Auerbach, & Joyner, 1992; Skarnes et al., 2011; Testa et al., 2004).

4.3.1.2 Aims of this project

In Parts A and B we established PYROXD1 as a new player in muscle disease and oxidative biology. The next goal was to establish an appropriate mouse model as a tool to study: (1) the role of PYROXD1 in fundamental biology; and (2) the role of PYROXD1 in disease pathogenesis.

More specifically, the aims for this project were:

Aim 1: To define the tissue-specific and developmental expression of murine *Pyroxd1*.

Aim 2: To develop a skeletal muscle knock-out of murine *Pyroxd1*.

4.3.1.3 Background

We utilised the knockout-first conditional Pyroxd1 Tm1a mouse strain from KOMP, available through the KOMP repository (https://www.komp.org/). While this strain had been generated by KOMP, no characteristaion had been carried out on this strain at time of purchase. The *Pyroxd1 Tm1a* allele (Figure 4.19A) is a knock-out-first conditional allele and serves three purposes: (1) β-galactosidase reports on the expression of *Pyroxd1*; (2) the genetrap knocks-out *Pyroxd1* expression at the transcript level; and (3) the *FRT* and *loxP* sites enable generation of a conditional *Pyroxd1* knock-out allele.

Components of the gene trap enable reporting of *Pyroxd1* expression by β-galactosidase. *FRT* sites flank the genetrap (Figure 4.19A). The *FRT* sites allow FLP-mediated excision of the gene trap, re-establishing wild type *Pyroxd1* expression. Exon 5 of *Pyroxd1* lies outside of the genetrap, and is flanked by *loxP* sites. The *loxP* sites flanking exon 5 of *Pyroxd1* allow cre-mediated excision of exon 5. Removal of exon 5 generates a frameshift predicted to induce nonsense mediated decay of the mRNA transcript. Cre-mediated excision of exon 5 of *Pyroxd1*

allows conditional temporal and spatial knock-out of *Pyroxd1* by ustilising cre-expressing mouse strains (http://www.mousephenotype.org/data/order/creline).

The *Tm1a* genetrap cassette is inserted within introns 4 and 5 of *Pyroxd1* and driven by the endogenous *Pyroxd1* promotor (Figure 4.19A). The *En2* splice acceptor (En2 SA) and SV40 polyadenylation sequence (pA) allows incorportion of *lacZ* into the *Pyroxd1* mRNA transcript (Figure 4.19B). There are two translation start sites from the *Pyroxd1 Tm1a* mRNA (Figure 4.19B, red arrows). The first is the endogenous translation start site within exon 1 of *Pyroxd1*. The second translation start site, mediated by the internal ribosome entry site (IRES), is at the ATG of l*acZ*. Two protein products are predicted to be generated from the one *Pyroxd1 Tm1a* mRNA transcript (Figure 4.19C). The first is *Pyroxd1* exons 1-4 plus 11 amino acids of the *En2 SA* sequence prior to the premature stop codon (PTC). The PTC is predicted to trigger nonsense-mediated decay, resulting in no Pyroxd1 protein generated from the *Pyroxd1 Tm1a* allele. The second predicted protein product is β-galactosidase. β-galactosidase reports on the expression of endogenous *Pyroxd1*. The presence of the *Tm1a* allele within endogenous *Pyroxd1* is predicted to generate a *Pyroxd1* knock-out allele at the mRNA level.

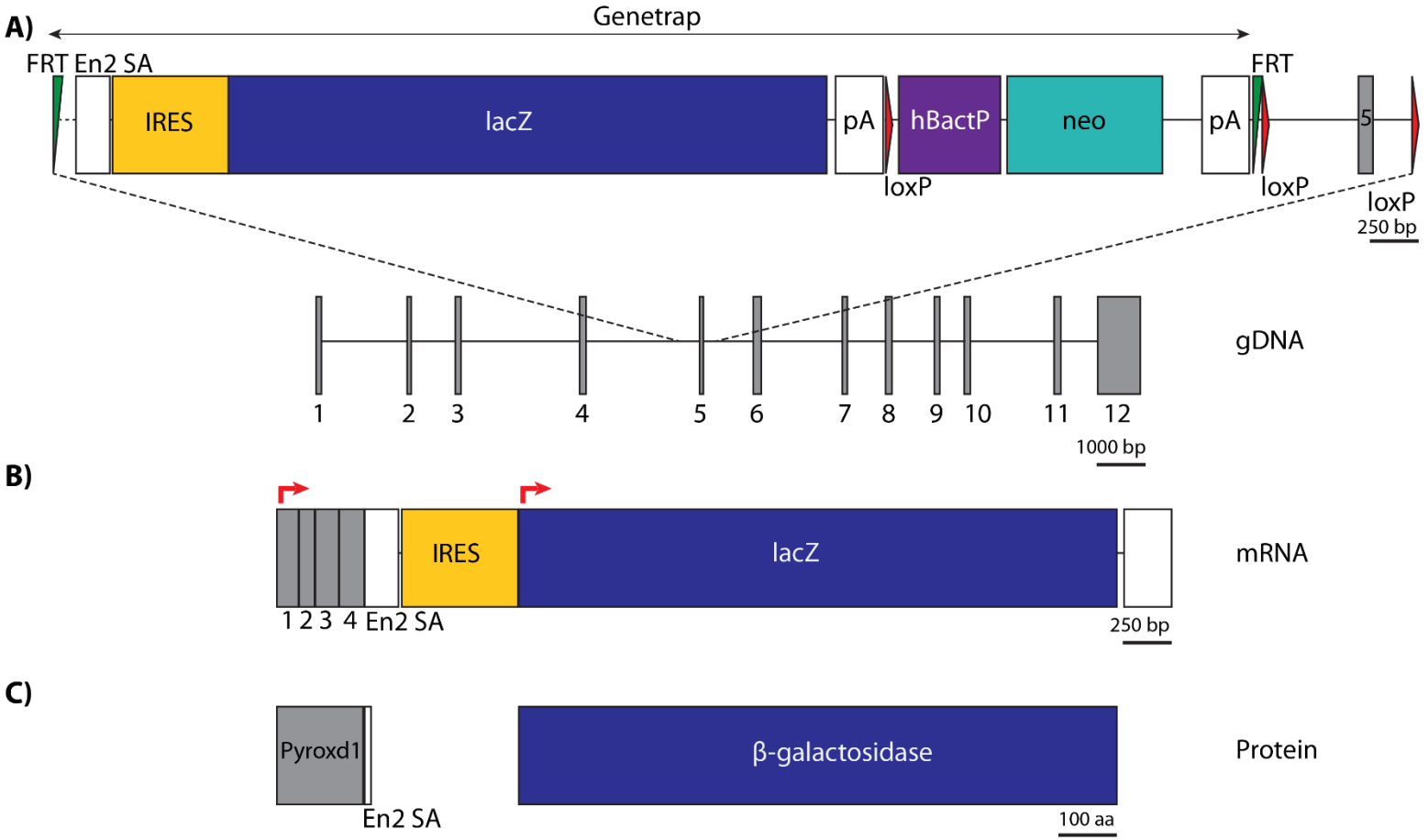

Figure 4.19: *Pyroxd1 Tm1a* conditional reporter mouse cassette. To scale schematic of **(A)** *Pyroxd1 Tm1a* KOMP cassette and points of insertion within the *Pyroxd1* locus; **(B)** Predicted messenger RNA of the *Pyroxd1 Tm1a* allele, translation initiation sites marked with red arrows; and **(C)** Predicted protein primary structure of *Pyroxd1 Tm1a.* Two protein products are predicted: (1) Pyroxd1 exons 1-4 with a premature stop codon 11 amino acids into the En2 sequence. This product would only be made if nonsense mediated decay did not degrade the mRNA transcript; and (2) Beta-galactosidase. FRT – flippase recognition target, En2 SA – En2 splice acceptor, IRES – internal ribosomal entry site, pA – SV40 polyadenylation sequence, loxP – lox sequence, hBactP – human beta actin promoter, neo – neomycin resistance gene, E – exon. The intron between FRT and En2 SA (876 bp) is not to scale.

4.3.2 Results

4.3.2.1 Pyroxd1 null-reporter mouse strain

Lethality of homozygous Pyroxd1$^{Tm1a/Tm1a}$ mice

Upon receiving Pyroxd1 Tm1a mice from KOMP, we carried out genotyping to confirm the gene trap cassette was inserted within the *Pyroxd1* locus, using two PCR reactions: (1) to identify the *Pyroxd1 Tm1a* allele (Figure 4.20A); and (2) to identify the *endogenous Pyroxd1* allele (Figure 4.20B).

We received five mice from KOMP, for which genotyping confirmed heterozygosity for the *Pyroxd1Tm1a* allele (Pyroxd1$^{Tm1a/WT}$), as expected (Figure 4.20). The genotyping strategy of the original embryonic stem cells was carried out across the 3' homology arm (Skarnes et al., 2011). This leaves the possibility of a non-homologous insertion event having taken place. We confirmed correct insertion of the 5' end of the *Pyroxd1 Tm1a* allele by Sanger sequencing (results not shown).

Interestingly, we observed no Pyroxd1$^{Tm1a/Tm1a}$ mice in nine litters of Pyroxd1$^{Tm1a/WT}$ crosses. We expected 50% Pyroxd1$^{Tm1a/WT}$, 25% Pyroxd1$^{WT/WT}$ and 25% Pyroxd1$^{Tm1a/Tm1a}$. I observed 77% Pyroxd1$^{Tm1a/WT}$ and 23% Pyroxd1$^{WT/WT}$ mice (Chi-squared p-value = 1.1×10^{-5}). Entertaining the possibility that global knock-out of *Pyroxd1* in Pyroxd1$^{Tm1a/Tm1a}$ embryos is embryonic lethal, the expected genotype ratios would become 67% heterozygous and 33% wild-type. When homozygous embryos are excluded from expected ratios, the chi-squared value is then not significant at 2.5% (chi-squared, p-value = 0.026 > 0.025).

In 165 offspring from Pyroxd1$^{Tm1a/WT}$ crosses I observed 0/41 expected Pyroxd1$^{Tm1a/Tm1a}$, based on Mendelian ratios. This data provided compelling evidence that Pyroxd1$^{Tm1a/Tm1a}$ mice did not survive to weaning (3 weeks of age). Consistent with our observations, KOMP released data indicating that homozygous knock-out of *Pyroxd1* results in pre-weaning lethality (based on 0 homozygotes among 87 neonates from heterozygous crosses, http://www.mousephenotype.org/data/genes/MGI:2676395). Further, global gene knock-out studies in human cell lines identified *PYROXD1* as a gene essential for cell survival (Blomen et al., 2015; Hart et al., 2015; T. Wang et al., 2015). Therefore, the next question became: When does embryonic lethality of Pyroxd1$^{Tm1a/Tm1a}$ mice occur?

A) Primers: Pyroxd1_Tm1a_F and Pyroxd1_R

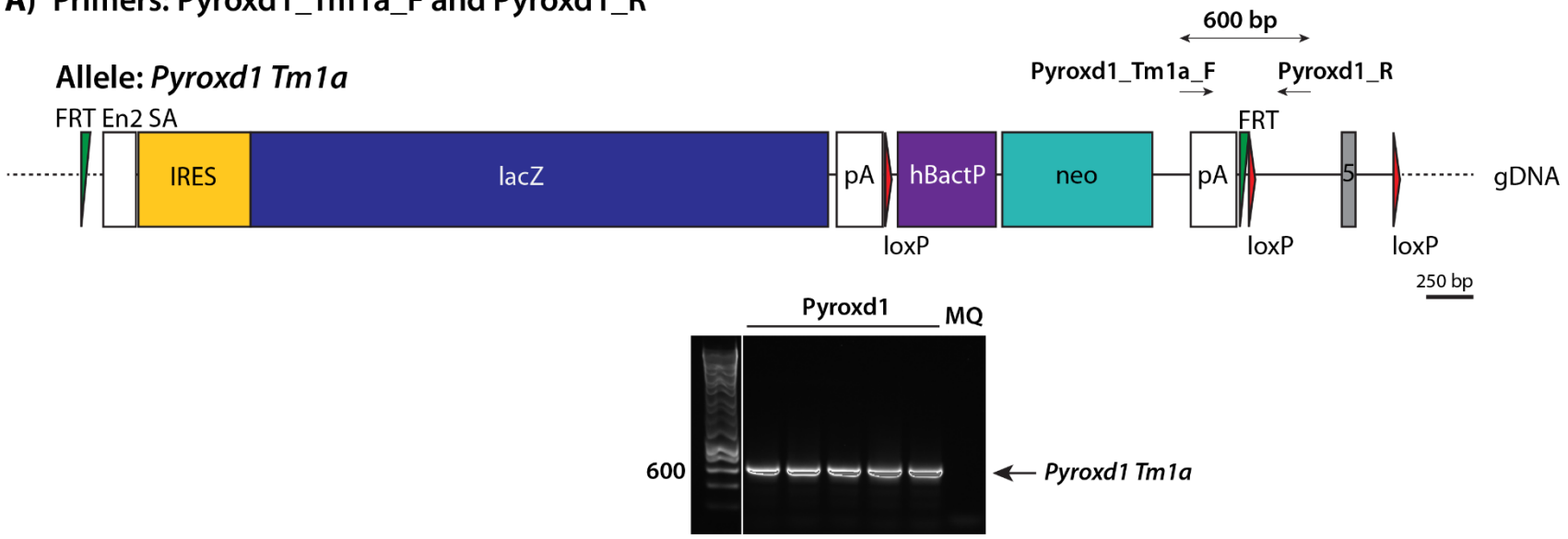

B) Primers: Pyroxd1_F and Pyroxd1_R

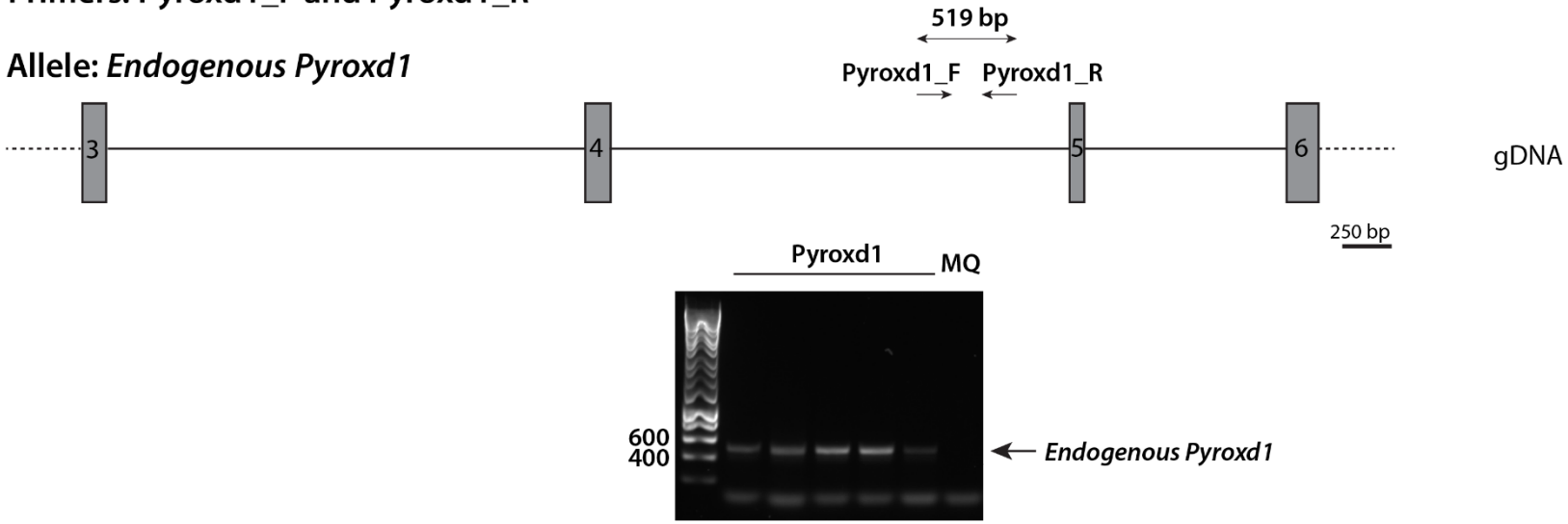

Figure 4.20: Genotyping of the *Pyroxd1 Tm1a* and *endogenous Pyroxd1* alleles.
(A) Screening of the *Pyroxd1 Tm1a* allele. *Upper:* To scale schematic of the *Pyroxd1 Tm1a* allele. Primer locations are indicated by black arrows (the start of each arrow marks the primer's start location, remainder of arrow is not to scale) and PCR product size above. ***Lower:*** Agarose gel of PCR products from Pyroxd1 (F0) screening for the *Pyroxd1 Tm1a* allele.; **(B) Screening of the *endogenous Pyroxd1* allele. *Upper:*** To scale schematic of the *endogenous Pyroxd1* allele with primer locations indicated by black arrows (the start of each arrow marks the primer's start location, remainder of arrow is not to scale) and PCR product size above. ***Lower:*** Agarose gel of PCR products from Pyroxd1 (F0) screening for the *endogenous Pyroxd1* allele. MQ – MilliQ water, horizontal filled lines – indicate introns, horizontal dashed lines – not to scale, numbering – indicate an exon, FRT – flippase recognition target, En2 SA – En2 splice acceptor, IRES – internal ribosomal entry site, pA – SV40 polyadenylation sequence, loxP – lox sequence, hBactP – human beta actin promoter, neo – neomycin resistance gene. The primers and PCR conditions utilised to screen for the *endogenous Pyroxd1* allele were designed such that the *Pyroxd1 Tm1a* allele would not be detected (PCR product is 7556 bp – too long to be efficiently amplified with a 40 second extension at 72°C).

We investigated whether Pyroxd1$^{Tm1/Tm1a}$ embryos were formed, but were reabsorbed prior to birth (ie, death was post-implantation). To address this question, we performed timed-mating of Pyroxd1$^{Tm1a/WT}$ mice, and genotyped two litters at embryonic day 10 (E10), approximately half gestation. The first dam carried 8 embryonic sacs, 4 of which were reabsorbed. The second dam carried 9 embryonic sacs, 3 of which did not contain an embryo. We expected 25% Pyroxd1$^{Tm1a/Tm1a}$ mice. Reabsorption of greater than 25% of embryos (50% and 33% respectively) meant it was possible Pyroxd1$^{Tm1a/Tm1a}$ embryos were formed, but reabsorbed by E10.

We collected a tail clip of each embryo and a portion of the amniotic sac of reabsorbed embryos for genotyping. The amniotic sac consists of embryonic tissue (Dobreva et al., 2012; Pereira et al., 2011). I did not observe any Pyroxd1$^{Tm1a/Tm1a}$ embryos or amniotic sacs at E10 (Figure 4.21). Absence of Pyroxd1$^{Tm1a/Tm1a}$ mice from two litters at E10 suggested Pyroxd1$^{Tm1a/Tm1a}$ embryos do not survive to E10.

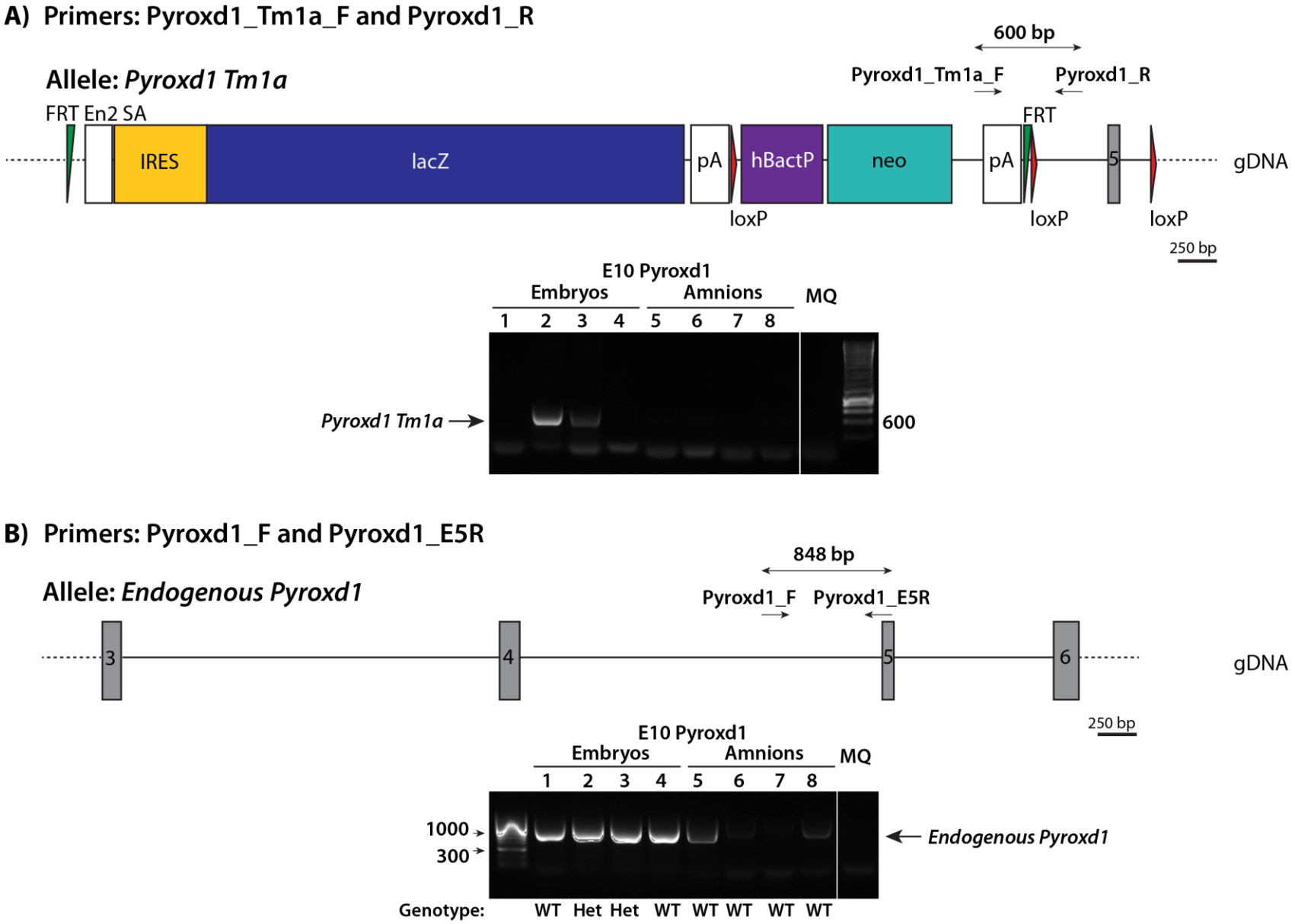
A) Primers: Pyroxd1_Tm1a_F and Pyroxd1_R
Allele: Pyroxd1 Tm1a
600 bp
Pyroxd1_Tm1a_F
Pyroxd1_R
FRT En2 SA
IRES
lacZ
pA
hBactP
neo
pA
FRT
5
gDNA
loxP
loxP
loxP
250 bp
E10 Pyroxd1
Embryos
Amnions
MQ
1 2 3 4 5 6 7 8
Pyroxd1 Tm1a
600
B) Primers: Pyroxd1_F and Pyroxd1_E5R
Allele: Endogenous Pyroxd1
848 bp
Pyroxd1_F
Pyroxd1_E5R
3
4
5
6
gDNA
250 bp
E10 Pyroxd1
Embryos
Amnions
MQ
1 2 3 4 5 6 7 8
1000
300
Endogenous Pyroxd1
Genotype:
WT Het Het WT WT WT WT WT

Figure 4.21: Homozygous *Pyroxd1 Tm1a* embryos were not observed at ED10.
(A) Screening of the *Pyroxd1 Tm1a* allele. ***Upper:*** To scale schematic of the *Pyroxd1 Tm1a* allele. Primer locations are indicated by black arrows and the PCR product size is specified above. ***Lower:*** Representative agarose gel of PCR products from Pyroxd1 E10 screening for the *Pyroxd1 Tm1a* allele.; **(B) Screening of the *endogenous Pyroxd1* allele.** ***Upper:*** To scale schematic of the *endogenous Pyroxd1* allele with primer locations indicated by black arrows and the PCR product size is specified above. ***Lower:*** Representative agarose gel of PCR products from Pyroxd1 E10 screening for the *endogenous Pyroxd1* allele. MQ – MilliQ water, horizontal filled lines – indicate introns, horizontal dashed lines – not to scale, numbering – indicate an exon, FRT – flippase recognition target, En2 SA – En2 splice acceptor, IRES – internal ribosomal entry site, pA – SV40 polyadenylation sequence, loxP – lox sequence, hBactP – human beta actin promoter, neo – neomycin resistance gene. The start of each arrow marks the primer's start location, the remainder of arrow is not to scale.

We assessed whether the lack of Pyroxd1$^{Tm1a/Tm1a}$ mice at E10 is due to the inability of Pyroxd1$^{Tm1a/Tm1a}$ embryos to implant within the uterus. C57BL/6 mouse embryos implant within the uterus between E4.5 and 5.5 (Bedzhov, Leung, Bialecka, & Zernicka-Goetz, 2014). We harvested embryos soon after fertilisation and cultured the embryos *ex vivo* until the late blastocyst stage. The late blastocyst stage should provide an adequate number of cells for genotyping, while avoiding the challenges associated with *in-vitro* culture of post-implantation embryos (Bedzhov et al., 2014).

To maximise the number of embryos per pregnancy and reduce the number of litters required to reach statistically significant numbers, we superovulated the dams prior to mating. Ovaries of pregnant dams were harvested at the zygote stage, E0.5 (Figure 4.22A). Pronuclei were cultured *ex vivo* and individually collected at E4.5 and genotyped as described above (Figure 4.22A). Pyroxd1$^{Tm1a/Tm1a}$ embryos were present at E4.5 (Figure 4.22B – embryos 6 & 7) indicating Pyroxd1$^{Tm1a/Tm1a}$ embryos are made, and survive to pre-implantation age. This narrowed the window of embryonic lethality to between E4.5 and E9.5.

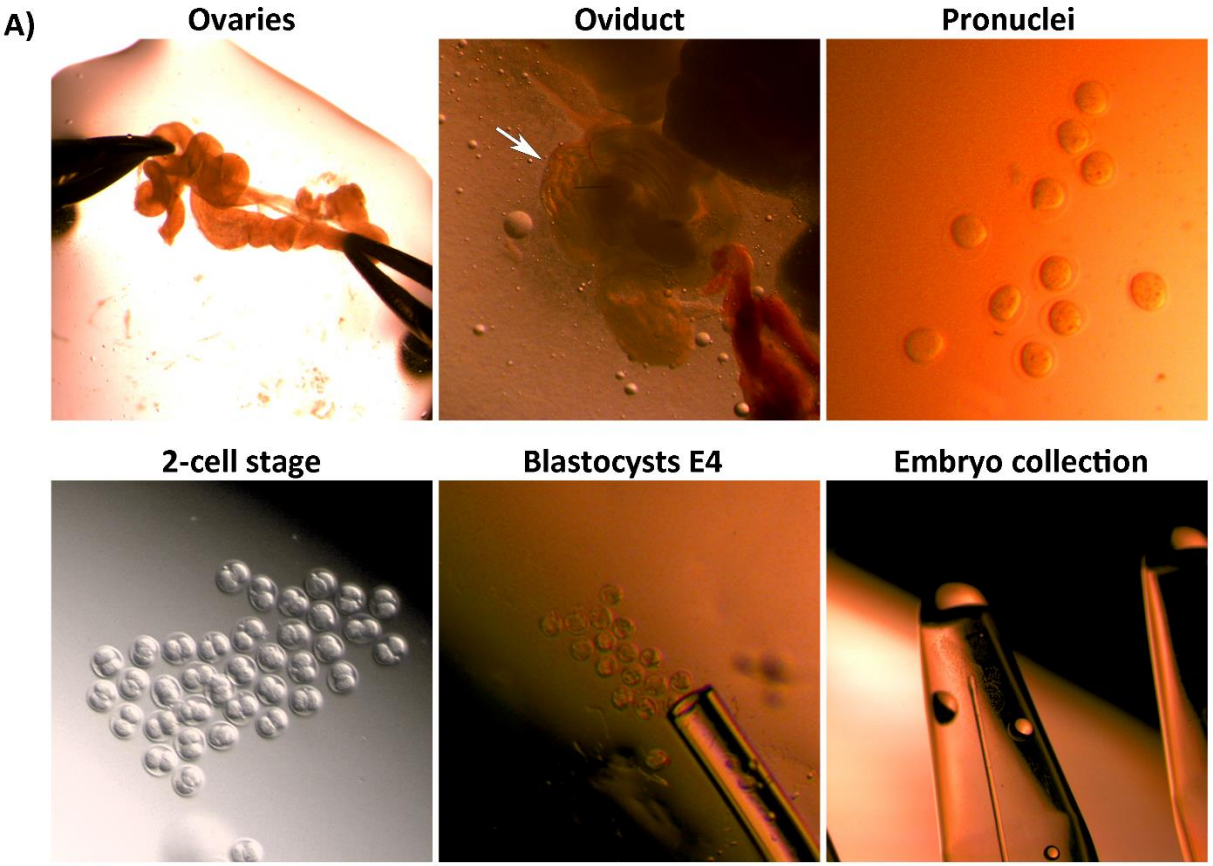
A)
Ovaries
Oviduct
Pronuclei
2-cell stage
Blastocysts E4
Embryo collection

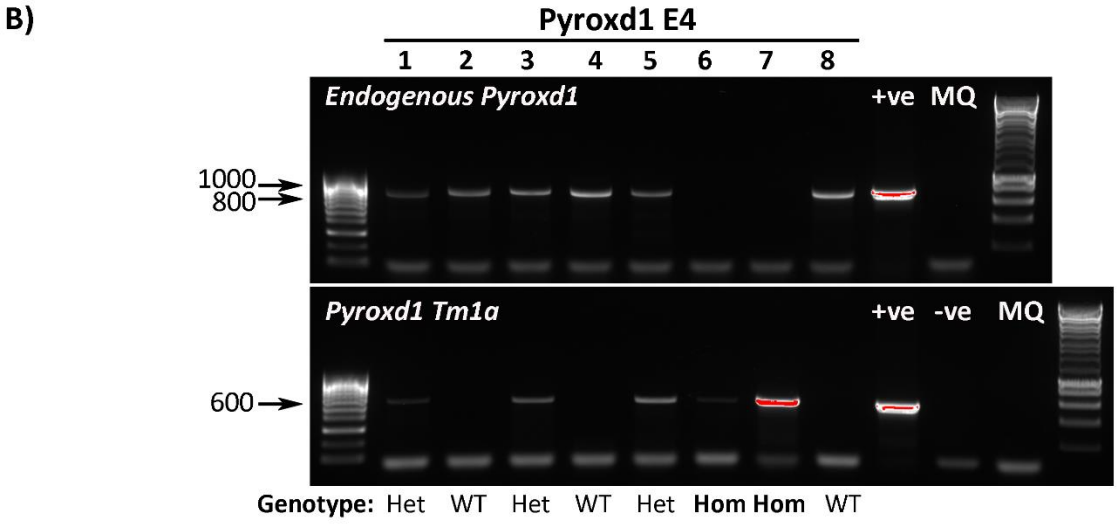
B)
Pyroxd1 E4
1 2 3 4 5 6 7 8
Endogenous Pyroxd1
+ve MQ
1000
800
Pyroxd1 Tm1a
+ve -ve MQ
600
Genotype: Het WT Het WT Het Hom Hom WT

Figure 4.22: Homozygous *Pyroxd1 Tm1a* embryos are present at E4. (A) Images taken on a Leica MIR microscope demonstrate the process of embryo collection: Three week old Pyroxd1$^{Tm1a/WT}$ females were superovulated and mated with Pyroxd1$^{Tm1a/WT}$ males. Ovaries were harvested at E0.5 with the oviduct showing distention (white arrow) from over-production of eggs. Fertilised eggs were collected and grown *ex vivo* to E4. Each embryo was collected into a separate PCR tube. **The process of embryo collection was carried out by Dr Frances Lemckert**; **(B)** Representative agarose gel of Pyroxd1 E4 embryos screened for the *endogenous Pyroxd1* and *Pyroxd1 Tm1a* alleles. Heterozygous Pyroxd1 gDNA was used as the positive control (+ve), MQ – MilliQ water. Embryos 6 and 7 are homozygous - A PCR band corresponding to *endogenous Pyroxd1* is not detected (upper gel) and a PCR band corresponding to *Pyroxd1 Tm1a* is detected (lower gel).

β-galactosidase reporting of *Pyroxd1* expression

To define the tissue-specific and developmental expression of murine *Pyroxd1* we utilised the *lacZ* reporter within the *Pyroxd1 Tm1a* allele of the Pyroxd1 Tm1a mouse strain. *LacZ* is controlled by the endogenous *Pyroxd1* promoter. Therefore, *lacZ* is expressed when and where endogenous *Pyroxd1* is expressed (refer to Figure 4.19). *LacZ* encodes β-galactosidase which can be detected with X-gal staining.

We carried out X-gal staining on whole-mount E9.5 Pyroxd1 Tm1a embryos and preliminary results indicate X-gal staining in the developing brain (Figure 4.23). Of note, X-gal staining was not observed in all Pyroxd1$^{Tm1a/WT}$ embryos, nor consistently in sequential sections of the same embryo. We harvested E15.5 and E18.5 Pyroxd1 Tm1a embryos and brain, heart, lung, quad, ovaries/testis, stomach, spleen, kidney, bladder and liver of 3 and 12 month-old Pyroxd1 Tm1a mice. Unfortunately, X-gal staining was unsuccessful on cryo-sections despite trying a number of conditions. We performed western blot of Pyroxd1$^{Tm1a/WT}$ tissue to determine protein levels of β-galactosidase, which was inconclusive (Appendix, Figure A.3). These results suggest very low levels of *Pyroxd1* expression, too low to be detected consistently with this technique.

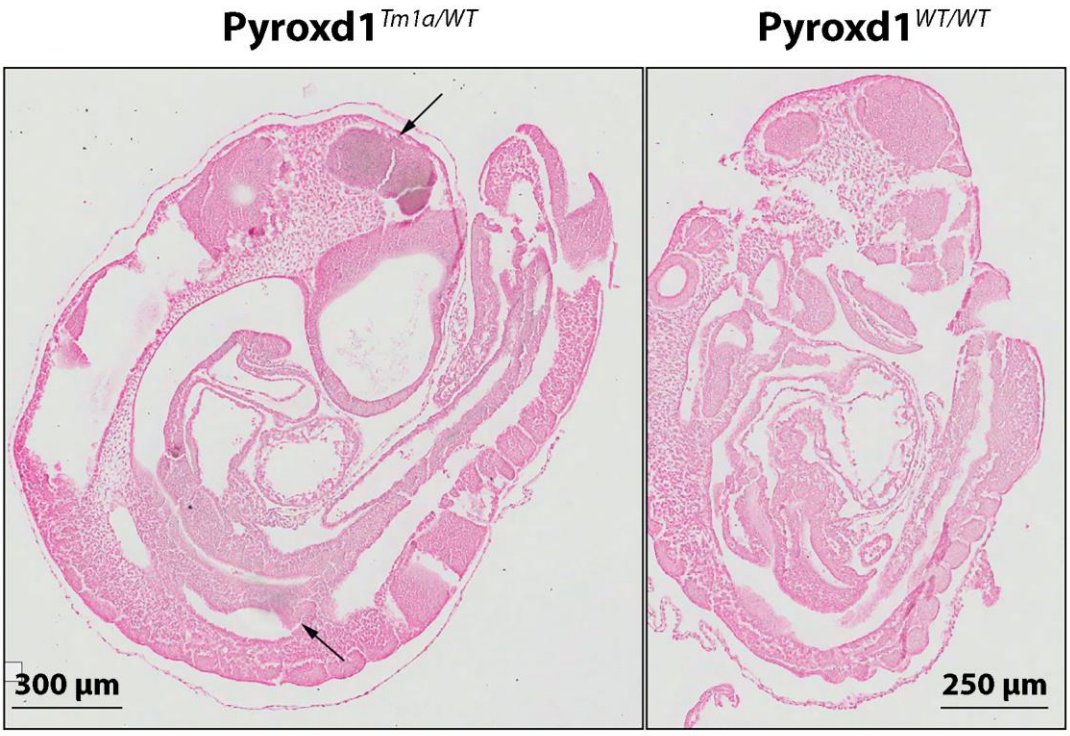

Figure 4.23: X-gal staining of the developing brain at E9.5 in the Pyroxd1$^{Tm1a/WT}$ mouse. X-gal staining was performed on E9.5 embryos from a Pyroxd1$^{Tm1a/WT}$ intercross. Embryos were wax-embedded and sectioned at 8µm. They were subsequently dewaxed, stained with nuclear fast red and imaged with a Scanscope microscope. X-gal staining was detected in the developing brain (black arrows) at E9.5 in the Pyroxd1$^{Tm1a/WT}$ which was absent from a littermate control.

4.3.2.2 Generation of a murine model with skeletal muscle knock-out of Pyroxd1

To further understand the role of Pyroxd1 in muscle biology and disease, we initiated a breeding program to derive a skeletal muscle knock-out of *Pyroxd1*. We anticipated a mouse model lacking Pyroxd1 protein within skeletal muscle would provide: (1) A *Pyroxd1*-myopathy disease model to study disease pathogenesis of *Pyroxd1*-myopathy; (2) A *Pyroxd1*-myopathy disease model to test treatments for *Pyroxd1*-myopathy; and (3) A system to study the biochemistry of Pyroxd1, by comparing Pyroxd1 wild type and Pyroxd1 knock-out tissue.

The breeding regime to generate a *Pyroxd1* skeletal muscle knock-out mouse line involved two breeding strategies, with multiple breeding steps. The first breeding strategy, designed to remove the gene trap, utilised the FLP-*FRT* system. The second breeding strategy, designed to knock-out both *Pyroxd1* alleles within skeletal muscle, utilised the Cre-*loxP* system controlled by *MyoD*.

Breeding strategy one: Gene trap removal

Background

A global *Pyroxd1* knock-out allele is induced by the gene trap within the *Pyroxd1 Tm1a* cassette (Figure 4.24). The gene trap cassette within the *Pyroxd1 Tm1a* allele is designed to be removed with the FLP-*FRT* system. *FRT* sites - 5'GAAGTTCCTATTCTCTAGAAAGTATAGGAACTTC3' – flank the gene trap cassette. The recombinase FLP (flippase) from *Saccharomyces cerevisiae* cuts at *FRT* sites removing the intervening sequence, regenerates one *FRT* site and maintains two *loxP* sites flanking exon 5 – the *PFLP* allele. To remove the gene trap cassette, we crossed the *Pyroxd1 Tm1a* mouse line with a global *FLP* expressing mouse line, FLPe, (Rodriguez et al., 2000) (Figure 4.24, kindly donated to The Kids Research Institute by The Victor Chang Cardiac Research Institute). The human beta-actin promoter regulates global *FLPe* expression with flippase activity seen by mouse E10.5 (Rodriguez et al., 2000).

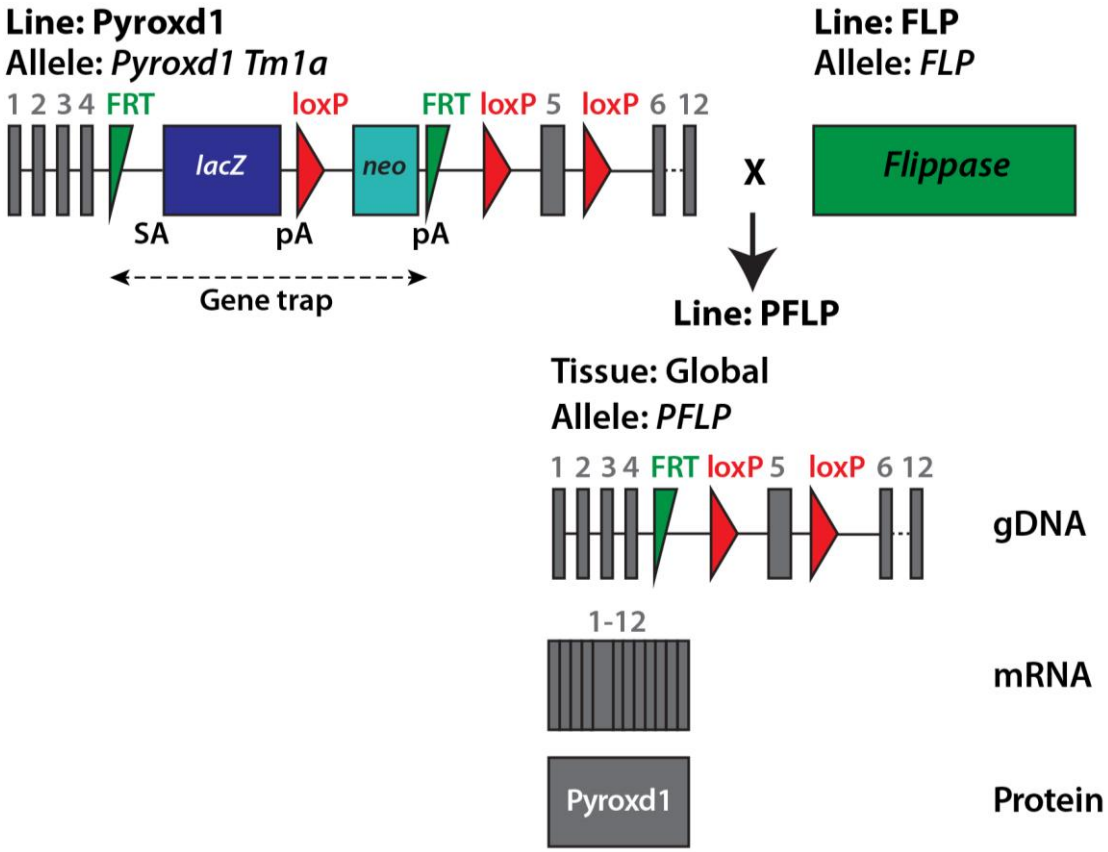

Figure 4.24: Predicted allele modification at the *Pyroxd1* locus to re-establish a wild type allele. Crossing the Pyroxd1 mouse line - carrying the *Pyroxd1 Tm1a* allele, with a FLP mouse line – carrying the *FLP* transgene, is predicted to remove the gene trap cassette. The recombinase FLP cuts at the two *FRT* sites flanking the gene trap, removing the intervening sequence. The allele generated – *PFLP* - contains one regenerated *FRT* site and two *loxP* sites flanking exon 5 within intronic sequence. The *PFLP* allele expresses wild-type *Pyroxd1* mRNA translated into wild-type Pyroxd1 protein. The resulting line – PFLP – is expected to carrying the *PFLP* allele in a global fashion. FRT – flippase recognition target, loxP – lox sequence, SA – splice acceptor, pA – SV40 polyadenylation sequence, neo – promoter driven neomycin resistance gene, numbering in grey indicate exons, horizontal filled lines indicate introns.

Breeding step one

The first breeding strategy involved two breeding steps: (1) Remove the gene trap cassette; and (2) breed the flippase transgene away and generate homozygous mice. The parental lines were Pyroxd1$^{Tm1a/WT}$ and homozygous FLPe mice (*FLP*$^{FLP/FLP}$). We were unable to use Pyroxd1$^{Tm1a/Tm1a}$ mice due to their embryonic lethality. We crossed Pyroxd1$^{Tm1a/WT}$ and FLP$^{FLP/FLP}$ which generated a new line – PFLP (Figure 4.25). We confirmed genotypes as depicted in Figure 4.26. FLP-mediated modification of the *Pyroxd1 Tm1a* allele generated the *PFLP* allele which was confirmed by Sanger sequencing (results not shown) and the unmodified *Pyroxd1 Tm1a* allele could not be detected by PCR (results not shown). Absence of the *Pyroxd1 Tm1a* allele suggests FLP recombinase excises the gene trap cassette in all nuclei

Breeding step two

The FLP cassette was then outbreed to avoid potential off target effects due to random insertion of the *FLP* transgene. PFLP$^{PFLP/WT,\ FLP/WT}$ (F1) were intercrossed (Figure 4.27) to generate the desired homozygous genotype, PFLP$^{PFLP/PFLP,WT/WT}$. From here onwards, the *FLP* genotype is not depicted in breeding schematics or explanations

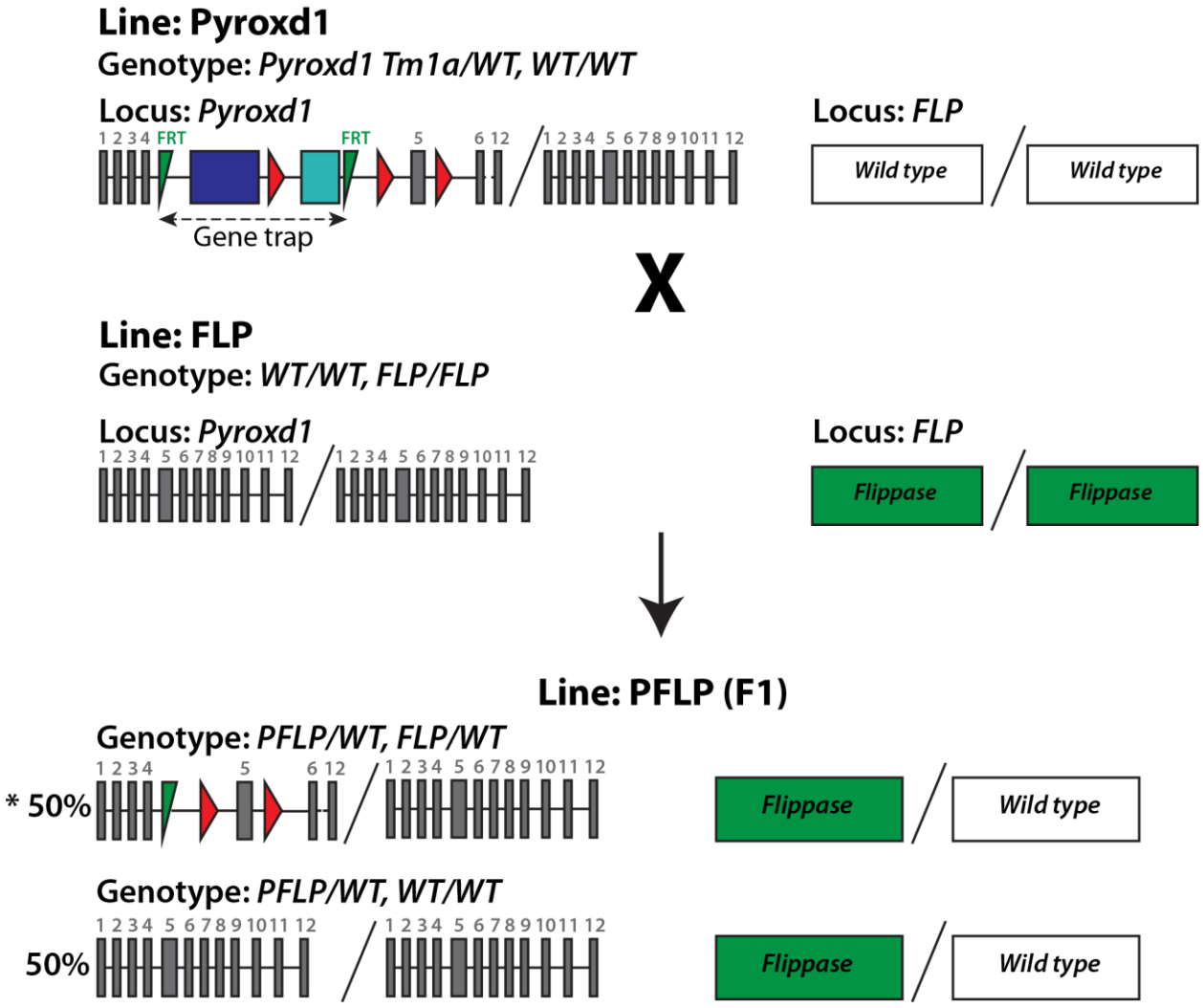

Figure 4.25: Breeding schematic to remove the gene trap from the *Pyroxd1 Tm1a* allele. Heterozygous Pyroxd1 mice were crossed with homozygous FLP mice. Flippase removes the genetrap cassette reverting the *Pyroxd1 Tm1a* allele to wild-type. A new mouse line is generated - PFLP. Predicted litter genotype proportions are marked as percentages and the desired genotype indicated with an asterisk. FRT – flippase recognition target, blue – LacZ, red – loxP site, cyan – promotor driven neomycin resistance gene, F1 – generation one, numbering in grey indicate exons, horizontal filled lines indicate introns.

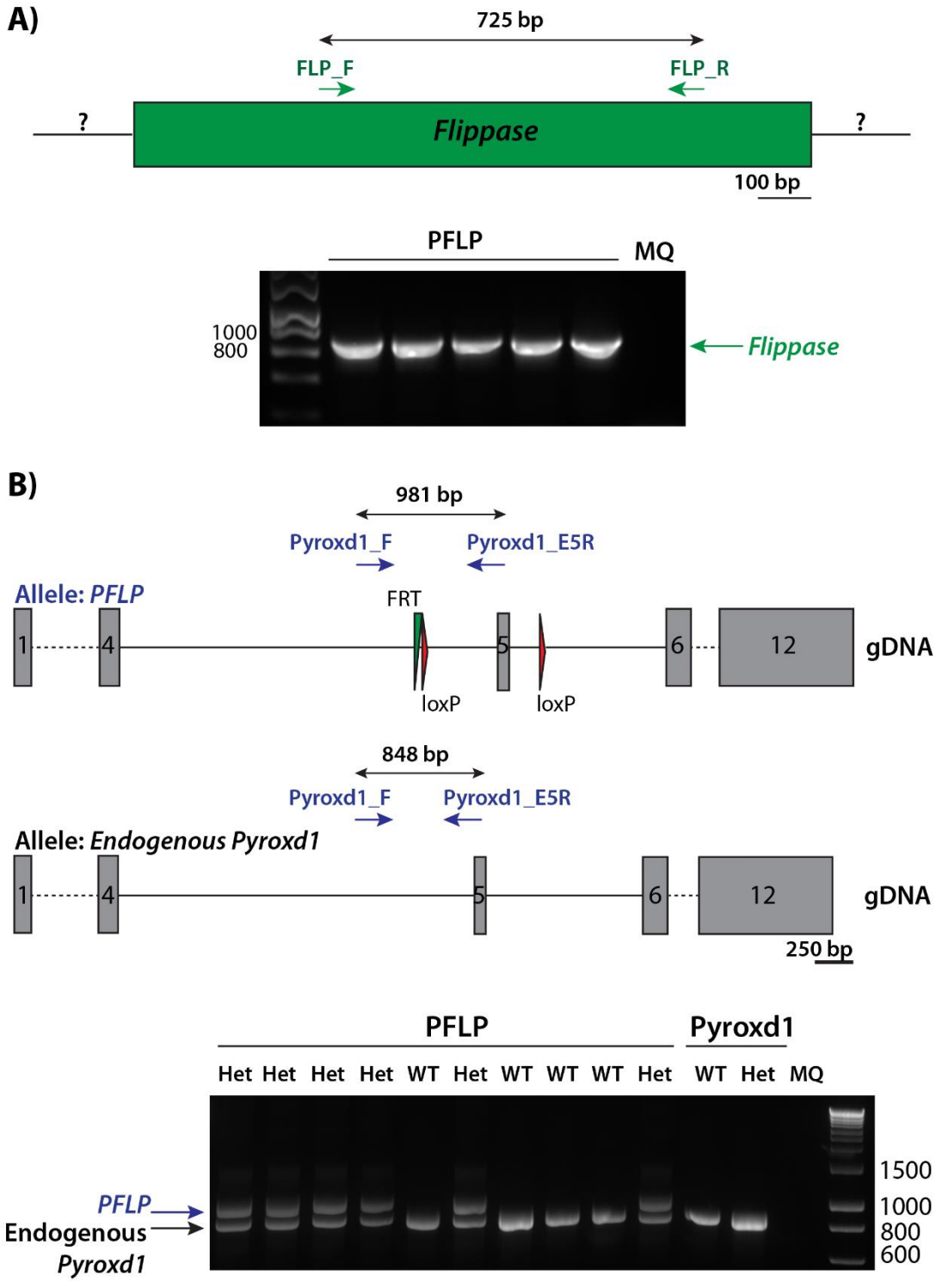
A)
725 bp
FLP_F
FLP_R
?
Flippase
?
100 bp
PFLP
MQ
1000
800
Flippase
B)
981 bp
Pyroxd1_F
Pyroxd1_E5R
Allele: PFLP
FRT
1
4
5
6
12
gDNA
loxP
loxP
848 bp
Pyroxd1_F
Pyroxd1_E5R
Allele: Endogenous Pyroxd1
1
4
5
6
12
gDNA
250 bp
PFLP
Pyroxd1
Het Het Het Het WT Het WT WT WT Het WT Het MQ
PFLP
Endogenous
Pyroxd1
1500
1000
800
600

Figure 4.26 Genotyping of the *FLP* and *PFLP* alleles. (A) Screening of the *FLP* allele. ***Upper:*** To scale schematic of the *FLP* allele. Primer locations are indicated in green arrows (the start of each arrow marks the primer's start location, remainder of arrow is not to scale) and PCR product size above. ***Lower:*** Representative agarose gel of PCR products from PFLP (F1) screening for the *FLP* transgene. MQ – MilliQ water; **(B) Screening of the *PFLP* and endogenous *Pyroxd1* alleles.** ***Upper:*** To scale schematic of the *PFLP* and endogenous *Pyroxd1* alleles with primer locations indicated by blue arrows (the start of each arrow marks the primer's start location, remainder of arrow is not to scale) and PCR product sizes indicated above respective alleles. Dashed lines – not to scale, FRT – flippase recognition site, loxP – loxP sequence, grey numbering indicate exons, horizontal filled lines indicate introns. ***Lower:*** Representative agarose gel of PCR products from PFLP (F1) – lanes 1-10; controls – lanes 11-13: Pyroxd1 wild type (WT), Pyroxd1 heterozygous (het) and MilliQ (MQ); base pair ladder – lane 14. The upper band indicates the *PFLP* allele and the lower band indicates the endogenous *Pyroxd1* allele. The primers and PCR conditions utilised to screen for *PFLP* and *endogenous Pyroxd1* alelles were designed such that the *Pyroxd1 Tm1a* allele would not be detected (PCR amplicon is 7885bp – too long to be amplified effectively with a 60 second extension at 72^{o}C).

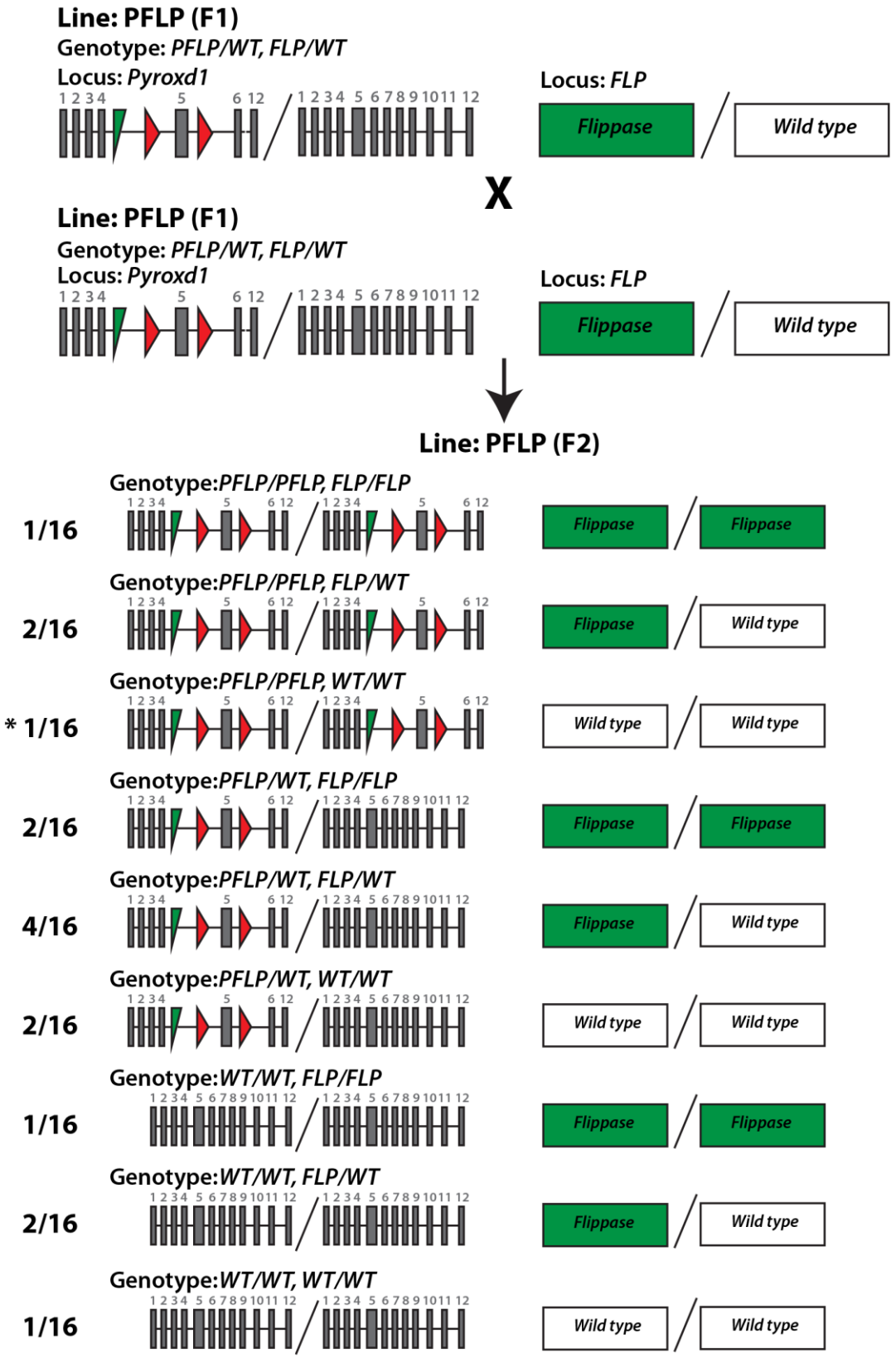
Line: PFLP (F1)
Genotype: PFLP/WT, FLP/WT
Locus: Pyroxd1
1 2 3 4 5 6 12 / 1 2 3 4 5 6 7 8 9 10 11 12
Locus: FLP
Flippase / Wild type
X
Line: PFLP (F1)
Genotype: PFLP/WT, FLP/WT
Locus: Pyroxd1
1 2 3 4 5 6 12 / 1 2 3 4 5 6 7 8 9 10 11 12
Locus: FLP
Flippase / Wild type
Line: PFLP (F2)
1/16 Genotype:PFLP/PFLP, FLP/FLP
1 2 3 4 5 6 12 / 1 2 3 4 5 6 12
Flippase / Flippase
2/16 Genotype:PFLP/PFLP, FLP/WT
1 2 3 4 5 6 12 / 1 2 3 4 5 6 12
Flippase / Wild type
* 1/16 Genotype:PFLP/PFLP, WT/WT
1 2 3 4 5 6 12 / 1 2 3 4 5 6 12
Wild type / Wild type
2/16 Genotype:PFLP/WT, FLP/FLP
1 2 3 4 5 6 12 / 1 2 3 4 5 6 7 8 9 10 11 12
Flippase / Flippase
4/16 Genotype:PFLP/WT, FLP/WT
1 2 3 4 5 6 12 / 1 2 3 4 5 6 7 8 9 10 11 12
Flippase / Wild type
2/16 Genotype:PFLP/WT, WT/WT
1 2 3 4 5 6 12 / 1 2 3 4 5 6 7 8 9 10 11 12
Wild type / Wild type
1/16 Genotype:WT/WT, FLP/FLP
1 2 3 4 5 6 7 8 9 10 11 12 / 1 2 3 4 5 6 7 8 9 10 11 12
Flippase / Flippase
2/16 Genotype:WT/WT, FLP/WT
1 2 3 4 5 6 7 8 9 10 11 12 / 1 2 3 4 5 6 7 8 9 10 11 12
Flippase / Wild type
1/16 Genotype:WT/WT, WT/WT
1 2 3 4 5 6 7 8 9 10 11 12 / 1 2 3 4 5 6 7 8 9 10 11 12
Wild type / Wild type

Figure 4.27: Breeding schematic to remove the *FLP* transgene and generate homozygous PFLP mice. PFLP (F1) heterozygous for *PFLP* and heterozygous for *FLP* were intercrossed to generate homozygous *PFLP* mice lacking the *FLP* allele. The progeny of this cross - PFLP (F2) have predicted litter genotype proportions marked as fractions and the desired genotype indicated with an asterisk. Green triangle – FRT site, red triangle – loxP site, numbering in grey indicate exons, F1 – generation 1, F2 – generation 2.

Second breeding strategy: Knock-out of Pyroxd1 in skeletal muscle

Background

The first breeding strategy was successful in generating the parental line – PFLP, where exon 5 of *PFLP* is flanked by LoxP sites. The second breeding strategy was designed to generate a *Pyroxd1* skeletal-muscle knock-out mouse model, utilising the Cre-*loxP* system controlled by *MyoD*.

The Cre-*loxP* system makes use of the cre enzyme which originates from bacteriophage P1 and cuts *loxP* sites – 5'ATAACTTCGTATAGCATACATTATACGAAGTTAT3', removing the intervening sequence (Sauer & Henderson, 1988). Exposure of the *PFLP* allele to cre recombinase results in cre cutting the *loxP* sites flanking exon 5 of *Pyroxd1*, removing the intervening sequence inclusive of exon 5. Removing exon 5 of *Pyroxd1* generates a frameshift with a premature stop codon within exon 6 at base pair 409. The premature stop codon is predicted to trigger nonsense-mediated decay of the *Pyroxd1* mRNA transcript. Degradation of *Pyroxd1* mRNA by nonsense-mediated decay would result in no Pyroxd1 protein generated from that allele. If nonsense-mediated decay is not triggered the, predicted, truncated Pyroxd1 protein formed would be p.Gln135fsValX (Figure 4.28); lacking oxidoreductase and nitrile reductase domains, and likely non-functional.

To allow skeletal muscle specific knock-out of *Pyroxd1* we chose to cross the PFLP mouse with a MyoD-cre transgenic mouse line (MDC) generated by J. C. Chen, Mortimer, Marley, and Goldhamer (2005). The MDC mouse line expresses *Cre* under the control of the human *MyoD* promotor and core enhancer (J. C. Chen et al., 2005) (Figure 4.30). *MyoD* encodes myoblast determination protein 1 (MyoD), a muscle-specific transcription factor that plays an important role directing skeletal muscle differentation. Transcription of skeletal-muscle

specific genes is activated by MyoD (Davis, Weintraub, & Lassar, 1987). Cre enzyme activity from MDC is first detected at E9.5, in the branchial arches (J. C. Chen et al., 2005). The branchial arches contain muscle progenitors, from which facial muscles develop (J. C. Chen et al., 2005). By E12.5, cre enzyme activity from MDC is seen extensively in limb and trunk muscles (J. C. Chen et al., 2005).

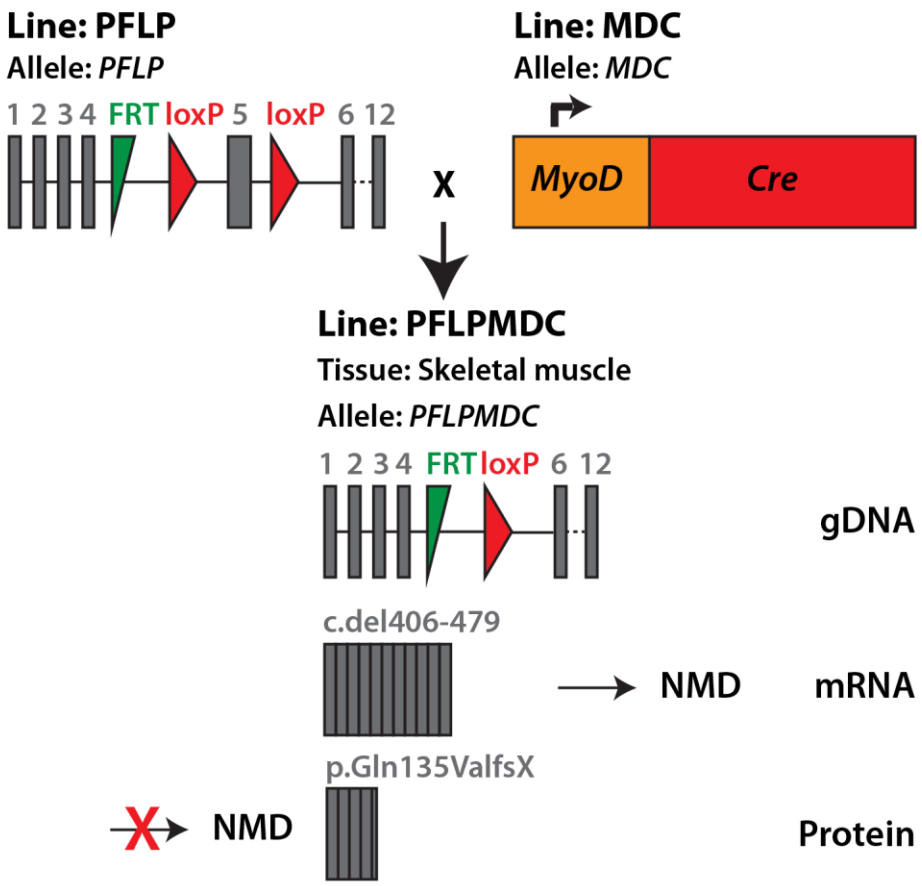

Figure 4.28: Predicted allele modification to establish a *Pyroxd1* knock-out allele in skeletal muscle. Crossing the PFLP mouse line - expressing the *PFLP* allele, with the MDC mouse line - expressing cre recominase under the control of skeletal-muscle specific promotor MyoD (black arrow), is predicted to generate a *Pyroxd1* knock-out allele in skeletal muscle - *PFLPMDC*. Cre cuts the *loxP* sites flanking exon 5 of *Pyroxd1*, removing exon 5. Removal of exon 5 - base pairs 406-479 - is out of frame. The premature stop codon within exon 6 (base pair 409) is predicted to induce nonsense-mediated decay of the *Pyroxd1* mRNA transcript. If nonsense mediated decay is not activated, a truncated Pyroxd1 protein would be produced of 136 amino acids – p.Gln135fsValX. The resulting line – PFLPMDC - is expected to carry the *PFLPMDC* allele only within skeletal muscle. PFLPMDC is expected to carry the *PFLP* allele in all tissues other than skeletal muscle. FRT – flippase recognition target, loxP – lox sequence, numbering in grey indicate exons, horizontal filled lines indicate introns.

Breeding step one: Introducing MyoD-Cre into the PFLP line

The first breeding step of the second breeding strategy required crossing of mice homozygous for PFLP (PFLP$^{PFLP/PFLP,\ WT/WT}$), with mice heterozygous for MyoD-Cre (MDC$^{+/-}$) (Figure 4.29). We chose to breed with MDC$^{+/-}$ mice as we did not know the integration site of the *MDC* transgene. We therefore reasoned that one copy of the *MDC* allele would limit off-target effects, and cre activity from one *MDC* allele would be sufficient for modification of the *PFLP* allele. The resulting progeny were a new line, PFLPMDC. Predicted genotype ratios of PFLPMDC (F1) were 50% PFLPMDC$^{PFLP/WT,\ MDC/WT}$ and 50% PFLPMDC$^{PFLP/WT,\ WT/WT}$. We wished to use PFLPMDC$^{PFLP/WT,\ MDC/WT}$ in the next breeding step. We expected PFLPMDC$^{PFLP/WT,\ MDC/WT}$ mice to have a MyoD-Cre modified knock-out *PFLPMDC* allele only in skeletal muscle.

Genotyping of PFLPMDC F1 progeny (Figure 4.30) required three PCRs to determine the presence of: (1) *PFLP* and endogenous *Pyroxd1* alleles (as before, Figure 4.30A); (2) the *MDC* allele (using intragenic primers, Figure 4.30B); and (3) the cre-modified knock-out allele *PFLPMDC* allele. Expected Mendelian ratios were observed among F1 PFLPMDC, progeny, 50% PFLPMDC$^{PFLP/WT,\ MDC/WT}$. PFLPMDC$^{PFLP/WT,\ WT/WT}$, (chi-squared, *p*-value = 1).

The gDNA used for genotyping originated from the earclip of 4 week old mice. If *MyoD* tightly restricted *cre* expression to the skeletal muscle, we would not expect any cre-mediated modification to the *PFLP* allele in the earclip. We investigated this by screening for the modified knock-out *PFLPMDC* allele (Figure 4.30C) utilising a forward primer within the *FRT* site and a reverse primer within the 3' *loxP* site.

In gDNA isolated from ear-clips, we detected the *PFLPMDC* allele. We observed the presence of a weak *PFLPMDC* PCR product (Figure 4.30C, lower band), which was confirmed by

Sanger sequencing (results not shown). Presence of the *PFLPMDC* allele was observed in ear clips from each mouse positive for *MDC.* The presence of detectable levels of the *PFLPMDC* allele was observed irrespective of which parent donated the *MDC* allele – dam or sire. The PCR reaction produced two products: a 904 bp band corresponding to the unmodified *PFLP* allele; and a 144 bp band corresponding to the knockout *PFLPMDC* allele. We observed a weak *PFLPMDC* band, suggesting a small subset of *PFLP* alleles had been modified by cre. The presence of low levels of cre-recombination within the earclip, suggests cre recombinase activity is not restricted to skeletal muscle.

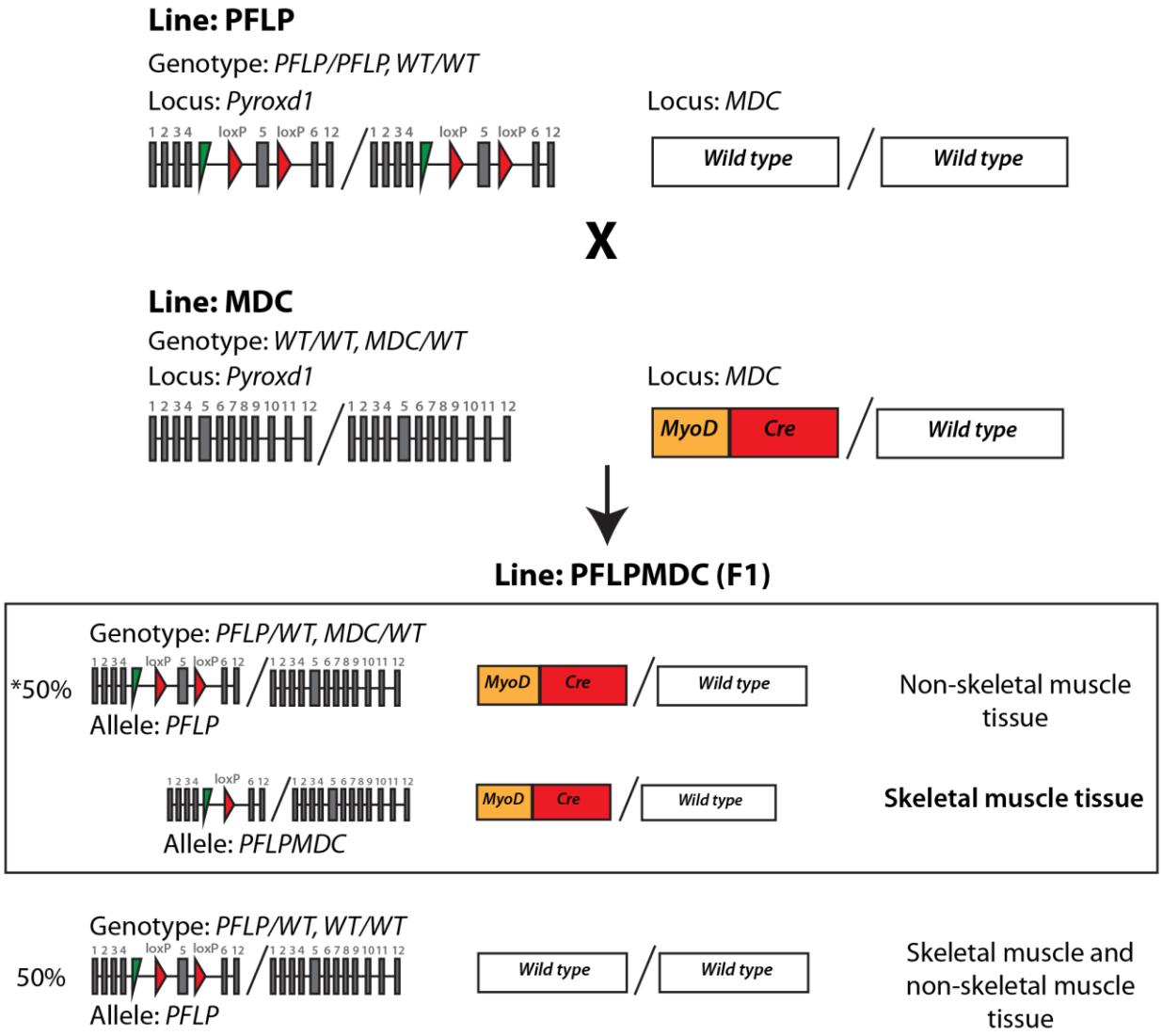

Figure 4.29: Breeding schematic to generate PFLPMDC F1. Homozygous PFLP – homozygous for the *PFLP* allele and wild-type homozygous for *MDC*, were crossed with heterozygous MDC – homozygous for endogenous *Pyroxd1* and heterozygous for *MDC*. *MDC* expresses *cre* under the control of skeletal muscle specific promotor *MyoD*. A new mouse line is generated – PFLPMDC generation one (F1). Predicted litter genotype proportions are marked as percentages and the desired genotype indicated with an asterisks. *PFLP/WT, MDC/WT*, mice are predicted to have cre activity only in the skeletal muscle. Cre cuts the *loxP* sites flanking exon 5 of *Pyroxd1*, removing exon 5 and inducing a knock-out allele– *PFLPMDC*. Green triangle - *FRT* site, red triangle – *loxP* site, numbering in grey indicate exons, horizontal filled lines indicate introns.

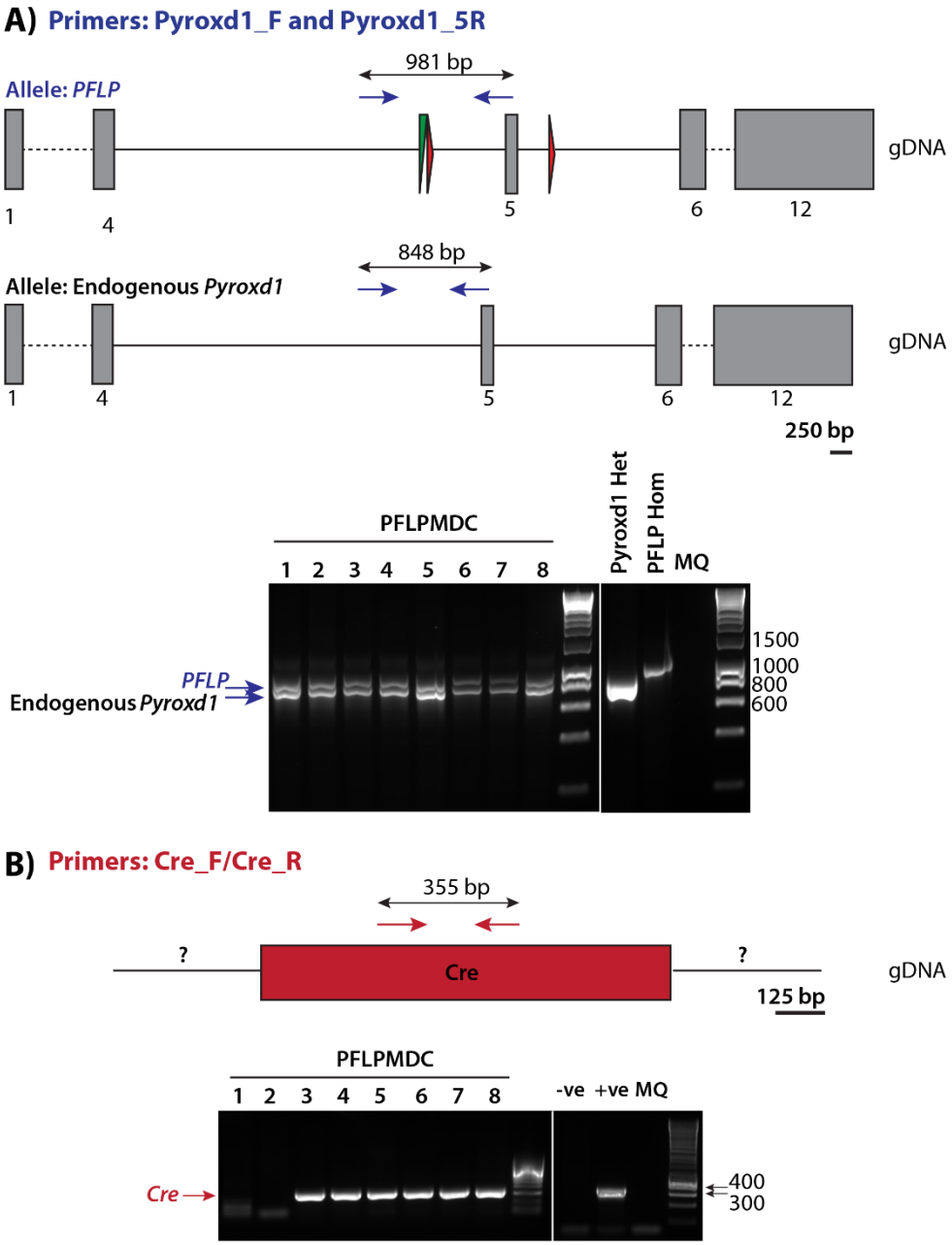

Figure 4.30: Cre recombinase activity is not restricted to skeletal muscle. (A) Screening for *PFLP* and *endgoneous Pyroxd1* - *Upper:* To scale schematic of the *PFLP* and endogenous *Pyroxd1* alleles with primer locations indicated by blue arrows (the start of each arrow marks the primer's start location, the remainder of the arrow is not to scale) and the PCR product sizes are indicated above the respective alleles. ***Lower:*** Representative agarose gel of PCR products from PFLPMDC generation one (F1). Lanes 1-8 – heterozygous PFLPMDC; Lanes 9 & 13 – base pair ladder; Lanes 10-12 - controls: Pyroxd1 heterozygous (Het), PFLP homozygous (hom) and MilliQ (MQ); The upper band indicates the *PFLP* allele and the lower band indicates the endogenous *Pyroxd1* allele.

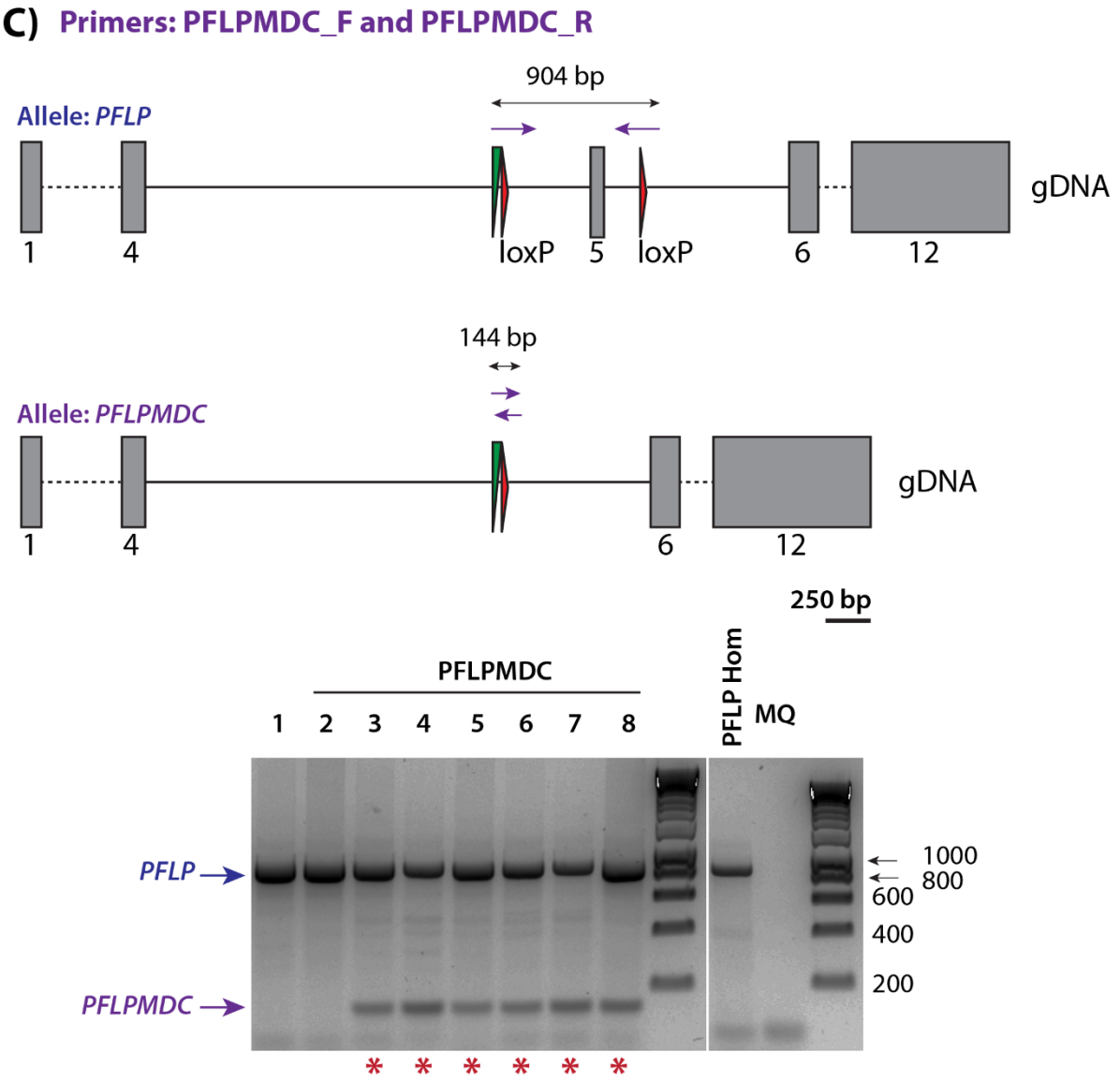

(B) Screening for *MDC* - *Upper:* To scale schematic of the *MDC* allele. Primer locations are indicated in red arrows (the start of each arrow marks the primer's start location, the remainder of the arrow is not to scale) and the PCR product size is indicated above. ***Lower:*** Representative agarose gel of PCR products from PFLPMDC (F1) screening for the *MDC*; Lanes 1-2 – PFLPMDC negative for *MDC;* Lanes 3-8 – PFLPMDC positive for *MDC*; Lanes 9 & 13 – base pair ladders; Lanes 10-12 – controls. **(C) Screening for *PFLPMDC* - *Upper***: To scale schematic of the *PFLP* and *PFLPMDC* alleles with primer locations indicated by purple arrows and PCR product sizes indicated above respective alleles. ***Lower:*** Representative colour-inverted agarose gel of PCR products from PFLPMDC (F1). The upper band indicates the *PFLP* allele and the lower band indicates the *PFLPMDC* allele. Red asterisks indicate samples positive for *MDC.* Lanes 1-2 – negative for *PFLPMDC*; Lanes 3-8 – positive for *PFLPMDC*; Lane 9 & 13 – base pair ladder; Lanes 10-12 – controls. Horizontal lines indicate introns, dashed lines – not to scale, grey boxes indicate exons, green triangle – *FRT* site, red triangle – *loxP* site.

Breeding step two: Generating PFLPMDC$^{\mathbf{PFLP/PFLP,\ MDC/WT}}$ mice

The next breeding step aimed to generate PFLPMDC$^{PFLP/PFLP,\ MDC/WT}$ mice. We crossed PFLPMDC$^{PFLP*/WT,\ MDC/WT}$ with PFLP$^{PFLP/PFLP}$, where *PFLP** refers to mice with low levels of the *PFLPMDC* allele in their earclip (Figure 4.31). As modification of the *PFLP* allele knocks-out *Pyroxd1,* we were anticipating low levels of modification in the earclip (see Figure 3.30) represented only low levels of modification to the *PFLP* allele in non-skeletal muscle tissue. Litters from this cross were expected to contain 25% of the desired experimental genotype, PFLPMDC$^{PFLP/PFLP,\ MDC/WT}$ - homozygous for *PFLP*, carrying one copy of *MDC* which is expected to induce skeletal muscle knock-out of *Pyroxd1*.

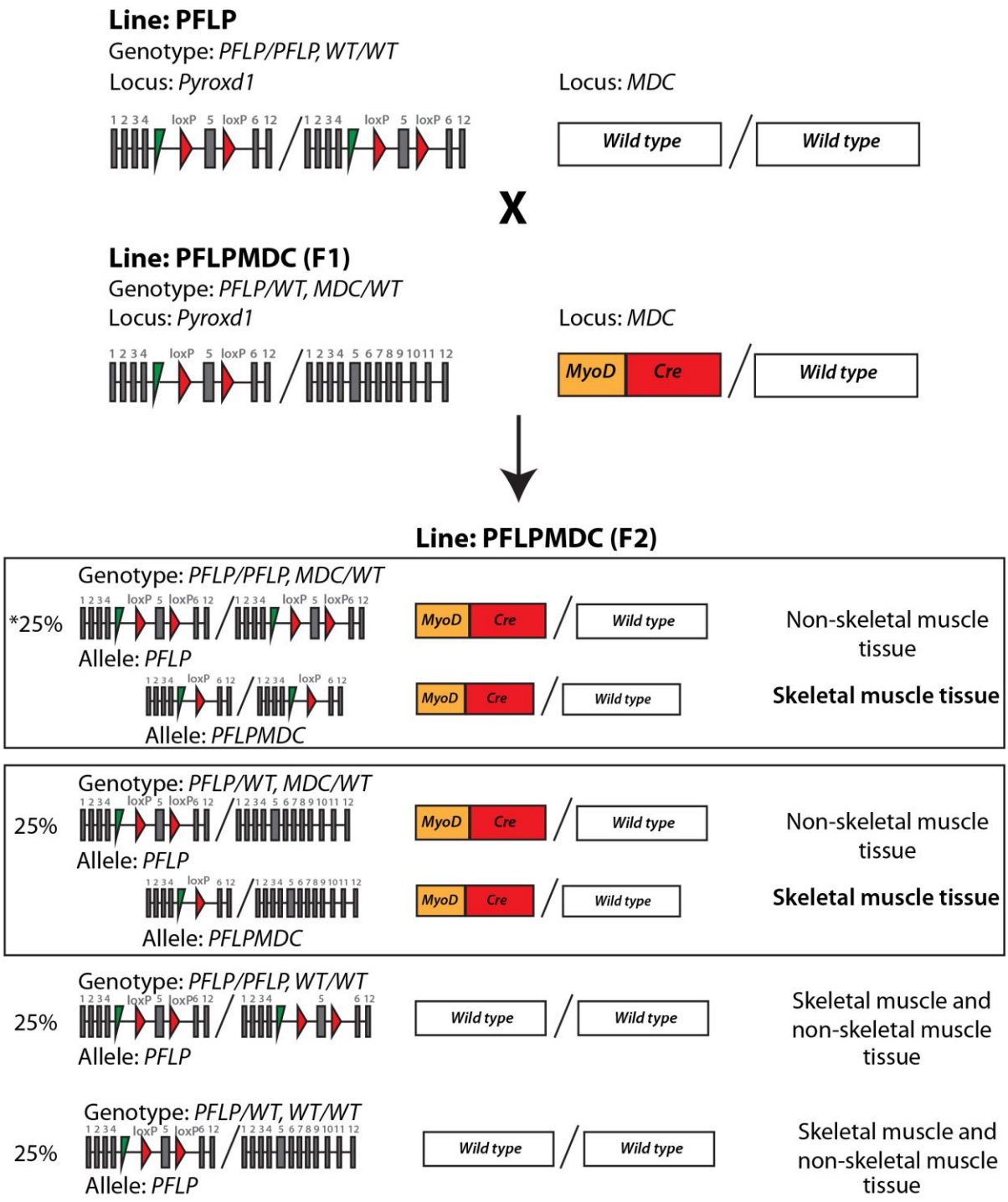

Figure 4.31: Breeding schematic to generate PFLPMDC F2. Homozygous PFLP – homozygous for the *PFLP* allele and wild-type homozygous for *MDC*, were crossed with PFLPMDC (F1) - heterozygous for *PFLP* and heterozygous for *MDC*. *MDC* expresses *cre* under the control of skeletal muscle specific promotor *MyoD*. PFLPMDC generation two (F2) progeny have predicted litter genotype proportions marked as percentages and the desired genotype indicated with an asterisks. *PFLP/PFLP, MDC/WT* and *PFLP/WT, MDC/WT* mice are predicted to have 100% of the *PFLP* allele modified to the *PFLPMDC* knock-out allele within skeletal muscle. Cre cuts the *loxP* sites flanking exon 5 of *Pyroxd1*, removing exon 5 and inducing a knock-out allele – *PFLPMDC*. Green triangle - *FRT* site, red triangle – *loxP* site, numbering in grey indicate exons, horizontal filled lines indicate introns.

Embryonic litters

We established in section 4.3.2.1 that global knock-out of *Pyroxd1* is embryonic lethal and we now had evidence that cre acted outside of skeletal muscle. The leakiness of cre was confirmed by a second study in our laboratory (*Capns1*, Frances Lemckert unpublished results).

The MyoD-Cre mouse strain has previously been used, with success, while showing cre activity in tissues other than skeletal muscle, including in female gametes (J. C. Chen et al., 2005). Thus we proceeded with care, electing to harvest embryonic animals for genotyping, as mice born unwell can be cannibalised by their mothers.

We crossed female PFLP$^{PFLP/PFLP}$ with male PFLPMDC$^{PFLP*/WT,\ MDC/WT}$, genotyping PFLPMDC (F2) progeny at E10. If homozygous PFLPMDC mice positive for *MDC* are observed at E10 – before the developmental time-point when widespread muscle-specific cre expression occurs (ED12.5 (J. C. Chen et al., 2005)) – this would indicate either: (1) *MDC*-mediated cre activity was not evident by E10; or (2) *MDC*-mediated cre activity prior to E10 was compatible with life.

Our results indicate cre is active outside of skeletal muscle by E10. We did not observe a PFLPMDC$^{PFLP/PFLP,\ MDC/WT}$ at E10 (Figure 4.32A & B) (non-mendelian inheritance, χ-squared, *p*-value = 0.04< 0.05) and the *MDC* allele was inherited in non-mendelian ratios (χ-squared, *p*-value = 0.007<0.01). Only 1 out of 11 mice (9%) were positive for *MDC* (Figure 4.32B, red asterisk indicates *MDC*-carrying mouse). We observed mendelian inheritance of the *PFLP* allele (χ-squared, *p*-value = 0.38) (Figure 4.32A, blue asterisks indicate homozygous mice). These results suggest: (1) PFLPMDC$^{PFLP/PFLP,\ MDC/WT}$ are not viable at E10; and (2) Cre activity in the early embryo or gamete(s) may be knocking-out *Pyroxd1* expression.

Activity from the *MDC* allele was not observed in the tail at E10. We did not observe *MDC*-mediated modification to the *PFLP* allele within the sole mouse positive for *MDC* (mouse 3) (Figure 4.32C, red asterisks). Mouse 3 was heterozygous for the *PFLP* allele (Figure 4.32A) and therefore inherited the *PFLP* allele from the PFLP$^{PFLP/PFLP,\ WT/WT}$ dam. This result makes it unlikely that cre activity in the early embryo knocks out *Pyroxd1* expression and is the cause of homozygous lethalities.

Genotyping results of the *PFLPMDC* allele support the hypothesis that cre is active within gametes of the dam or sire, and a null allele is transmitted to the progeny. Evidence supporting cre-activity in gametes is provided through detection of a recombined *PFLP* allele (*PFLPMDC*) in the tail of PFLPMDC$^{PFLP/PFLP,\ WT/WT}$ mice (Figure 4.32C, blue asterisks) that do not have *cre.* PFLPMDC$^{PFLP/PFLP,\ WT/WT}$ mice must have inherited one recombined *PFLP* allele from the PFLPMDC$^{PFLP*/WT,MDC/WT}$ sire. The presence of *PFLPMDC* in all mice who have inherited a *PFLP* allele from the PFLPMDC$^{PFLP*/WT,MDC/WT}$ sire, ie. all mice genotyping homozygous for *PFLP*, suggests all *PFLP* alleles within male gametes have been modified to the *PFLPMDC* knock-out allele. Therefore, the inheritable genotype of male (F1) PFLPMDC$^{PFLP*/WT,MDC/WT}$ mice in reality is PFLPMDC$^{PFLPMDC/WT,\ MDC/WT}$ (Figure 4.33).

Strain: PFLP (F4) female X PFLPMDC (F1) male

Genotype: *PFLP/PFLP, WT/WT* *PFLP/WT, MDC/WT*

Progeny: PFLPMDC (F2) E10

A) Primers: Pyroxd1_F2 and Pyroxd1_R2

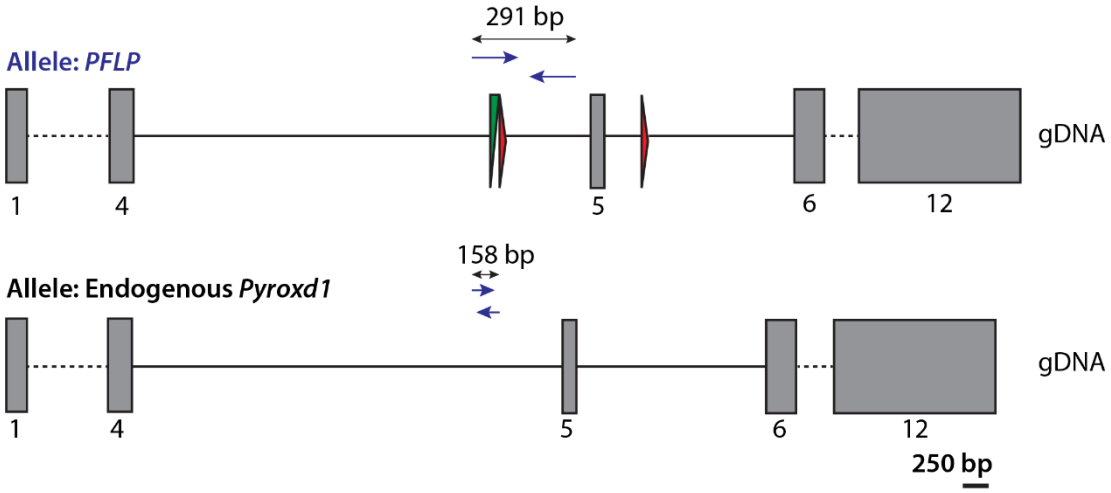

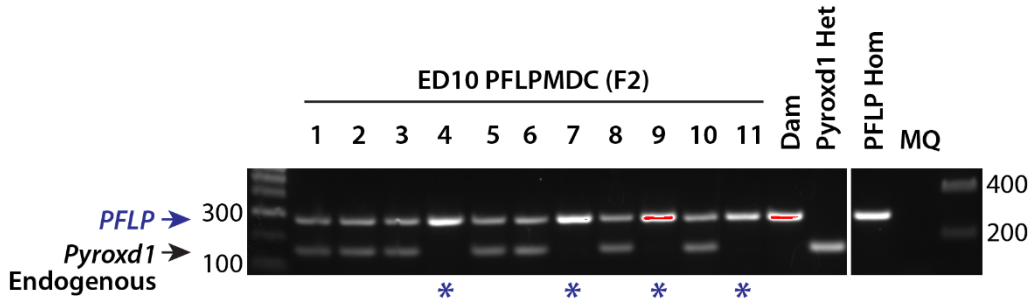

B) Primers: Cre_F2/Cre_R2

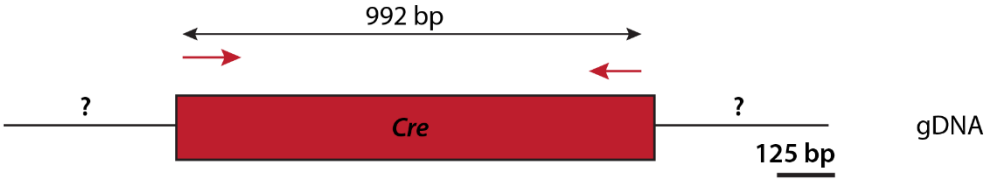

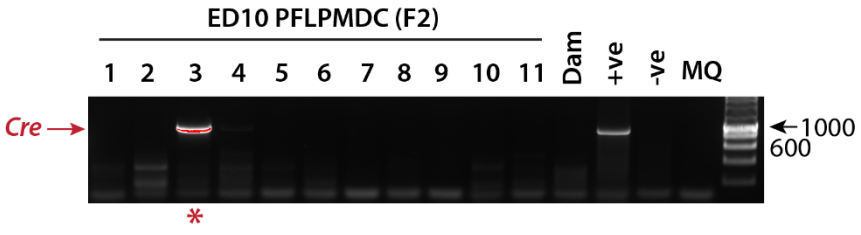

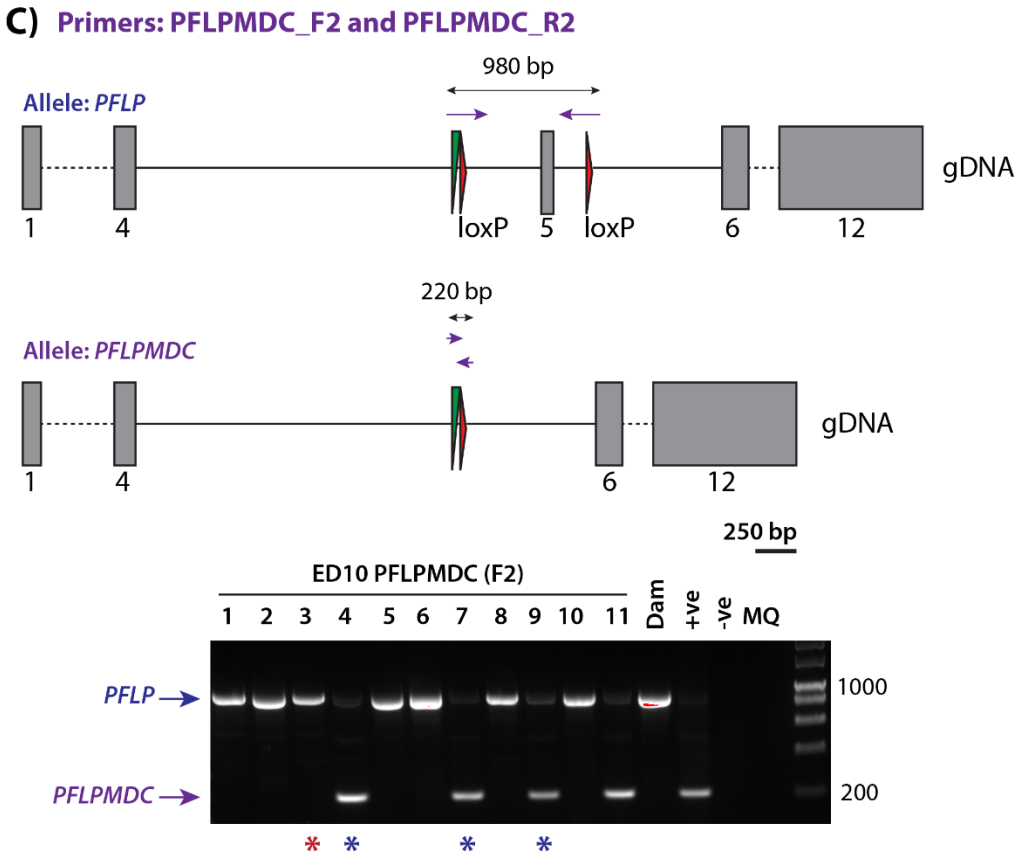

Figure 4.32: *PFLPMDC* is present in male gametes. (A) Screening for *PFLP* and *endogenous Pyroxd1* - *Upper:* To scale schematic of the *PFLP* and endogenous *Pyroxd1* alleles with primer locations indicated by blue arrows and the PCR product sizes indicated above respective alleles. ***Lower:*** Agarose gel of PCR products from PFLPMDC generation two (F2) at E10): Lanes 2-12 – PFLPMDC (F2); Lane 12-16 – controls: Mother (Dam), Pyroxd1 heterozygous (Het), PFLP homozygous (Hom) and MilliQ (MQ); Lanes 1 & 17 – base pair ladder; The upper band indicates the *PFLP* allele and the lower band indicates the endogenous *Pyroxd1* allele. Blue asterisks indicate *PFLP* homozygotes. **(B) Screening for *MDC* - *Upper:*** To scale schematic of the *MDC* allele. Primer locations are indicated in red arrows and PCR product size above. ***Lower:*** Agarose gel of PCR products from PFLPMDC generation two (F2) at E10: Lanes 1-11 – PFLPMDC (F2); Lanes 12-15 – controls; Lane 16 – base pair ladder. **(C) Screening for *PFLPMDC* - *Upper***: To scale schematic of the *PFLP* and *PFLPMDC* alleles with primer locations indicated by purple arrows and PCR product sizes indicated above respective alleles. ***Lower:*** Agarose gel of PCR products from PFLPMDC generation two (F2) at E10. The upper band indicates the *PFLP* allele and the lower band indicates the *PFLPMDC* allele. Red asterisks indicate samples positive for *MDC.* Blue asterisks indicate samples absent for *MDC* and positive for *PFLPMDC.* Lanes 1-11 – PFLPMDC (F2); Lanes 12-15 – controls; Lane 16 – base pair ladder. Horizontal lines indicate introns, dashed lines – not to scale, grey boxes indicate exons, green triangle – *FRT* site, red triangle – *loxP* site. The start of each arrow marks the primer's start location, remainder of arrow is not to scale.

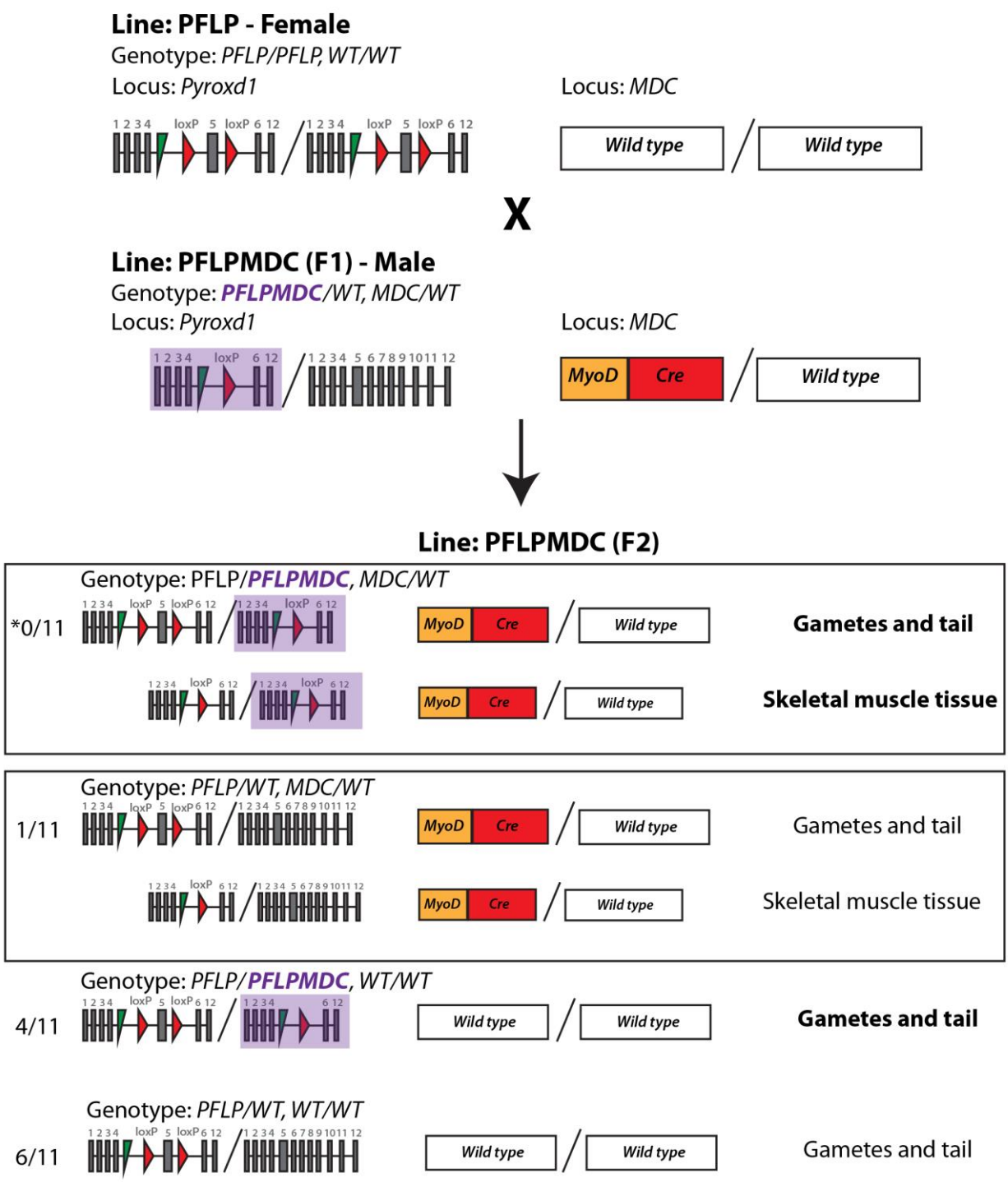
Line: PFLP - Female
Genotype: PFLP/PFLP, WT/WT
Locus: Pyroxd1
Locus: MDC
1 2 3 4 loxP 5 loxP 6 12 / 1 2 3 4 loxP 5 loxP 6 12
Wild type / Wild type
X
Line: PFLPMDC (F1) - Male
Genotype: PFLPMDC/WT, MDC/WT
Locus: Pyroxd1
Locus: MDC
1 2 3 4 loxP 6 12 / 1 2 3 4 5 6 7 8 9 10 11 12
MyoD Cre / Wild type
Line: PFLPMDC (F2)
Genotype: PFLP/PFLPMDC, MDC/WT
*0/11
MyoD Cre / Wild type
Gametes and tail
MyoD Cre / Wild type
Skeletal muscle tissue
Genotype: PFLP/WT, MDC/WT
1/11
MyoD Cre / Wild type
Gametes and tail
MyoD Cre / Wild type
Skeletal muscle tissue
Genotype: PFLP/PFLPMDC, WT/WT
4/11
Wild type / Wild type
Gametes and tail
Genotype: PFLP/WT, WT/WT
6/11
Wild type / Wild type
Gametes and tail

Figure 4.33: Breeding schematic of actual PFLPMDC (F2). ***Parental lines:*** Homozygous female PFLP (F4) – homozygous for the *PFLP* allele and wild-type homozygous for *MDC;* based on genotyping results, male PFLPMDC (F1) - heterozygous for *PFLPMDC* and heterozygous for *MDC.* The *PFLPMDC* allele inherited from the sire is tracked in purple. Homozygous PFLPMDC progeny inherited a *PFLP* allele from the dam and a *PFLPMDC* allele from the sire. We expect cre-mediated modification of the *PFLP* allele inherited from the dam to a *PFLPMDC* allele in the skeletal muscle of *MDC* carrying mice. Heterozygous PFLPMDC mice who have inherited a *PFLP* allele from the dam are expected to be modified to *PFLPMDC* only in *MDC* carrying mice. PFLPMDC (F2) litter genotypes are marked as fractions and the desired genotype indicated with an asterisk. Green triangle - *FRT* site, red triangle – *loxP* site, numbering in grey indicate exons, horizontal filled lines indicate introns.

We then reversed the cross. We crossed a male PFLP$^{PFLP/PFLP,\ WT/WT}$ with a female (F1) PFLPMDC$^{PFLP*/WT,\ MDC/WT}$, genotyping PFLPMDC (F2) progeny at E10. This procedure involved a terminal caesarian. The sacrificed PFLPMDC (F1) female carried eight embryonic sacs at E10 (Figure 4.34A). Five embryos were evident. Two embryos had completely reabsorbed by E10 (Figure 4.34A, embryos 2 and 5, white asterisks) and one embryo had been reabsorbed with the aminotic sac remaining (Figure 4.34B, embryo 6). A tail clip was taken for genotyping purposes from all embryos, and from the remaining amniotic sac of embryo 6 (Figure 4.34A, genotyping tissue indicated by schematics). From here-in the amniotic sac of embryo 6 is stated as an embryo and indicated in Figure 4.34 with a dashed white circle.

We observed two PFLPMDC$^{PFLP/PFLP,\ MDC/WT}$ mice at E10 - embryos 3 and 6 (Figure 4.34A and B, blue and red asterisks respectively). We had generated the experimental genotype. Embryo 6 had been reabsorbed by E10. This result indicates that when the *MDC* allele is inherited from the dam, PFLPMDC$^{PFLP/PFLP,\ MDC/WT}$ mice are viable at E10. We observed mendelian inheritance. The *MDC* locus was inherited in a mendelian fashion (Chi-squared, *p*-value = 0.41). We observed four embryos positive for *MDC* (Figure 4.34C, red asterisks) – embryos 3, 4, 6 and 7. The *Pyroxd1* locus was also inherited in a mendelian fashion (Chi-squared, *p*-value = 0.41). We observed four embryos homozygous for the *PFLP* allele (Figure 4.34B, blue asterisks) – embryos 1, 3, 6 and 8. Activity from the *MDC* allele was detected outside of skeletal muscle. However, cre activity from the *MDC* allele was not consistent between embryos. We observed *MDC* activity within the tail of E10 embryo 4. Embryo 4 is PFLPMDC$^{PFLP/WT,\ MDC/WT}$ (Figure 4.34A and B). The *PFLP* allele can only have been inherited by the PFLP$^{PFLP/PFLP,\ WT/WT}$. We observed a weak *PFLPMDC* band in embryo 4 (Figure 4.35C). This raises the possibility that *MDC*-mediated cre is active in all mouse tissues, at low levels. The *PFLPMDC* allele could not have been present in the gametes forming mouse 4. The presence of a strong *PFLP* PCR product in mouse 4 (Figure 4.34B) suggests modification to

the *PFLP* allele is mosaic – *MDC*-mediated cre activity is not evident in all nuclei. Importantly, we did not detect the *PFLPMDC* allele in mouse 7 (Figure 4.34C) which is PFLPMDC$^{PFLP/WT,\ MDC/WT}$.

Our results suggest the MyoD-cre reporter mouse is confounded by 'leaky' expression that can include the gametes of both sire and dam. These preliminary results suggest female gametes are 'less leaky'.

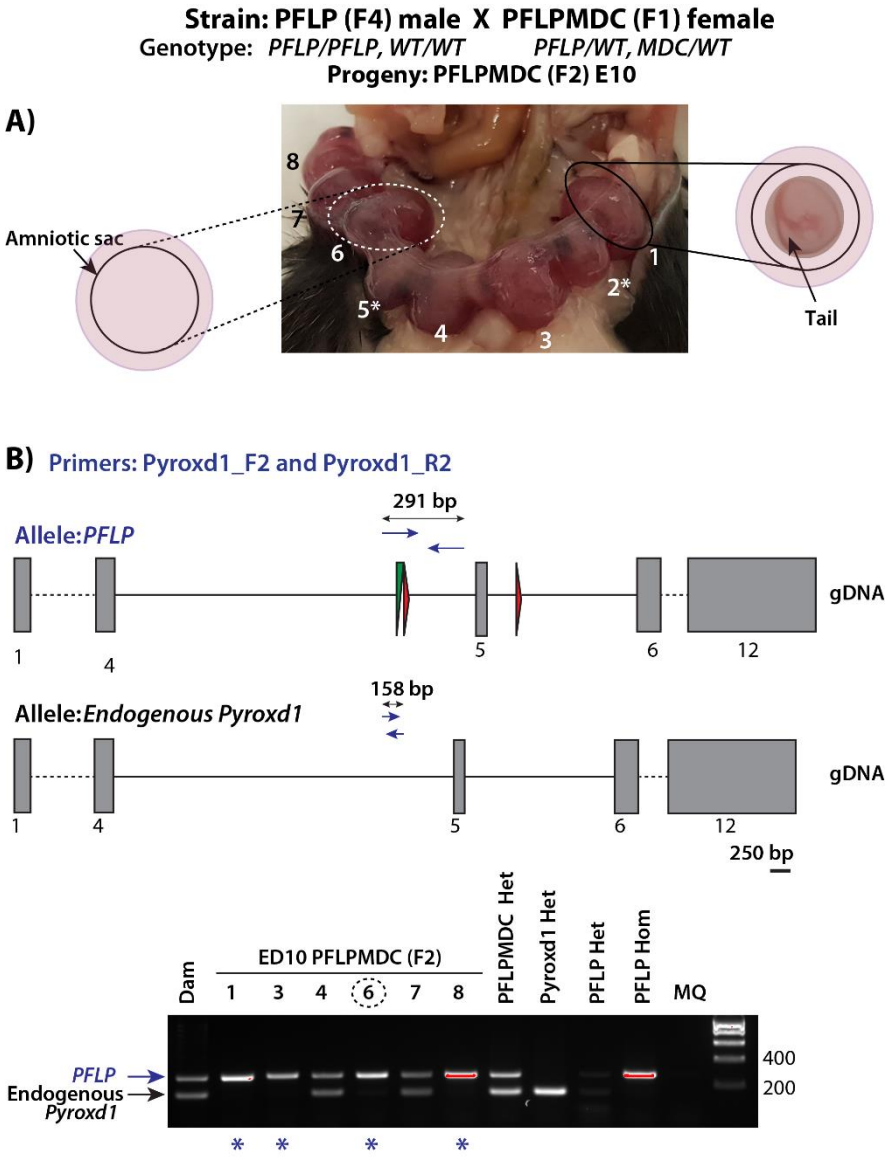

Figure 4.34: Mice homozygous for *PFLP* and positive for *MDC* survive to E10. (A) Embryonic sacs of E10 litter indicating reabsorbed embryos – white asterisks, and schematics indicating genotyping tissues. **(B) Screening for *PFLP* and endogenous *Pyroxd1* - *Upper:*** To scale schematic of the *PFLP* and endogenous *Pyroxd1* alleles with primer locations indicated by blue arrows (the start of each arrow marks the primer's start location, remainder of arrow is not to scale) and PCR product sizes indicated above respective alleles. ***Lower:*** Agarose gel of PCR products from PFLPMDC generation two (F2) at E10: Lane 1 – Mother (Dam); Lanes 2-7 – PFLPMDC (F2); Lanes 8-12 – controls: PFLPMDC heterozygoute (Het), Pyroxd1 Het, PFLP Het, PFLP homozygous (Hom) and MilliQ (MQ); Lane 13 – base pair ladder. The upper band indicates the *PFLP* allele and the lower band indicates the endogenous *Pyroxd1* allele. Blue asterisks indicate *PFLP* homozygotes. **(C) Screening for *MDC* - *Upper:*** To scale schematic of the *MDC* allele. Primer locations are indicated in red arrows (the start of each arrow marks the primer's start location, remainder of arrow is not to scale) and PCR

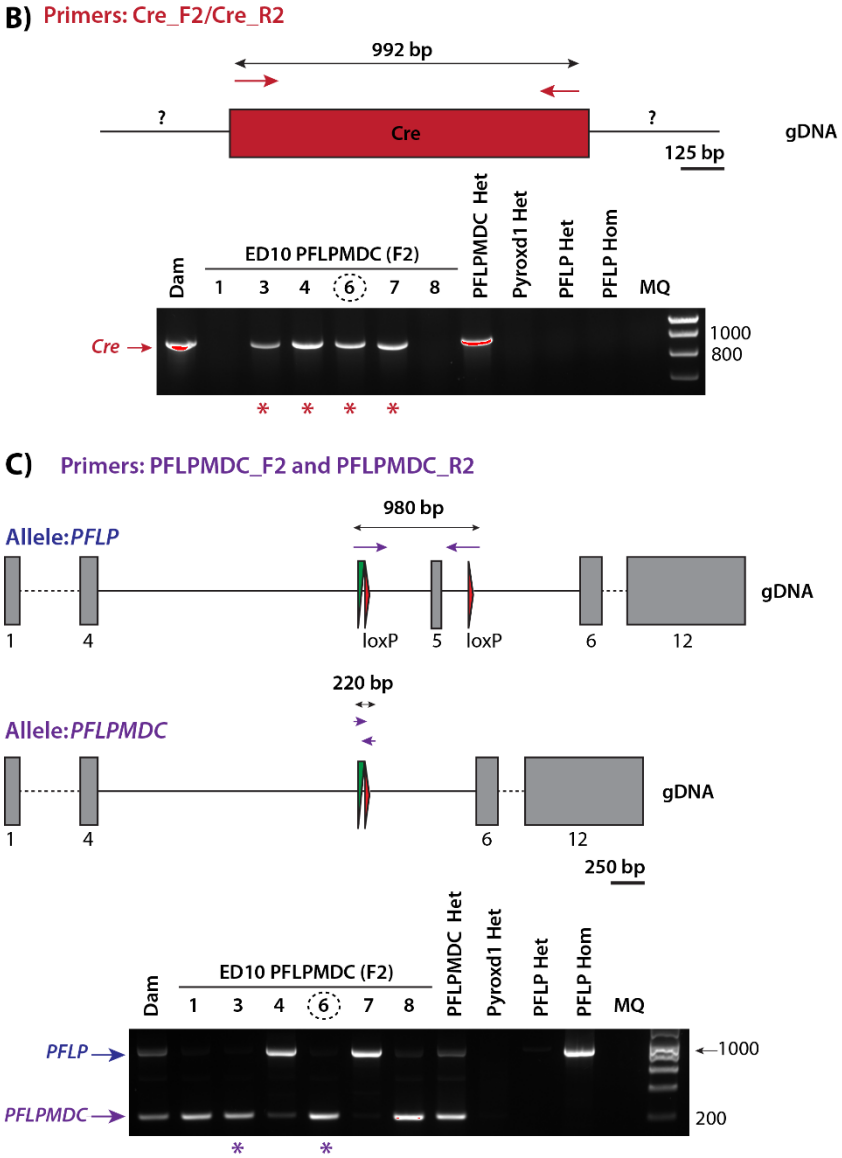

product size above. ***Lower:*** Agarose gel of PCR products from PFLPMDC generation two (F2) at embryonic day 10 (E10): Lane 1 – Mother (Dam); Lanes 2-7 – PFLPMDC (F2); Lanes 8-12– controls: PFLPMDC heterozygote (Het), Pyroxd1 Het, PFLP Het, PFLP homozygous (Hom) and MilliQ (MQ); Lane 13 – base pair ladder. Red asterisks indicate *MDC* positive mice; **(D) Screening for *PFLPMDC* - *Upper***: To scale schematic of the *PFLP* and *PFLPMDC* alleles with primer locations indicated by purple arrows (the start of each arrow marks the primer's start location, remainder of arrow is not to scale) and PCR product sizes indicated above respective alleles. ***Lower:*** Agarose gel of PCR products from PFLPMDC generation two (F2) at embryonic day 10 (E10): Lane 1 – Mother (Dam); Lanes 2-7 – PFLPMDC (F2); Lanes 8-12 – controls: PFLPMDC heterozygoute (Het), Pyroxd1 Het, PFLP Het, PFLP homozygous (Hom) and MilliQ (MQ); Lane 13 – base pair ladder. The upper band indicates the *PFLP* allele and the lower band indicates the *PFLPMDC* allele. Purple asterisks indicate mice homozygous for *PFLP* positive for *MDC.* Green triangle – *FRT* site, red triangle – *loxP* site, dashed lines – not to scale, grey boxes indicate exons, horizontal lines indicate introns.

Neonatal litters

The next step was to determine if the experimental genotype was viable at birth. We crossed a male PFLP$^{PFLP/PFLP,\ WT/WT}$ with a female (F1) PFLPMDC$^{PFLPMDC/WT,\ MDC/WT}$, genotyping two litters of PFLPMDC (F2) progeny at day 1 from gDNA extracted from tail clips (Figure 4.35). We anticipated a severe, potentially prenatally lethal, phenotype in mice lacking *Pyroxd1* within skeletal muscle. Three independent studies have identified *PYROXD1* as a gene essential for cell viability (Blomen et al., 2015; Hart et al., 2015; T. Wang et al., 2015). Therefore, we chose to genotype as soon after birth as possible, inkeeping with ethical guidelines of GMO monitoring.

We successfully derived mice with conditional knock-out of *PYROXD1* in skeletal muscle that survive to birth (though likely succumb a few days of age) (Figure 4.35A, blue asterisks indicate homozygous *PFLP* mice and Figure 4.35B, red asterisks indicates *MDC* positive homozygous *PFLP* mice). Two litters were genotyped with 5 and 8 live pups, respectively. The later litter contained 2 of the experimental genotype, PFLPMDC$^{PFLPMDC/PFLP,\ MDC/WT}$. Unfortunately, the two mice of the experimental genotype did not survive past day 2. White milk spots were observed indicating these mice were able to suckle. It is unclear if this is stochastic, environmental or genotype-related. We speculate that death was due to weakness of the diaphragm causing respiratory failure as the mice appeared runty, but no further defining features were observed. (Note: since preparation of this thesis, further skeletal muscle KO mice have been born, with similar results, suggesting survival to birth followed by neonatal lethality).

Across the two litters we observed mendelian inheritance. Mendelian inheritance of the *Pyroxd1* locus (chi-squared, *p*-value = 0.78) and the *MDC* locus (chi-squared, *p*-value = 0.63)

suggested we were not loosing any PFLPMDC$^{PFLP/PFLPMDC,\ MDC/WT}$ mice between E10 and day 1.

As observed in E10 litters, we detected the *PFLPMDC* knock-out allele outside of skeletal muscle and in the absence of *MDC. We* observed the *PFLPMDC* allele in the tail clips of all mice homozygous for *PFLP* (Figure 4.35A and C – mice 4, 5 and 8), where only mouse 8 carries *MDC* (Figure 4.35B red asterisks and Figure 4.35C purple asterisks). This result confirms that the *PFLPMDC* allele is present within female gametes.

We achieved the generation of mouse lines that can be used for future study of Pyroxd1 in fundamental biology and disease. Tissues from this skeletal muscle conditional knock-out of *Pyroxd1* will provide an extremely valuble resource to determine the role and potential substrates of Pyroxd1.

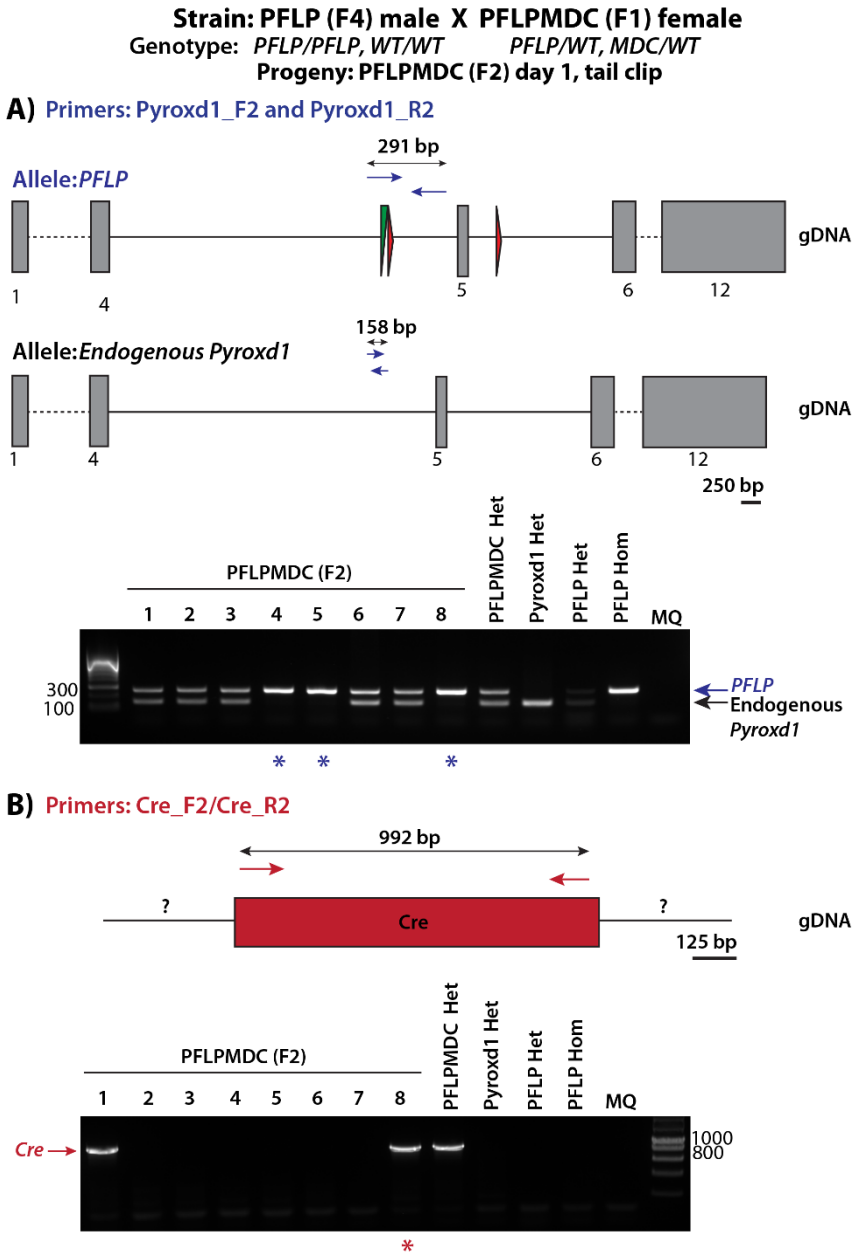

Figure 4.35: Mice homozygous for *PFLP* and positive for *MDC* survive to birth. (A) Screening for *PFLP* and *endogenous Pyroxd1* - *Upper:* To scale schematic of the *PFLP* and endogenous *Pyroxd1* alleles with primer locations indicated by blue arrows (the start of each arrow marks the primer's start location, remainder of arrow is not to scale) and PCR product sizes indicated above respective alleles. ***Lower:*** Agarose gel of PCR products from PFLPMDC generation two (F2) at embryonic day 10 (E10): Lane 1 –base pair ladder; Lanes 2-9 – PFLPMDC (F2); Lanes 10-14 – controls: PFLPMDC heterozygote (Het), Pyroxd1 Het, PFLP Het, PFLP homozygous (Hom) and MilliQ (MQ). The upper band indicates the *PFLP* allele and the lower band indicates the endogenous *Pyroxd1* allele. Blue asterisks indicate *PFLP* homozygotes.

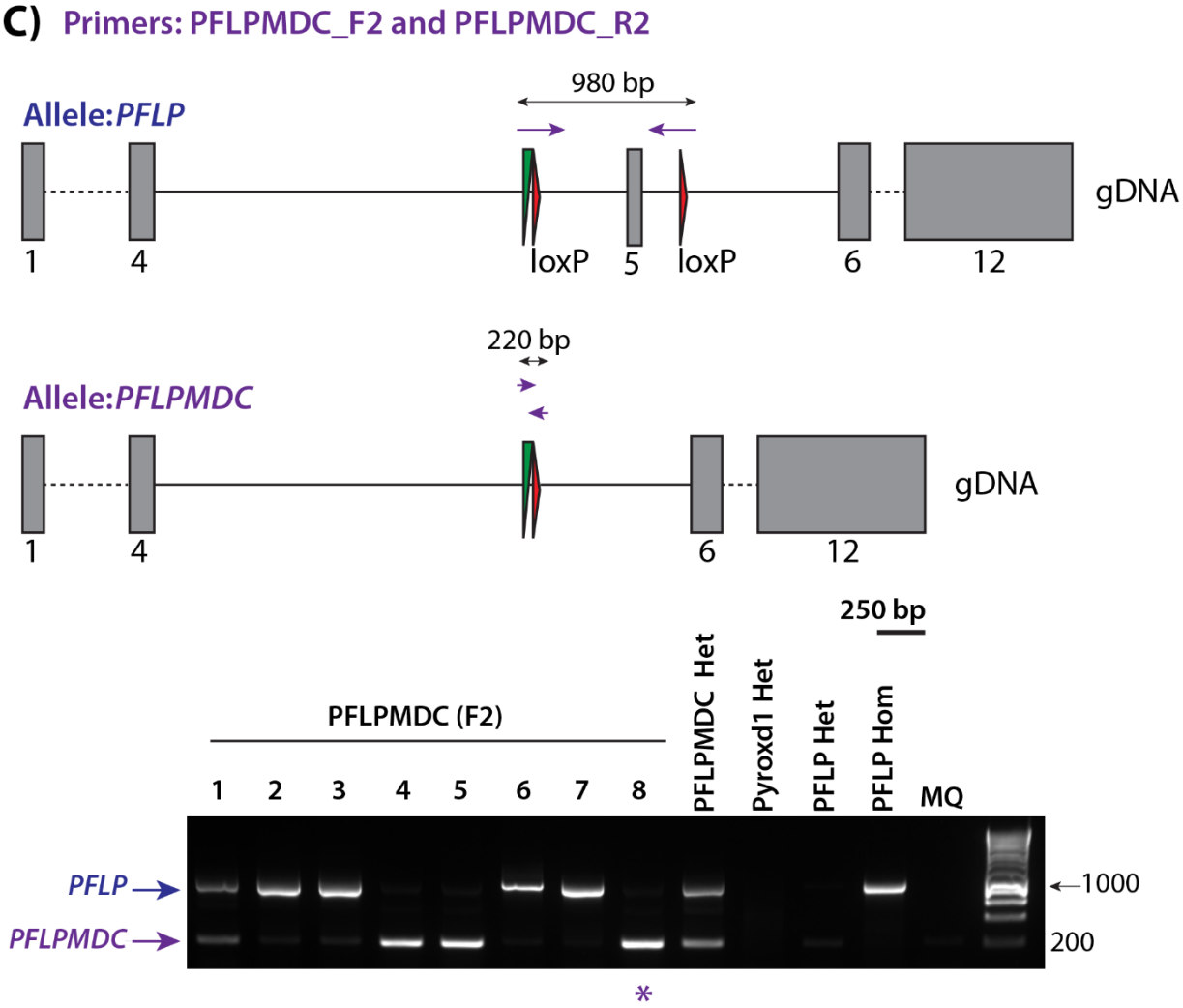

(B) Screening for *MDC* - *Upper:* To scale schematic of the *MDC* allele. Primer locations are indicated by red arrows (the start of each arrow marks the primer's start location, remainder of arrow is not to scale) and PCR product size above. ***Lower:*** Agarose gel of PCR products from PFLPMDC generation two (F2) at embryonic day 10 (E10): Lanes 1-8 – PFLPMDC (F2); Lanes 9-13 – controls: PFLPMDC heterozygote (Het), Pyroxd1 Het, PFLP Het, PFLP homozygous (Hom) and MilliQ (MQ); Lane 14 – base pair ladder. Red asterisks indicate *MDC* positive mice; **(C) Screening for *PFLPMDC* - *Upper***: To scale schematic of the *PFLP* and *PFLPMDC* alleles with primer locations indicated by purple arrows (the start of each arrow marks the primer's start location, remainder of arrow is not to scale) and PCR product sizes indicated above respective alleles. ***Lower:*** Agarose gel of PCR products from PFLPMDC generation two (F2) at embryonic day 10 (E10): Lanes 1-8 – PFLPMDC (F2); Lanes 9-13 – controls: PFLPMDC heterozygote (Het), Pyroxd1 Het, PFLP Het, PFLP homozygous (Hom) and MilliQ (MQ); Lane 14 – base pair ladder. The upper band indicates the *PFLP* allele and the lower band indicates the *PFLPMDC* allele. Purple asterisks indicate mice homozygous for *PFLP* positive for *MDC*. Green triangle – *FRT* site, red triangle – *loxP* site, dashed lines – not to scale, grey boxes indicate exons, horizontal lines indicate introns.

4.4 Discussion, conclusions and future directions

Through an international collaboration, we identified variants within *PYROXD1* as a new genetic cause of early-onset congenital myopathy. We provide the first characterisation of PYROXD1 as a nuclear-cytoplasmic oxidoreductase. Collectively, this study highlights oxidative distress as a core mechanistic pathway in the myopathies. We derived a mouse model of *Pyroxd1* deficiency and determined that global loss of *Pyroxd1* is embryonic lethal in mice. We subsequently developed a murine model with skeletal muscle knock-out of *Pyroxd1* as a means to elucidate the role of *PYROXD1* in biology and disease. The phenotypic characterisation of this mouse model is currently in progress in our laboratory and exceeds the scope of this PhD thesis.

4.4.1 Cell biology and biochemistry of PYROXD1

Localisation of PYROXD1 in skeletal muscle

We have carried out preliminary studies on the localisation of PYROXD1 within skeletal muscle. By confocal microscopy we observe striated patterning of PYROXD1 co-staining with desmin and myotilin. At this resolution it is unclear if PYROXD1 is within the sarcomere, or lies above the sarcomere in the sarcoplasmic reticulum. Super-resolution microscopy would allow more specific localisation of PYROXD1 within skeletal muscle. This could then help to identify possible proteins which PYROXD1 reduces.

We observed an increase in nuclear-PYROXD1 staining within patient skeletal muscle, coupled with reduced cytoplasmic-PYROXD1 staining compared to controls. This raises the question whether PYROXD1 translocates to the nucleus under oxidative distress. It will be important to test this hypothesis and define the nuclear localisation signal within PYROXD1

that mediates nuclear translocation. This may also help to identify possible substrates PYROXD1 reduces within the nucleus.

Identifying PYROXD1 substrates

Identifying the essential substrates PYROXD1 reduces will lend insight into the development of each of the pathological hallmarks in PYROXD1 related myopathy. Skeletal muscle from the skeletal muscle knockout, PFLPMDC$^{PFLPMDC/PFLP,\ MDC/WT}$, mouse can be used to experimentally determine the substrates of mouse Pyroxd1. Mass spectrometry can be carried out on PFLPMDC$^{PFLPMDC/PFLP,\ MDC/WT}$ and PFLPMDC$^{PFLPMDC/PFLP,\ WT/WT}$ skeletal muscle to look for substrates that Pyroxd1 reduces, utilising such methods as ICAT (isotope coded affinity tag) (Baez, Reisz, & Furdui, 2015). However, considering the dominant nuclear localisation of PYROXD1, PYROXD1 may also, or instead, modify DNA or RNA.

4.4.2 Mouse models

Embryonic lethality of Pyroxd1$^{Tm1a/Tm1a}$ mice

We found Pyroxd1$^{Tm1a/Tm1a}$ embryos were formed upon genotyping embryos at E4.5 and absent at E9.5. This refined embryonic lethality to between E4.5 and E9.5. Presence of the Pyroxd1$^{Tm1a/Tm1a}$ global knock-out genotype does not necessarily mean these embryos are absent, and therefore surviving in the absence of Pyroxd1 protein. It is important to note that up to ~E4.5, the fertilised embryo undergoes cell division, but without an overall increase in size. Thus, cytoplasmic components are subdivided into each daughter cell. Perhaps it is only when the mass of the embryo expands, and levels of Pyroxd1 present in the gamete from the Pyroxd1$^{Tm1a/WT}$ parent are sufficiently diluted, when lethality occurs. It is also important to consider the half-life of Pyroxd1 (currently known) and the role it would play in the length of time Pyroxd1 protein from the Pyroxd1$^{Tm1a/WT}$ parent may be active within the gamete.

X-gal staining of Pyroxd1$^{Tm1a/WT}$ mice

Preliminary experiments with wax embedded and sectioned embryos showed X-gal staining of the developing brain of E9.5 Pyroxd1$^{Tm1a/WT}$ embryos. We were unsuccessful when X-gal staining was carried out after cryo-preservation and cryo-sectioning of samples. We hypothesised that *Pyroxd1* expression was low, as observed with human *PYROXD1* mRNA (refer to Figure 4.3), resulting in low β-galactosidase levels, as observed with human PYROXD1 levels (refer to Figure 4.3), which was washed out through tissue-processing and wash steps during X-gal staining. X-gal staining *pre*-sectioning has been shown to produce better results compared to X-gal staining *post*-sectioning in a past study (Shimada, Komatsu, Nakashima, Poschl, & Nifuji, 2012).

One option would be to carry out X-gal staining and subsequent wax-embedding on late gestation embryos and adult mouse tissues to determine developmental and tissue-specific expression of *Pyroxd1*. A second, to carry out conventional immunohistochemistry using an antibody raised against mouse Pyroxd1. Both of which were beyond the scope of this thesis. An alternative would be to take advantage of recent methodological advances such as CUBIC (**C**lear, **U**nobstructed Brain/**B**ody **I**maging Cocktails and **C**omputational analysis, (Susaki et al., 2015)). Tissues are cleared of lipids and can be subsequently stained with antibodies and 3D imaging performed (Susaki et al., 2014). CUBIC would enable high resolution imaging of the expression of Pyroxd1 protein throughout development and tissues.

Successful generation of the experimental genotype

We were successful in generating the desired experimental genotype – PFLPDMC$^{PFLPMDC/PFLP,MDC/WT}$ - which should induce skeletal muscle knock-out of *Pyroxd1*. The important next steps are to: (1) Characterise the extent to which the *PFLP* allele is modified to the knock-out

PFLPMDC allele within skeletal muscle; and (2) determine the extent of Pyroxd1 protein knock-out within skeletal muscle.

The ethical way forward

The experimental genotype survives to birth when the PFLPMDC$^{PFLPMDC/WT,\ MDC/WT}$ parent is the dam. However, initial progeny of this genotype do not survive past two days. Experimentation on embryonic litters may be necessary to obtain high quality skeletal muscle tissue, and to minimise impact to the mice. We do not have certain evidence that lack of survival is genotype-related or indeed the cause of death. However, respiratory failure due to weak diaphragm muscles is one explanation to why a *Pyroxd1* skeletal muscle knock-out mouse may survive in the womb, but not after birth. Prior to generating an experimental cohort, it would need to be determined if: (1) the experimental genotype can survive to birth when the PFLPMDC$^{PFLPMDC/PFLP}$ parent is the sire; and (2) the experimental genotype can survive past day two. An alternative approach, experimentation on embryonic litters, would inkeep with ethical guidelines of reducing the number of mice used and the impact to animals.

Characterising the effects of 'leaky' cre

Our results indicate cre activity outside of skeletal muscle, inclusive of gametes. These results suggest that PFLPMDC$^{PFLPMDC/PFLP,\ MDC/WT}$ carry one knock-out, *PFLPMDC,* allele in all tissues. Additionally, cre activity observed outside of skeletal muscle may reduce *Pyroxd1* expression to levels inducing a phenotype. It will be important to determine: (1) The extent to which *PFLP* has been modified to the knock-out *PFLPMDC* allele in tissues outside of skeletal muscle; and (2) the extent of Pyroxd1 protein knock-out in tissues outside of skeletal muscle. This characterisation will become vital when interpreting the phenotype of the PFLPMDC mouse.

Limitations of transgenic mice

We show that *cre* is not under tight regulation by *MyoD* in the MyoD-cre mouse line. We observe cre activity outside of skeletal muscle. This highlights the importance of characterising mouse strains generated by crossing temporal and/or spatial cre-expressing mouse strains with mouse strains carrying the conditional knock-out allele of interest. This limitation is important to characterise for phenotype interpretation and ethical production of genetically modified mouse lines.

The integration site of the transgenes used in this study were unknown at the time of this project. The integration site of a transgene may be within an endogenous gene, disrupting gene function and possibly result in the display of a phenotype. In one line of c-myc transgenic mice, the *c-myc* transgene deletes exon 1 of *Gtf2ird1* resulting in reduced mRNA expression of *Gtf2ird1* (Durkin, Keck-Waggoner, Popescu, & Thorgeirsson, 2001). Loss of one copy of the human homologue, *GTF2IRD1,* is associated with Williams-Beuren syndrome. Alternatively, the transgene may lie on the same chromosome as the conditional-allele to be targeted, interfering with mendelian inheritance. We chose to outbred the *FLP* transgene due to its unknown influence on mouse phenotype. It is also interesting to note that using the MyoD-Cre mouse line to target *loxP* sites within the *Pyroxd1* locus (chromosome 6) was successful, whilst targeting *loxP* sites within the *Capsn1* locus (chromosome 7) was unsuccessful. One explanation to this, is that the location of the *MDC* locus is on chromosome 7 in close proximity to *Capsn1*, interfering with gene function and/or mendelian inheritance. This highlights the possible ethical benefit of mapping the location of transgenes prior to crossing, to reduce the number of mice required to generate the experimental genotype. The integration site of transgenes within seven mouse lines has been carried out using targeted locus amplification (Cain-Hom et al., 2017). Furthermore, gene insertion had resulted in structural rearrangements which could be identified with this technique. Knowledge of the integration site and structural rearrangements at the integration site aids not only planning of crosses, but phenotype

interpretation. Mapping of the *MDC* transgene with targeted locus amplification will be important to understand the limitations of the *Pyroxd1* skeletal muscle knock-out, PFLPMDC$^{PFLPMDC/PFLP,\ MDC/WT}$, mouse which can be applied to phenotype interpretation.

4.4.3 PYROXD1-myopathy therapies

Using CRISPR/Cas-9 technology to generate an inducible Pyroxd1$^{N155S/N155S}$ mouse, the common mis-sense patient variant, would allow testing of potential treatments of *PYROXD1*-myopathy on a mouse model that more closely mimics *PYROXD1*-patients. The inducibility of the strain would enable further testing on whether *Pyroxd1*-myopathy can be reversed, or if treatment needs to be effective prior to end-stage muscle. An inducible Pyroxd1 global knock-out mouse would allow further investigations into why Pyroxd1 is essential for life. The combination of these mouse models with our *Pyroxd1*-skeletal muscle KO mouse model will be important to further understand the link between *Pyroxd1*-myopathy, myofibrillar myopathy and neurodegeneration; and to determine whether any oxidative treatments targeting neurodegenerative diseases could also target the myopathies.

Chapter 5 - Materials and methods

5.1 Ethics approval

Ethics approval was obtained from The Human Research Ethics Committes of the Children's Hospital of Westmead (10/CHW/45) for all human aspects within this thesis. Ethics approval from the Children's Medical Research Institute and The Children's Hopsital at Westmead's Animal Ethics Committee was obtained for the generation of (K342) and experimentation on (K348) mouse strains in this thesis.

5.2 Immunolabelling

Antibodies

All antibodies and conditions used in this thesis are stated in Table 5.1 and Table 5.2

Table 5.1 Primary antibodies

Protein (clone)	Antibody type	Dilution	Supplier (Catalogue number)
α-skeletal actin	Polyclonal rabbit, IgG	WB: 1:2000	Sophie Clement, Univeristy of Geneva
Sarcomeric actin (5C5)	Monoclonal mouse, IgM	WB 1:20,000	Sigma (A2172)
Desmin* (DE-R-11)	Monoclonal mouse, IgG	WB 1:1000; IHC 1:50 (Fix:3% PFA 15 mins and cold methanol 10 mins; Block: 2%BSA/PBS)	Novocastra (NCL-L-DES-DERII)
Filamin	Polyclonal, rabbit IgG	WB 1:2500; IHC 1:250 (Fix: 3% PFA 3 mins and cold methanol 5 mins; Block: 2% BSA/PBS)	Gift from Isin Dalkilic, Harvard Medical School, Boston
αβ-crystalin (G2JF)	Monoclonal mouse, IgG	WB 1:100; IHC 1:25 (Fix: 3% PFA 3 mins; Block: 2% BSA/PBS)	Novocastra (NCL-ABCrys-512)
α-actinin-2 (4B2)	Monoclonal rabbit, IgG	WB: 100,000	Gift from Alan Beggs Harvard Medical School, Boston
GAPDH (6C5)	Monoclonal mouse, IgG	WB 1:10,000	Millipore (MAB374)
Myotilin (RSO34)	Monoclonal mouse, IgG	WB 1:2000; IHC 1:20 (Fix:3% PFA 15 mins and cold methanol 10 mins; Block 2%BSA/PBS)	Novocastra (NCL-MYOTILIN)
Leiomodin-1	Polyclonal rabbit, IgG	WB 1:1000	Abcam (Ab104858)

Leiomodin-2	Polyclonal rabbit, IgG	WB 1:1000	Santa Cruz Biotechnology, Inc (sc-135493)
Leiomodin-3	Polyclonal, rabbit IgG	WB 1:10,000	Proteintech (14948-1-AP)
KLHL40 (KBTBD5)	Polyclonal rabbit, IgG	WB 1:10,000	Sigma Aldrich (HPA024463)
Smooth muscle actin (asm-1)	Monoclonal mouse, IgM	WB 1:1000	Leica Biosystems, Novocastra Ltd (NCL-SMA)
Cardiac actin	Monoclonal mouse, IgG	WB 1:1500	American Research Products Inc, USA
Beta-tubulin	Polyclonal rabbit, IgG	WB 1:2,000	Developmental studies hybridoma bank, The univeristy of Iowa, USA (E7-C 8H4)
Slow Myosin	Monoclonal mouse, IgG	WB 1:7000	Chemicon (MAB1628)
Fast Myosin (MY32)	Monoclonal mouse, IgG	WB 1:10,000	Sigma Aldrich (M4276)
FLAG (M2)	Monoclonal mouse, IgG	WB 1:5000	Sigma Aldrich (F1804)
eIF2-α	Monoclonal mouse, IgG	WB 1:1000	Cell signalling technology (L57A5)
P- eIF2-α$^{\#}$	Monoclonal rabbit, IgG	WB 1:1000	Cell signalling technology (119A11)
PYROXD1	Polyclonal rabbit, IgG	WB 1:1,000 (tissues and fibroblasts 20 µg, transfected cells 5µg, incubation O/N); IHC 1:50 (Fix:3% PFA 15 mins and cold methanol 10 mins; Block 2%BSA/PBS, incubation O/N)	Abcam (ab122458); Abcam (ab204560); Sigma Aldrich (504-260)
α-actinin (EA-53)	Monoclonal mouse, IgG	WB 1:2500	Sigma Aldrich (A7811)
Emerin	Monoclonal mouse, IgG	WB 1:300	Novocasta (NCL-Emerin)

TDP-43 (2E2-D3)	Monoclonal mouse, IgG	IHC 1:750 (Block: 10% FBS/PBS)	Abcam (ab57105)
β-galactosiadse	Polyclonal rabbit, IgG	WB 1:1000	Molecular probes (A-11132)

*Secondary antibody 1:4500; # PPI 1:50 used in lysis buffer; WB – Western blot; IHC – Immunohistochemistry

Table 5.2: Secondary antibodies

Secondary antibody	Dilution	Supplier (Catalogue number)
HRP congugated anti-rabbit	WB 1:2000	GE Healthcare Biosciences (NA934-1ML)
HRP congugated anti-mouse	WB 1:2000	GE Healthcare Biosciences (NA931-1ML)
Alexa Fluor 488 congugated anti-rabbit	IHC 1:200	Life technologies (A21260)
Alexa Fluor 488 congugated anti-mouse	IHC 1:200	Life technologies (A21202)
Alexa Fluor 555 congugated anti-rabbit	IHC 1:200	Life technologies (A21428)
Alexa Fluor 555 congugated anti-mouse	IHC 1:200	Life technologies (A21424)
DAPI - 405	IHC 1:5000	Life technologies (D1306)

Immunohistochemistry

8 µm tissue cryosections were cut on a Leica CM 1950 cryostat, collected onto glass slides (HD Scientific supplies Ptd Ltd) and circled with a Liquid Blocker Super Pap Pen (Sigma Aldrich, Z377821-1EA). Sections were fixed (as stated in Table 5.1), washed three times 10 dips in phosphate buffered saline (PBS, Amresco, E703-1L) and blocked for 10 minutes (as stated in Table 5.1). 50 µl of Primary antibody (Table 5.1), diluted in block, was applied to the tissue section and incubated at room temperature (RT) for 2 hours, or overnight (O/N) in a humidified chamber at 4ºC. Tissues were washed 5 times ten dips in PBS, blocked for 10 minutes and 50 µl of secondary antibody (Table 5.2), diluted in block, was incubated at RT for 1 hour. Sections were washed 3 times ten dips and mounted in Prolong Gold with DAPI (molecular probes, life technologies, P36941) or ImmunoMount (Thermo Scientific, 9990402). Where two fixation conditions are stated, one wash step was performed after the first fixation condition.

Immunocytochemistry

Cos-7 cells and primary human fibroblasts were seeded onto glass coverslips (No. 1 thickness, TAAB Laboratory Equipment LTD) in 24-well plates (In vitro technologies, FAL353047) and immunocytochemistry was carried out when cells were 65% confluent. Coverslips were washed three times 10 dips in Hanks Balanced Salt Solution (HBSS, Life Technologies, 14025-092) and then inverted onto a 50 µl droplet of 3% paraformaldyhyde (PFA, Sigma-Aldrich, P6148) on a parafilm-covered glass plate. Slides were washed three times 10 dips in HBSS and inverted onto a droplet of cold methanol for ten minutes. Slides were washed three times ten dips in HBSS, blocked for 10 minutes in 2% bovine serum albumin (BSA, Sigma-Aldrich, A7906)/HBSS and inverted onto 50 µl of primary antibody (Table 5.1), diluted in 2% BSA/HBSS, O/N in a humidified chamber at 4ºC. Slides were washed five times in HBSS, blocked for ten minutes in 2% BSA/HBSS and inverted onto a 50 µl droplet of secondary antibody (Table 5.2) diluted in 2% BSA/HBSS for one hour at RT. Slides were washed three times in HBSS and mounted using Prolong Gold with DAPI (molecular probes, life technologies, P36941).

Zenon labelling

Zenon labelling allows co-staining with two or more antibodies raised in the same species. Zenon Mouse IgG_1 labelling kits were used to co-label skeletal muscle sections with cardiac actin and slow myosin, neonatal myosin or developmental myosin – all of which are monoclonal mouse IgG antibodies (Table 5.3). Frozen muscle biopsy sections cut at 8 µm were blocked in 2% BSA for 10 minutes. During the incubation, cardiac actin was tagged with the Zenon Alexa Fluor 555 label (Invitrogen, Z25005), and each respective myosin was tagged with the Zenon Alexa Fluor 488 (Invitrogen, Z25002) for 5 minutes at room temperature. IgG fragments were then added to each reaction (equal volume to Zenon label) for 5 minutes to bind unbound label. Antibody/label/block mixtures were combined and added to muscle

sections and incubated at room temperature for 2 hours. Muscle sections were then washed 3 times in 1 x PBS. DAPI (1 µg/ml) was applied for 5 minutes, sections washed 4 times in 1 x PBS and mounted with Immunomount (Thermo Scientific, 9990402).

Table 5.3: Antibodies used in Zenon labelling

Protein	**Clone**	**Company (Catalogue number)**	**Ratio (antibody: label)**
Neonatal myosin	WB-MHCn	Novocastra (NCL-MHCn)	4:1
Developmental myosin	RNMy2/9D2	Novocastra (NCL-MHCd)	4:1
Slow myosin	NOQ7.5 4D	Millipore, (MAB1628)	0.6:6
α-Cardiac actin	Ac1-20.4.2	Progen, (61075)	2:1

Imaging

Imaging was performed on an Olympus BX50 microscope linked to a SPOT digital imaging camera (Diagnostics) or a Leica SP5 confocal microscope using LAS AF software.

Western blotting

Tissue samples were cryosectioned at 8 µm and solubilised in 100 µl of 2x solubilisation buffer with 1:500 protease inhibitors (PI, Sigma-Aldrich P8340) (Table 5.1) per 100 mm^2 of cryosectioned tissue. Cells were harvested from a 6-well plate. Media was removed and cells were washed three times in 2 ml of dPBS $–Ca^{2+}/-Mg^{2+}$ (ThermoFischer Scientific, 14190250), scraped in 1 mL of dPBS $–Ca^{2+}/-Mg^{2+}$ and spun at 300 RCF for 3 min at 4ºC. dPBS was removed and 150 µl of 2 x solubilisation buffer with 1:500 PI was added to the cell pellet. After the addition of solubilising buffer to either tissues or cells the solution was mixed, sonicated and left to solubilise for 20 minutes on ice. Samples were then heated for 3 min at 94ºC,

vortexed and spun down. Protein concentrations were determined by bicinchoninic acid assay (BCA assay,Thermo Scientific, 23225) as per the manufacturer's instructions, or a loading gel assessing actin and myosin levels when patient skeletal muscle was under examination. 2x or 4x loading buffer was added to the sample dependent on concentration. Samples were either immediately run on western blot or stored at -80ºC.

Protein separation was performed on NuPAGE Bis-Tris 10%, 10-well and 12-well gels (ThermoFisher Scientific, NP0301BOX and NP030B) or CriterionXT Bis-Tris 10%, 18 well (Biorad, 345-0112) gels in MOPS running buffer (Table 5.4) at 150 V for one hour with 5µl of PagerulerPlus prestained protein ladder (Thermoscientic, 26620). Proteins were transferred onto PVDF membranes (GE Healthcare, 3030-917) in transfer buffer (Table 5.4) at 400 mA for 1 hour (Invitrogen gels) or 1.5 hours (Biorad gels). Membranes were blocked in 5% skim milk/Phosphate buffer saline – 0.1% Tween 20 (PBST) for 1 hour at room temperature (RT) before incubating the membrane in primary antibody (Table 5.1) for 2 hours at room temperature or overnight at 4ºC. Membranes were washed 5 times 5 min in PBST, blocked for 15 minutes and incubated with the secondary antibody congugated to Horse radish protein (HRP) (Table 5.2) for 1 hour at room temperatre. The membrane was washed 5 x 5 mins in PBST and developed using ECL chemiluminescent (GE Healthcare, RPN2106) reagents and hyperfilm (VWR, 28906837).

Coomassie was used in some western blot analyses to determine myosin and actin protein levels. The membrane was incubated in Coomassie (45% methanol, 45% MilliQ water, 10% acetic acid, 0.25 g Brilliant Blue) for 1 hour at RT and destained (60% MilliQ water, 30% methanol, 10% acetic acid) until bands were clear. In some cases western blot membranes were striped of antibodies before being reprobed with a second primary antibody. Membranes were incubated with striping buffer (62.5 mM Tris, 2% SDS, 0.1 M beta-mercaptoethanol [Amresco,

0482-100 mL] for 20 minutes at 55ºC. The membrane was rinsed of β-mercaptoethanol by washing with PBST following by blocking for 30 min.

Single fibre isolation for western blot was carried out on human skeletal muscle kindly donated by Dr Neil Street, Children's Hospital at Westmead. Mechanical dissection was carried out in paraffin oil. Single muscle fibres were washed in relax solution (Table 5.4): glycerol v:v with 1:50 phosphatase inhibitors (PPI, Sigma-Aldrich) and 1:500 PI. Fibres were solubilised in 2 x solubilising buffer (Table 5.4) in 1:50 PPI and 1:500 PI and put straight on dry ice. Protein concentrations were determined by a BCA assay and 250 ng of protein was run on western blot to allow for fibre typing and experimental probes of a single fibre.

Non-reducing blots were solubilised without DTT, not heated and with N-ethylmaleimide (NEM, 5 mM final, Sigma-Aldrich, E3876) in the solubilising and loading buffer to quench free thiols.

Table 5.4: Solutions used for solubilisation and single fibre dissection

Solution	Reagents
2x SDS solubilising buffer	125 mM Tris, 4% SDS
2x SDS loading buffer	125 mM Tris, 4% SDS, 20% glycerol, Bromophenol blue (BMP); 1:20 DL-Dithiothreitol (DTT, 50 mM stock)
4 x SDS loading buffer	125 mM Tris, 4% SDS, 40% glycerol, BMP, 1:10 DTT (50 mM stock)
MOPS	50 mM 3-(N-Morpholino)propanesulfonic acid 4-morpholinepropanesulfonic acid (MOPS); 50 mM Tris; 0.1% SDS; 1 mM EDTA
Transfer buffer	25 mM Tris; 192 mM glycerol; 0.075% SDS; 15% methanol added fresh before use
Relax solution	40.76 mM Kpropionate, 100 mM BES, 6.97 mM EGTA, 6.48 mM MgCl2,6 mM Na2ATP, 1 mM DTT, 14.5 mM creatine phosphate, pH 7.1 and pCa 9 at 15 °C
Reagents were obtained from Sigma-Aldrich	

5.3 Expression constructs, cloning and sequencing

Details of the source and sub-cloning of expression constructs are in Table 5.5 and sequencing primers in Table 5.6. All restriction enzymes were purchased from New England Biolabs. Blunting was carried out with Klenow (New England Biolabs, M0210S) and DNA was purified with the Jetquick gel extraction kit (Astral, G420050) prior to ligation with T4 DNA ligase (Sigma-Aldrich, 10481220001). Transformations were carried out with TOP10 chemically competent cells (Thermo Fisher Scientific, C404003) and the HI SPEED Maxi Kit (Qiagen, 12663) or the Virogene MiniPlus plasmid DNA extraction system (Diagnostic technology, GF2002) were used to prepare DNA for sequencing, cloning and transfections. Sequencing was carried out at the Australian Genome Research Facility Ltd (Sydney, Australia) and analysed using Sequencher 4.8 (Gene Codes Corporation, Michigan, USA).

To generate the insert for pcDNA3.1 $_{FLAGKozak}$HumanLMOD3 and TOPO-VA we carried out primer annealing with the primers listed in Tables 5.5 and 5.6. 10 µl of 10 µM forward and reverse primers were mixed and heated at 94ºC for 30 seconds, followed by decreasing the PCR by 1ºC per second to 4ºC.

Table 5.5: Expression constructs and cloning

Construct	Vector or source	Restriction enzymes used to cut the vector	Insert	Restriction enzymes used to cut the insert	Sequencing primers (Sigma Aldrich)	Accession number
pcDNA3.1-MouseLmod3MycHis	Gift from Prof Eric Olsen, Department of Molecular Biology, University of Texas Southwestern Medical Center, Dallas, United States (Garg et al 2014)				T7-F;BGH-R; 2bF-Lmod3; 2aR-Lmod3	NM_001081157.1
pEGFP-NI-HumanKLHL40	Gift from Prof Nigel Laing, Centre for Medical Research, The University of Western Australia & the Harry Perkins Institute of Medical Research, Perth, WA, Australia				CMV-F; EBV-R; KLHL40-F; KLHL40-R	NM_152393
pcDNA3.1-MouseKlhl40MycHis	Gift from Prof Eric Olsen, Department of Molecular Biology, University of Texas Southwestern Medical Center, Dallas, United States (Garg et al 2014)				T7-F; BGH-R;	NM_028202.3
pcDNA3.1-HumanLMOD1	GenScript USA Inc				N/A	NM_012134
pMT3-FLAGHumanLMOD3	Generated prior to this study (Yuen et al 2014)				N/A	BC121019
pEGFP-NI-Empty	Generated prior to this study (PhD student Natalie Woolger)				N/A	N/A
TOPO-Empty	Thermo Fisher (45-0641)				N/A	N/A
pcDNA3.1-HumanLMOD3	pcDNA3.1-MouseLMOD3MycHis	BamHI, blunt, XhoI	pMT3-FLAGHumanLMOD3	NcoI, blunt, SalI	CMV-F; BGH-R	BC121019
pcDNA3.1-HumanLMOD2	pcDNA3.1-MouseLMOD3MycHis	BamHI, blunt, XhoI	pMT3-FLAGhumanLMOD2 (Yuen et al)	SmaI/SaI	CMV-F; BGH-R	AK300698.1, BAG62379.1
pcDNA3.1-Empty	pcDNA3.1-HumanLMOD3	BamHI/XhoI. Blunt. Re-ligate.			BGH-R	N/A
pCMV10(-KanR)-Empty	pCMV10-3xFLAGMouseKlhl40HA (Gift from Prof Eric Olsen, Department of Molecular Biology, University of Texas Southwestern Medical Center, Dallas, United States (Garg et al 2014))	HindIII/XbaI. Blunt. Re-ligate.			CMV-F	N/A
pMT3HumanLMOD3 delta 1-38	pMT3-FLAGHumanLMOD3	PstI	N/A	Cut. Re-ligate.	pMT2-F	Modified from BC121019

pcDNA3.1 FLAGKozakHumanLMOD3	pcDNA3.1-HumanLMOD3	HindIII/KpnI	Annealed KozakFLAG_F/KozakFLAG_R		CMV-F; BGH-R	BC121019
TOPO-VA	TOPO-Empty	XhoI/EcoRI	Annealed VA-F_Oligo and VA-R_Oligo		VA-F; VA-R	N/A
pEGFP-C1 -GFP WT human PYROXD1	GenScript USA Inc.	N/A	N/A	N/A	pEGFP-CI; EBV-R	NM_024854
pEGFP C1 -GFP N155S human PYROXD1	pEGFP-C1 -GFP WT human PYROXD1	EcoR1/EcoR1	pUC57 mutant PYROXD1 (GenScript USA Inc)	EcoR1/EcoR1	PYROXD1-F; PYROXD1-R; pEGFP-c term;pEGFP_CI	Modified from NM_024854
pEGFP C1-GFP Q372H human PYROXD1	pEGFP-C1 -GFP WT human PYROXD1	EcoRV/Spe1	pUC57 mutant PYROXD1 (GenScript USA Inc)	EcoRV/Spe1	EBV_R; PYROXD1-F; PYROXD1-R; pEGFP-c term;pEGFP-C1	Modified from NM_024854
pEGFP-C1 WT human PYROXD1	pEGFP-C1 -GFP WT human PYROXD1	AgeI/BspE1	N/A	Cut. Blunted. Re-ligated.	PYROXD1-F; PYROXD1-R; CMV-F; pEGFP-c term	NM_024854
pEGFP-C1 N155S human PYROXD1	pEGFP C1 -GFP N155S human PYROXD1	AgeI/BspE1	N/A	Cut. Blunted. Re-ligated.	PYROXD1-F; PYROXD1-R; CMV-F; pEGFP-c term	Modified from NM_024854
pEGFP-C1 Q372H human PYROXD1	pEGFP C1-GFP Q372H human PYROXD1	AgeI/BspE1	N/A	Cut. Blunted. Re-ligated.	PYROXD1-F; PYROXD1-R; CMV_F; pEGFP-c term	Modified from NM_024854

Table 5.6: Sequencing and annealing primers

Primer name	Primer sequence (5'-3')
2bF_Lmod3	CAATCAGAGGCACATGTTGG
2aR_Lmod3	GCTGCTGTTTTTGCTCTTCC
BGH-R	TAGAAGGCACAGTCGAGG
CMV-F	CGCAAATGGGCGGTAGGCGTG
EBV-R	GTGGTTTGTCCAAACTCATC
KLHL40-F	TTCCTGGGATCCTCAATGAC
KLHL40-R	TCCTTGGTAACCAGGCTGAC
KozakFLAG-F	AGCTTGCCACCATGGATTACAAGGATGACGACGATAAGG GTAC
KozakFLAG-R	CCTTATCGTCGTCATCCTTGTAATCCATGGTGGCA
pEGFP-CI	CATGGTCCTGCTGGAGTTCGTG
pEGFP-c term	CCATTATAAGCTGCAATAAACAAGTTAAC
pMT2_F	ACAATGACATCCACTTTGC
PYROXD1-F	GCAGGAGCAGCTGAATTCTT
PYROXD1-R	TTCCACATAGACAGGCCACA
T7-Fwd	TAATACGACTCACTATAGGG
VA-F	GAGCCTGTAAGCGGGCACTCTT
VA-R	GAAGCCAAAAGGAGCGCTCCCC
VA-F_Oligo	TCGAGCCTGTAAGCGGGCACTCTTCCGTGGTCTGGTGGAT AAATTCGCAAGGGTATCATGGCGGACGACCGGGGTTCGA ACCCCGGATCCGGCCGTCCGCCGTGATCCATGCGGTTACC GCCCGCGTGTCGAACCCAGGTGTGCGACGTCAGACAACG GGGGAGCGCTCCTTTTGGCTTCCG
VA-R_Oligo	AATTCGGAAGCCAAAAGGAGCGCTCCCCCGTTGTCTGACG TCGCACACCTGGGTTCGACACGCGGGCGGTAACCGCATGG ATCACGGCGGACGGCCGGATCCGGGGTTCGAACCCCGGTC GTCCGCCATGATACCCTTGCGAATTTATCCACCAGACCAC GGAAGAGTGCCCGCTTACAGGC

5.4 Cell culture and transfections

Transfections

Cell lines and culture media conditions are stated in Table 5.7. Lipofectimine LTX (Thermo Fischer Scientific, 94756) was used to transfect COS-7 cells as per manufacturer's instructions. Briefly, 6-well plates were seeded at a cell concentration of 2.5 x 10^5 and transfected after 16 hours. A total concentration of 3 µg of plasmid DNA was used, evenly divided in co-transfections. Plasmid DNA was incubated with optimem and PLUS reagent (Thermo Fischer Scientific, 10964-021) for 5 min at RT, and Lipofectamine LTX and optimem were incubated for 5 min at RT. Mixtures were combined and incubated at RT for 20 min. The mixture was added to cells dropwise. Antibiotic media was used during the transfection and changed to antibiotic-containing media four hours post-transfection. HEK293T cells were transfected with polyethylenimine (PEI, Poysciences). Cells were seeded on Poly-D-lysine coated plates (Incubated for 5 min at RT, washed once with dPBS) at 30% to be transfected at 80% confluency. PEI and NaCl (8.3 µl PEI, 100 µl 0.9% NaCl) were mixed, DNA (3µg) added, mixed and incubated for 20 min at RT. The mixture was added to cells dropwise. Co-transfection studies carried out in Chapter 3 were harvested for western blot 48 hours post-transfection. Single transfections carried out in Chapter 4 were harvested 24 hours post-transfection. Transfected cells to be used for immunocytochemistry were re-seeded onto coverslips 8 hours post-transfection and stained 24 hours post-transfection.

MG132 treatment

MG132 (final concentration 10 µM, Sigma-Aldrich C2211) treatment of Cos-7 cells was carried out 24 hours post-transfection and harvested after incubation for a further 24 hours.

Mouse tail fibroblast outgrowth

Tail fibroblasts were outgrown from a tail clip of a Pyroxd1$^{Tm1a/WT}$ mouse. The tail clip was wiped with an iodine wipe and immersed in 70% ethanol for 10 seconds before washing 5 times in PBS/gentamicin 1:200. A T25 flask was coated with collagen (1:50, 10 min) and scratch marks were made on which cut up tissue were placed to assist cell adherence. Enough media was added to cover the base of the flask. The flask was incubated undisturbed for two days to allow outgrowth.

Table 5.7: Cell lines and media

Cell	**Culture media**
Cos-7	DMEM/ F12 (Gibco 1133-032); 10% Heat inactivated Foetal calf serum (HI FCS); 50 µg/mL Gentamycin (Gibco 15710-072)
HEK293T	DMEM (Gibco 11995-065); 10% HI FCS; 50 µg/mL Gentamycin;
Primary human fibroblasts	DMEM /F12; 20% HI FCS; 10% aminomax (Gibco 11269-016); 20% HI FCS; 50 µg/mL Gentamycin
Primary human myoblasts	*Differentiation media:* DMEM /F12; 3% heat inactivated horse serum; 20%, 1 x Insulin-Selenium-Transferrin (51300-044); 50 µg/mL Gentamycin *Growth media:* DMEM /HAMS F12 (11330-032; 10% aminomax; 20% HI FCS; 50 µg/mL Gentamycin
Primary mouse fibroblasts outgrowth media	*Outgrowth media:* DMEM /F12; 10% aminomax; 20% HI FCS; 50 µg/mL Gentamycin *Growth media:* DMEM /F12; 10% HI FCS; 50 µg/mL Gentamycin

5.5 PCR and cDNA synthesis of PHF

RNA extraction

Primary human fibroblasts were cultured to 100% confluency in a T75 tissue culture flask (In vitro technologies, FAL353136) and lysed with TRIzol reagent (Ambion, 15596018). A TissueLyser II (Qiagen) was used at 25hertz for 1 minute bursts, interluded with incubation on ice, until cells were homogenised. The homogenised mix was spun at 12,000 g for 10 minutes at 4ºC, the supernatant transferred to a fresh tube and incubated at RT for 5 minutes. Chloroform (0.2 ml/1 mL of TRIzol used) was added, mixed, and incubated at RT for 3 minutes. The mixture was spun at 12,000 g for 15 minutes at 4ºC and the upper aqueous layer transferred to a new tube. Isopropanol (0.5 mL/ 1 mL of TRIzol used) was added to precipitate the RNA and incubated at RT for 10 minutes. The mixture was spun at 12,000 x g for 10 minutes at 4ºC and the supernatant discarded. The pellet was washed once with 75% ethanol, vortexed, spun at 7,500g for 5 minutes at 4ºC and re-suspended in Diethyl pyrocarbonate (DEPC)-treated water (Thermo Fisher Scientific, AM9915G).

cDNA synthesis

Immediately after RNA re-suspension cDNA synthesis was performed. 1 µg of RNA was mixed with 2 µl of primers ($Oligo(dt)_{20,}$ Invitrogen 55063; or random primers $p(dn)_{6,}$ Roche 11043921) and made up to 12 µl with DEPC-treated water. The mixture was heated for 5 minutes at 65ºC then chilled on ice for 2 minutes. Synthesis reagents (1 x: 4 µl 5X First strand, 2 µl [DTT,0.1M, Sigma-Aldrich, D9779], 1 µl dNTP [10 mM, Thermo, R1121] and 1 µl Superscript III [Thermo fischer scientific, 18080-044]) were added to the mixture and incubated for: 5 minutes at 25ºC, 1.5 hours at 50ºC, and 15 minutes at 70ºC). cDNA was diluted to 10 ng/µl with DEPC-treated water.

Polymerase chain reaction

To investigate extension of intron 3 and intron 4 we used PYROXD1Splice_F (5' AGGGAAGTTCGTGGTGGTC3')/PYROXD1-3R (5'TGAAAAGAGGCAGGCAAAAC3') and PYROXD1Splice_F/PYROXD_4R (5'CCCTTCTGCCCTTACAGTTTAG3') respectively. PCR conditions were: 95ºC for 2 minutes; 35 cycles of 95ºC for 30 seconds, 62ºC for 30 seconds, 72ºC for 30 seconds; 72ºC for 5 minutes. PCR products were run on a 1% Tris-acetate- Ethylenediaminetetraacetic acid (TAE, Astral Scientific, AM0796) agarose (Astral, BIOD0012) gel.

5.6 Mouse work

Source of mouse lines and breeding

Mouse husbandry was carried out by the Kids Research Institute transgenic facility staff. We imported the Pyroxd1 Tm1a line from the KOMP repository (https://www.komp.org/). We received heterozygous mice and generated a Pyroxd1 Tm1a colony by crossing with Black/6J mice present within the transgenic's facility. The FLP mouse line (FLPe, B6.Cg_Tg(ACTFLPe)9205DYM/J) was kindly donated to The Kids Research Institute by The Victor Chang Cardiac Research Institute and originated from The Jackson Laboratory (https://www.jax.org/line/005703). Pyroxd1$^{Tm1a/wt}$ mice were crossed with FLP$^{FLP/FLP}$ mice to generate first generation heterozygous PFLP$^{PFLP/WT,\ FLP/WT}$ mice. PFLP$^{PFLP/WT,\ FLP/WT}$ mice were intercrossed to generate homozygous second generation PFLP$^{PFLP/PFLP,WT/WT}$ mice. MDC mice were kindly shared by Dr Aaron Schindler at the Kids Research Institute and originated from the Jackson Laboratory. PFLP$^{PFLP/PFLP,\ WT/WT}$ were crossed with MDC$^{+/-}$ mice to generate first generation PFLPMDC$^{PFLP*/WT,\ MDC/WT}$ mice, where *PFLP** denotes detectable MDC-mediated recombination in the earclip. PFLP$^{PFLP/PFLP,WT/WT}$ were crossed with PFLPMDC$^{PFLP*/WT,\ MDC/WT}$ to generate second generation homozygous mice PFLPMDC$^{PFLPMDC/PFLP,\ MDC/WT}$. The Pyroxd1 Tm1a colony was maintained by crossing Pyroxd1$^{Tm1a/wt}$ mice with Black/6J mice. The PFLP colony was maintained by intercrossing PFLP$^{PFLP/PFLP,\ WT/WT}$.

Mouse genotyping

Genomic DNA preparation

Genotyping was carried out on earclips of weaned mice and tail clips of neonates and gestational mice. Tissue was digested in 200 µl STE (100 mM Tris [Astral, BIO3094T], pH 8.5; 5 mM Ethylenediaminetetraacetic acid [EDTA, Sigma-Aldrich E5134]; 0.2% Sodium dodecyl sulphate [SDS, Astral, DG093] 200 mM sodium chloride [NaCl, VWR, 27810.364])/Proteinase K [Final 0.4 µg/µl; Stock 20 µg/µl, Sigma-Aldrich P2308]) at 55ºC for

three hours. To deactivate proteinase K the temperature was raised to 70ºC for five minutes. Samples were quenched on ice, spun for 1 minute and the supernatant was transferred to a fresh tube to which 0.1 volumes of 3M Sodium acetate [NaOAc, Sigma-Aldrich S2889] and 2 volumes of 100% ethanol were added. Samples were inverted to mix and spun at 17,000 RCF for 20 minutes at 4ºC. The supernatant was removed, the pellet washed in 5 volumes of 70% ethanol and spun as before. The supernatant was removed and the pellet allowed to air dry before re-suspending DNA in 100 µl of MilliQ water.

PCR reactions

The primers used to screen for each allele are stated in Table 5.8, primer sequences in Table 5.9 and PCR conditions in Table 5.10. The 1 x master mix for all mouse genotyping consisted of: 2 µl gDNA (20 ng/µl), MilliQ 7.8 µl, 1.25 µl foward primer (10 µM), 1.25 µl reverse primer (10 µM), 0.2 µl Taq DNA Polymerase (1 Unit, Life technologies 10342-020), 7.5 µl Buffer D (Astral Scientific, M07205D). Primers were purchased from Sigma-Aldrich.

Table 5.8: Primers used to screen mouse alleles

Allele	Forward primer	Reverse primer	Size (bp)
Cre	Cre_F	Cre_R	355
Cre	Cre_F2	Cre_R2	992
FLP	FLP_F	FLP_R	725
PFLP	PFLPMDC_F	PFLPMDC_R	904
PFLPMDC	PFLPMDC_F	PFLPMDC_R	144
PFLP	PFLPMDC_F2	PFLPMDC_R2	980
PFLPMDC	PFLPMDC_F2	PFLPMDC_R2	220
Endogenous Pyroxd1	Pyroxd1_F	Pyroxd1_R	519
Endogenous Pyroxd1	Pyroxd1_F	Pyroxd1_E5R	848
PFLP	Pyroxd1_F	Pyroxd1_E5R	981
PFLP	Pyroxd1_F2	Pyroxd1_R2	291
Endogenous Pyroxd1	Pyroxd1_F2	Pyroxd1_R2	158
Pyroxd1 Tm1a	Pyroxd1_Tm1a_F	Pyroxd1_R	600

Table 5.9: Genotyping primer sequences

Primer	Primer sequence (5'-3')
Cre_F	CATCGTCGGTCCGGGCTGCC
Cre_F2	CTGACCGTACACCAAAATTTG
Cre_R	CCCCCAGGCTAAGTGCCTTC
Cre_R2	CACCAGCTTGCATGATCTCC
FLP_F	CACTGATATTGTAAGTAGTTTGC
FLP_R	CTAGTGCGAAGTAGTGATCAGG
PFLPMDC_F	CCGAACTTCCTATTCCGAAG
PFLPMDC_F2	CGTTCCCAAAGGCGCATAA
PFLPMDC_R	CACCCTAACCAGCACAACAA
PFLPMDC_R2	AACACACACCCTAACCAGCA
Pyroxd1_E5R	CAGAGCAATGCCACCATTC
Pyroxd1_F	TGAACTTGATGGCAGGGGTTAGAGG
Pyroxd1_F2	ATGTACATGGTGTCGTCGTC
Pyroxd1_R	ACCCAGTTATGACTGAACCTGTCCC
Pyroxd1_R2	CAGGGCACATGGAATAGGAG
Pyroxd1_Tm1a_F	GGGATCTCATGCTGGAGTTCTTCG

Table 5.10: Mouse genotyping PCR conditions

Primer combination	PCR conditions
Cre_F/Cre_R	94^{o}C 5 min; 38 cycles of 94^{o}C for 30 sec, 61^{o}C for 30 sec, 72^{o}C for 30 sec; 72^{o}C 10 min
Cre_F2/Cre_R2	94^{o}C 5 min; 38 cycles of 94^{o}C for 30 sec, 58^{o}C for 30 sec, 72^{o}C for 30 sec; 72^{o}C 10 min
FLP_F/FLP_R	94^{o}C 3 min; 35 cycles of 94^{o}C for 30 sec, 58^{o}C for 60 sec, 72^{o}C for 60 sec; 72^{o}C 2 min
PFLPMDC_F/PFLPMDC_R	94^{o}C 2 min; 35 cycles of 95^{o}C for 10 sec, 54^{o}C for 30 sec, 72^{o}C for 90 sec; 72^{o}C 8 min
PFLPMDC_F2/PFLPMDC_R2	95^{o}C 2 min; 35 cycles of 95^{o}C for 10 sec, 60^{o}C for 30 sec, 72^{o}C for 65 sec; 72^{o}C 8 min
Pyroxd1_F/Pyroxd1_R	94^{o}C 5 min; 10 cycles decreasing 1^{o}C/cycle of 94^{o}C for 15 sec, 65^{o}C for 30 sec, 72^{o}C for 60 sec; 30 cycles of 94^{o}C for 15 sec, 55^{o}C for 30 sec, 72^{o}C 60 sec; 72^{o}C 5 min
Pyroxd1_F/Pyroxd1_E5R	94^{o}C 5 min; 10 cycles decreasing 1^{o}C/cycle of 94^{o}C for 15 sec, 65^{o}C for 30 sec, 72^{o}C for 60 sec; 30 cycles of 94^{o}C for 15 sec, 55^{o}C for 30 sec, 72^{o}C 60 sec; 72^{o}C 5 min
Pyroxd1_F2/Pyroxd1_R2	95^{o}C 2 min; 35 cycles of 95^{o}C for 10 sec, 61^{o}C for 30 sec, 72^{o}C for 60 sec; 72^{o}C 8 min
Pyroxd1_Tm1a_F/Pyroxd1_R	94^{o}C 5 min; 10 cycles decreasing 1^{o}C/cycle of 94^{o}C for 15 sec, 65^{o}C for 30 sec, 72^{o}C for 60 sec; 30 cycles of 94^{o}C for 15 sec, 55^{o}C for 30 sec, 72^{o}C 60 sec; 72^{o}C 5 min

Super-ovulation, embryo and tissue harvests

The Kids Research Institute's transgenics facility staff superovulated 4-week old females with 5IU pregnant mare serum gonadotropin (PSMG) 2 days prior to mating and 5IU human chorionic gonadotropin (HCG) the day of mating. At expected E0.5, females were culled by cervical dislocation and Dr Frances Lemckert harvested the ovaries, dissected embryos from the oviduct and digested the matrix surrounding the embryos with hyaluronidase. Embryos were prepared for *ex vivo* culture in 3cm petri dishes in a 10µl droplet of EmbryoMax KSOM media (Millipore, MR-020P-5D) flooded with filter sterilised mineral oil. Embryos were left undisturbed in a 37ºC, 5% CO_2 humidified incubator until E4. At E4 embryos were collected into individual PCR tubes. DNA was extracted by adding 5µl Potassium hydroxide (10 mM), heating for 10 minutes at 95ºC, chilling on ice and adding 5 µl 10mM TRIS-HCL to neutralise the sample. PCR screening carried out as described above with Pyroxd1_F/Pyroxd1_E5R and Pyroxd1_Tm1a_F/Pyroxd1_R primers.

Mice used for tissue harvesting were culled by cervical dislocation. Tissues were harvested and immediately frozen in thawing 2-methylbutane (Sigma-Aldrich, 270343-1L). After allowing 2-methyl butane to evaporate on dry ice, samples were stored at -80ºC.

Beta-galactosidase assay

E9.5 embryos were harvested from a Pyroxd1$^{Tm1a/WT}$ intercross. Embryos were washed twice in PBS, fixed in 4% PFA for 10 minutes, washed three times in PBS and immersed in X-gal stain (10 mL PBS, 100 µl potassium ferricyanide [0.5 M, Sigma-Aldrich 702587], 100 µl ferrocyanide [0.5 M, Sigma-Aldrich P9387], 20 µl $MgCl_2$ [Sigma-Aldrich, M-8266], 10 µl Tween-20 [Biochemicals, BIO0777], 250 µl X-gal [40 mg/mL Thermo-Scientific R0401, in Dimethylformamide, Sigma-Aldrich, 227056]) overnight at 37ºC. Embryos were washed twice in PBS and stored in 4% PFA until wax embedding. Wax embedding, de-waxing and

counterstaining of E9.5 embryos was carried out under the guidance of Vanessa Jones at the Children's Medical Research Institute (CMRI). Embryos were incubated in PBS for 1 hour, MilliQ water for 2 hours, washed in 70% ethanol followed by a 10 min incubation in fresh 70% ethanol. Sequential 10 minutes washes in 80% ethanol, 90% ethanol followed by three sequential 10 minutes washed in 100% ethanol were performed. Embryos were immersed in xylene for 5 min and a further 10 min incubation in fresh xylene. Embryos were imbedded in wax at 65ºC for 30 minutes three times and left overnight at room temperature to set. Sections were cut at 8 µm with a microtome. Sections were then de-waxed and co-stained as follows: Sections were immersed twice in xylene for 1 minute each followed by sequential one minute washes in 100% ethanol (twice), 90% ethanol, 70% ethanol, 50% ethanol and 25% ethanol. Slides were rinsed for one minute in MilliQ water prior to a 20 sec emersion in Nuclear fast red (Sigma-Aldrich, N3020) followed by a one minute rinse in MilliQ and a dip in 70% ethanol, 90% ethanol and one minute incubations in 90% ethanol and two in 100% ethanol. Slides were emersed twice in histolene, the first for 3 minutes, the second for 2 min, and immediately mounted with Immunomount. Sections were imaged on an Aperio Leica scanner ready Scanscope and analysed with Aperio ImageScope v12.1.0.5029.

Chapter 6 - References

Abbott, M., Jain, M., Pferdehirt, R., Chen, Y., Tran, A., Duz, M. B., . . . Burrage, L. C. (2017). Neonatal fractures as a presenting feature of LMOD3-associated congenital myopathy. *Am J Med Genet A, 173*(10), 2789-2794. doi:10.1002/ajmg.a.38383

Adams, J., Kelso, R., & Cooley, L. (2000). The kelch repeat superfamily of proteins: propellers of cell function. *Trends Cell Biol, 10*(1), 17-24.

Agrawal, P. B., Greenleaf, R. S., Tomczak, K. K., Lehtokari, V. L., Wallgren-Pettersson, C., Wallefeld, W., . . . Beggs, A. H. (2007). Nemaline myopathy with minicores caused by mutation of the CFL2 gene encoding the skeletal muscle actin-binding protein, cofilin-2. *Am J Hum Genet, 80*(1), 162-167. doi:10.1086/510402

Agrawal, P. B., Strickland, C. D., Midgett, C., Morales, A., Newburger, D. E., Poulos, M. A., . . . Beggs, A. H. (2004). Heterogeneity of nemaline myopathy cases with skeletal muscle alpha-actin gene mutations. *Ann Neurol, 56*(1), 86-96. doi:10.1002/ana.20157

Al-Hakim, A. K., Zagorska, A., Chapman, L., Deak, M., Peggie, M., & Alessi, D. R. (2008). Control of AMPK-related kinases by USP9X and atypical Lys(29)/Lys(33)-linked polyubiquitin chains. *Biochem J, 411*(2), 249-260. doi:10.1042/BJ20080067

Albagli, O., Dhordain, P., Deweindt, C., Lecocq, G., & Leprince, D. (1995). The BTB/POZ domain: a new protein-protein interaction motif common to DNA- and actin-binding proteins. *Cell Growth Differ, 6*(9), 1193-1198.

Aparicio, O., Razquin, N., Zaratiegui, M., Narvaiza, I., & Fortes, P. (2006). Adenovirus virus-associated RNA is processed to functional interfering RNAs involved in virus production. *J Virol, 80*(3), 1376-1384. doi:10.1128/JVI.80.3.1376-1384.2006

Argyrou, A., & Blanchard, J. S. (2004). Flavoprotein Disulfide Reductases: Advances in Chemistry and Function *Progress in Nucleic Acid Research and Molecular Biology* (Vol. Volume 78, pp. 89-142): Academic Press.

Baez, N. O., Reisz, J. A., & Furdui, C. M. (2015). Mass spectrometry in studies of protein thiol chemistry and signaling: opportunities and caveats. *Free Radic Biol Med, 80*, 191-211. doi:10.1016/j.freeradbiomed.2014.09.016

Baird, T. D., & Wek, R. C. (2012). Eukaryotic initiation factor 2 phosphorylation and translational control in metabolism. *Adv Nutr, 3*(3), 307-321. doi:10.3945/an.112.002113

Bardwell, V. J., & Treisman, R. (1994). The POZ domain: a conserved protein-protein interaction motif. *Genes Dev, 8*(14), 1664-1677.

Beck, J., Maerki, S., Posch, M., Metzger, T., Persaud, A., Scheel, H., . . . Sumara, I. (2013). Ubiquitylation-dependent localization of PLK1 in mitosis. *Nat Cell Biol, 15*(4), 430-439. doi:10.1038/ncb2695

Bedzhov, I., Leung, C. Y., Bialecka, M., & Zernicka-Goetz, M. (2014). In vitro culture of mouse blastocysts beyond the implantation stages. *Nat Protoc, 9*(12), 2732-2739. doi:10.1038/nprot.2014.186

Berkenstadt, M., Pode-Shakked, B., Barel, O., Barash, H., Achiron, R., Gilboa, Y., . . . Raas-Rothschild, A. (2018). LMOD3-Associated Nemaline Myopathy: Prenatal Ultrasonographic, Pathologic, and Molecular Findings. *J Ultrasound Med*. doi:10.1002/jum.14520

Blomen, V. A., Majek, P., Jae, L. T., Bigenzahn, J. W., Nieuwenhuis, J., Staring, J., . . . Brummelkamp, T. R. (2015). Gene essentiality and synthetic lethality in haploid human cells. *Science, 350*(6264), 1092-1096. doi:10.1126/science.aac7557

Boczkowska, M., Rebowski, G., Kremneva, E., Lappalainen, P., & Dominguez, R. (2015). How Leiomodin and Tropomodulin use a common fold for different actin assembly functions. *Nat Commun, 6*, 8314. doi:10.1038/ncomms9314

Bomont, P., Cavalier, L., Blondeau, F., Ben Hamida, C., Belal, S., Tazir, M., . . . Koenig, M. (2000). The gene encoding gigaxonin, a new member of the cytoskeletal BTB/kelch repeat family, is mutated in giant axonal neuropathy. *Nat Genet, 26*(3), 370-374. doi:10.1038/81701

Brown, C. Y., Mize, G. J., Pineda, M., George, D. L., & Morris, D. R. (1999). Role of two upstream open reading frames in the translational control of oncogene mdm2. *Oncogene, 18*(41), 5631-5637. doi:10.1038/sj.onc.1202949

Buhler, M., Steiner, S., Mohn, F., Paillusson, A., & Muhlemann, O. (2006). EJC-independent degradation of nonsense immunoglobulin-mu mRNA depends on 3' UTR length. *Nat Struct Mol Biol, 13*(5), 462-464. doi:10.1038/nsmb1081

Busch, H., & Goldknopf, I. L. (1981). Ubiquitin - protein conjugates. *Mol Cell Biochem, 40*(3), 173-187.

Cain-Hom, C., Splinter, E., van Min, M., Simonis, M., van de Heijning, M., Martinez, M., . . . Warming, S. (2017). Efficient mapping of transgene integration sites and local structural changes in Cre transgenic mice using targeted locus amplification. *Nucleic Acids Res, 45*(8), e62. doi:10.1093/nar/gkw1329

Canning, P., Cooper, C. D., Krojer, T., Murray, J. W., Pike, A. C., Chaikuad, A., . . . Bullock, A. N. (2013). Structural basis for Cul3 protein assembly with the BTB-Kelch family of E3 ubiquitin ligases. *J Biol Chem, 288*(11), 7803-7814. doi:10.1074/jbc.M112.437996

Cenik, B. K., Garg, A., McAnally, J. R., Shelton, J. M., Richardson, J. A., Bassel-Duby, R., . . . Liu, N. (2015). Severe myopathy in mice lacking the MEF2/SRF-dependent gene leiomodin-3. *J Clin Invest, 125*(4), 1569-1578. doi:10.1172/JCI80115

Chalfie, M., Tu, Y., Euskirchen, G., Ward, W. W., & Prasher, D. C. (1994). Green fluorescent protein as a marker for gene expression. *Science, 263*(5148), 802-805.

Chastagner, P., Israel, A., & Brou, C. (2006). Itch/AIP4 mediates Deltex degradation through the formation of K29-linked polyubiquitin chains. *EMBO Rep, 7*(11), 1147-1153. doi:10.1038/sj.embor.7400822

Chau, V., Tobias, J. W., Bachmair, A., Marriott, D., Ecker, D. J., Gonda, D. K., & Varshavsky, A. (1989). A multiubiquitin chain is confined to specific lysine in a targeted short-lived protein. *Science, 243*(4898), 1576-1583.

Chen, J. C., Mortimer, J., Marley, J., & Goldhamer, D. J. (2005). MyoD-cre transgenic mice: a model for conditional mutagenesis and lineage tracing of skeletal muscle. *Genesis, 41*(3), 116-121. doi:10.1002/gene.20104

Chen, W. L., Lin, J. W., Huang, H. J., Wang, S. M., Su, M. T., Lee-Chen, G. J., . . . Hsieh-Li, H. M. (2008). SCA8 mRNA expression suggests an antisense regulation of KLHL1 and correlates to SCA8 pathology. *Brain Res, 1233*, 176-184. doi:10.1016/j.brainres.2008.07.096

Chereau, D., Boczkowska, M., Skwarek-Maruszewska, A., Fujiwara, I., Hayes, D. B., Rebowski, G., . . . Dominguez, R. (2008). Leiomodin is an actin filament nucleator in muscle cells. *Science, 320*(5873), 239-243. doi:10.1126/science.1155313

Chowdhury, B., Tsokos, C. G., Krishnan, S., Robertson, J., Fisher, C. U., Warke, R. G., . . . Tsokos, G. C. (2005). Decreased stability and translation of T cell receptor zeta mRNA with an alternatively spliced 3'-untranslated region contribute to zeta chain down-regulation in patients with systemic lupus erythematosus. *J Biol Chem, 280*(19), 18959-18966. doi:10.1074/jbc.M501048200

Cirak, S., von Deimling, F., Sachdev, S., Errington, W. J., Herrmann, R., Bonnemann, C., . . . Voit, T. (2010). Kelch-like homologue 9 mutation is associated with an early onset autosomal dominant distal myopathy. *Brain, 133*(Pt 7), 2123-2135. doi:10.1093/brain/awq108

Clarke, N. F. (2011). Congenital fiber-type disproportion. *Semin Pediatr Neurol, 18*(4), 264-271. doi:10.1016/j.spen.2011.10.008

Collins, F. S., Finnell, R. H., Rossant, J., & Wurst, W. (2007). A new partner for the international knockout mouse consortium. *Cell, 129*(2), 235. doi:10.1016/j.cell.2007.04.007

Conen, P. E., Murphy, E. G., & Donohue, W. L. (1963). Light and Electron Microscopic Studies of "Myogranules" in a Child with Hypotonia and Muscle Weakness. *Can Med Assoc J, 89*, 983-986.

Conley, C. A. (2001). Leiomodin and tropomodulin in smooth muscle. *Am J Physiol Cell Physiol, 280*(6), C1645-1656. doi:10.1152/ajpcell.2001.280.6.C1645

Conley, C. A., Fritz-Six, K. L., Almenar-Queralt, A., & Fowler, V. M. (2001). Leiomodins: larger members of the tropomodulin (Tmod) gene family. *Genomics, 73*(2), 127-139. doi:10.1006/geno.2000.6501

Consortium, G. T. (2013). The Genotype-Tissue Expression (GTEx) project. *Nat Genet, 45*(6), 580-585. doi:10.1038/ng.2653

Costa, C. F., Rommelaere, H., Waterschoot, D., Sethi, K. K., Nowak, K. J., Laing, N. G., . . . Machesky, L. M. (2004). Myopathy mutations in alpha-skeletal-muscle actin cause a range of molecular defects. *J Cell Sci, 117*(Pt 15), 3367-3377. doi:10.1242/jcs.01172

Couto, N., Wood, J., & Barber, J. (2016). The role of glutathione reductase and related enzymes on cellular redox homoeostasis network. *Free Radic Biol Med, 95*, 27-42. doi:10.1016/j.freeradbiomed.2016.02.028

Cowan, J. L., & Morley, S. J. (2004). The proteasome inhibitor, MG132, promotes the reprogramming of translation in C2C12 myoblasts and facilitates the association of hsp25 with the eIF4F complex. *Eur J Biochem, 271*(17), 3596-3611. doi:10.1111/j.0014-2956.2004.04306.x

Davis, R. L., Weintraub, H., & Lassar, A. B. (1987). Expression of a single transfected cDNA converts fibroblasts to myoblasts. *Cell, 51*(6), 987-1000.

de Wet, J. R., Wood, K. V., DeLuca, M., Helinski, D. R., & Subramani, S. (1987). Firefly luciferase gene: structure and expression in mammalian cells. *Mol Cell Biol, 7*(2), 725-737.

Dhanoa, B. S., Cogliati, T., Satish, A. G., Bruford, E. A., & Friedman, J. S. (2013). Update on the Kelch-like (KLHL) gene family. *Hum Genomics, 7*, 13. doi:10.1186/1479-7364-7-13

Dobreva, M. P., Lhoest, L., Pereira, P. N., Umans, L., Camus, A., Chuva de Sousa Lopes, S. M., & Zwijsen, A. (2012). Periostin as a biomarker of the amniotic membrane. *Stem Cells Int, 2012*, 987185. doi:10.1155/2012/987185

Donner, K., Ollikainen, M., Ridanpaa, M., Christen, H. J., Goebel, H. H., de Visser, M., . . . Wallgren-Pettersson, C. (2002). Mutations in the beta-tropomyosin (TPM2) gene--a rare cause of nemaline myopathy. *Neuromuscul Disord, 12*(2), 151-158.

Dubowitz, V., & Sewry, C. A. (2007). *Muscle Biopsy: A practical approach* (Third ed.): Saunders, Elsevier. Ltd.

Dubowitz, V., Sewry, C. A., & Oldfors, A. (2013). *Muscle Biology* (4 ed.): Sauder, Elsevier Ltd.

Durkin, M. E., Keck-Waggoner, C. L., Popescu, N. C., & Thorgeirsson, S. S. (2001). Integration of a c-myc transgene results in disruption of the mouse Gtf2ird1 gene, the

homologue of the human GTF2IRD1 gene hemizygously deleted in Williams-Beuren syndrome. *Genomics, 73*(1), 20-27. doi:10.1006/geno.2001.6507

Engel, A. G., & Franzini-Armstrong, C. (2004). *Myology: Basic and Clinical* (3 ed. Vol. 1).

Farr, A., & Roman, A. (1992). A pitfall of using a second plasmid to determine transfection efficiency. *Nucleic Acids Res, 20*(4), 920.

Farrell, P. J., Balkow, K., Hunt, T., Jackson, R. J., & Trachsel, H. (1977). Phosphorylation of initiation factor elF-2 and the control of reticulocyte protein synthesis. *Cell, 11*(1), 187-200.

Feng, J. J., & Marston, S. (2009). Genotype-phenotype correlations in ACTA1 mutations that cause congenital myopathies. *Neuromuscul Disord, 19*(1), 6-16. doi:10.1016/j.nmd.2008.09.005

Finley, D., Sadis, S., Monia, B. P., Boucher, P., Ecker, D. J., Crooke, S. T., & Chau, V. (1994). Inhibition of proteolysis and cell cycle progression in a multiubiquitination-deficient yeast mutant. *Mol Cell Biol, 14*(8), 5501-5509.

Flick, K., Ouni, I., Wohlschlegel, J. A., Capati, C., McDonald, W. H., Yates, J. R., & Kaiser, P. (2004). Proteolysis-independent regulation of the transcription factor Met4 by a single Lys 48-linked ubiquitin chain. *Nat Cell Biol, 6*(7), 634-641. doi:10.1038/ncb1143

Fowler, V. M., & Dominguez, R. (2017). Tropomodulins and Leiomodins: Actin Pointed End Caps and Nucleators in Muscles. *Biophys J, 112*(9), 1742-1760. doi:10.1016/j.bpj.2017.03.034

Friedman, J. S., Ray, J. W., Waseem, N., Johnson, K., Brooks, M. J., Hugosson, T., . . . Swaroop, A. (2009). Mutations in a BTB-Kelch protein, KLHL7, cause autosomal-dominant retinitis pigmentosa. *Am J Hum Genet, 84*(6), 792-800. doi:10.1016/j.ajhg.2009.05.007

Frontera, W. R., & Ochala, J. (2015). Skeletal muscle: a brief review of structure and function. *Calcif Tissue Int, 96*(3), 183-195. doi:10.1007/s00223-014-9915-y

Furukawa, M., He, Y. J., Borchers, C., & Xiong, Y. (2003). Targeting of protein ubiquitination by BTB-Cullin 3-Roc1 ubiquitin ligases. *Nat Cell Biol, 5*(11), 1001-1007. doi:10.1038/ncb1056

Garg, A., O'Rourke, J., Long, C., Doering, J., Ravenscroft, G., Bezprozvannaya, S., . . . Olson, E. N. (2014). KLHL40 deficiency destabilizes thin filament proteins and promotes nemaline myopathy. *J Clin Invest, 124*(8), 3529-3539. doi:10.1172/JCI74994

Goebel, H. H., Anderson, J. R., Hubner, C., Oexle, K., & Warlo, I. (1997). Congenital myopathy with excess of thin myofilaments. *Neuromuscul Disord, 7*(3), 160-168.

Gupta, V. A., & Beggs, A. H. (2014). Kelch proteins: emerging roles in skeletal muscle development and diseases. *Skelet Muscle, 4*, 11. doi:10.1186/2044-5040-4-11

Gupta, V. A., Ravenscroft, G., Shaheen, R., Todd, E. J., Swanson, L. C., Shiina, M., . . . Beggs, A. H. (2013). Identification of KLHL41 Mutations Implicates BTB-Kelch-Mediated Ubiquitination as an Alternate Pathway to Myofibrillar Disruption in Nemaline Myopathy. *Am J Hum Genet, 93*(6), 1108-1117. doi:10.1016/j.ajhg.2013.10.020

Halim, D., Wilson, M. P., Oliver, D., Brosens, E., Verheij, J. B., Han, Y., . . . Miano, J. M. (2017). Loss of LMOD1 impairs smooth muscle cytocontractility and causes megacystis microcolon intestinal hypoperistalsis syndrome in humans and mice. *Proc Natl Acad Sci U S A, 114*(13), E2739-E2747. doi:10.1073/pnas.1620507114

Hart, T., Chandrashekhar, M., Aregger, M., Steinhart, Z., Brown, K. R., MacLeod, G., . . . Moffat, J. (2015). High-Resolution CRISPR Screens Reveal Fitness Genes and Genotype-Specific Cancer Liabilities. *Cell, 163*(6), 1515-1526. doi:10.1016/j.cell.2015.11.015

Hershko, A., Heller, H., Elias, S., & Ciechanover, A. (1983). Components of ubiquitin-protein ligase system. Resolution, affinity purification, and role in protein breakdown. *J Biol Chem, 258*(13), 8206-8214.

Hicke, L., & Dunn, R. (2003). Regulation of membrane protein transport by ubiquitin and ubiquitin-binding proteins. *Annu Rev Cell Dev Biol, 19*, 141-172. doi:10.1146/annurev.cellbio.19.110701.154617

Hughes, T. A., & Brady, H. J. (2005). Expression of axin2 is regulated by the alternative 5'-untranslated regions of its mRNA. *J Biol Chem, 280*(9), 8581-8588. doi:10.1074/jbc.M410806200

Hunt, L. T., & Dayhoff, M. O. (1977). Amino-terminal sequence identity of ubiquitin and the nonhistone component of nuclear protein A24. *Biochem Biophys Res Commun, 74*(2), 650-655.

Huxley, A. F., & Niedergerke, R. (1954). Structural changes in muscle during contraction; interference microscopy of living muscle fibres. *Nature, 173*(4412), 971-973.

Huxley, H., & Hanson, J. (1954). Changes in the cross-striations of muscle during contraction and stretch and their structural interpretation. *Nature, 173*(4412), 973-976.

Ilkovski, B., Clement, S., Sewry, C., North, K. N., & Cooper, S. T. (2005). Defining alpha-skeletal and alpha-cardiac actin expression in human heart and skeletal muscle explains the absence of cardiac involvement in ACTA1 nemaline myopathy. *Neuromuscul Disord, 15*(12), 829-835. doi:10.1016/j.nmd.2005.08.004

Ilkovski, B., Nowak, K. J., Domazetovska, A., Maxwell, A. L., Clement, S., Davies, K. E., . . . Cooper, S. T. (2004). Evidence for a dominant-negative effect in ACTA1 nemaline myopathy caused by abnormal folding, aggregation and altered polymerization of mutant actin isoforms. *Hum Mol Genet, 13*(16), 1727-1743. doi:10.1093/hmg/ddh185

Ito, N., Phillips, S. E., Yadav, K. D., & Knowles, P. F. (1994). Crystal structure of a free radical enzyme, galactose oxidase. *J Mol Biol, 238*(5), 794-814.

Jain, R. K., Jayawant, S., Squier, W., Muntoni, F., Sewry, C. A., Manzur, A., . . . Laing, N. G. (2012). Nemaline myopathy with stiffness and hypertonia associated with an ACTA1 mutation. *Neurology, 78*(14), 1100-1103. doi:10.1212/WNL.0b013e31824e8ebe

Jin, L., Pahuja, K. B., Wickliffe, K. E., Gorur, A., Baumgartel, C., Schekman, R., & Rape, M. (2012). Ubiquitin-dependent regulation of COPII coat size and function. *Nature, 482*(7386), 495-500. doi:10.1038/nature10822

Johnston, J. J., Kelley, R. I., Crawford, T. O., Morton, D. H., Agarwala, R., Koch, T., . . . Biesecker, L. G. (2000). A novel nemaline myopathy in the Amish caused by a mutation in troponin T1. *Am J Hum Genet, 67*(4), 814-821. doi:10.1086/303089

Kabsch, W., Mannherz, H. G., Suck, D., Pai, E. F., & Holmes, K. C. (1990). Atomic structure of the actin: DNase I complex. *Nature, 347*(6288), 37-44.

Kaindl, A. M., Ruschendorf, F., Krause, S., Goebel, H. H., Koehler, K., Becker, C., . . . Huebner, A. (2004). Missense mutations of ACTA1 cause dominant congenital myopathy with cores. *J Med Genet, 41*(11), 842-848. doi:10.1136/jmg.2004.020271

Kalvakolanu, D. V., Bandyopadhyay, S. K., Tiwari, R. K., & Sen, G. C. (1991). Enhancement of expression of exogenous genes by 2-aminopurine. Regulation at the post-transcriptional level. *J Biol Chem, 266*(2), 873-879.

Kasahara, K., Kawakami, Y., Kiyono, T., Yonemura, S., Kawamura, Y., Era, S., . . . Inagaki, M. (2014). Ubiquitin-proteasome system controls ciliogenesis at the initial step of axoneme extension. *Nat Commun, 5*, 5081. doi:10.1038/ncomms6081

Kasai, M., Asakura, S., & Oosawa, F. (1962). The cooperative nature of G-F transformation of actin. *Biochim Biophys Acta, 57*, 22-31.

Kaufman, R. J. (1997). DNA transfection to study translational control in mammalian cells. *Methods, 11*(4), 361-370. doi:10.1006/meth.1996.0434

Kaufman, R. J., Davies, M. V., Pathak, V. K., & Hershey, J. W. (1989). The phosphorylation state of eucaryotic initiation factor 2 alters translational efficiency of specific mRNAs. *Mol Cell Biol, 9*(3), 946-958.

Kaufman, R. J., & Murtha, P. (1987). Translational control mediated by eucaryotic initiation factor-2 is restricted to specific mRNAs in transfected cells. *Mol Cell Biol, 7*(4), 1568-1571.

Kouchi, K., Takahashi, H., & Shimada, Y. (1993). Incorporation of microinjected biotin-labelled actin into nascent myofibrils of cardiac myocytes: an immunoelectron microscopic study. *J Muscle Res Cell Motil, 14*(3), 292-301.

Kozak, M. (1987). An analysis of 5'-noncoding sequences from 699 vertebrate messenger RNAs. *Nucleic Acids Res, 15*(20), 8125-8148.

Kozak, M. (1989). Circumstances and mechanisms of inhibition of translation by secondary structure in eucaryotic mRNAs. *Mol Cell Biol, 9*(11), 5134-5142.

Kozak, M. (1991a). An analysis of vertebrate mRNA sequences: intimations of translational control. *J Cell Biol, 115*(4), 887-903.

Kozak, M. (1991b). Effects of long 5' leader sequences on initiation by eukaryotic ribosomes in vitro. *Gene Expr, 1*(2), 117-125.

Kozak, M. (1991c). Structural features in eukaryotic mRNAs that modulate the initiation of translation. *J Biol Chem, 266*(30), 19867-19870.

Kozak, M. (1997). Recognition of AUG and alternative initiator codons is augmented by G in position +4 but is not generally affected by the nucleotides in positions +5 and +6. *EMBO J, 16*(9), 2482-2492. doi:10.1093/emboj/16.9.2482

Laing, N. G. (1995). Inherited disorders of contractile proteins in skeletal and cardiac muscle. *Curr Opin Neurol, 8*(5), 391-396.

Laing, N. G., Dye, D. E., Wallgren-Pettersson, C., Richard, G., Monnier, N., Lillis, S., . . . Nowak, K. J. (2009). Mutations and polymorphisms of the skeletal muscle alpha-actin gene (ACTA1). *Hum Mutat, 30*(9), 1267-1277. doi:10.1002/humu.21059

Laing, N. G., Wilton, S. D., Akkari, P. A., Dorosz, S., Boundy, K., Kneebone, C., . . . et al. (1995). A mutation in the alpha tropomyosin gene TPM3 associated with autosomal dominant nemaline myopathy NEM1. *Nat Genet, 10*(2), 249. doi:10.1038/ng0695-249

Lecker, S. H., Goldberg, A. L., & Mitch, W. E. (2006). Protein degradation by the ubiquitin-proteasome pathway in normal and disease states. *J Am Soc Nephrol, 17*(7), 1807-1819. doi:10.1681/ASN.2006010083

Lehtokari, V. L., Pelin, K., Sandbacka, M., Ranta, S., Donner, K., Muntoni, F., . . . Wallgren-Pettersson, C. (2006). Identification of 45 novel mutations in the nebulin gene associated with autosomal recessive nemaline myopathy. *Hum Mutat, 27*(9), 946-956. doi:10.1002/humu.20370

Li, Q. K., Singh, A., Biswal, S., Askin, F., & Gabrielson, E. (2011). KEAP1 gene mutations and NRF2 activation are common in pulmonary papillary adenocarcinoma. *J Hum Genet, 56*(3), 230-234. doi:10.1038/jhg.2010.172

Li, S., Mo, K., Tian, H., Chu, C., Sun, S., Tian, L., . . . Sun, L. V. (2016). Lmod2 piggyBac mutant mice exhibit dilated cardiomyopathy. *Cell Biosci, 6*, 38. doi:10.1186/s13578-016-0101-y

Liang, X. Q., Avraham, H. K., Jiang, S., & Avraham, S. (2004). Genetic alterations of the NRP/B gene are associated with human brain tumors. *Oncogene, 23*(35), 5890-5900. doi:10.1038/sj.onc.1207776

Lin, Z., Li, S., Feng, C., Yang, S., Wang, H., Ma, D., . . . Tan, X. (2016). Stabilizing mutations of KLHL24 ubiquitin ligase cause loss of keratin 14 and human skin fragility. *Nat Genet, 48*(12), 1508-1516. doi:10.1038/ng.3701

Littlefield, R., Almenar-Queralt, A., & Fowler, V. M. (2001). Actin dynamics at pointed ends regulates thin filament length in striated muscle. *Nature Cell Biology, 3*, 544. doi:10.1038/35078517

https://www.nature.com/articles/ncb0601_544#supplementary-information

Littlefield, R. S., & Fowler, V. M. (2008a). Thin filament length regulation in striated muscle sarcomeres: Pointed-end dynamics go beyond a nebulin ruler. *Seminars in Cell & Developmental Biology, 19*(6), 511-519. doi:10.1016/j.semcdb.2008.08.009

Littlefield, R. S., & Fowler, V. M. (2008b). Thin filament length regulation in striated muscle sarcomeres: pointed-end dynamics go beyond a nebulin ruler. *Semin Cell Dev Biol, 19*(6), 511-519. doi:10.1016/j.semcdb.2008.08.009

Liu, N., Nelson, B. R., Bezprozvannaya, S., Shelton, J. M., Richardson, J. A., Bassel-Duby, R., & Olson, E. N. (2014). Requirement of MEF2A, C, and D for skeletal muscle regeneration. *Proc Natl Acad Sci U S A, 111*(11), 4109-4114. doi:10.1073/pnas.1401732111

Lorenz, W. W., Cormier, M. J., O'Kane, D. J., Hua, D., Escher, A. A., & Szalay, A. A. (1996). Expression of the Renilla reniformis luciferase gene in mammalian cells. *J Biolumin Chemilumin, 11*(1), 31-37. doi:10.1002/(SICI)1099-1271(199601)11:1<31::AID-BIO398>3.0.CO;2-M

Louis-Dit-Picard, H., Barc, J., Trujillano, D., Miserey-Lenkei, S., Bouatia-Naji, N., Pylypenko, O., . . . Jeunemaitre, X. (2012). KLHL3 mutations cause familial hyperkalemic hypertension by impairing ion transport in the distal nephron. *Nat Genet, 44*(4), 456-460, S451-453. doi:10.1038/ng.2218

Ly, T., Moroz, N., Pappas, C. T., Novak, S. M., Tolkatchev, D., Wooldridge, D., . . . Kostyukova, A. S. (2016). The N-terminal tropomyosin- and actin-binding sites are important for leiomodin 2's function. *Mol Biol Cell, 27*(16), 2565-2575. doi:10.1091/mbc.E16-03-0200

MacArthur, D. G., Seto, J. T., Raftery, J. M., Quinlan, K. G., Huttley, G. A., Hook, J. W., . . . North, K. N. (2007). Loss of ACTN3 gene function alters mouse muscle metabolism and shows evidence of positive selection in humans. *Nat Genet, 39*(10), 1261-1265. doi:10.1038/ng2122

Makela, T. P., Saksela, K., & Alitalo, K. (1989). Two N-myc polypeptides with distinct amino termini encoded by the second and third exons of the gene. *Mol Cell Biol, 9*(4), 1545-1552.

Malfatti, E., Bohm, J., Lacene, E., Beuvin, M., Romero, N. B., & Laporte, J. (2015). A Premature Stop Codon in MYO18B is Associated with Severe Nemaline Myopathy with Cardiomyopathy. *J Neuromuscul Dis, 2*(3), 219-227. doi:10.3233/JND-150085

Mathews, M. B., & Shenk, T. (1991). Adenovirus virus-associated RNA and translation control. *J Virol, 65*(11), 5657-5662.

Meriin, A. B., Gabai, V. L., Yaglom, J., Shifrin, V. I., & Sherman, M. Y. (1998). Proteasome inhibitors activate stress kinases and induce Hsp72. Diverse effects on apoptosis. *J Biol Chem, 273*(11), 6373-6379.

Miyatake, S., Mitsuhashi, S., Hayashi, Y. K., Purevjav, E., Nishikawa, A., Koshimizu, E., . . . Matsumoto, N. (2017). Biallelic Mutations in MYPN, Encoding Myopalladin, Are Associated with Childhood-Onset, Slowly Progressive Nemaline Myopathy. *Am J Hum Genet, 100*(1), 169-178. doi:10.1016/j.ajhg.2016.11.017

A Mouse for All Reasons. (2007). *Cell, 128*(1), 9-13. doi:https://doi.org/10.1016/j.cell.2006.12.018

Mouse Genome Sequencing, C., Waterston, R. H., Lindblad-Toh, K., Birney, E., Rogers, J., Abril, J. F., . . . Lander, E. S. (2002). Initial sequencing and comparative analysis of the mouse genome. *Nature, 420*(6915), 520-562. doi:10.1038/nature01262

Mustacich, D., & Powis, G. (2000). Thioredoxin reductase. *Biochem J, 346 Pt 1*, 1-8.

Nance, J. R., Dowling, J. J., Gibbs, E. M., & Bonnemann, C. G. (2012). Congenital myopathies: an update. *Curr Neurol Neurosci Rep, 12*(2), 165-174. doi:10.1007/s11910-012-0255-x

Nanda, V., & Miano, J. M. (2012). Leiomodin 1, a new serum response factor-dependent target gene expressed preferentially in differentiated smooth muscle cells. *J Biol Chem, 287*(4), 2459-2467. doi:10.1074/jbc.M111.302224

Nejepinska, J., Malik, R., Filkowski, J., Flemr, M., Filipowicz, W., & Svoboda, P. (2012). dsRNA expression in the mouse elicits RNAi in oocytes and low adenosine deamination in somatic cells. *Nucleic Acids Res, 40*(1), 399-413. doi:10.1093/nar/gkr702

Nejepinska, J., Malik, R., Moravec, M., & Svoboda, P. (2012). Deep sequencing reveals complex spurious transcription from transiently transfected plasmids. *PLoS One, 7*(8), e43283. doi:10.1371/journal.pone.0043283

Nejepinska, J., Malik, R., Wagner, S., & Svoboda, P. (2014). Reporters transiently transfected into mammalian cells are highly sensitive to translational repression induced by dsRNA expression. *PLoS One, 9*(1), e87517. doi:10.1371/journal.pone.0087517

North, K. N., Yang, N., Wattanasirichaigoon, D., Mills, M., Easteal, S., & Beggs, A. H. (1999). A common nonsense mutation results in alpha-actinin-3 deficiency in the general population. *Nat Genet, 21*(4), 353-354. doi:10.1038/7675

Nowak, K. J., Ravenscroft, G., & Laing, N. G. (2013). Skeletal muscle alpha-actin diseases (actinopathies): pathology and mechanisms. *Acta Neuropathol, 125*(1), 19-32. doi:10.1007/s00401-012-1019-z

Nowak, K. J., Sewry, C. A., Navarro, C., Squier, W., Reina, C., Ricoy, J. R., . . . Laing, N. G. (2007). Nemaline myopathy caused by absence of alpha-skeletal muscle actin. *Ann Neurol, 61*(2), 175-184. doi:10.1002/ana.21035

Nowak, K. J., Wattanasirichaigoon, D., Goebel, H. H., Wilce, M., Pelin, K., Donner, K., . . . Laing, N. G. (1999). Mutations in the skeletal muscle alpha-actin gene in patients with actin myopathy and nemaline myopathy. *Nat Genet, 23*(2), 208-212. doi:10.1038/13837

Olive, M., Janue, A., Moreno, D., Gamez, J., Torrejon-Escribano, B., & Ferrer, I. (2009). TAR DNA-Binding protein 43 accumulation in protein aggregate myopathies. *J Neuropathol Exp Neurol, 68*(3), 262-273. doi:10.1097/NEN.0b013e3181996d8f

Orrick, L. R., Olson, M. O., & Busch, H. (1973). Comparison of nucleolar proteins of normal rat liver and Novikoff hepatoma ascites cells by two-dimensional polyacrylamide gel electrophoresis. *Proc Natl Acad Sci U S A, 70*(5), 1316-1320.

Palombella, V. J., Rando, O. J., Goldberg, A. L., & Maniatis, T. (1994). The ubiquitin-proteasome pathway is required for processing the NF-kappa B1 precursor protein and the activation of NF-kappa B. *Cell, 78*(5), 773-785.

Pappas, C. T., Mayfield, R. M., Henderson, C., Jamilpour, N., Cover, C., Hernandez, Z., . . . Gregorio, C. C. (2015). Knockout of Lmod2 results in shorter thin filaments followed by dilated cardiomyopathy and juvenile lethality. *Proc Natl Acad Sci U S A, 112*(44), 13573-13578. doi:10.1073/pnas.1508273112

Pereira, P. N., Dobreva, M. P., Graham, L., Huylebroeck, D., Lawson, K. A., & Zwijsen, A. N. (2011). Amnion formation in the mouse embryo: the single amniochorionic fold model. *BMC Dev Biol, 11*, 48. doi:10.1186/1471-213X-11-48

Pettitt, S. J., Liang, Q., Rairdan, X. Y., Moran, J. L., Prosser, H. M., Beier, D. R., . . . Skarnes, W. C. (2009). Agouti C57BL/6N embryonic stem cells for mouse genetic resources. *Nat Methods, 6*(7), 493-495. doi:10.1038/nmeth.1342

Pickart, C. M., & Fushman, D. (2004). Polyubiquitin chains: polymeric protein signals. *Curr Opin Chem Biol, 8*(6), 610-616. doi:10.1016/j.cbpa.2004.09.009

Pintard, L., Willems, A., & Peter, M. (2004). Cullin-based ubiquitin ligases: Cul3-BTB complexes join the family. *EMBO J, 23*(8), 1681-1687. doi:10.1038/sj.emboj.7600186

Pollard, T. D. (1986). Rate constants for the reactions of ATP- and ADP-actin with the ends of actin filaments. *J Cell Biol, 103*(6 Pt 2), 2747-2754.

Puente, X. S., Pinyol, M., Quesada, V., Conde, L., Ordonez, G. R., Villamor, N., . . . Campo, E. (2011). Whole-genome sequencing identifies recurrent mutations in chronic lymphocytic leukaemia. *Nature, 475*(7354), 101-105. doi:10.1038/nature10113

Quinlan, K. G., Seto, J. T., Turner, N., Vandebrouck, A., Floetenmeyer, M., Macarthur, D. G., . . . North, K. N. (2010). Alpha-actinin-3 deficiency results in reduced glycogen phosphorylase activity and altered calcium handling in skeletal muscle. *Hum Mol Genet, 19*(7), 1335-1346. doi:10.1093/hmg/ddq010

Ramirez-Martinez, A., Cenik, B. K., Bezprozvannaya, S., Chen, B., Bassel-Duby, R., Liu, N., & Olson, E. N. (2017). KLHL41 stabilizes skeletal muscle sarcomeres by nonproteolytic ubiquitination. *Elife, 6*. doi:10.7554/eLife.26439

Rath, A., Glibowicka, M., Nadeau, V. G., Chen, G., & Deber, C. M. (2009). Detergent binding explains anomalous SDS-PAGE migration of membrane proteins. *Proc Natl Acad Sci U S A, 106*(6), 1760-1765. doi:10.1073/pnas.0813167106

Ravenscroft, G., Miyatake, S., Lehtokari, V. L., Todd, E. J., Vornanen, P., Yau, K. S., . . . Laing, N. G. (2013). Mutations in KLHL40 are a frequent cause of severe autosomal-recessive nemaline myopathy. *Am J Hum Genet, 93*(1), 6-18. doi:10.1016/j.ajhg.2013.05.004

Rodriguez, C. I., Buchholz, F., Galloway, J., Sequerra, R., Kasper, J., Ayala, R., . . . Dymecki, S. M. (2000). High-efficiency deleter mice show that FLPe is an alternative to Cre-loxP. *Nat Genet, 25*(2), 139-140. doi:10.1038/75973

Rothstein, J. D. (2009). Current hypotheses for the underlying biology of amyotrophic lateral sclerosis. *Ann Neurol, 65 Suppl 1*, S3-9. doi:10.1002/ana.21543

Saito, Y., Komaki, H., Hattori, A., Takeuchi, F., Sasaki, M., Kawabata, K., . . . Nishino, I. (2011). Extramuscular manifestations in children with severe congenital myopathy due to ACTA1 gene mutations. *Neuromuscul Disord, 21*(7), 489-493. doi:10.1016/j.nmd.2011.03.004

Sambuughin, N., Swietnicki, W., Techtmann, S., Matrosova, V., Wallace, T., Goldfarb, L., & Maynard, E. (2012). KBTBD13 interacts with Cullin 3 to form a functional ubiquitin ligase. *Biochem Biophys Res Commun, 421*(4), 743-749. doi:10.1016/j.bbrc.2012.04.074

Sambuughin, N., Yau, K. S., Olive, M., Duff, R. M., Bayarsaikhan, M., Lu, S., . . . Goldfarb, L. G. (2010). Dominant mutations in KBTBD13, a member of the BTB/Kelch family, cause nemaline myopathy with cores. *Am J Hum Genet, 87*(6), 842-847. doi:10.1016/j.ajhg.2010.10.020

Sandaradura, S. A., Bournazos, A., Mallawaarachchi, A., Cummings, B. B., Waddell, L. B., Jones, K. J., . . . Cooper, S. T. (2017). Nemaline myopathy and distal arthrogryposis

associated with an autosomal recessive TNNT3 splice variant. *Hum Mutat*. doi:10.1002/humu.23385

Sanoudou, D., & Beggs, A. H. (2001). Clinical and genetic heterogeneity in nemaline myopathy--a disease of skeletal muscle thin filaments. *Trends Mol Med, 7*(8), 362-368.

Sarikas, A., Hartmann, T., & Pan, Z. Q. (2011). The cullin protein family. *Genome Biol, 12*(4), 220. doi:10.1186/gb-2011-12-4-220

Sauer, B., & Henderson, N. (1988). Site-specific DNA recombination in mammalian cells by the Cre recombinase of bacteriophage P1. *Proc Natl Acad Sci U S A, 85*(14), 5166-5170.

Schiaffino, S., & Reggiani, C. (2012). *Muscle: Fundamental biology and mechanism of disease* (J. A. Hill & E. N. Olson Eds. 1st ed. Vol. Two).

Schroder, J. M., Durling, H., & Laing, N. (2004). Actin myopathy with nemaline bodies, intranuclear rods, and a heterozygous mutation in ACTA1 (Asp154Asn). *Acta Neuropathol, 108*(3), 250-256. doi:10.1007/s00401-004-0888-1

Seto, J. T., Lek, M., Quinlan, K. G., Houweling, P. J., Zheng, X. F., Garton, F., . . . North, K. N. (2011). Deficiency of alpha-actinin-3 is associated with increased susceptibility to contraction-induced damage and skeletal muscle remodeling. *Hum Mol Genet, 20*(15), 2914-2927. doi:10.1093/hmg/ddr196

Sheterline, P., Clayton, J., & Sparrow, J. C. (1998). *Actin* (Fourth ed.): Oxford: Oxford University Press.

Shi, Y., Mowery, R. A., Ashley, J., Hentz, M., Ramirez, A. J., Bilgicer, B., . . . Shaw, B. F. (2012). Abnormal SDS-PAGE migration of cytosolic proteins can identify domains and mechanisms that control surfactant binding. *Protein Sci, 21*(8), 1197-1209. doi:10.1002/pro.2107

Shibata, S., Zhang, J., Puthumana, J., Stone, K. L., & Lifton, R. P. (2013). Kelch-like 3 and Cullin 3 regulate electrolyte homeostasis via ubiquitination and degradation of WNK4. *Proc Natl Acad Sci U S A, 110*(19), 7838-7843. doi:10.1073/pnas.1304592110

Shikama, Y., Hu, H., Ohno, M., Matsuoka, I., Shichishima, T., & Kimura, J. (2010). Transcripts expressed using a bicistronic vector pIREShyg2 are sensitized to nonsense-mediated mRNA decay. *BMC Mol Biol, 11*, 42. doi:10.1186/1471-2199-11-42

Shimada, A., Komatsu, K., Nakashima, K., Poschl, E., & Nifuji, A. (2012). Improved methods for detection of beta-galactosidase (lacZ) activity in hard tissue. *Histochem Cell Biol, 137*(6), 841-847. doi:10.1007/s00418-012-0936-1

Shimomura, C., & Nonaka, I. (1989). Nemaline myopathy: comparative muscle histochemistry in the severe neonatal, moderate congenital, and adult-onset forms. *Pediatr Neurol, 5*(1), 25-31.

Shy, G. M., Engel, W. K., Somers, J. E., & Wanko, T. (1963). Nemaline Myopathy. A New Congenital Myopathy. *Brain, 86*, 793-810.

Skarnes, W. C., Auerbach, B. A., & Joyner, A. L. (1992). A gene trap approach in mouse embryonic stem cells: the lacZ reported is activated by splicing, reflects endogenous gene expression, and is mutagenic in mice. *Genes Dev, 6*(6), 903-918.

Skarnes, W. C., Rosen, B., West, A. P., Koutsourakis, M., Bushell, W., Iyer, V., . . . Bradley, A. (2011). A conditional knockout resource for the genome-wide study of mouse gene function. *Nature, 474*(7351), 337-342. doi:10.1038/nature10163

Skwarek-Maruszewska, A., Boczkowska, M., Zajac, A. L., Kremneva, E., Svitkina, T., Dominguez, R., & Lappalainen, P. (2010). Different localizations and cellular behaviors of leiomodin and tropomodulin in mature cardiomyocyte sarcomeres. *Mol Biol Cell, 21*(19), 3352-3361. doi:10.1091/mbc.E10-02-0109

Sobczak, K., & Krzyzosiak, W. J. (2002). Structural determinants of BRCA1 translational regulation. *J Biol Chem, 277*(19), 17349-17358. doi:10.1074/jbc.M109162200

Soldati, T., Schafer, B. W., & Perriard, J. C. (1990). Alternative ribosomal initiation gives rise to chicken brain-type creatine kinase isoproteins with heterogeneous amino termini. *J Biol Chem, 265*(8), 4498-4506.

Sorscher, D. H., & Cordeiro-Stone, M. (1994). Inhibition of reporter gene expression in mammalian cells. Effects of distinct carcinogen lesions in DNA. *Carcinogenesis, 15*(5), 1093-1096.

Sparrow, J. C., Nowak, K. J., Durling, H. J., Beggs, A. H., Wallgren-Pettersson, C., Romero, N., . . . Laing, N. G. (2003). Muscle disease caused by mutations in the skeletal muscle alpha-actin gene (ACTA1). *Neuromuscul Disord, 13*(7-8), 519-531.

Spence, J., Gali, R. R., Dittmar, G., Sherman, F., Karin, M., & Finley, D. (2000). Cell cycle-regulated modification of the ribosome by a variant multiubiquitin chain. *Cell, 102*(1), 67-76.

Steinhilb, M. L., Turner, R. S., & Gaut, J. R. (2001). The protease inhibitor, MG132, blocks maturation of the amyloid precursor protein Swedish mutant preventing cleavage by beta-Secretase. *J Biol Chem, 276*(6), 4476-4484. doi:10.1074/jbc.M008793200

Stogios, P. J., & Prive, G. G. (2004). The BACK domain in BTB-kelch proteins. *Trends Biochem Sci, 29*(12), 634-637. doi:10.1016/j.tibs.2004.10.003

Sumara, I., Quadroni, M., Frei, C., Olma, M. H., Sumara, G., Ricci, R., & Peter, M. (2007). A Cul3-based E3 ligase removes Aurora B from mitotic chromosomes, regulating mitotic progression and completion of cytokinesis in human cells. *Dev Cell, 12*(6), 887-900. doi:10.1016/j.devcel.2007.03.019

Sun, L., & Chen, Z. J. (2004). The novel functions of ubiquitination in signaling. *Curr Opin Cell Biol, 16*(2), 119-126. doi:10.1016/j.ceb.2004.02.005

Susaki, E. A., Tainaka, K., Perrin, D., Kishino, F., Tawara, T., Watanabe, T. M., . . . Ueda, H. R. (2014). Whole-brain imaging with single-cell resolution using chemical cocktails and computational analysis. *Cell, 157*(3), 726-739. doi:10.1016/j.cell.2014.03.042

Susaki, E. A., Tainaka, K., Perrin, D., Yukinaga, H., Kuno, A., & Ueda, H. R. (2015). Advanced CUBIC protocols for whole-brain and whole-body clearing and imaging. *Nat Protoc, 10*(11), 1709-1727. doi:10.1038/nprot.2015.085

Terenzi, F., deVeer, M. J., Ying, H., Restifo, N. P., Williams, B. R., & Silverman, R. H. (1999). The antiviral enzymes PKR and RNase L suppress gene expression from viral and non-viral based vectors. *Nucleic Acids Res, 27*(22), 4369-4375.

Testa, G., Schaft, J., van der Hoeven, F., Glaser, S., Anastassiadis, K., Zhang, Y., . . . Stewart, A. F. (2004). A reliable lacZ expression reporter cassette for multipurpose, knockout-first alleles. *Genesis, 38*(3), 151-158. doi:10.1002/gene.20012

Tian, L., Ding, S., You, Y., Li, T. R., Liu, Y., Wu, X., . . . Xu, T. (2015). Leiomodin-3-deficient mice display nemaline myopathy with fast-myofiber atrophy. *Dis Model Mech, 8*(6), 635-641. doi:10.1242/dmm.019430

Ulrich, H. D. (2002). Degradation or maintenance: actions of the ubiquitin system on eukaryotic chromatin. *Eukaryot Cell, 1*(1), 1-10.

Wallgren-Pettersson, C., & Laing, N. G. (2001). Report of the 83rd ENMC International Workshop: 4th Workshop on Nemaline Myopathy, 22-24 September 2000, Naarden, The Netherlands. *Neuromuscul Disord, 11*(6-7), 589-595.

Wang, T., Birsoy, K., Hughes, N. W., Krupczak, K. M., Post, Y., Wei, J. J., . . . Sabatini, D. M. (2015). Identification and characterization of essential genes in the human genome. *Science, 350*(6264), 1096-1101. doi:10.1126/science.aac7041

Wang, Y., Newton, D. C., Robb, G. B., Kau, C. L., Miller, T. L., Cheung, A. H., . . . Marsden, P. A. (1999). RNA diversity has profound effects on the translation of neuronal nitric oxide synthase. *Proc Natl Acad Sci U S A, 96*(21), 12150-12155.

Weber, A., Pennise, C. R., Babcock, G. G., & Fowler, V. M. (1994). Tropomodulin caps the pointed ends of actin filaments. *J Cell Biol, 127*(6 Pt 1), 1627-1635.

Werner, A., Iwasaki, S., McGourty, C. A., Medina-Ruiz, S., Teerikorpi, N., Fedrigo, I., . . . Rape, M. (2015). Cell-fate determination by ubiquitin-dependent regulation of translation. *Nature, 525*(7570), 523-527. doi:10.1038/nature14978

Yanagiya, A., Suyama, E., Adachi, H., Svitkin, Y. V., Aza-Blanc, P., Imataka, H., . . . Sonenberg, N. (2012). Translational homeostasis via the mRNA cap-binding protein, eIF4E. *Mol Cell, 46*(6), 847-858. doi:10.1016/j.molcel.2012.04.004

Yatsenko, A. N., Roy, A., Chen, R., Ma, L., Murthy, L. J., Yan, W., . . . Matzuk, M. M. (2006). Non-invasive genetic diagnosis of male infertility using spermatozoal RNA: KLHL10 mutations in oligozoospermic patients impair homodimerization. *Hum Mol Genet, 15*(23), 3411-3419. doi:10.1093/hmg/ddl417

Yerlikaya, A., Kimball, S. R., & Stanley, B. A. (2008). Phosphorylation of eIF2alpha in response to 26S proteasome inhibition is mediated by the haem-regulated inhibitor (HRI) kinase. *Biochem J, 412*(3), 579-588. doi:10.1042/BJ20080324

Yuan, W. C., Lee, Y. R., Huang, S. F., Lin, Y. M., Chen, T. Y., Chung, H. C., . . . Chen, R. H. (2011). A Cullin3-KLHL20 Ubiquitin ligase-dependent pathway targets PML to potentiate HIF-1 signaling and prostate cancer progression. *Cancer Cell, 20*(2), 214-228. doi:10.1016/j.ccr.2011.07.008

Yuan, W. C., Lee, Y. R., Lin, S. Y., Chang, L. Y., Tan, Y. P., Hung, C. C., . . . Chen, R. H. (2014). K33-Linked Polyubiquitination of Coronin 7 by Cul3-KLHL20 Ubiquitin E3 Ligase Regulates Protein Trafficking. *Mol Cell, 54*(4), 586-600. doi:10.1016/j.molcel.2014.03.035

Yuen, M., Sandaradura, S. A., Dowling, J. J., Kostyukova, A. S., Moroz, N., Quinlan, K. G., . . . Clarke, N. F. (2014). Leiomodin-3 dysfunction results in thin filament disorganization and nemaline myopathy. *J Clin Invest, 124*(11), 4693-4708. doi:10.1172/JCI75199

Zhang, D. D., Lo, S. C., Sun, Z., Habib, G. M., Lieberman, M. W., & Hannink, M. (2005). Ubiquitination of Keap1, a BTB-Kelch substrate adaptor protein for Cul3, targets Keap1 for degradation by a proteasome-independent pathway. *J Biol Chem, 280*(34), 30091-30099. doi:10.1074/jbc.M501279200

Zipper, L. M., & Mulcahy, R. T. (2002). The Keap1 BTB/POZ dimerization function is required to sequester Nrf2 in cytoplasm. *J Biol Chem, 277*(39), 36544-36552. doi:10.1074/jbc.M206530200

Zollman, S., Godt, D., Prive, G. G., Couderc, J. L., & Laski, F. A. (1994). The BTB domain, found primarily in zinc finger proteins, defines an evolutionarily conserved family that includes several developmentally regulated genes in Drosophila. *Proc Natl Acad Sci U S A, 91*(22), 10717-10721.

Chapter 7 - Appendix

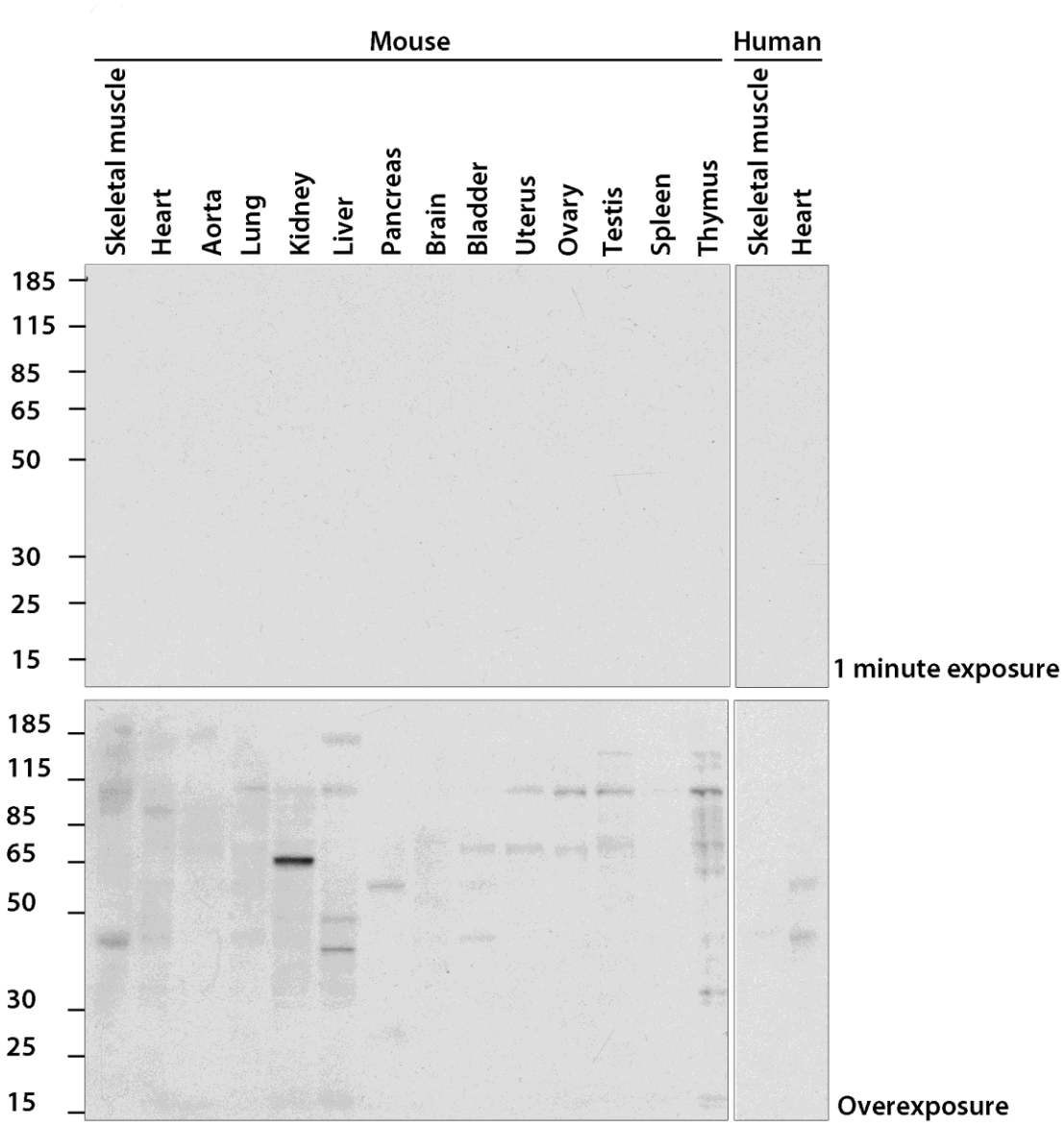

Figure A.1: Detection of IgG within tissue samples by anti-rabbit secondary antibody does not explain the banding pattern we see in mouse tissues with leiomodin antibodies. Western blot of tissues harvested from a wild type C57BL/6J mouse (lanes 1-14), human skeletal muscle (lane 15) and human heart (lane 16). Membranes were probed with the anti-rabbit secondary only. The upper blot shows no IgG detection. The lower blot is an overexposure showing a 65 kDa band only within the kidney sample.

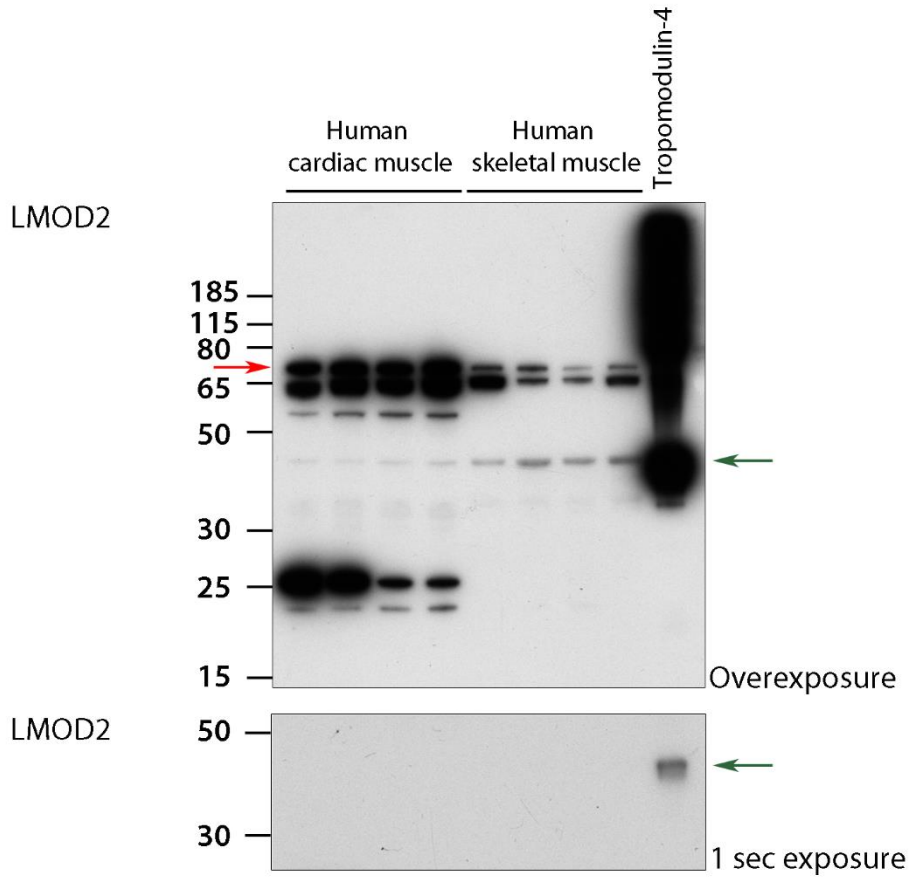

Figure A.2: The leiomodin-2 antibody cross-reacts with tropomodulin-4. Western blot of four human heart samples (10 µg), four human skeletal muscle samples (10 µg) and recombinant human tropomodulin-4 (1µg) probed for leiomodin-2 (LMOD2). The upper blot is an overexposure showing the canonical leiomodin-2 isoform (red arrow). A weak band at 45 kDa in cardiac and skeletal muscle samples aligns with recombinant tropomodulin-4 (green arrow). The position of the recombinant tropomodulin-4 is shown with a 1 second exposure (lower blot, green arrow). Human cardiac samples – ventricle; Human skeletal muscle – 5 years, 15-year quadriceps male, 31-year male, 57-year female.

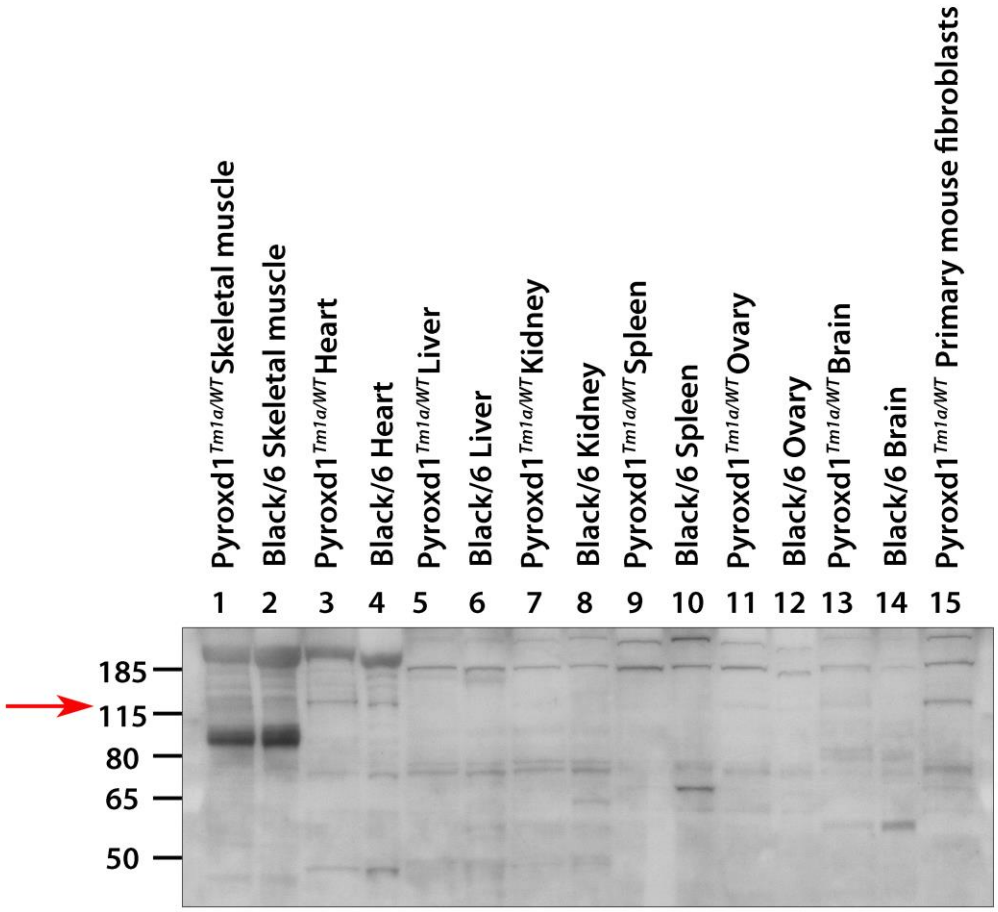

Figure A.3: Membranes probed with an antibody against β-galactosidase detects a band in negative-control mouse tissue. Western blot of tissues from Pyroxd1$^{Tm1a/WT}$ and Black/6 mice probed with an antiboday against β-galatosidase (A-11132, Molecular probes, 116 kDa). A weak band at 116 kDa is detected in Pyroxd1$^{Tm1a/WT}$ and Black/6 mouse tissues.